

# Flow mediated dilatation (FMD) assessment via an MRI integrated signal intensity (IntSI) approach: A comparison with ultrasound

by

Omodele Abosedo Olowoyeye

A thesis submitted in conformity with the requirements  
for the degree of Doctor of Philosophy

Institute of Medical Science

University of Toronto

© Copyright by Omodele A Olowoyeye 2017

# Flow mediated dilatation (FMD) assessment via an MRI integrated signal intensity (IntSI) approach: A comparison with ultrasound

Omodele A Olowoyeye

Doctor of Philosophy

Institute of Medical Science

University of Toronto

2017

## Abstract

Endothelial dysfunction is a precursor of atherosclerosis. Flow mediated dilatation (FMD) is a measure of endothelial function. Ultrasound (US) is often used during FMD studies, but US-FMD is technically challenging. MRI methods for FMD rely on high spatial resolution but this entails a trade off involving temporal resolution and SNR. An adequate temporal sampling frequency is however required to detect the peak dilatation. In this thesis, concepts in hemodynamics and MRI physics were explored in order to develop a reliable MRI-FMD technique that is comparable with US-FMD. The approach was to measure the luminal area as a function of the integrated signal intensity (IntSI) of the lumen, since signal intensity increases with area. An equation was derived to account for concurrent velocity based increases in signal intensity. Phantom studies showed the IntSI technique as a reliable means of measuring the luminal area, provided that certain assumptions are not violated. Next, the IntSI technique was adapted for in vivo application. The popliteal artery was the artery of choice based on its anatomical advantages. The velocity profile and time averaged velocities of the popliteal artery were determined from spectral Doppler analysis, in order to design an in vivo technique that is compatible with the assumptions on which the IntSI technique is based. When applied in vivo, the IntSI technique overestimated luminal area measurements compared to a conventional MRI

approach. Numerical optimization was used to obtain a correction factor to account for the bias. Subsequently, the IntSI technique was applied for measuring the luminal area during MRI-FMD and compared with US-FMD. The IntSI technique provided repeatable FMD measurements. Although the thesis did not demonstrate that the popliteal MRI-FMD using the IntSI technique was superior to US-FMD, it was non-inferior to US-FMD.

## Acknowledgments

I am deeply grateful to Dr Alan Moody for offering me an opportunity to attain this milestone in my academic pursuits. I appreciate your wisdom, counsel and great sense of humor. Thank you for your time and patience. Thanks, for giving direction at every point during this PhD project, for guiding me and getting me out of “cul- de-sacs” that I often wandered into. My sincere appreciation to my program advisory committee (PAC) members: Dr David Jenkins, Dr Graham Wright and Dr General Leung. Thank you for making time for me, despite your busy schedules. Thank you for paying attention to detail and for ensuring that this work is of good scientific quality.

It has been a great privilege working with past and present members of the vascular biology imaging research group (VBIRG). The laughter, the jokes, the birthday celebrations and the many other social interactions still put a smile on my face. You guys rock! Special thanks to Dr Stephanie Chiu, for the time you spent, patiently going over many MRI physics concepts with me. I am extremely grateful to you, for making the complex simple. I also appreciate all those who volunteered for the FMD study. Thanks for your time and for bearing with the slight discomfort associated with the procedure.

I thank my father, Oladele Arigbabu (Professor of Neurosurgery), for stimulating my young inquisitive mind. Thank you for encouraging me in my quest for knowledge. I also appreciate my step-mum, aunts, uncles, siblings, friends and in-laws. My parents-in-law, Oladayo and Modupe Olowoyeye, have been such a great support. Thank you for your encouragement, understanding and prayers.

My husband, Olufemi, has made a lot of sacrifice to ensure that I complete this PhD. Thank you so much darling. I could not have done it without you. I dedicate this thesis to you and our children, (Joshua, Esther and Mokorinayo). Thank you all, for bearing with my time constraints over the past couple of years. Special thanks to Joshua, for giving me a refresher course on high school physics and for your ideas on the flow phantom.

Most importantly, I thank God Almighty for granting me the grace to see this thesis to completion.

## Contributions

This thesis was written by the author, Omodele Olowoyeye, with corrections based on feedback from some individuals. The author also

- Derived the IntSI equation which was used to calculate area as a function of the integrated signal intensity of the lumen by adjusting for velocity dependent increases in signal intensity.
- Prepared the experimental protocol and submitted it for review at Sunnybrook hospital.
- Recruited volunteers for the study
- Performed the ultrasound procedures at Sunnybrook Hospital.
- Carried out the literature review
- Post-processed the images and analyzed the data.

The author's program advisory committee (PAC) members and other individuals contributed to the completion of the thesis.

Dr. Alan Moody (Supervisor and PAC Member) – He provided mentorship, guidance and counsel. He made available all tools required for the research. He was involved in all aspects of planning and execution of the research. He contributed to all chapters of the thesis. He also reviewed the thesis and manuscripts for publication.

Dr Graham Wright (PAC Member) – He provided mentorship and counsel. He critically assessed the theoretical basis of the thesis. He contributed towards ensuring that MRI physics concepts applied in the thesis were appropriate. He offered in guidance in data analysis. He contributed to all chapters of the thesis. He also reviewed the thesis and manuscripts for publication.

Dr. David Jenkins (PAC Member) – He provided mentorship and counsel. He critically assessed the physiological basis of the thesis. He offered guidance in data analysis. He contributed to chapter 6 of the thesis. He also reviewed the thesis and manuscripts for publication.

Dr. General Leung (PAC Member) – He proposed the concept of measuring area as a function of the integrated signal intensity of the lumen. He helped with the design of the MRI sequences. He provided counsel and critically assessed the theoretical basis of the thesis. He contributed towards ensuring that MRI physics concepts applied in the thesis were appropriate. He obtained

ethical clearance for the study and supervised the testing of the MRI sequence on healthy volunteers at St Michael's hospital. He also reviewed the thesis and manuscripts for publication.

Anthony Sheen (MRI technologist) – He carried out the MRI procedures at St Michael's hospital in consultation with Dr Leung.

Ruby Endre and Gary Detzler (MRI technologists) – Performed the MRI procedures at Sunnybrook hospital using the protocol designed at St Michael's hospital.

Dr. Pascal Tyrrell – Helped with the sample size determination, application of statistical methods and provided guidance in interpretation of the results.

Dr. Stephanie Chiu – Taught the author how to optimize sequences on an MRI scanner. She explained difficult MRI concepts to the author and gave a feedback on whether the approach considered was in line with established MRI physics principles or not. She also proof read the thesis and offered suggestions.

Micheal Pozzobon – Designed and fabricated the flow phantom at the advance machine shop of Sunnybrook Hospital.

Bart Schraa (Siemens Healthineers Canada) – Provided k-space simulations and explained the k-space trajectory used to fill the center of k-space on the Siemens scanners.

Loreta Sinn – The second rater for the inter-rater reproducibility study in chapter 5.

# Table of Contents

Acknowledgments.....	iii
Contributions.....	iv
Table of Contents.....	vi
List of Tables .....	xii
List of Figures.....	xiii
List of Abbreviations .....	xvii
Chapter 1 General Introduction and Thesis Organization.....	1
1.1 General Introduction.....	2
1.2 Thesis Organization .....	3
Chapter 2 Literature Review.....	5
2.1 Introduction.....	6
2.2 Arterial biology, pathophysiology and hemodynamics .....	7
2.2.1 Arterial biology.....	7
2.2.2 Endothelial dysfunction and vascular pathophysiology .....	13
2.2.3 Hemodynamics .....	18
2.3 Methods of evaluating vascular function.....	24
2.3.1 Measuring changes in blood flow and vascular reactivity.....	25
2.3.2 Measuring macrovascular endothelial function via flow mediated dilatation .....	26
2.3.2.8 Magnetic resonance imaging (MRI) based FMD in comparison to ultrasonography.....	39
2.4 Basic MRI physics and sequence optimization techniques .....	45
2.4.1 Spin resonance and relaxation .....	45
2.4.2 Signal acquisition.....	47
2.4.3 Pulse sequences.....	48
2.4.4 Image formation.....	51

2.4.5	Effects of sequence parameters on SNR, temporal resolution and/or spatial resolution.....	52
2.4.6	MR angiography .....	55
2.5	Thesis Aims and Hypotheses .....	61
2.5.1	Thesis Aims .....	61
2.5.2	Hypotheses.....	61
Chapter 3 Developing an MRI integrated signal intensity (IntSI) technique for measuring the luminal area and testing it in a flow phantom .....		
		62
3.1	Abstract.....	63
3.2	Introduction.....	64
3.2.1	Limitations of current FMD measurement techniques .....	64
3.2.2	Another approach for measuring area.....	65
3.2.3	Hypothesis.....	67
3.3	Materials and Methods.....	68
3.3.1	Effects of the sequence on the vascular contrast and scan time .....	68
	The CNR efficiency per unit volume was also calculated by dividing the CNR efficiency with the voxel volume.....	69
3.3.2	Deriving the integrated signal intensity equation for measuring luminal area on a spoiled gradient recalled echo (GRE) sequence.....	69
3.3.3	The phantom study.....	76
3.3.4	Statistical analyses .....	81
3.4	Results.....	83
3.4.1	Effects of the sequence on the vascular contrast and scan time .....	83
3.4.2	Effect of the velocity and entrance length mismatch on the IntSI technique. ....	84
3.4.3	Effects of pixel-to-luminal area ratio on the IntSI technique .....	85
3.4.4	Reliability of area measures using the IntSI technique versus the pixel counting approach.....	86
3.5	Discussion.....	90
3.5.1	Choosing an appropriate bright blood sequence.....	90



3.5.2	The IntSI technique and assumptions .....	90
3.5.3	Effect of the velocity profile on the IntSI technique.....	91
3.5.4	Effect of exceeding the threshold velocity on the IntSI technique .....	92
3.5.5	Effect of the pixel-to-luminal area ratio on the IntSI technique .....	92
3.5.6	Reliability of the IntSI technique.....	93
3.5.7	Comparing the IntSI technique with pixel counting.....	94
3.6	Supplementary Methods .....	95
Chapter 4 Popliteal artery spectral Doppler waveform analysis for in vivo adaptation of the IntSI technique.....		96
4.1	Abstract.....	97
4.2	Introduction.....	98
4.2.1	The assumption of parabolic flow in the popliteal artery .....	98
4.2.2	The assumption that the maximal velocity in the popliteal artery does not exceed the TOF threshold velocity .....	99
4.2.3	The pixel intensity when there is no flow during imaging .....	100
4.3	Materials and Methods.....	103
4.3.1	Theoretical calculation for the highest velocity compatible with a given entrance length for parabolic flow in the popliteal artery.....	103
4.3.2	Subject selection and control of factors that affect reactive hyperemia .....	104
4.3.3	The Ultrasound technique .....	104
4.3.4	Post processing.....	105
4.3.5	Statistical analyses .....	107
4.4	Results.....	108
4.4.1	The velocity profile of the popliteal artery .....	108
4.4.2	The maximum time averaged velocity for the threshold value.....	108
4.4.3	The time averaged velocity at baseline for the steady state value .....	109
4.5	Discussion.....	113
4.5.1	The assumption of parabolic flow in the popliteal artery .....	113
4.5.2	The assumption that the maximal velocity in the popliteal artery does not exceed the TOF threshold velocity .....	114

4.5.3	The pixel intensity when there is no flow during imaging .....	115
4.5.4	Conclusion .....	116
4.6	Supplementary .....	117
Chapter 5	Measuring the area of the popliteal artery with the IntSI technique .....	118
5.1	Abstract .....	119
5.2	Introduction .....	120
5.2.1	Vascular contrast and vessel segmentation .....	120
5.2.2	The pixel intensity when there is no flow ( $P_{SS}$ ) versus $P_B$ .....	121
5.2.3	Sequence optimization .....	121
5.2.4	Hypothesis .....	123
5.3	Materials and Methods .....	124
5.3.1	Optimizing the MRI sequence .....	124
5.3.2	Reliability of area measurements obtained with the IntSI technique .....	126
5.3.3	The correction factor .....	131
5.3.4	Statistical analyses .....	134
5.4	Results .....	136
5.4.1	Mathematical modeling for optimizing the MRI sequence .....	136
5.4.2	Reliability of area measurements with the IntSI technique .....	137
5.4.3	Effects of adding a correction factor to the IntSI equation .....	137
5.5	Discussion .....	140
5.5.1	Mathematical modeling .....	140
5.5.2	Comparison between the IntSI technique and high resolution imaging .....	141
5.5.3	Effects of adding a correction factor to the IntSI equation .....	142
5.5.4	Conclusion .....	142
5.6	Supplementary methods .....	143
5.6.1	An outline of the background subtraction technique .....	143
Chapter 6	Comparing popliteal MRI-based FMD using the IntSI technique with brachial US-FMD in healthy volunteers .....	144
6.1	Abstract .....	145

6.2	Introduction.....	146
6.2.1	Flow mediated dilatation and reactive hyperemia .....	146
6.2.2	Limitations of ultrasonography.....	147
6.2.3	Pros and cons of MRI-FMD .....	147
6.2.4	Assessing FMD and reactive hyperemia with the IntSI technique .....	148
6.2.5	Choice of the artery for measuring MRI- FMD using the IntSI technique.....	149
6.2.6	Hypothesis.....	150
6.3	Materials and Methods.....	151
6.3.1	Subject selection and control of factors that affect FMD .....	151
6.3.2	Brachial ultrasound FMD technique .....	152
6.3.3	Popliteal ultrasound FMD technique .....	153
6.3.4	Popliteal MRI-FMD technique .....	157
6.3.5	Statistical analysis.....	161
6.4	Results.....	163
6.4.1	Imaging and post processing duration .....	163
6.4.2	Characteristics of the volunteers.....	163
6.4.3	Agreement between brachial US-FMD and popliteal US-FMD.....	164
6.4.4	Popliteal Ultrasound FMD study .....	165
6.4.5	Popliteal MRI-FMD study .....	167
6.4.6	Agreement between the ultrasound and MRI based measurements .....	169
6.4.7	Variability of the ultrasound and MRI based measurements.....	172
6.4.8	Qualitative assessment of reactive hyperemia with the IntSI technique.....	173
6.4.9	Box plot for the TTP using each FMD technique.....	174
6.4.10	Indices of peak vasodilatation and various parameters.....	175
6.5	Discussion.....	176
6.5.1	Agreement between brachial ultrasound FMD and popliteal ultrasound FMD...177	177
6.5.2	Agreement between popliteal US-FMD and popliteal MRI-FMD.....	177
6.5.3	Agreement between brachial US-FMD and popliteal MRI FMD .....	179
6.5.4	Qualitative assessment of reactive hyperemia with the IntSI technique.....	179
6.5.5	Adequacy of the sampling interval of the MRI-FMD using the IntSI technique	180
6.5.6	Correlation between indices of peak vasodilatation and various parameters .....	180

6.5.7	Study limitations .....	180
6.5.8	Conclusion .....	182
6.6	Supplementary .....	183
6.6.1	Supplementary methods.....	183
6.6.2	Supplementary results.....	185
Chapter 7 Concluding Summary, General Discussion and Future Directions.....		187
7.1	Concluding Summary .....	188
7.1.1	Summary of the Literature Review.....	188
7.1.2	Summary of the Original Research.....	188
7.2	General Discussion .....	192
7.2.1	Why the MRI-based IntSI technique for FMD? .....	192
7.2.2	Adaptations that were required for in vivo application of the IntSI technique....	194
7.2.3	Effect of $P_B$ on the reliability of area measurements with the IntSI technique....	195
7.2.4	MRI-FMD using the IntSI technique versus ultrasonography.....	195
7.3	Future Directions .....	200
7.3.1	Usage of an adaptive diastolic trigger delay .....	200
7.3.2	Effect of subject characteristics, diet and exercise on FMD.....	200
7.3.3	Carotid endothelial function, carotid stiffness and aortic compliance,.....	200
References.....		203

## List of Tables

Table 2-1. A comparison between different methods used for assessing vascular function .....	39
Table 2-2. A summary of the spatial resolution, temporal resolution and reproducibility of different MRI-FMD studies .....	44
Table 3-1. Pixel areas, CNRs and scan times of the two bright blood sequences in a volunteer.	83
Table 3-2. Testing for non-inferiority between the pixel counting (Pcount) technique at 0.4 mm <sup>2</sup> pixels and those of the IntSI technique (at 0.4 mm <sup>2</sup> and 1.4 mm <sup>2</sup> pixels respectively).....	89
Table 4-1. Velocities for different phases of the cardiac cycle at baseline, during cuff inflation and during reactive hyperaemia. ....	110
Table 4-2. Duration of the different phases of the popliteal waveform.....	111
Table 5-1. Luminal area measurements of the popliteal artery obtained by high resolution imaging and the IntSI technique without (0.4P <sub>B</sub> ) and with (0.5P <sub>B</sub> ) the correction factor respectively. ....	138
Table 6-1. General characteristics of the study population.....	163
Table 6-2. Summary of the test-retest repeatability of brachial US-FMD, popliteal US-FMD and popliteal MRI-FMD .....	172
Table 6-3. Testing for non-inferiority between the intrasubject coefficient of variability (CV <sub>w</sub> ) of the FMD techniques.....	172
Table 6-4. Summary of the association between FMD and TTP in the popliteal artery with general characteristics of the volunteers. ....	175
Table 6-5. Test-retest reliability results for brachial US-FMD.....	185
Table 6-6. Test-retest reliability results for popliteal US-FMD .....	185
Table 6-7. Test-retest reliability results for popliteal MRI-FMD .....	186

## List of Figures

Figure 2-1. The endothelium and adjacent smooth muscle cell.....	14
Figure 2- 2. Shows laminar flow with a fully formed parabolic profile. ....	21
Figure 2- 3. Developing parabolic profile and the required entrance length .....	22
Figure 2-4. Effect of the magnetic field and RF pulse on the spins.....	46
Figure 2-5. Longitudinal and transverse relaxation times. ....	46
Figure 2-1. Fat and water have different longitudinal and transverse magnetization.....	48
Figure 2-7. A spin echo sequence comprising of a 90° pulse followed by a 180° refocusing pulse. .....	49
Figure 2-8. Inversion recovery sequence . ....	50
Figure 2-9. A trade-off exists between SNR, temporal and spatial resolution and the three variables are affected by various scan parameters.....	52
Figure 2-10. Effects of velocity on signal intensity.....	58
Figure 3-1. An illustration of the effect of increases the luminal area and velocity on signal intensity.....	66
Figure 3-2. Illustrations of the relationships between transverse magnetization, the number of RF pulses and blood velocity.....	72
Figure 3-3. The TOF effect within the lumen and that within a small central voxel.....	73
Figure 3-4. The phantom set-up.....	77
Figure 3-5. An image of the lower half of the flow phantom using a spoiled GRE sequence. ....	82

Figure 3-6. Box plot showing the effects of velocity and entrance length mismatch on area measurements obtained with the IntSI technique. ....	84
Figure 3-7. A scatter plot of the relative difference between observed and expected luminal area measurements versus the area ratio with the line of best fit shown.....	85
Figure 3-8. Scatter plots of observed area versus the known area using the pixel counting approach and the IntSI technique. ....	87
Figure 3-9. Bland Altman plots and ICCs (with 95% confidence intervals) of the known luminal area versus area obtained with the IntSI technique (IntSI) and the high resolution/pixel counting approach (Pcount) respectively.....	89
Figure 4-1. Cardiac gating with a diastolic trigger delay ensures that imaging does not occur during the high velocities of systole. ....	101
Figure 4-2. A schematic drawing of the spectral Doppler tracing at baseline and during hyperemia respectively. ....	105
Figure 4-3. Post processing to obtain $TAV_{max}$ and $TAV_{mean}$ .....	106
Figure 4-4. Spectral Doppler ultrasound of the popliteal artery. ....	109
Figure 4-5. Scatter plots of $TAV_{mean}$ against $TAV_{max}$ at baseline (a), during distal occlusion (b) and during reactive hyperemia (c). ....	111
Figure 5-1. As the luminal pixel intensities increase, the fitted paraboloid becomes steeper and the radius of curvature (r) becomes smaller.....	128
Figure 5-2. Application of the sliding paraboloid background subtraction technique in vivo... ..	131
Figure 5-3. The effects of retrograde and anterograde flow on the partial volume of signal void and saturated spins within the central voxel is illustrated. ....	132
Figure 5-4. Using the solver function in excel to numerically optimize the correction factor... ..	133

Figure 5-5. Images of the knee, with the popliteal artery lying posterior to the femoral condyles. .....	134
Figure 5-6. A plot of SNR versus scan time. ....	136
Figure 5-7. The scatter plots show that areas calculated using $0.5P_B$ were closer to the line of unity than those using $0.4P_B$ . ....	138
Figure 5-8. A comparison between the IntSI technique and the high resolution imaging approaches for measuring area.....	139
Figure 6-1. A schematic representation of the changes in the cross-sectional area of the vessel lumen and the blood velocity over time.....	152
Figure 6-2. Positioning for US-FMD.....	155
Figure 6-3. An ultrasound image of the popliteal artery, before and after being converted to a binary form.....	156
Figure 6- 4. Positive and negative generalized logistic curves are illustrated in broken lines, with a double Richards curve superimposed as a thick line.. ....	157
Figure 6-5. The set up for the popliteal MRI-FMD. The knee was immobilized within the knee coil and the pneumatic cuff was placed distal to the popliteal artery. ....	159
Figure 6-6. A fitted curve (red) in the post cuff deflation data of a volunteer.....	161
Figure 6-7. A comparison between brachial US-FMD and popliteal US-FMD. ....	164
Figure 6-8. A comparison between test and retest measurements of the baseline popliteal area using ultrasonography. ....	165
Figure 6-9. A comparison between test and retest measurements of popliteal FMD using ultrasonography.....	166



Figure 6-10. A comparison between test and retest measurements of the baseline popliteal area using MRI. .... 167

Figure 6-11. A comparison between test and retest measurements of popliteal FMD using MRI. .... 168

Figure 6-12. A comparison between popliteal FMD baseline area measurements using US versus MRI in 19 subjects.. .... 169

Figure 6-13. A comparison between popliteal US-FMD and popliteal MRI-FMD in 19 subjects. Each subject was scanned twice.. .... 170

Figure 6-14. A plot of reactive hyperemia calculated from US-based blood flow measurements versus the MRI surrogate that was calculated using the IntSI as a measure of blood flow..... 173

## List of Abbreviations

$\Delta L$	The maximal distance by which fresh spins advance into the slice
$\rho_c$	Lin's concordance correlation coefficient
A	Pixel area
A	Luminal area
Area ratio	The ratio of the pixel area to the luminal area
CR	Coefficient of Repeatability
GRE	Gradient recall echo
ICC	Intraclass correlation coefficient
IntSI	The integrated signal intensity of the luminal pixels
L	The slice thickness
$M_0$	The longitudinal magnetization at equilibrium
$M_{SS}$	The longitudinal magnetization at steady state
$M'_{SS}$	The transverse magnetization at steady state
MD	Mean Difference
NEX	Number of excitations
$P_B$	The brightest (central) pixel intensity of an unperturbed artery during the diastolic data acquisition period.
$P_{max}$	The brightest (central) pixel's intensity when there is flow during data acquisition
$P_{SS}$	The brightest (central) pixel's intensity when there is no flow during data acquisition
RF	Radiofrequency
$\bar{v}$	The mean luminal velocity
$V_{max}$	The maximal luminal velocity
$V_P$	The mean velocity within the central luminal voxel

---

**Chapter 1    General Introduction and Thesis  
Organization**

---

## 1.1 General Introduction

Endothelial dysfunction is a reversible precursor of atherosclerosis. Atherosclerosis results in complications such as heart attack and stroke (Chhabra, 2009). Endothelial dysfunction as a condition complies with various criteria for disease screening programs by the World Health Organization (Wilson & Jungner, 1968). Screening for endothelial dysfunction in high-risk groups provides an opportunity for early interventions aimed at improving vascular function. Macrovascular endothelial function can be assessed with a physiological test called flow mediated dilatation.

Ultrasound is the imaging modality commonly used to assess FMD. It is readily available and affordable. However, it is operator dependent and this inherent limitation of ultrasound may contribute to intra and inter-operator variability of FMD. In addition, ultrasound based FMD is technically challenging (Corretti et al., 2002). An ultrasound operator is expected to complete 100 scans under the supervision of an experienced investigator before conducting independent studies. In addition, the operator is expected to complete 100 scans annually in order to maintain a level of adequate expertise (Corretti et al., 2002). These guidelines are not easily attainable, making ultrasound based FMD not readily applicable for routine clinical practice. In addition, ultrasound measures the vessel diameter on longitudinal images, then the area is calculated based on the assumption that the lumen has a circular cross-section (Wilkinson & Webb, 2001). However, if the lumen is oval, areas calculated from the measured diameter will be smaller than expected. In addition, the maximal dilatation will be underestimated because the FMD response occurs in multiple directions across the imaging plane and by measuring only changes on the longitudinal axis subtle changes in the vessel caliber might be undetected (Chaudhry et al., 2007).

MRI does not have these limitations of ultrasound. It offers cross-sectional imaging and is not highly dependent on the operator. Although MRI is perceived to be more expensive than ultrasonography, cost-effectiveness analysis might favor MRI over ultrasonography as an imaging modality for FMD. This is possible if the MRI technique is more reliable than ultrasound technique, in which case the MRI cost may be offset by decreasing the sample size required in experimental groups. In addition, if the time required to perform MR-FMD is short

enough for the study to be included in time already earmarked for a comprehensive cardiovascular MRI study, then there will be no added cost for performing the study.

However, MRI is limited by a trade-off between spatial resolution and temporal resolution. Due to this limitation, MRI-FMD is often calculated by measuring the peak dilatation at 60 seconds (Corretti et al., 2002), but the time to peak dilatation may differ from 60 seconds. In order to accurately represent the peak dilatation during FMD, sampling interval should be less than  $\frac{1}{2}$  the time to peak according to the sampling theorem (Luke, 1999). The thesis focuses on how to obtain reliable area measurements at an adequate sampling frequency using MRI. If the MRI-FMD technique designed in this thesis is more repeatable than US-FMD, then the MRI-FMD technique may be suitable for multicenter studies.

## **1.2 Thesis Organization**

This thesis explores using an MRI technique to reliably obtain serial area measurements with less dependence on spatial resolution compared to a pixel counting area measurement approach. Chapter 2 reviews literature relevant to flow mediated dilatation, concepts in MRI physics and hemodynamics. It also contains the thesis hypotheses and research aims. Chapter 3 focuses on the theoretical basis of the integrated signal intensity (IntSI) area measurement technique and describes how different bright blood sequences were considered in order to determine which sequence would provide velocity information, optimal SNR, spatial and temporal resolution. Then it explains how the chosen sequence was applied and highlights assumptions made while designing the IntSI technique. It gives details on how the central pixel's signal intensity was used as a means of controlling the impact of velocity on the integrated signal intensity of the lumen. In this chapter, phantom experiments were used to test assumptions made while deriving the IntSI equation. The reliability of area measurements with the IntSI equation was also assessed in phantoms.

Chapter 4 is a step towards in vivo application of the IntSI technique. Spectral Doppler analysis was used to assess the profile and maximal velocity of blood flow in the popliteal artery so that the technique could be adapted for imaging a pulsatile artery. In chapter 5, the optimal sequence parameters for MRI-FMD were mathematically modeled and a post-processing technique to interrogate images and calculate FMD was described. Then the IntSI technique was used to

measure the luminal area of the popliteal artery and the measurements obtained were tested for agreement with a pixel counting approach. In Chapter 6, the IntSI approach for measuring area during popliteal MRI-FMD is applied in healthy volunteers. In this chapter, the test-retest repeatability of the popliteal MRI-FMD technique is compared with the brachial and popliteal US-FMD. Chapter 7 entails future directions such as applying the IntSI technique to assess the effects of subject characteristics on FMD. It also considers the possibility of using the IntSI technique for measuring arterial distensibility.

---

## **Chapter 2 Literature Review**

---

## 2.1 Introduction

The World Health Organization has criteria for disease screening (Wilson & Jungner, 1968) and these include

1. The condition should be an important health problem.
2. There should be a treatment for the condition.
3. Facilities for diagnosis and treatment should be available.
4. There should be a latent stage of the disease.
5. There should be a test or examination for the condition.
6. The test should be acceptable to the population.
7. The natural history of the disease should be adequately understood.
8. There should be an agreed policy on whom to treat.
9. The total cost of finding a case should be economically balanced in relation to medical expenditure as a whole.
10. Case-finding should be a continuous process, not just a "once and for all" project.

Endothelial dysfunction complies with many of the above criteria for disease screening. It is a reversible condition with an adequately understood natural history (Chhabra, 2009). Endothelial dysfunction occurs with inflammatory processes such as diabetes (Bagg et al., 2001). It might also be an underlying factor in other disease states such as preeclampsia (Yinon et al. 2010), bipolar disorder (Westman et al. 2013) and sickle cell anemia (Mohandas et al. 1985). If left untreated, endothelial dysfunction progresses to atherosclerosis and its associated complications such as heart attack and stroke which are important health conditions (Chhabra, 2009).

Cardiovascular diseases such as heart disease and stroke are two of the three leading causes of death in Canada (Statistics Canada 2011). These diseases cost the Canadian economy more than \$20.9 billion every year in healthcare services and decreased productivity (Conference Board of Canada 2011). It is important to be able to identify endothelial dysfunction in high-risk groups so that early interventions can be applied to improve vascular function.

Imaging modalities and physiologic tools have been used for monitoring the development, progression and therapeutic outcomes in patients with cardiovascular diseases or non-symptomatic high-risk groups. Many of these evaluation techniques have their limitations, as



reviewed in this chapter. Of all the imaging modalities, flow mediated dilatation assessment using ultrasonography (US-FMD) is frequently used. Equipment required for the US-FMD technique are relatively affordable and available but ultrasonography in general, is operator dependent and ultrasound based FMD is technically challenging (Corretti et al., 2002). MRI does not share these limitations of ultrasonography although it may have a higher cost per unit time. However, a cost effectiveness analysis might show MR-FMD to be relatively cheaper than ultrasound. For example, if MRI is more reliable than ultrasonography as a measurement technique for FMD, the MRI cost may be offset by decreasing the sample size required in experimental groups. In addition, if the time required to perform MR-FMD is short enough for the study to be included in time already earmarked for a comprehensive cardiovascular MRI study, then there will be no added cost for performing the study.

During an FMD study, the vessel rapidly changes in size and a high sampling frequency is needed to detect the peak dilatation, while high spatial resolution is needed for accuracy of luminal area measurement made by counting the luminal pixels. With MRI, there is a trade-off between spatial resolution and temporal resolution; this can be a drawback in applying MRI for FMD. If it is possible to design an MRI technique that obtains reliable serial area measurements at a sampling interval less than  $\frac{1}{2}$  the time to peak dilatation and the approach when applied for FMD is more repeatable than US-FMD, then the MRI-FMD technique may be suitable for multicenter studies.

The literature review is divided into three parts. The first part (section 2.2) reviews arterial biology, pathophysiology and hemodynamics. The second part (section 2.3) examines methods of measuring endothelial function and the limitations of various methods. The third part (section 2.4) explores the basic concepts in MRI physics and possible methods of optimizing MRI-FMD.

## 2.2 Arterial biology, pathophysiology and hemodynamics

### 2.2.1 Arterial biology

Each peripheral artery comprises of the tunica intima, media and adventitia (Uzwiak, 2014). The inner layer, the tunica intima comprises of a single layer of squamous endothelial cells, connective tissue and an elastic fiber base (Deanfield et al., 2007). The tunica media is the middle layer and is responsible for the vessel wall thickness and vascular tone (Standring, 2009).

This layer contains elastic tissue and one or more layers of smooth muscle cells arranged in a spiral around the long axis of the vessel. The smooth muscle cells control the blood pressure and flow rate by contracting or relaxing while the elastic fibres provide elastic recoil following distension of the artery after each cardiac pulsation (Uzwiak, 2014). The tunica adventitia is the outermost layer. It shields the vessel from injury, nourishes it and secures it to surrounding structures (Standring, 2009). It is surrounded by a mesh capillaries, lymphatics and that provide nutrients, drainage and stimuli respectively (Wheeler & Brenner, 1995).

The endothelial cells are exposed to the blood flowing in the lumen and they produce physiologically active substances (Uzwiak, 2014). Vasodilators produced include nitric oxide (NO), prostacycline (PGI<sub>2</sub>), adenosine, hydrogen peroxide(H<sub>2</sub>O<sub>2</sub>), etc., while vasoconstrictors include endothelin-1, angiotensin II, thromboxane A<sub>2</sub>, H<sub>2</sub>O<sub>2</sub>, superoxide anion (O<sub>2</sub><sup>-</sup>), etc., (Félétou & Vanhoutte, 2006). In healthy states, there is a balance between the vasodilators and vasoconstrictors (Félétou & Vanhoutte, 2006). Apart from regulating the vascular tone, endothelial cells inhibit platelet aggregation, white blood cell adhesion, and vascular smooth muscle cell proliferation (Moens et al., 2005). They also produce vascular endothelial growth factor (VEGF) which affects the growth and metabolism of surrounding tissue (Hoeben et al., 2004).

The proportion of elastic fibers and smooth muscle cells in the tunica media of each artery differ based on the function of the artery. Large arteries such as the aorta and the common carotid arteries are classified as elastic arteries. These arteries have many elastic fibers in their tunica media and are able to stretch to accommodate increased flow during systole while undergoing an elastic recoil that forces blood downstream during diastole (Uzwiak, 2014). Medium sized arteries contain relatively less elastic fibers than elastic arteries and have relatively more vascular smooth muscle cells. They include amongst others, the axillary, brachial, femoral and popliteal arteries. Prominent smooth muscle cells in these arteries help regulate blood flow via vasoconstriction and vasodilatation (Uzwiak, 2014). Arterioles are small arteries that control blood pressure. They are described as resistance vessels. When they constrict, blood pressure increases and when they dilate, there is a pressure drop leading to hyperemia. Arterioles are subject to stimuli by vasoactive substances and a network of sympathetic nerves lying on the outer layer of the arteries (Uzwiak, 2014).

### 2.2.1.1 The endothelium and nitric oxide

Nitric oxide (NO) is a potent vasodilator which plays a prominent role in the regulation of the arterial tone by activating cyclic guanosine monophosphate (cGMP) in the vascular smooth muscle cell (Joyner & Dietz, 1997). The NO-cGMP pathway is triggered when a healthy endothelium is stimulated by vasoactive substances or increased shear stress (Tousoulis et al., 2005). Specialized ion channels on endothelial cell membranes, such as calcium-activated potassium channels, open in response to shear stress and vasoactive stimuli (Corretti et al., 2002). The opening of the potassium channels hyperpolarizes the cell, leading to an influx of calcium ions (Corretti et al., 2002). Calcium triggers the conversion of L-arginine to NO by endothelial nitric oxide synthase (eNOS). Other vasoactive agents like adenosine, bradykinin, serotonin, substance P and VEGF also increase calcium entry into the cell, thereby activating eNOS (Dawson et al., 2006; Deanfield et al., 2007). After production as illustrated in figure 2-1, NO diffuses through the endothelial cells into the vascular smooth muscle cells where it influences the conversion of GTP to cGMP by guanylate cyclase (Corretti et al., 2002). cGMP probably produces vasodilatation by activating a cGMP-dependent protein kinase, inhibiting calcium entry into the vascular smooth muscle cells, activating potassium channels, or decreasing inositol trisphosphate (IP<sub>3</sub>) (Archer et al., 1994). Regular episodes of shear stress in the conduit artery during ischemic preconditioning (Luca et al., 2013) or physical exercise (Kelm, 2002) increases the expression of eNOS as well as superoxide dismutase expression (Kelm, 2002).

Furchgott and Zawadzki initially called NO an endothelial relaxing factor in 1980 when they observed that rabbit aorta needed to have an intact endothelium in order to respond to acetylcholine (Celermajer 1997). NO is a highly reactive molecule, with a half-life in blood ranging from 0.05 to 1.8ms. It is rapidly degraded in human plasma to its metabolic products such as nitrite, nitrate and S-nitrosothiols (Rassaf et al., 2002). NO has an odd number of electrons, which enables it to combine with oxygen free radicals to form the peroxynitrate ion. It may also be degraded by accepting or losing an electron to form the nitroxyl anion (NO<sup>-</sup>) or nitrosonium ion respectively (Kelm, 1998). When exogenous NO is administered intravascularly, it swiftly combines with substances in the plasma and red blood cells. It combines with plasma albumin or thiols resulting in S-nitrosoalbumin and S-nitrosothiols respectively. When directly

exposed to red blood cells (RBC), it combines with oxyhemoglobin in the RBC resulting in nitrate and methemoglobin. It may also attach to the heme portion of deoxyhemoglobin and produce nitrosylhemoglobin (Rassaf et al., 2002). Because NO is short lived in the blood, developing exogenous strategies to improve its bioavailability and improve endothelial function is a challenge.

Some authors claim that NO is predominantly responsible for flow dependent vasodilatation in conduit vessels like the radial (Joannides et al., 1995), brachial (Doshi et al., 2001) and femoral (Kooijman et al., 2008) arteries. Administration of a nitric oxide inhibitor such as NG-monomethyl-L-arginine (L-NMMA) prior to a hyperemic stimulus, nullifies the expected vasodilatory response of these macrovessels (Joannides et al., 1995; Doshi et al., 2001; Kooijman et al., 2008). Although, other authors state that NO is not obligatory for flow dependent vasodilatation of conduit arteries (Pyke et al., 2010; Wray et al., 2014). Nevertheless, flow dependent vasodilatation is used as a marker of systemic nitric oxide bioavailability (Pyke & Tschakovsky, 2005). In the microcirculation, NG-monomethyl-L-arginine only reduces the vasodilatory response of resistance vessels by 30% which suggests that chemicals like endothelium-derived hyperpolarising factor may play a part in microvascular vasodilatation (Newby et al., 1997; Sandoo et al., 2011).

### **2.2.1.2 The endothelium and other vasoactive agents**

Adenosine and adenosine triphosphate (ATP) are ischemic metabolites that may have a direct effect or an endothelial dependent effect on the microvascular smooth muscle cells. Their effect depends on the site of formation (Pasini et al., 2000; Mortensen et al., 2009). Adenosine and ATP act directly on the vascular smooth muscle cells (VSMCs) but they also have a lesser, indirect effect by stimulating receptors on the endothelium, which result in nitric oxide production and relaxation of VSMCs (Mortensen et al., 2009). Adenosine is produced in the interstitium or intraluminally by endothelial cells, platelets, red blood cells and white blood cells (Pasini et al., 2000). It provides the microvasculature with major compensatory dilatory stimuli during periods of skeletal muscle ischemia (Casey & Joyner, 2009). ATP is produced from the red blood cells during low oxygen tension and when the cells are mechanically distorted (Mortensen et al., 2009). In addition to their indirect vasodilatory effects via nitric oxide production, adenosine and ATP also act indirectly by increasing production of prostaglandins

(Casey & Joyner, 2009). Administration of NO antagonists and/or cyclooxygenase pathway blockers leads to a decrease in the vasodilatory effect of infused ATP (Mortensen et al., 2009). Prostacyclin (PGI<sub>2</sub>) is a vasodilator produced by the endothelium from arachidonic acid via the cyclooxygenase pathway and it acts independently of nitric oxide (Caughey et al., 2001; Deanfield et al., 2007). Activation of prostacyclin (IP) receptors and/or intracellular peroxisome proliferator-activated receptors (PPAR)β on the VSMC membrane triggers the effects of prostacyclin (Mitchell et al., 2008; Ozkor & Quyyumi, 2011). In addition to its vasodilatory abilities, prostacyclin decreases thrombosis risk by preventing platelet activation and it reduces cholesterol uptake and hypertrophy of the VSMCs (Nakayama 2006).

Endothelium-derived hyperpolarizing factors are substances whose endothelium dependent vasodilatory ability cannot be blocked either by inhibitors of NO synthase or cyclooxygenase (Ozkor & Quyyumi, 2011). They include chemicals like Bradykinin, and Hydrogen peroxide, which stimulate calcium-activated potassium (K<sup>+</sup><sub>Ca</sub>) channels, hyperpolarize the smooth muscle cells and lead to muscle relaxation (Ozkor & Quyyumi, 2011). The role of endothelium-derived hyperpolarizing factors in endothelial function is not completely defined and research is still ongoing (Arrebola-Moreno et al., 2012). Cytochrome-derived factors and possibly C-type natriuretic peptide have been suggested to be involved in this process, however, the effects may vary in different vascular beds (Arrebola-Moreno et al., 2012).

Endothelin-1 is a potent vasoconstrictor produced by the endothelium (Yanagisawa et al., 1988). It acts in a paracrine manner on endothelin type A (ETA) receptors on VSMCs, effecting vasoconstriction by increasing intracellular calcium (Wynne et al., 2009). It also acts in an autocrine manner when produced by smooth muscle cells in vitro (Kohan et al., 2011). Interestingly, this vasoactive chemical acts on endothelial ETA receptors, leading to NO and/or prostacyclin production (Berger et al., 2001), with resultant vasodilatation, in the absence of concomitant stimulation of the endothelin receptors on the VSMCs (Iglarz et al., 2015). Blockage of endothelin receptors in those with heart failure improves endothelium dependent vasodilatation (Berger et al., 2001).

Various chemicals stimulate endothelin-1 production in vitro such as cytokines, angiotensin II, thrombin, shear stress, hypoxia (Kohan et al., 2011). Wall shear stress also stimulates endothelin-

1 production (Berger et al., 2001). Angiotensin II is a vasoconstrictor produced by the endothelium that mediates some of its actions through endothelin-1 (Kohan et al., 2011). Angiotensin II (Ang II) causes vasoconstriction directly by stimulating angiotensin-II type 1 receptor (AT-1) present on the vasculature. It also acts indirectly by increasing sympathetic tone and arginine vasopressin release (Lavoie, 2003). Stimulation of the angiotensin-II type II receptor (AT-II) on the other hand results in vasodilatation and it has antiproliferative effects on the VSMCs (Atlas 2007).

### 2.2.1.3 The vascular smooth muscle cells and the myogenic response

The vascular smooth muscle cells of the tunica media response to vasoactive agents produced by the endothelium by contracting or relaxing. This regulates the blood pressure and flow rate (Clark & Pyne-Geithman, 2005). They may also respond to direct stimuli. For example, they relax following non-invasive administration of sublingual nitroglycerin, an exogenous nitric oxide donor, resulting in non-endothelial dependent vasodilatation (Corretti et al., 2002). Angiotensin II triggers vascular smooth muscle cells contraction, hypertrophy and sometimes hyperplasia via the AT1 receptor (Griendling et al., 1997). VSMCs contract in response to the effect of myosin light-chain kinase and the contraction can be maintained with minimal energy consumption (Clark & Pyne-Geithman 2005). Thin filament proteins regulate the phosphorylation mechanisms and tension generation in the VSMCs (Clark & Pyne-Geithman 2005).

The Bayliss effect or myogenic response is a mechanism by which resistant vessels respond to changes in the blood pressure in an attempt to regulate the blood flow. It was named after William Maddock Bayliss, a physiologist who discovered it in 1902 (Voets & Nilius, 2009). He observed that when vascular smooth muscle cells are stretched because of increased intraluminal pressure, the muscle cells contract, while they relax with a decrease in the blood pressure. Therefore, these microvessels constrict with high blood flow and dilate with low blood flow. The myogenic response can be demonstrated by all resistance vessels in vitro, but the reactions of these microvessels differ in vivo depending on their size (Pohl et al., 2000). In vivo, smaller arterioles contract with increased transmural pressure and relax when the pressure decreases, while larger arterioles and small arteries do not show this response. The reason for this

discrepancy is that the increased flow responsible for increased transmural pressure also causes shear stress on the endothelial lining of the blood vessel leading to NO production. NO counteracts the myogenic response, therefore the vessel size does not change (Pohl et al., 2000).

#### 2.2.1.4 Peripheral resistance and hyperemia

Peripheral resistance in the circulatory system is mainly due to the VSMCs of the microvasculature (Levy et al. 2008). Large arterioles and small arteries contribute up to 40-55% of the peripheral resistance in cardiac and skeletal muscles (Pohl et al., 2000). Hyperemia is a situation in which there is increased blood flow to the distal tissues (Padilla et al., 2006). It may be reactive or active. The reactive type of hyperemia occurs when a brief ischemic episode in non-active tissues causes decreased transmural pressure, lack of oxygen, with a build-up of metabolites and these result in decreased peripheral resistance, vasodilatation and increased flow (Bliss, 1998). Functional or active hyperemia, on the other hand, occurs when an exercising tissue experiences increased blood flow due to increased demand for oxygen and nutrients, with an associated build-up of vasodilatory metabolites (Padilla et al., 2006). The first 30 seconds of reactive hyperemia is due to decreased intramural pressure with a resultant decrease in the myogenic effect while the accumulation of vasodilatory metabolites plays a greater role in the hyperemic response for periods beyond 30 seconds (Björnberg et al. 1990). When the occlusion is relieved, the pressure gradient created by the dilated vascular bed leads to increased flow and hyperemia (Granger et al., 1983). With a gradual clearance of the accumulated metabolites and restoration of the transmural pressure, the artery returns to its pre-dilatation size (Granger et al., 1983).

#### 2.2.2 Endothelial dysfunction and vascular pathophysiology

Endothelial dysfunction has been defined as “the partial or complete loss of balance between vasoconstrictors and vasodilators, growth promoting and growth inhibiting factors, proatherogenic and antiatherogenic factors” (Quyyumi, 1998). In particular, it results when there is a decrease in production and/or local bioavailability of NO with a concomitant increase in endothelial derived vasoconstrictors such as endothelin-1 and angiotensin II (Chhabra, 2009). Abnormality with pathways for endothelium-dependent hyperpolarization of the vascular smooth muscle and imbalance in the levels of prostanoids, such as prostacyclin, thromboxane A<sub>2</sub>, and/or

isoprostanes can contribute to, or individually cause endothelial dysfunction (Félétou & Vanhoutte, 2006).

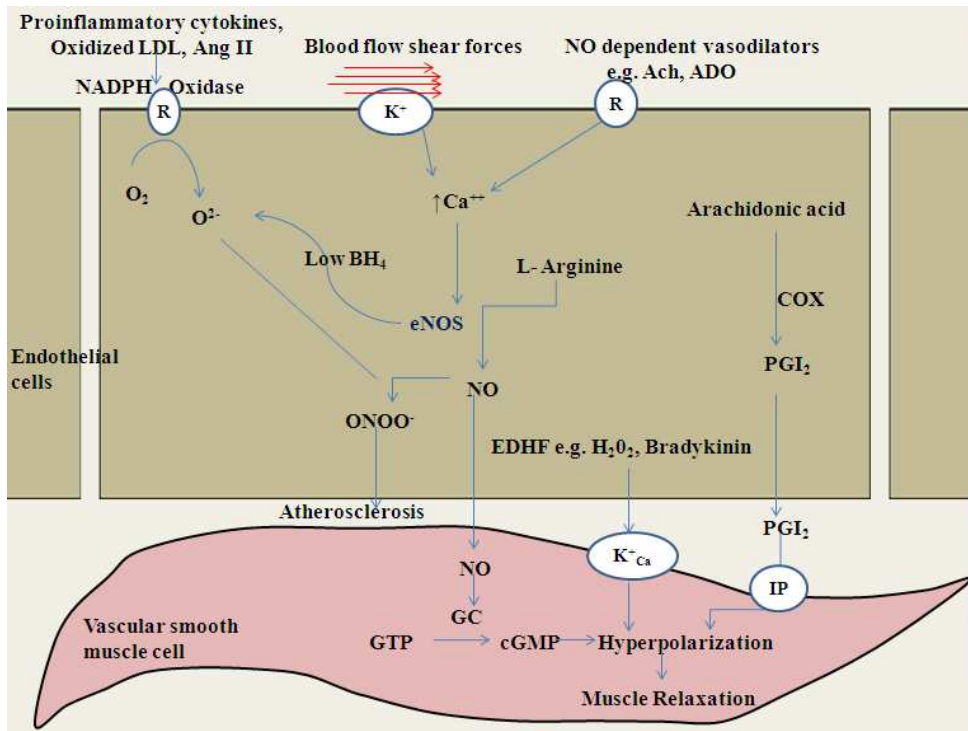


**Figure 2-1. The endothelium and adjacent smooth muscle cell.**

Nitric oxide is produced by the endothelial cells as a result of wall shear stress. It diffuses into the smooth muscle cell where it triggers muscle relaxation. PGI<sub>2</sub> and EDHF also cause vasodilatation. When BH<sub>4</sub> is low or reactive oxygen species are produced from other sources such as NADPH oxidase, ONOO<sup>-</sup> is formed which reduces the bioavailability of NO. ONOO<sup>-</sup> causes injury to the vascular wall and leads to atherosclerosis.

Apart from hypertension and diabetes, endothelial dysfunction has been implicated in other pathophysiological processes, such as renal failure, coronary syndrome, microalbuminuria, thrombosis, intravascular coagulation, sickle cell anaemia, bipolar disorder, preeclampsia, dyslipidemia, hyperhomocysteinemia, rheumatoid arthritis, periodontitis, low birth weight, mental stress, sleep apnea syndrome (Celermajer, 1997; Félétou & Vanhoutte, 2006; de Montalembert *et al.*, 2007; Yinon *et al.*, 2010; Sandoo *et al.*, 2011; Szijgyarto, 2013; Westman *et al.*, 2013). Endothelial dysfunction has also been associated with physiological states such as aging and menopause (Celermajer *et al.* 1994) and there might also be some genetic predisposition (Chhabra, 2009). In addition, habits such as cigarette smoking and a sedentary



lifestyle may contribute to endothelial dysfunction (Félétou & Vanhoutte, 2006). Endothelial dysfunction is considered a systemic disease, affecting both conduit arteries and the microcirculation. Endothelial dysfunction might independently affect both conduit and resistance vessels in those at risk for dysfunction (Sandoo et al., 2011).

### 2.2.2.1 Reactive oxygen species and endothelial dysfunction

Inflammatory processes such as diabetes, result in the release of highly reactive oxygen species (ROS) such as the peroxide ion from the mitochondrial and enzymatic sources within the endothelial cells (Dunn & Nelson, 2010). The endothelium is also exposed to ROS like the hypochlorite ion and hydroxyl radical (OH<sup>•</sup>) (Xu & Touyz, 2006). NADPH oxidase present on endothelial cell membranes is a major source of ROS in vascular cells (Xu & Touyz, 2006). ROS is produced when Angiotensin II acts on NAD(P)H oxidase receptors (Levy et al. 2008), (Figure 2-1).

Endothelial nitric oxide synthase (eNOS) could also be a potential source of O<sup>2-</sup> (Verhaar, 2004). Although the usual function of eNOS is to generate NO from L-arginine (in collaboration with several cofactors and prosthetic groups as well as the oxygen molecule and NADPH), it sometimes produces ROS (Verhaar, 2004). eNOS has an N-terminal oxygenase domain that binds tetrahydrobiopterin (BH<sub>4</sub>), oxygen, and L-arginine. This is linked by a calmodulin (CaM)-recognition site to a C-terminal reductase domain which binds NADPH, flavin mononucleotide (FMN) and flavin adenine dinucleotide (FAD) (Alderton et al., 2001). Normally, when calcium binds to the calmodulin site, which lies between the oxygenase and reductase domain of eNOS, there is a transfer of electrons from NADPH located at the reductase domain to the oxygenase domain. In the presence of tetrahydrobiopterin (BH<sub>4</sub>), this donated electron combines with O<sub>2</sub> and then L-arginine, resulting in the production of NO and L-citrulline. Skewing of this process when BH<sub>4</sub> is unavailable is called eNOS uncoupling (Verhaar, 2004). At this point, eNOS becomes a producer of O<sup>2-</sup> because the O<sub>2</sub> accepts the electron but fails to combine with L-arginine and rather turn into O<sup>2-</sup> (Wever et al., 1997), as shown in Figure 2-1. This rapidly combines with available NO forming peroxynitrite ion (ONOO<sup>-</sup>), hence a vicious cycle ensues (Mungrue & Husain, 2002). ONOO<sup>-</sup> is a powerful oxidant and it is extremely damaging to cells because it oxidizes proteins and membrane lipids (Szabó et al., 2007; Dunn & Nelson, 2010). In

states of oxidative stress and inflammation, BH<sub>4</sub> undergoes oxidation and is no longer bioavailable (Xu & Touyz, 2006). eNOS can also be activated by bradykinin during inflammation. Here, NO is generated in a non-calcium dependent manner, but this is not sufficient to counter the vasoconstrictive forces (Lowry et al., 2013).

#### 2.2.2.2 Vasoconstriction, rarefaction and endothelial dysfunction

In those at risk for endothelial dysfunction, hypertrophic remodeling of arterioles and capillary rarefaction leads to increased peripheral resistance (Levy et al 2008). Reduced bioavailability of NO results in a decrease in the forces that oppose the normal myogenic reflex in resistant vessels, therefore, vasoconstriction occurs (Pohl et al., 2000). Persistent vasoconstriction causes hypertrophy of the VSMCs and this may progress to hypertension. Vascular remodeling during periods of prolonged myogenic response occurs following the production of angiotensin II partly from the endothelium (Levy et al. 2008). In dysfunctional states, thromboxane is also produced which causes vasoconstriction and smooth muscle cells proliferation, however, some compensatory but insufficient upregulation of prostacyclin occurs in the absence of NO in an attempt to protect against the effect of these vasoconstrictors (Mitchell et al., 2008).

Microvascular rarefaction, which is a reduction in the number of resistance vessels in the tissue is associated with endothelial dysfunction and may contribute to the development of hypertension (Levy et al, 2008). Interestingly, in spontaneously hypertensive rats, rarefaction of the microvessels and apoptosis of the endothelial cells may be prevented by administering scavengers of superoxide anion (Kobayashi et al., 2005). These rats, therefore, do not develop hypertension as expected. In those already hypertensive, treatment with the scavenger is associated with decreased arterial blood pressure and improved endothelium-dependent vasodilatation (Cuzzocrea et al., 2004; Félétou & Vanhoutte, 2006).

Sometimes, blood vessels may be unresponsive to vasodilatory stimuli, even in the presence of a healthy endothelium. In this case, impairment of the VSMCs may be an underlying factor (Clark & Pyne-Geithman 2005). VSMC impairment occurs in diseases such as hypertension, ischemia and infarction (Clark & Pyne-Geithman 2005). Dysfunction of the VSMCs may be differentiated from endothelial dysfunction by administering sublingual nitroglycerine (Corretti et al., 2002).

### 2.2.2.3 Plaque formation, Intraplaque hemorrhage and endothelial dysfunction

Dysfunctional endothelial cells are more permeable to low density lipoprotein (LDL) and the presence of LDL in the endothelial cells triggers secretion of proinflammatory cytokines that attract leukocytes as well as platelets (Singh et al., 2002). Monocytes migrate into the subendothelial space of the intima, differentiate into macrophages, engulf LDL present in the intima and become foam cells (Falk, 2006). Eventually, the foam cells die but the fat deposit remains within the intima. The endothelium also secretes cytokines that encourage migration into the subendothelial space. VSMC proliferation occurs, leading to plaque formation. After a while, simple diffusion across the endothelium becomes insufficient for nourishing the intraplaque cells, leading to the production of more reactive oxygen species. These stimulate intraplaque angiogenesis and vasculogenesis by encouraging VSMC proliferation, differentiation, migration, growth and apoptosis (Xia et al., 2007). The oxygen free radicals upregulate proangiogenic factors like vascular endothelial growth factor A (VEGF-A) and basic fibroblast growth factor (bFGF), which encourage vascular growth and collateral formation restoring distal blood flow. They also influence extracellular matrix production (Xu & Touyz, 2006).

Endothelial dysfunction, generalized inflammation and metabolic factors associated with atherosclerosis also occur in these new vessels (Levy, et al. 2008). Therefore they may vasoconstrict or rupture, resulting in ischemia and intraplaque hemorrhage (Levy, et al. 2008). Hemoglobin released from lysed red blood cells contains heme, which comprises of an iron atom enclosed within a porphyrin ring (Richards et al., 2010). Iron promotes the formation of more reactive oxygen species via Fenton chemistry (Step 1:  $\text{Fe}^{2+} + \text{H}_2\text{O}_2 \rightarrow \text{Fe}^{3+} + \text{OH}\cdot + \text{OH}^-$ ; Step 2:  $\text{Fe}^{3+} + \text{H}_2\text{O}_2 \rightarrow \text{Fe}^{2+} + \text{OOH}\cdot + \text{H}^+$ ), resulting in a vicious cycle. (Levy, et al. 2008) (Richards, et al Devey 2010)

### 2.2.2.4 Thrombosis and endothelial dysfunction

Inflammation renders the intima surface thrombogenic. It encourages platelet adhesion, aggregation and deposition on dysfunction cell membranes (Elahi et al., 2009). Endothelial dysfunction encourages thrombus formation by increasing the secretion of procoagulatory factors such as tissue factor as well as plasminogen activator inhibitor (Chhabra, 2009). Increased

production of Angiotensin II may also upregulate inflammatory mediators and adhesion molecules (Levy et al., 2008). In the early stages of decreased nitric oxide bioavailability, the antithrombotic property of endothelial cells might be partially preserved by compensatory upregulation of prostacyclin (Arrebola-Moreno et al., 2012), thereby counteracting the effects of thromboxane in causing platelet activation, (Mitchell et al., 2008).

## 2.2.3 Hemodynamics

### 2.2.3.1 The driving forces within the arterial system

Daniel Bernoulli, a physician and a mathematician summarized in an equation that the total energy (TE) acting on non-viscous fluid in a straight tube consists of lateral pressure on the fluid (P) due to acceleration and deceleration, gravitational pressure and kinetic energy (Badeer, 2001).

$$TE = \text{lateral pressure} + \text{gravitational energy} + \text{Kinetic energy}$$

In adapting this equation for arterial flow, the lateral or intravascular pressure (P) comprises of the forward forces provided by cardiac contraction plus the elastic recoil of the large arteries and in addition, the hydrostatic pressure acting on the blood (Badeer, 2001; Faber & Stouffer, 2008). The hydrostatic pressure and gravitational forces are types of potential energy ( $\rho gh$ ) that depend on the weight of the blood, the acceleration due to gravity and the distance (h) between a specific arterial segment and the heart (Zierler & Sumner, 2014). While the kinetic energy ( $\frac{1}{2} \rho \bar{v}^2$ ) is the work done due to motion and it depends on the velocity and the density of the fluid (Faber & Stouffer, 2008). The total energy per unit volume of blood TE can be approximated with equation 2.1 (Zierler & Sumner, 2014).

$$TE = P + \rho gh + \frac{1}{2} \rho \bar{v}^2 \quad (2.1)$$

where P is the lateral or intravascular pressure,  $\rho$  is the blood density, g is the acceleration due to gravity, h is the distance from the heart,  $\bar{v}$  is the velocity of a blood particle moving in a straight line.

Therefore, blood will flow from a region of higher kinetic energy to a region of lower kinetic energy but the total energy will be conserved because the gravitational energy will increase (Faber & Stouffer, 2008).

### 2.2.3.2 Blood flow, pressure gradient and resistance to flow

Blood flow within the peripheral arterial system depends on the pumping action of the heart, the elastic recoil of the conduit arteries and distal microvasculature resistance (Faber & Stouffer, 2008). In the resting state, there is a forward flow in systole, followed by some flow reversal due to the high resistance offered by constricted microvascular arteries (Zierler & Sumner, 2014). Subsequently, there is a second phase of forward flow occurring due to the elastic recoil of the large arteries. For this reason, the pressure pulse contour in an unperturbed peripheral artery is triphasic and there is minimal flow in diastole due to the high peripheral resistance (Zierler & Sumner, 2014). When there is increased oxygen demand and accumulation of metabolites in the tissues, the microvascular arteries dilate leading to a pressure gradient that drives blood downstream at an increased flow rate and diastolic flow increases. The relationship between blood flow (Q), the pressure gradient ( $\Delta P$ ) and resistance to flow (R) is summarized by an equation similar to Ohm's Law in electrical circuits (Klabunde, 2007).

$$Q = \frac{\Delta P}{R} \quad (2.2)$$

Bernoulli equation is inadequate because it assumes that the fluid lies in a frictionless system and as a result, it does not account for the energy losses due to resistance to flow that occurs in vivo (Zierler & Sumner, 2014). A French physician named Poiseuille and a German named Hagen later addressed the shortcomings of Bernoulli equation (Badeer, 2001). They observed that the pressure gradient ( $\Delta P$ ) between two points on a rigid tube containing water varied directly with quantity of flow (Q), the coefficient of viscosity( $\eta$ ) and the distance between the two points (L). They also observed that it varied inversely with the fourth power of the radius (r), as shown in equation 2.3 (Badeer, 2001).

$$\Delta P = \frac{Q8L\eta}{\pi r^4} \quad (2.3)$$

Therefore, blood flow rate (Q) increases drastically with the radius of the vessel and it also increases with the pressure gradient. While the flow rate decreases with the distance between the two points and the fluid viscosity (Badeer, 2001). The great impact of the radius on the flow rate can be demonstrated using equation 2.4. If the radius of a tube doubles, it results in a sixteen fold increase in the flow rate.

$$Q = \frac{\Delta P \pi r^4}{8L\eta} \quad (2.4)$$

Using flow analogy of Ohms law,  $\Delta P = Q \cdot R$ , the relationship between all the factors that contribute to flow resistance can be extracted from equation 2.4, as shown in equation 2.5 (Zierler & Sumner, 2014)

$$R = \frac{8L\eta}{\pi r^4} \quad (2.5)$$

However, when applying the Hagen-Poiseuille equation for arterial flow, it is assumed that the vessel is straight, cylindrical and has rigid walls (Secomb & Pries, 2007). Other assumptions are that blood is an ideal Newtonian fluid with constant viscosity, while the flow is steady and laminar (Secomb & Pries, 2007).

### 2.2.3.3 Volumetric flow rate and flow continuity

In a closed flow system, the flow at every point within the system will be the same based on the law of conservation of momentum (Faber & Stouffer, 2008). Therefore if flow moves from a larger artery to a smaller artery the quantity of flow remains the same as long as there is no branching, but the velocity will increase (Zierler & Sumner, 2014).

$$Q = \bar{v}_1(\pi r^2)_1 = \bar{v}_2(\pi r^2)_2 \quad (2.6 a)$$

Where  $\bar{v}$  and  $\pi r^2$  are the mean velocities and luminal areas of the larger and smaller arteries.

Velocity can be introduced into the Hagen-Poiseuille equation by substituting for Q (Armengol et al., 2008)

$$\Delta P = \frac{Q8L\eta}{\pi r^4} = \frac{\bar{v}(\pi r^2)8L\eta}{\pi r^4} = \frac{\bar{v}8L\eta}{r^2} \quad (2.6 b)$$

If the pressure difference ( $\Delta P$ ), length (L) and viscosity ( $\eta$ ) are constant, as the radius or velocity increases, the quantity of flow (Q) increases. During local vasodilatation, both the radius and velocity increase (Badeer, 2001).

### 2.2.3.4 Energy losses due to wall shear stress and the effect on the velocity profile

The Hagen-Poiseuille equation assumes that the flow within a rigid cylindrical tube is in layers (laminar) therefore, there will be shear forces between the layers of flow (Zierler & Sumner, 2014). The shear rate ( $\gamma$ ) is the ratio of the change in velocity to the change in radius and it can

also be expressed as a function of the mean velocity ( $\bar{v}$ ) and the diameter (D) as shown below (Papaioannou & Stefanadis, 2005).

$$\dot{\gamma} = \frac{dv}{dr} \quad \text{or} \quad \dot{\gamma} = \frac{8\bar{v}}{D} \quad (2.7)$$

The amount of shear stress ( $\tau$ ) on the endothelium is calculated as a product of the coefficient of viscosity( $\eta$ ) and the shear rate (Westerhof, 2010).

$$\tau = \dot{\gamma}\eta \quad (2.8)$$

The amount of vasodilatation that occurs in conduit arteries following reactive hyperemia varies with wall shear stress but the viscosity, a factor needed to calculate shear stress is not usually measured during FMD studies (Papaioannou & Stefanadis, 2005). However, since the blood viscosity remains constant during the FMD study, shear rate is used to quantify the viscous shear forces instead (Pyke 2007),(Betik 2004). There is greater shear stress and resistance to flow at the wall compared to the center leading to the formation of a parabolic flow profile (Secomb & Pries, 2007). With parabolic flow, the central concentric lamina has the maximal velocity and the velocity decreases as the lamina gets closer to the vessel wall as illustrated in Figure 2-2. In addition, the mean velocity ( $\bar{v}$ ) is half of the maximal velocity ( $V_{\max}$ ) while the velocity at a given radius (r) from the center of the lumen is given by equation 2.9 (Hashemi, 2010). The velocity of the lamina closest to the vessel wall is zero because viscous fluids satisfy the no slip condition which states that there is no difference in velocity between a solid boundary and the adjacent fluid (Secomb & Pries, 2007).

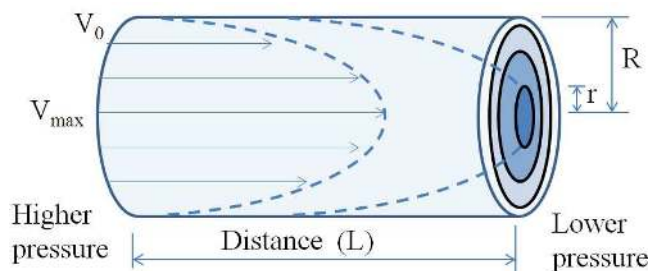


**Figure 2- 2. Shows laminar flow with a fully formed parabolic profile.** The flow is due to the pressure difference across the length of the tube. The maximal flow is at the center while there is no flow at the arterial wall.

$$V_r = V_{\max} \left( 1 - \frac{r^2}{R^2} \right) \quad (2.9)$$

Where R is the luminal radius.

### 2.2.3.5 Reynold's phenomenon, Turbulence, Entrance length for fully developed parabolic flow

Hagen-Poiseuille equation assumes that the flow is laminar however turbulence sometimes occurs as observed by Osborne Reynolds (Badeer, 2001). The Reynolds number is a dimensionless value that expresses the ratio of the inertial forces to the viscous forces that the fluid experiences (Zierler & Sumner, 2014). The Reynolds number increases with the mean velocity ( $\bar{v}$ ) and the diameter of the artery (D) while it varies inversely with the kinematic viscosity ( $\rho/\eta$ ) as shown in equation 2.10 (Mott, 2006). When the Reynolds number exceeds 2,000, turbulence occurs (Faber & Stouffer, 2008). Turbulence is unlikely in the normal peripheral arteries because the Reynolds number is usually lower than 2000 (Zierler & Sumner, 2014).

$$Re = \frac{\bar{v}D}{k_v} \quad (2.10)$$

where  $K_v$  is the kinematic viscosity.

The flow profile in peripheral arteries varies during the systolic and diastolic phases of each cardiac cycle and the velocity profile averaged across the entire cardiac cycle has a slightly blunted parabolic shape (Ade et al., 2012). Blunted parabolic velocity profiles commonly occur when flow moves from a large vessel into a smaller one and the phenomenon is called the entrance effect (Ferrara, 2000).

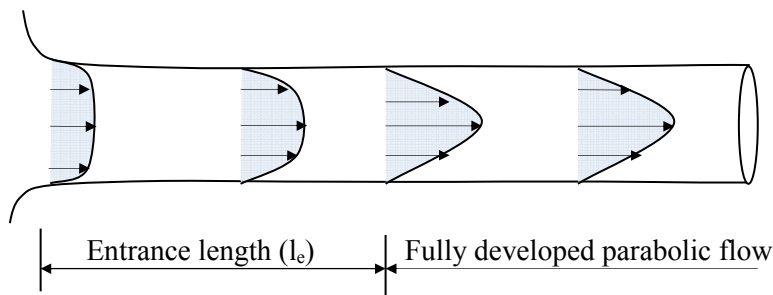


**Figure 2-3. Developing parabolic profile and the required entrance length**

(Adapted from Auld & Srinivas 2005)

The arterial flow profile also becomes blunted or skewed at points of bifurcations, branching, curvature or stenosis, with the flow profile not returning to a fully formed parabolic type until the blood has traversed a distance within the artery (Zierler & Sumner, 2014). Therefore, flow within



the artery can be divided into the developing parabolic zone and the fully formed parabolic zone (Tongpun, 2014) as shown in Figure 2-3.

The entrance length is the distance it takes for the velocity profile to revert to a fully formed parabolic shape and this distance depends on the Reynolds number as well as the diameter of the artery (Secomb & Pries, 2007). The larger the diameter and the higher the Reynolds number, the longer the entrance length. The entrance length for laminar and turbulent flow can be calculated with equations 2.11 and 2.12 respectively (Tongpun et al, 2014). These equations show that in the presence of turbulence, the entrance length will increase.

$$l_e = 0.06 D Re \quad (2.11)$$

$$l_e = 4.4 D(Re)^{1/6} \quad (2.12)$$

where  $l_e$  is the entrance length for fully developed laminar flow,  $D$  is the luminal diameter,  $Re$  is the Reynolds number, while 0.06 and 4.4 are constants specific for laminar and turbulent flow respectively. The implications of a high Reynolds number or a large diameter is that the flow in that particular artery might not become a fully formed parabolic type throughout the length of the artery and the velocity profile will be blunted (Zierler & Sumner, 2014).

### 2.2.3.6 Pulsatile flow and the Womersley number

In addition to viscous forces that explain the parabolic flow profile, arterial flow also experiences inertial forces because arterial flow is pulsatile in nature (Womersley, 1955). Inertial forces are present mainly at central portion of the flow while viscous forces occur at the boundary. The Womersley number ( $\alpha$ ) is a dimensionless number used to define the relationship between these two forces and characterize the flow profile (Womersley, 1955).

$$\alpha^2 = \frac{\text{Transient Inertial forces}}{\text{viscous forces}} = \frac{\rho \cdot \omega \cdot \bar{v}}{\mu \cdot V \cdot R^{-2}} \quad (2.13)$$

$$\alpha = R \left( \frac{\rho \cdot \omega}{\mu} \right)^{\frac{1}{2}} = R \left( \frac{\omega}{k_v} \right)^{\frac{1}{2}} \quad (2.14)$$

where  $\bar{v}$  is the mean velocity,  $R$  is the radius of the artery,  $\rho$  is the blood density,  $\mu$  is the dynamic viscosity of the blood,  $k_v$  is the kinematic viscosity of blood,  $\omega$  is the angular frequency of the arterial waveform ( $2\pi/R-R$  interval) (Du *et al.*, 2015).

The Womersley number decreases as the vessel size decreases (Ponzini *et al.*, 2010). At diameters of 10 mm, 4 mm and 1 mm for the aorta, large arteries (e.g brachial) and small arteries respectively, the values for  $\alpha$  may be calculated as 10, 4, and 1 when the blood density is  $10^3 \text{ kg/m}^3$  and the kinematic viscosity is  $5 \times 10^{-3} \text{ Pa}\cdot\text{s}$  (van de Vosse & van Dongen, 1998).

When  $\alpha$  is less than 1, the inertial forces are minimal, therefore it does not need to be taken into account when calculating the entrance length ( $l_e$ ) required for development of a parabolic velocity profile. However, when the  $\alpha$  is greater than 1, the entrance length ( $l_e$ ) is calculated as (Yamanaka *et al.*, 1999)

$$l_e = 0.3 \cdot Re \cdot \delta \quad (2.15)$$

where  $Re$  is the Reynolds number and  $\delta$  is the Stokes boundary layer, or oscillatory boundary layer.

Stokes boundary layer ( $\delta$ ) can be calculated as (Fung, 1997; Hansen & Shadden, 2016)

$$\delta = \frac{R}{\alpha} \quad (2.16)$$

where  $R$  is the radius of the arterial lumen and  $\alpha$  is the Womersley number of the specific artery. So the entrance length for pulsatile flow could also be calculated as

$$l_e = 0.3 \cdot Re \cdot \frac{R}{\alpha} \quad (2.17)$$

## 2.3 Methods of evaluating vascular function

Endothelial function can be evaluated using biomarkers and bioassays or by measuring endothelial progenitor cells, microparticles and glycocalyx (Thuillez & Richard, 2005; Lekakis *et al.*, 2011). It can also be assessed from blood flow and vascular reactivity studies (Chhabra, 2009). Direct assessment of endothelial function in the coronary arteries can be obtained by administering intracoronary vasodilatory agents during cardiac catheterization (Tousoulis *et al.*, 2005). This is considered the gold standard for assessing endothelial function and predicting acute cardiovascular events in those with and without CAD (Halcox *et al.*, 2002; Al Mheid & Quyyumi, 2013). However this method is highly invasive and has radiation risks, so it may not be appropriate as a screening tool in those at risk for endothelial dysfunction (Celermajer, 2008).

There are other less invasive or non-invasive, non-ionizing blood flow and vascular reactivity techniques for assessing endothelial function and we will focus on these for the purposes of this thesis.

### 2.3.1 Measuring changes in blood flow and vascular reactivity

#### 2.3.1.1 Strain-gauge venous occlusion plethysmography with intrabrachial infusion of endothelial agonists or reactive hyperemia

This method uses strain gauge plethysmography to measure changes in the forearm volume following occlusion of the draining vein (Wythe et al., 2015). It involves placing a blood pressure cuff around the upper arm and inflating the cuff well above the venous pressure but below the diastolic pressure. Therefore, the arterial inflow would remain unaltered but blood entering the forearm would not drain out (Wilkinson & Webb, 2001). This leads to an increase in the forearm volume which is measured with a mercury-in-silastic strain gauge placed around the examined forearm (Whitney, 1953). As long as the perfusion pressure stays the same, any increase in forearm volume, (the surrogate for arterial flow rate) is ascribed to a decrease in the peripheral resistance due to vasodilatation of the microvasculature (Benjamin et al., 1995). The arterial inflow will continue until the venous pressure matches the perfusion pressure (Wilkinson & Webb, 2001). Circulation in the hand is usually excluded from the assessment because confounding factors such as the ambient temperature markedly affect the hyperemic response observed in the wrist (Lenders et al., 1991).

Infusion of endothelial agonists such as acetylcholine through the brachial artery increases forearm blood flow and forearm volume in a NO dependent manner (Deanfield et al., 2007). Strain-gauge venous occlusion plethysmography with intrabrachial infusion of endothelial agonists is an acceptable method for early detection of endothelial dysfunction because it is reliable, reproducible and practical. However, it is not routinely applied as a screening tool for endothelial dysfunction because it is a bit invasive (Wilkinson & Webb, 2001; Deanfield et al., 2007). Strain gauge plethysmography can also be used to measure reactive hyperemia. This procedure is similar to the first however in this case, the distal cuff is placed on the forearm and inflated to 50mmHg above the systolic blood pressure for 5 minutes in order to cause distal

ischemia with serial forearm blood flow samples taken every 15 seconds after the occlusion is relieved (Tousoulis et al., 2005). When the occlusion is relieved, there is a surge of blood through the conduit artery and into the peripheral vascular bed leading to an increase in the volume of the forearm. Although venous plethysmography is able to assess microvascular function and it is less operator dependent than ultrasonography, its role in assessing macrovascular function is not completely clear. Some suggest that the endothelial function in these two vascular beds are independent of each other (Tousoulis et al., 2005; Deanfield et al., 2007; Sandoo et al., 2011).

### **2.3.1.2 Peripheral arterial tonometry (PAT)**

The fingertip pulse amplitude tonometry has also been used as a non-invasive marker for endothelial function (Celermajer, 2008). In this technique, a digital pneumatic plethysmographic cuff is placed on a finger and baseline volume changes are recorded as a measure of blood flow. Then proximal occlusion is effected by placing a blood pressure cuff on the ipsilateral upper arm for 5 minutes and hyperemia induced changes in the digital pulse amplitude is detected with a probe (Arrebola-Moreno et al., 2012). To nullify systemic influences, concurrent measurements obtained from the other index fingertip are used to normalize the measured hyperemic response (Celermajer, 2008). PAT and ultrasound-FMD have similar prognostic values in positively predicting cardiovascular events but it is not clear if their prognostic values are independent of each other (Matsuzawa et al., 2015). Concerning the reproducibility of PAT, a study suggested that PAT is more reproducible than ultrasound FMD because it is less operator dependent (Arrebola-Moreno et al. 2012) however another study disagrees (Onkelinx et al., 2012). Nevertheless, PAT does not provide the added information on macrovascular function which is predominantly nitric oxide dependent (Arrebola-Moreno et al., 2012).

### **2.3.2 Measuring macrovascular endothelial function via flow mediated dilatation**

In 1992, Celermajer and his co-authors reported that ultrasound could be used to non-invasively assess vascular function by measuring the flow-mediated dilatation (FMD) that occurs in conduit arteries like the brachial artery secondary to wall shear stress during reactive hyperemia (Celermajer et al. 1992). They created forearm ischemia with a blood pressure cuff that was

inflated up to 200mmHg for 4-5minutes and measured the percent increase in the arterial diameter between the baseline diameter and the maximal diameter recorded when the occlusion was relieved (Deanfield et al., 2007). This macrovascular flow-dependent dilatation in response to distal ischemia is predominantly mediated by nitric oxide (Joannides et al., 1995),(Stout, 2009). Forearm ischemia leads to a buildup of metabolites in the distal vascular bed with associated microvascular dilatation. Once the occlusion is relieved, there is a surge of blood through the feeding artery to supply the ischemic tissue and the resultant increased shear stress on the endothelium stimulates nitric oxide production and flow mediated dilatation occurs (Stout, 2009). Nitric oxide is predominantly responsible for flow dependent vasodilatation that occurs in macro vessels like the radial (Joannides et al., 1995), brachial (Doshi et al., 2001) and femoral (Kooijman et al., 2008) arteries following distal occlusion. Flow mediated dilatation is traditionally expressed as a percentage change in vessel diameter following reactive hyperemia, with the average baseline diameter being the reference point (Celermajer et al., 1992; Sorensen et al., 1995). Ultrasound based brachial artery flow-mediated dilatation (FMD) is widely accepted as the non-invasive gold standard for clinical research on the macrovascular endothelial function (Deanfield et al., 2007; Stoner et al., 2013). Ultrasound is readily available and affordable, however it is operator dependent and this inherent limitation of ultrasound may contribute to intra and inter operator variability of ultrasound based FMD studies (Corretti et al., 2002).

### **2.3.2.1 Clinical relevance, prognostic value and reproducibility of FMD**

FMD impairment occurs in those at risk for endothelial dysfunction before the onset of structural atherosclerotic changes in the vessel wall (Celermajer et al., 1992) and it is highly predictive of cardiovascular disease (Schroeder et al., 1999). FMD is lower in those with hypercholesterolemia or diabetes compared with healthy controls and the time to peak dilatation in these population is longer (Donald et al., 2008). FMD is recommended as a surrogate end point for intervention trials such as nutritional effects on cardiovascular health (Cudmore et al., 2012). For instance, walnuts and cocoa flavanols have a positive effect on flow mediated dilatation ( EFSA Panel on Dietetic Products, 2011),(EFSA Panel on Dietetic Products, 2012). However, some other dietary interventions have not shown a similar effect on endothelial function despite using experienced personnel and a strict FMD protocol. For example supplementation with the cocoa/tea flavonoid: epicatechin and tea flavonoid: quercetin did not

affect flow-mediated dilatation in healthy adults (Dower et al. 2015a) even though it improved biomarkers of endothelial dysfunction (Dower et al. 2015b). In another study, Hawthorn standardized extract known for its cardioprotective effects did not improve endothelial dependent vasodilatation in healthy and prehypertensive individuals (Asher et al., 2012).

In women with a previous history of preeclampsia, there is an association between prior occurrence of this disease and endothelial dysfunction (Agatista et al., 2004; Paradisi et al., 2006; Germain et al., 2007) and FMD is able to separate women with a history of early-onset preeclampsia from those who had developed preeclampsia later in their pregnancies (Yinon et al., 2010). This ability of FMD to differentiate between the groups is quite useful because early onset preeclampsia is said to be due to a dysfunction in the placental vasculature while late onset preeclampsia is not (Crispi et al., 2006). However, FMD does not always show an association with cardiovascular risk factors or cardiovascular events. In a control matched study on women with previous glucose intolerance in pregnancy, an association between previous pregnancy related glucose intolerance and endothelial dysfunction was not found even though impaired glucose tolerance is a well known for its association with diabetes and other cardiovascular risk factors (Brewster et al., 2013). Similarly, in a long term study on 1574 apparently healthy male firefighters over approximately seven years, there was no association between FMD and subsequent cardiovascular events (Anderson et al., 2011).

These differences in the ability of FMD to demonstrate improvements in endothelial function or show an association between endothelial function and cardiovascular risk may be due to its reproducibility. A case in point is results observed in two different control matched groups with type 1 diabetes mellitus. In the first group, there was a significant difference in the endothelial function of those with diabetes compared with the healthy controls, while in the second group, there was no disparity in the FMD of those with disease versus healthy controls (Hamilton et al., 2011). Power calculations show that a 4-8% intra-subject increase in FMD is beyond that due to variability, therefore, it is significant and to determine that an intervention is beneficial during clinical trials, the improvement in FMD should be at least 2% (Sorensen et al., 1995).

There have been inconsistent reports on the reproducibility of FMD (Hamilton et al., 2011). At a single experienced FMD laboratory, the coefficient of variation of ultrasound FMD was as low

as 9-10% in three reproducibility studies, spanning 1 week, 1 month, and 3 months respectively and the low variability was ascribed to thorough standardization of the technique, the use of a stereotactic clamp for probe immobilization and rigorous training of the operators (Donald et al., 2008). In this study, the variability was higher between subject than within subjects (Donald et al., 2008). The group reported similar results in a large, single-centre epidemiological study in children (Donald et al., 2010). This same group conducted a multicentre clinical trial to compare the variability between three centers, and the mean absolute difference in percent FMD for test-retest studies were 1.04%, 0.99%, and 1.45% at 48hours, 3 months and 9 months intervals respectively (Charakida et al., 2013). In another multicenter study involving seven centers and healthy volunteers, the same day coefficient of variation ranged from 7.6% to 11.9% across the centers, while the coefficient of variation after 30 days interval ranged from 11.6% to 16.1% across the centers (Ghiadoni et al., 2012).

All these studies show good reproducibility of FMD in the hands of highly trained personnel and with strict adherence to a rigorous protocol (Corretti et al., 2002). The higher variability seen in the multicenter trial (Charakida et al., 2013) at 9 months interval, despite no change in the volunteers cardiovascular risk profile, implies that over time even experienced sonographers might find it challenging to identify and repeat data acquisition at the previous arterial segment used for imaging (Charakida et al., 2013). However for FMD to be readily applicable in the diverse clinical settings, it has to be reproducible over time and less operator dependent, unlike the present situation in which the study is only performed in sophisticated research laboratories (Hamilton et al., 2011).

The reproducibility of FMD is affected by other things apart from the operator (Stoner & Sabatier, 2011). For example, expressing FMD simply as a percentage may limit the statistical power because if the variance of the baseline diameter is large between groups, the percent FMD will be skewed towards groups with smaller baseline values (Vickers, 2001). A better option is to use the analysis of covariance (ANCOVA) with the baseline diameter as a covariate in order to improve the statistical power of the analysis (Stoner et al., 2013). Another factor affecting the reproducibility of FMD is the confounding effect of shear stress as FMD depends on the magnitude of the shear stress (Pyke & Tschakovsky, 2005). Various methods that have been devised to account for the confounding effect of shear rate and baseline diameter on

vasodilatation will be discussed further in this section. In addition, the peak dilatation is transient because it depends on the short-lived increased shear stress that occurs during reactive hyperemia and the peak value may not be adequately captured during the study due to measurement error (Stoner & Sabatier, 2011). A shear rate-diameter-response curve can be used to address the effect of shear stress in order to accurately assess the endothelial function (Stoner et al., 2013). The operator dependence of ultrasound FMD contributes to the measurement error and this can be reduced repeating the test several times (Stoner et al., 2013).

### 2.3.2.2 Effects of baseline diameter, hyperemia, and shear rate on flow mediated dilatation (FMD).

FMD depends on the wall shear stress that occurs during reactive hyperemia and this depends on the pressure gradient between the conduit artery and the microvasculature and this in turn depends on the microvascular resistance (Gibbs et al., 2011). In apparently healthy individuals, FMD inversely correlates with the resting microvascular resistance, an estimate calculated as the quotient of mean arterial blood pressure and forearm blood flow (Lauer et al., 2008). Based on the relationship between reactive hyperemia and FMD, one expects that the peak FMD will occur at the same time as the peak hyperemia. Interestingly, this is not the case as there is a delay between the peak of the hyperemic response and the maximal vessel diameter during FMD. It is suggested that the reason for the delayed response is that when the wall shear stress is high, there is increased transmural pressure and an associated vasoconstrictory myogenic response by the vascular smooth muscle cells. Consequently, although nitric acid is released throughout the period of elevated shear stress, its vasodilatation effect is only appreciated when the transmural pressure decreases and the myogenic response wanes (Jiang et al., 2011).

Reactive hyperemia is calculated as the ratio of the maximum flow recorded after the cuff deflation to the baseline flow (Celermajer et al., 1992). However, this is not a very good estimate of the degree of shear stress that the macrovascular endothelium is exposed to because the quantity of flow increases as the baseline diameter increases while the shear stress decreases as the baseline diameter increases (Pyke & Tschakovsky, 2005). As discussed in section 2.2.3.4, shear stress is a product of the coefficient of viscosity ( $\eta$ ) and the shear rate (Westerhof, 2010). The blood viscosity is not routinely measured during FMD studies since it does not vary within the study. Rather, shear rate is used to quantify the degree of wall shear (Betik et al., 2004; Pyke



& Tschakovsky, 2007). Shear rate depends on the mean velocity and the arterial size (Papaioannou & Stefanadis, 2005). The higher the velocity, the greater the wall shear rate and the smaller the vessel size, the greater the wall shear rate. For a given flow rate, the velocity increases as the vessel size decreases due to the law of conservation of momentum (Faber & Stouffer, 2008). This partly explains why smaller arteries show a greater FMD response than larger ones (Celermajer et al., 1992). The conduit artery vasomotor tone (CAVT), may be another reason for the inverse relationship between FMD and the baseline diameter (Lauer et al., 2008). CAVT is calculated as the change in diameter from baseline to maximal (NTG) dilatation as a percentage of the maximal (NTG) dilatation (Schächinger & Zeiher, 1995). When the baseline CAVT is high, FMD is higher and it has been suggested that the resting microvascular resistance regulates FMD by adjusting baseline CAVT (Lauer et al., 2008).

A third reason why the smaller arteries show a better FMD response is because flow mediated dilatation is usually expressed as the relative change in arterial size from the baseline value, meaning that for a given absolute increase in the arterial size, if the baseline value is small, the percentage increase in FMD will be large (Charakida et al., 2010). The percentage FMD index is supposed to scale the change in diameter to the baseline diameter but this technique has the potential to add bias to conclusions made on endothelial function between groups because of the negative correlation between it and the baseline diameter (Atkinson & Batterham, 2013). In addition, the percentage FMD index has a high variability and roughly two-thirds of the variability is ascribed to the baseline diameter of the artery (Celermajer et al., 1992; Pyke et al., 2004). However, the baseline diameter itself is important as a predictor of cardiovascular risk and subclinical progression of atherosclerosis (Halcox et al., 2009; Yeboah et al., 2009; Atkinson, 2014).

Normalizing the FMD response to the area under the shear rate graph was proposed as a means of determining whether a poor FMD response is because of macrovascular endothelial dysfunction or because the shear stress was low (Pyke & Tschakovsky, 2007). This approach has been criticized because normalizing FMD with the shear rate-AUC is not able to reflect the effect of shear stress on the degree of vasodilatation that occurs at each time points during FMD (Harris et al., 2010). In addition, there is not sufficient evidence in support of an association between FMD shear stress-AUC in children and older adults (Thijssen et al., 2009). Healthy

older adults have a low shear rate so normalizing FMD with their low shear rate gives results suggestive that their endothelial function is preserved despite the fact that endothelial dysfunction is associated with aging (Celermajer et al., 1994; Padilla et al., 2009).

Analysis of covariance (ANCOVA) has been suggested as a better approach for ratio normalization of FMD with shear rate (Harris & Padilla, 2007; Atkinson et al., 2009). However, others have expressed reservations about using ANCOVA because this approach is based on assumptions such as the data being normally distributed, at least moderate correlation between shear and FMD, a linear relationship in existence between shear and diameter with the intercept for the regression slope at zero and the variance being similar between groups (Tschakovsky et al., 2007; Stoner et al., 2013). However, these assumptions may not always hold true as observed in a study involving children, young and older adults (Atkinson et al., 2009). In this study, the y-intercept for the SR-FMD regression graph was greater than zero, the relationship between the normalized FMD and SR was nonlinear and unstable, the data was not normally distributed and the variance differed between the groups (Atkinson et al., 2009).

Another option put forward is that FMD should be expressed by manipulating the shear stimulus using progressive durations of forearm ischemia and plotting shear rate: diameter dose response curve where the slope of the curve represents the endothelial function (Stoner et al., 2008; Stoner & Sabatier, 2011). Advantages of this approach are that the effect of the shear stimulus on FMD is reflected in a way that does not violate statistical assumptions and measurement reliability will improve with this method (Stoner & Sabatier, 2011).

Another method for assessing the effect of shear rate on FMD is by adding exercise or hand warming to the protocol (Betik et al., 2004; Stoner & McCully, 2012). This approach was considered because reactive hyperemia provides a brief an uncontrolled shear stimulus while exercise is likely to result in a more sustained stimulus that can be matched with the vasodilatory response (Pyke & Jazuli, 2011). The relationship between the ischemic induced shear stimulus and vasodilatation is comparable to that of handgrip exercise induced or hand warming induced shear stimuli and vasodilatation (Pyke & Jazuli, 2011; Stoner & McCully, 2012). In fact, handgrip exercise detects vascular dysfunction in young healthy smokers unlike reactive hyperemia based FMD (Findlay et al., 2013). An important point is that it is difficult to identify

if the dilatation that occurs secondary to sustained shear stress is NO dependent (Stoner & Sabatier, 2011). Some evidence exists in support of the opinion that sustained shear stress is not NO dependent (Mullen et al., 2001) but there is also contrary evidence suggesting that NO plays a part in handgrip exercise FMD (Wray et al., 2011). If the intention of an FMD study is to determine NO bioavailability, then it is better to use a method that is clearly nitric oxide dependent (Pyke & Tschakovsky, 2005).

In addition, normalizing FMD with the shear rate is said to be inappropriate since they both factors are independently affected by the baseline diameter (Atkinson, 2014). Rather, allometric scaling has been proposed as a means of removing the dependence of FMD on baseline diameter so that the true effect of shear rate on FMD can be measured (Atkinson, 2014). Allometry, also called biological scaling, denotes how measured changes in biological rates or magnitudes vary with the size (Gittleman, 2016). Biological rates such as basal metabolic rate, life span, growth rate, heart rate, etc, and magnitudes such as tree heights, aortic lengths, mitochondrial densities, etc, all obey allometric scaling laws (West & Brown, 2005).

FMD is a change in magnitude that varies with baseline diameter and shear rate. With allometric scaling, the percent FMD and shear rate are logarithmically transformed before their ratio is calculated in order to determine the nature, size, and consistency of the relationship that exists between the two variables (Atkinson et al., 2009). So instead of expressed FMD as a percentage of the baseline, or normalizing the percent FMD with the shear rate, a power function is used to define the vasodilatation (Atkinson et al., 2009).

$$\text{Normalized FMD} = \text{FMD}/\text{SR}^k$$

where  $k$  is the coefficient of allometry (an exponential term that expressed the relationship between the variables).

Allometric scaling is said to pose new interpretive challenges because scaling the FMD response with the baseline diameter might weaken the relationship between flow dependent vasodilatation and CVD because percent FMD integrates the independent prognostic values of baseline diameter and change in diameter on cardiovascular disease outcomes (Al Mheid & Quyyumi, 2013). They also questioned whether FMD should be allometrically scaled to a different measure of body size rather than the baseline diameter. However, proponents of allometric scaling disagree on these two points based on the fact that several studies have implicated the baseline

diameter as a confounded when expressing endothelial function based on percent FMD and they also believe that the baseline diameter is the appropriate body size variable to use since it is the denominator of the percent FMD expression (Atkinson & Batterham, 2014).

Therefore, in order to present a clear picture of the FMD response, it is advisable to state the baseline diameter, absolute change in diameter, percent change in diameter and the shear rate (AUC) etc., when reporting the effect of an intervention on macroendothelial function (Corretti et al., 2002; Charakida et al., 2010).

### 2.3.2.3 The need for evaluating FMD over a period rather than a time point.

The maximal increase in vessel diameter occurs within 45 to 60 seconds after the occlusion is relieved (Corretti et al., 1995; Uehata et al., 1997). This is why many studies just measure the vessel diameter at baseline and then obtain a second measurement approximately one minute after the cuff is deflated (Schroeder et al., 1999; Teragawa et al., 2001; Martins et al., 2008; Onkelinx et al., 2012).

However, in a brachial FMD study in which serial post cuff deflation diameter measures were obtained from young healthy, sedentary older and trained older subjects, about 42% of the subjects had their peak diameters outside the one minute time point (Black et al., 2008). In the younger age group the maximal diameter occurs around 50 seconds while in both older age groups, the time to peak dilatation was approximately 80 seconds. In a similar but more recent study involving young and healthy subjects versus middle age obese African American women, this age related difference in the time to peak was not demonstrated as both groups attained the peak values by 45 seconds (Marinos et al., 2015). It is important to obtain serial area measurement even if the peak dilatation occurs around the 45-60 seconds, because missing the peak dilatation may reduce the reproducibility of the study (Liuni et al., 2010; Marinos et al., 2015). In conduit arteries, the maximal dilatation is expected to have occurred by 5 minutes post cuff deflation and the vessel caliber returned to close to the baseline value (Black et al., 2008; Irace et al., 2008; Liuni et al., 2010; Marinos et al., 2015).

The maximal FMD is considered more a more reproducible measure of endothelial function than FMD at 60 seconds or the time to peak dilatation (Donald et al., 2008; Marinos et al., 2015). The

time to peak dilatation is very variable within groups and it is not able to distinguish between healthy individuals, those at risk for dysfunction or those with underlying disease (Donald et al., 2008; Liuni et al., 2010).

#### **2.3.2.4 Cuff occlusion duration and pressure**

It is recommended that cuff duration for FMD studies should be standardized since the amount of hyperemic and vasodilatory response observed during FMD varies with the cuff duration time (Leeson et al., 1997; Corretti et al., 2002). Cuff durations of approximately 5 minutes produce better vasodilatory effects than 1 or 3 minutes of occlusion but extending the cuff duration beyond 5 minutes does not result in any extra vasodilatory response (Corretti et al., 1995; Leeson et al., 1997). For this reason, 5 minutes of occlusion is the norm for FMD studies since it is more tolerable than longer occlusions times (Corretti et al., 2002). Although cuff durations greater than 5 minutes are associated with increased vasodilatory effects, the regular practice of 5 minutes occlusion is accepted because prolonged occlusion includes non-flow mediated vasodilatory pathways (Harris et al., 2010). The cuff is usually inflated to 50 mmHg above the systolic pressure for brachial ultrasound studies (Corretti et al., 2002). For popliteal artery studies, occlusion pressures range from >200mmHg to > 250mmHg (Nishiyama et al., 2007; Thijssen et al., 2008). In a study on the popliteal artery using five suprasystolic occlusion pressures ranging from 175mmHg to 300mmHg, the occlusion pressure did not have a significant effect on the FMD (Mclay, 2012). In addition, a literature search on published FMD reports, showed no difference the variability of FMD using occluding pressure less than 275mmHg versus pressures between 275 to 300mmHg (Bots et al., 2005). Therefore the occluding pressure does not contribute to the variability in FMD.

#### **2.3.2.5 Distal or proximal placement of the cuff: Which is more appropriate for measuring NO-dependent dilatation?**

The imaging site for brachial FMD is usually just above the elbow, with the inflatable cuff placed either above or below the elbow (Corretti et al., 2002). The volume of tissue ischemic created by the occluding cuff affects reactive hyperemia and FMD (Betik et al., 2004). Application of the cuff on the upper arm, proximal to the imaging site is associated with greater reactive hyperemia and increased wall shear stress (Mannion et al., 1998). It is also associated

with a larger and more persistent FMD response (Betik et al., 2004). Upper arm cuff occlusion better differentiates between those with coronary risk factors and other individuals (Vogel et al., 2000). However, other things contribute to larger dilatation seen with proximal cuffing apart from NO. For example, decreased transmural pressure at the imaged arterial segment during proximal cuff occlusion leads to loss of myogenic tone and vasodilatation (Doshi et al., 2001). Ischemia of the imaged artery is also associated with the release of other vasodilatory metabolites (e.g. potassium, adenosine, ATP) which may act directly on the vascular smooth muscle cells (Doshi et al., 2001).

When the occlusion cuff is placed on the forearm distal to the transducer location, the amount of discomfort experienced is comparable to that during venipuncture, while placement of the cuff above the elbow is associated with greater discomfort probably as a result of ischemic injury (Mannion et al., 1998). In addition, upper arm occlusion is technically more challenging because the artery collapses with proximal occlusion and there might be some soft tissue displacement as the cuff is inflated, therefore the image may become distorted and adjustments have to be made (Corretti et al., 2002). More importantly, FMD measurements obtained with distal occlusion of the vessel are more reproducible than those obtained with proximal occlusion (Peretz et al., 2007).

### 2.3.2.6 Patient and environmental factors

Various external factors may contribute to the observed changes in the luminal area during flow mediated dilatation studies. Some of these factors may be environmental such as temperature and seasonal variations FMD is higher in the summer than the winter and reactive hyperemia (the driving force behind FMD) is greater at warmer room temperatures (Widlansky et al., 2007). The circadian rhythm has been implicated in the variability of FMD, but there is disagreement on the possibility of a diurnal effect (Harris et al., 2006). Some studies claim that FMD is lower in the morning and it increases as the day goes by (Otto et al., 2004; Jones et al., 2010) and exercise is said to abolish diurnal variation (Jones et al., 2010). Other say that FMD does not demonstrate diurnal variations (Etsuda et al., 1999; Kim et al., 2015).

Physiological factors such as menstrual cycle based hormonal influences also affect FMD. Flow mediated dilatation is higher during the follicular phase of the menstrual cycle compared with the

luteal phase because high endogenous estrogen levels in the follicular phase upregulate PGI<sub>2</sub> and NOS expression (Hashimoto et al., 1995; Binko et al., 1998; Jun et al., 1998). Coffee ingestion also contributes to the variability in FMD. Coffee contains anti-oxidants which improve endothelial function but caffeine inhibits soluble guanylate cyclase required for relaxation of the VSMC (Strinden & Steliwagen, 1984; Buscemi et al., 2010). Vitamin C and other antioxidants improve endothelial function, while intake of food rich in saturated fat and smoking decrease flow mediated dilatation (Taddei et al., 1998; Koulouris et al., 2010; Findlay et al., 2013). Physical exercise is another factor that might influence FMD (Tinken et al., 2008). FMD worsens during viral illnesses (Celermajer, 2008).

To reduce the effect of environmental and patient related factors during FMD, subjects are asked to fast overnight and they are scanned in a temperature controlled room after a period of rest (Corretti et al., 2002). The test is carried out in the morning to reduce the effects of circadian variation (Stoner & McCully, 2012). For intra-day reproducibility studies, 30 minutes is an acceptable interval between the test and retest because the artery will have returned to its baseline value by then (Harris et al., 2006). The retest is preferably performed within two hours in order to avoid a possible diurnal variation occurring with the FMD measurements since repeating FMD with this time frame does not affect the size of the FMD response (Järvisalo et al., 2006; Harris et al., 2006). Subjects are required to refrain from vitamin C, E or multivitamin preparations for up to 72 hours before the study (Harris et al., 2010) and are asked not to take vasoactive medication (Corretti et al., 2002). Female subjects are scanned during the same phase of their cycle to reduce the effect of hormonal variations (Hashimoto et al., 1995). They are also requested to abstain from exercise for 12 hours before the study (Harris et al., 2010).

### **2.3.2.7 Operator dependence of ultrasound based FMD**

Ultrasound based FMD is highly operator dependent and technically challenging (Corretti et al., 2002). When the level of competence of the operator is inadequate, image acquisition, as well as post processing, is affected and these may contribute to the measurement error of the technique. The operator has to maintain proper positioning of the ultrasound transducer throughout the investigation to prevent distortion of the imaging plane and measurement error (Leeson et al., 2006). Strategies used to improve the image stability and reproducibility of FMD include the use

of stereotactic clamps for stabilizing the transducer and custom designed arm immobilizers (Donald et al., 2008; Padilla et al., 2008).

With longitudinal imaging, the diameter is measured and areas calculated from it (Wilkinson & Webb, 2001). However, compression of the artery by pressure from an overlying ultrasound probe may alter the circular shape of the vessel, making it oval instead (Chaudhry et al., 2007). Therefore baseline areas derived from the measured baseline diameter will be smaller than it should be. In addition, the maximal dilatation will be underestimated because the FMD response occurs in multiple directions across the imaging plane and by measuring only changes on the longitudinal axis subtle changes in the vessel caliber might be undetected (Chaudhry et al., 2007). Compound cross-sectional ultrasound imaging was developed as a means of improving the sensitivity and accuracy of ultrasound FMD by ensuring that any increase in the area is detected but inadequate image definition of the lateral walls may still be a limitation (Chaudhry et al., 2007; Stroz & Fenster, 2010).

Another issue is that to measure the diameter, the anterior wall, as well as the posterior wall need to be adequately defined and the wall definition is affected by the angle of insonation (Wilkinson & Webb, 2001). A 90° insonation angle is ideal for B mode imaging, while 60° or less is required for optimal spectral Doppler imaging (Corretti et al., 2002; Harris et al., 2010). Therefore if B mode and spectral Doppler data are acquired simultaneously in an attempt to obtain serial diameter and velocity measurements, there will be a compromise between the two ideal insonation angles, with a value much less than 90° being used (Padilla et al., 2009; Jiang et al., 2011; Thijssen et al., 2011b). In order to avoid compromising on the ideal insonation angle for B-mode and spectral Doppler imaging respectively, some authors obtain the data separately at specific intervals (Padilla et al., 2006; Parker et al., 2006; Harris et al., 2006). This approach is also applicable for older scanners that do not have the capability to obtain B-mode and spectral Doppler data simultaneously.

Operator dependence is a factor when manually post processing the acquired images. The introduction of fast semi-automated techniques has helped to reduce the subjectivity and improve measurement reliability (Donald et al., 2008). The Brachial Analyzer software (Medical Imaging Applications, Coralville, Iowa, USA) has been used for post processing in several studies (Sonka



et al., 2002; Rudolph et al., 2007; Widlansky et al., 2007; Harrison et al., 2011; Charakida et al., 2013). A similar software is the FMD Studio system and it shows some agreement with the Brachial Analyzer (Faita *et al.*, 2011a). An advantage of the FMD Studio is that it assesses data on-line, real time (Faita *et al.*, 2011a).

In order to improve the competence of those performing FMD studies, the international brachial artery reactivity task force recommends guidelines for brachial ultrasound FMD and as part of their submission; an ultrasound operator is expected to complete 100 scans under the supervision of an experienced investigator before conducting independent studies. In addition, the operator is expected to complete 100 scans annually in order to maintain a level of adequate expertise (Corretti et al., 2002). Ultrasound based FMD may not readily be suitable for routine clinical practice partly because these guidelines are not easily attainable. Sonographers with such a high level of competence for FMD assessment are not readily available. Depending on the demand as well as the population size, the number of FMDs performed by a skilled sonographer might not be up to 100 annually, and spending time scanning volunteers in order to maintain competence might not be a feasible alternative because sonographers are a limited resource and their time is quite valuable (Alley et al., 2014).

### 2.3.2.8 Magnetic resonance imaging (MRI) based FMD in comparison to ultrasonography

Magnetic resonance imaging is an alternative to ultrasound imaging. In 2002, it was first applied for assessing macrovascular endothelial function (Sorensen et al., 2002). Just like ultrasound, it is non-invasive and non-ionizing (Voehringer et al., 2008). Unlike ultrasound imaging, it is not operator dependant because any competent MRI technologist with minimal additional training can perform MRI-FMD.

**Table 2-1. A comparison between different methods used for assessing vascular function**

	Advantage	Disadvantage
Plethymography	Cheap Assesses the resistance arteries Low operator dependence	Does not assess the conduit artery
Ultrasound	Relatively affordable and available Non-invasive Non-ionizing High axial resolution	Measures diameter and the areas obtained from the diameter may be inaccurate Operator dependence may affect intra and interobserver variability.

	High temporal resolution Assesses both conduit and resistance arteries	Technically challenging, steep learning curve Achieving and maintaining competence is time consuming. Poor image quality in the presence of fat and calcification Image resolution decreases with depth of penetration. The imaging plane may shift with longitudinal imaging
Peripheral arterial tonometry	Assesses the resistance arteries Low operator dependence	Does not assess the conduit artery
Magnetic resonance imaging	Low operator dependence Non-invasive Non-ionizing Assesses both conduit and resistance arteries Reproducible Reasonable learning curve Not limited by depth or surrounding structures such as gas, fat or calcifications The imaging plane is fixed	Long appointment waiting times Expensive Not suitable for those with metallic implants Not suitable for those with claudication Trade off between spatial and temporal resolution

With axial MRI, the actual luminal area can be obtained whereas with longitudinal ultrasound imaging only the diameter is measured and the area is derived from this value based on the assumption of a circular shape luminal cross-sectional area (Wilkinson & Webb, 2001). In addition multi-directional changes in vessel caliber vessel can be adequately detected during FMD studies (Leeson et al., 2006). Operator dependence and reproducibility improve because the imaging plane is repeatedly placed at a fixed position, perpendicular to the artery of interest (Silber et al., 2005; Cavalcante et al., 2011). MRI can be used to assess other cardiovascular structures such as the heart, great vessels and vascular beds. With this imaging modality, deeper vessels like the aorta are easier to visualize because the resolution does not decrease with the depth of penetration unlike ultrasound imaging (Uppot et al., 2007). In addition, there is good tissue characterization and the images obtained are not rendered suboptimal by the presence of fat, gas or calcifications (Leeson et al., 2006; Lee et al., 2007; Voehringer et al., 2008).

FMD can be assessed as part of a comprehensive cardiovascular evaluation. When FMD is performed in addition to aortic pulse wave velocity and distensibility assessment on a 3T MRI scanner, the entire assessment can be completed within an hour (Shan et al., 2012). Inclusion of

FMD assessment in the examination protocol will only add a little bit of extra time to the total examination duration because the imaging plane is easy to define and maintain, in addition the patient would have already been screened and positioned on the examination table. The ability to perform several techniques during one examination provides an opportunity for a comprehensive assessment of a person's cardiovascular health (Leeson et al., 2006; Voehringer et al., 2008).

### 2.3.2.9 Applications, reproducibility and limitations of current MRI techniques for FMD

Different groups have applied MRI techniques for FMD assessment (Sorensen et al., 2002; Wiesmann et al., 2004; Leeson et al., 2006; Lee et al., 2007; Oliver et al., 2012; Shan et al., 2012). Most of these techniques mimicked the US version by the use of brachial FMD. All the studies reviewed used cardiac gated 2D bright blood sequences such as phase contrast (Silber et al., 2005), segmented fast imaging using low angle shot (FLASH) technique (Sorensen et al., 2002) and balanced steady-state free precession (SSFP) GRE sequences. The balanced SSFP sequences are called different names by different equipment vendors (Chavhan et al., 2008). The fast imaging employing steady-state acquisition (FIESTA) technique by General electric medical systems, the true fast imaging with steady-state precession (true FISP) by Siemens and the balanced FFE by Philips are balanced SSFP sequences that have been used to delineate the vessel lumen when assessing endothelial function (Wiesmann et al., 2004; Leeson et al., 2006; Chavhan et al., 2008; Shan et al., 2012). Many reproducibility studies used a 1.5T scanner (Sorensen et al., 2002; Wiesmann et al., 2004; Leeson et al., 2006). Two of the studies used a 3T scanner (Oliver et al., 2012; Shan et al., 2012). An important advantage of higher magnetic field strength is improved SNR and this makes it possible to improve spatial and/or temporal resolution (Pamboucas & Nihoyannopoulos, 2006).

Most techniques used a surface receiver coil in order to improve the signal to noise ratio except one study that used an 8-channel phased-array body coil (Shan et al., 2012) and another that did not specify the type of receiver coil used (Oliver et al., 2012). Phase contrast imaging has the advantage being able to measure vessel wall shear rate (Silber et al., 2005). It shows an inverse relationship between the baseline diameter and the wall shear rate and an inverse relationship between the baseline diameter and FMD (Silber et al., 2001). In a test-retest repeatability study on healthy controls using a balanced SSFP sequence, the mean difference for baseline MRI area

measurements was  $-0.11 \pm 0.56 \text{ mm}^2$  and the mean difference for measures of the maximal MRI area post occlusion was  $-0.03 \pm 0.76 \text{ mm}^2$ , while the coefficients of variability baseline and maximal MRI area measurements were 5% and 6% respectively (Wiesmann et al., 2004). In this study, the mean difference for repeat FMD studies was  $0.75 \pm 4.8\%$  with a coefficient of variability of 32% (Wiesmann et al., 2004). This group subsequently published another paper in 2006 and the coefficients of variability for MRI-FMD in healthy volunteers reduced to 30% while the mean difference reduced to  $0.7 \pm 3.9$  (Leeson et al., 2006). In earlier study by a different group on male patients referred for coronary angiography, the coefficient of variability for MRI-FMD was 23%, with a mean difference of  $0.48 \pm 2.2$  (Sorensen et al., 2002).

In the three studies above, only one image was obtained post reactive hyperemia and this was at 60 seconds after the cuff was released. This might explain why the variability for MRI-FMD was so poor, as it has been observed with ultrasound that calculating the FMD from the area of the image obtained at 60 seconds post cuff deflation is less reproducible than using the maximal value from a series of images obtained post cuff deflation (Donald et al., 2008). In addition, a 1.5T scanner was used which might result in poor tissue contrast and difficulty with delineating the luminal boundary, leading to measurement errors. In a more recent study in which serial measurements were obtained every 15 minutes using a 3T MRI scanner and a balanced SSFP sequence, the intra-observer coefficient of variability was 15% while the test-retest coefficient of variability was 24% (Oliver et al., 2012). Improving the sampling frequency beyond 4 images per minute requires a compromise on spatial resolution and/or the signal to noise ratio as will be discussed later in this chapter. In another study using a 3T scanner and a balanced SSFP sequence, the coefficient of variability for FMD was 5% (Shan et al., 2012) which is comparable with current results from other studies using ultrasound (Ghiadoni et al., 2012).

Different studies have been designed to compare MRI and ultrasound for measuring the baseline arterial size and FMD. In a study using a balanced SSFP sequence, brachial ultrasound diameter measurements at baseline and during cuff inflation correlated strongly ( $r = 0.83$  &  $0.82$  respectively) with brachial MRI cross-sectional areas at baseline and during cuff inflation respectively. Here, the mean difference between the baseline ultrasound and MRI areas was  $1.1 \pm 0.6 \text{ mm}^2$  (Wiesmann et al., 2004). Baseline areas were calculated from the baseline ultrasound diameters with the assumption that the area is circular. With phase contrast imaging, there was a

strong correlation between diameters measured using ultrasound and MRI, but the value obtained with phase contrast MRI was about 0.4 mm larger than the ultrasound measurement (Silber et al., 2001). Similarly, the MRI diameters were derived from the luminal areas with the assumption of a circular lumen. In a study, MRI-FMD showed some correlation with ultrasound-FMD ( $r=0.62$ ) with a mean difference in FMD between the two modalities being  $-0.16\pm 1.76\%$  (Wiesmann et al., 2004). An earlier study claimed that MRI-FMD is more reproducible than ultrasound-FMD (CoV for US:80%, CoV for MRI:23%) but they did not specify whether efforts were made to reduce operator dependence of the ultrasound data (Sorensen et al., 2002). The comparable results obtained with MRI-FMD makes the technique more attractive than ultrasound because MRI has the advantage of not being as technically challenging as ultrasound.

MRI using an SSFP sequence is able to show a difference in brachial FMD between patients with type 2 diabetes mellitus and healthy matched controls (Lee et al., 2007). MRI using balanced SSFP also demonstrates a lower FMD in hypertensive diabetic patient compared to non-hypertensive diabetic patients (Shan et al., 2014). Impairment of brachial MRI-FMD is seen in chronic users of an intramuscular contraceptive agent and smokers too (Sorensen et al., 2002; Wiesmann et al., 2004). In those with coronary artery disease, brachial MRI-FMD is inversely associated with the severity of the disease (Kylintireas et al., 2011). MRI-FMD shows an improvement in brachial endothelial function following statin treatment in those with recently diagnosed coronary artery disease (Lee et al., 2008).

The luminal area may be measured by manual delineation (Wiesmann et al., 2004; Leeson et al., 2006; Lee et al., 2007; Oliver et al., 2012) or using an automated process (Sorensen et al., 2002). Automation is less subjective and less time consuming when delineating the lumen (Jackson et al., 2009). Spatial resolution is important for clear definition of the luminal boundary during luminal segmentation and area measurements. Manual methods visually define the luminal boundary while automated methods apply edge detection algorithms to determine the luminal boundary with or without a pre-defined signal intensity threshold (Chia, 1999; Jackson et al., 2009). Both manual and automated methods are based on the product of the number of pixels within the defined region and the pixel area (Chia, 1999). Area measurements using pixel counting may result in the vessel size being over- or under-estimated because only pixels above a specific signal intensity threshold are included (Chia, 1999).

**Table 2-2. A summary of the spatial resolution, temporal resolution and reproducibility of different MRI-FMD studies**

	Sorensen et al. 2002	Silber et al. 2005	Wiesmann et al., 2004	Leeson et al. 2006	Shan et al. 2012	Oliver et al. 2012	
Magnet	1.5T	1.5T	1.5T Siemens	1.5T Siemens	3T GE	3T Philips	
Imaging Sequence	Segmented FLASH GRE	Phase Contrast	True FISP	True FISP	FIESTA		
Pixel (mm)	$0.27 \times 0.27$	$0.6 \times 0.3$	$0.31 \times 0.31$	$0.31 \times 0.31$	$1.16 \times 1.16$	$0.2 \times 0.2$	
Slice thickness (mm)		3			6		
Scan duration	12 cardiac cycles	25 seconds	11-19 cardiac cycles	11-19 cardiac cycles		15 seconds	
FMD	Coefficient of variability	23%		32%	30%	5%	24 %
	Mean difference (%)	$0.48 \pm 2.2$		$0.75 \pm 4.80$	$0.7 \pm 3.9$	$0.02 \pm 0.76$	

The smallest pixel size found in the literature is  $0.2 \times 0.2$  mm using a 3T scanner (Oliver et al., 2012). However, the authors did not specify the slice thickness used. The smallest slice thickness documented is 3 mm, with a pixel size of  $0.3 \times 0.3$  mm (Lee et al., 2007). The slice thickness should be as small as possible because thick slices might lead to partial volume effect with associated overestimation of the diameter if the imaging plane is not exactly perpendicular to the vessel (Oelhafen et al., 2006). Terms used in MRI such as the partial volume effect will be discussed further in the MRI physics section.

The scan duration for the studies reviewed ranged from 12 -25 seconds as shown in table 2-2, with phase contrast imaging having the longest scan time. Most of the studies only measured the vessel diameter at baseline and at 60 seconds after the occlusive cuff was deflated based on the previous research which suggests that peak dilatation occurs around 60 seconds post cuff deflation (Corretti et al., 2002). Only one study measured the vessel diameter at multiple time points (Oliver et al., 2012). In this study, a temporal resolution of 15 seconds was achieved using a 3T scanner with a pixel size of  $0.2 \times 0.2$  mm but the authors did not state the slice thickness

used (Oliver et al., 2012). Obtaining the vessel diameter only at one time point post cuff deflation might be inappropriate if the time to peak dilatation is before or after this time point because FMD will be inaccurately measured. This may obscure the true picture of endothelial function in the presence of disease or improvements in endothelial function with interventions may not be detected (Black et al., 2008). However, measuring at various time points may require high temporal resolution. To accurately detect the peak dilatation, the Nyquist sampling interval should be less than  $\frac{1}{2}$  the time to peak (Luke, 1999). With ultrasonography, time to peak as low as 25.8 seconds has been detected (Fernandes et al., 2014). Based on this, the sampling interval during MRI-FMD should be less than 13 seconds in order to obtain sufficient samples that are representative of the dynamic changes in arterial size during reactive hyperemia. The likelihood of identifying the peak dilatation will increase as the sampling interval decreases below 13 seconds.

## 2.4 Basic MRI physics and sequence optimization techniques

### 2.4.1 Spin resonance and relaxation

Water is a major component of the human body. Protons within the water molecules spin on their axis like small magnets in a disorderly manner (van Geuns et al., 1999). When a patient is placed within a magnetic field, the axis of these protons aligns either in the direction of the magnetic field ( $B_0$ ) or in the exactly opposite direction. However, the protons continue to spin around their axis at a frequency called the Larmor frequency (MMcRobbie et al., 2006). At this point, the sum of the magnetic fields from each of the protons or the net magnetization is called the longitudinal magnetization ( $M_z$ ) (Pooley, 2005).

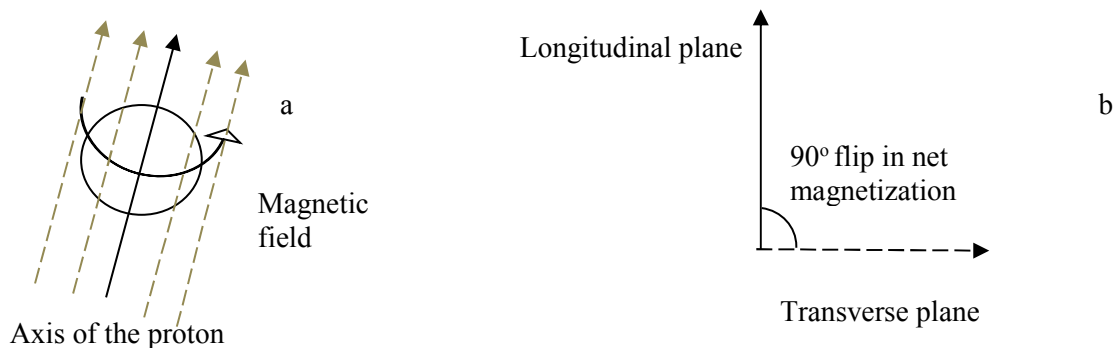


**Figure 2-4. Effect of the magnetic field and RF pulse on the spins.** (a) A proton spinning on its axis and also aligned within the magnetic field. (b) Application of a 90° RF pulse results in a flip in net magnetization from the longitudinal plane to the transverse plane.

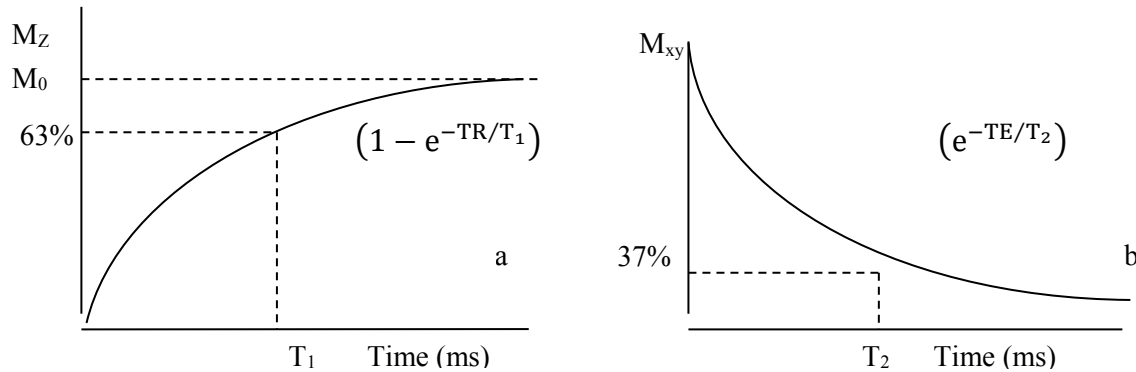


**Figure 2-5. Longitudinal and transverse relaxation times.** (a) The time it takes to attain 63% of the equilibrium longitudinal magnetization ( $M_0$ ) is called the longitudinal relaxation time or  $T_1$ . (b) The time it takes for the transverse magnetization to decay to 37% of its maximum value is called the transverse relaxation time or  $T_2$ .

When a 90° radio frequency (RF) pulse that is centered around the Larmor frequency is applied to the magnetized tissue, it causes more protons to align in the opposite direction, which is a higher energy state (van Geuns et al., 1999). It also makes the protons spin in phase with resultant 90° flip in the net magnetization. The net magnetization is then called the transverse magnetization ( $M_{xy}$ ) (Pooley, 2005) as shown in Figure 2-4. On switching off the RF pulse, the excited protons gradually lose their magnetization and return to the lower energy state (Khademi, 2012). The relaxation time is the time taken for the protons to return to their initial energy state and it differs with the tissue imaged. This difference in the relaxation times of different tissues is used to provide tissue contrast during MR imaging (Buxton, 2009).

There are two types of relaxation times, namely the longitudinal relaxation time or  $T_1$  and the transverse relaxation time or  $T_2$  (Hendrick, 2008). The longitudinal relaxation time ( $T_1$ ) is the time it takes for the longitudinal magnetization to attain 63% of its final value when a 90° pulse is used (Figure 2-5) or the time within which 63% of the excited protons realign with the magnetic field (Pooley, 2005; Hornak, 2006a). Various tissues have different  $T_1$  values depending on how fast their longitudinal magnetization re-grows. The transverse relaxation time

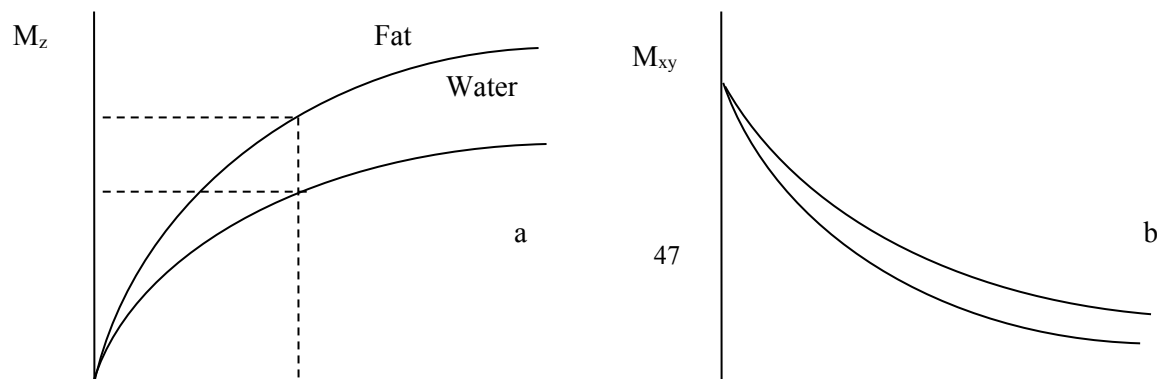


( $T_2$ ) is the time it takes for the transverse magnetization to decay to 37% of its initial value or the time it for 37% of the protons to dephase (Pooley, 2005; Hornak, 2006a). The rate at which different tissues lose their magnetization will vary.

## 2.4.2 Signal acquisition

A receiver coil placed around the patient detects the energy released when the RF pulse is switched off. The energy is converted into a signal called the free induction decay. The signal is initially strong then gradually gets dampened as the protons lose their energy (Armstrong & Keevil, 1991). The rate of signal damping depends on the  $T_2$  relaxation time of the tissue and the inhomogeneity of the external magnetic field. The signal decay due to the magnetic field inhomogeneity is called  $T_2^*$  effects (Brix et al., 2008). The time between the application of the  $90^\circ$  RF pulse and maximal echo detected by the receiver coil is called the echo time (TE), while the time between the  $90^\circ$  RF pulse and onset of another  $90^\circ$  RF pulse is called the repetition time (TR) (Pooley, 2005). Images are created by choosing a repetition time at which point the different tissues within the imaged volume will have attained different degrees of longitudinal magnetization recovery or by adjusting the echo time since the rate at which different tissue lose their magnetization may vary (Lipton, 2008).

For example, fat and water recover their longitudinal magnetization and lose their transverse magnetization at different rates. The  $T_1$  of fat is shorter than that of water so if the TR fixed at a point where these tissues show a differential in recovery (Figure 2-6a) then the signals produced will differ and there will be good tissue contrast. On the other hand, the  $T_2$  of fat is longer that of water so the TE can be adjusted in order to create a contrast between the tissues as shown in figure 2-6b (Bitar et al., 2006). Another factor that affects the quantity of signal produced and characterizes different tissues is the amount of protons within the tissue or proton density ( $\rho$ ). The higher the proton density, the higher the signal (Armstrong & Keevil, 1991).  $T_1$ ,  $T_2$  and  $\rho$  tissue characteristics can be exploited to produce image contrast (Oshio & Jolesz, 1993).



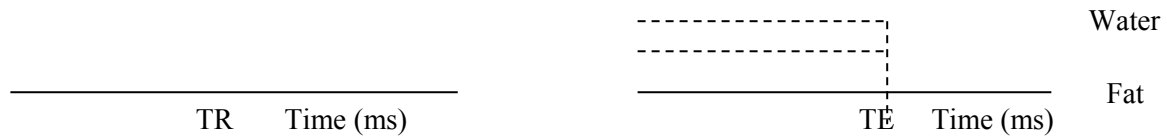


**Figure 2-6. Fat and water have different longitudinal and transverse magnetization.** (a) The longitudinal magnetization of fat and water recover at different rates. So if the  $90^\circ$  RF pulse is repeated within a short TR, the two tissues will produce signals with different amplitude. (b) The rate of transverse magnetization decay of the two tissues differs. So the TE can be adjusted to show contrast between fat and water signals.

### 2.4.3 Pulse sequences

The addition of more RF pulses and/or gradients produces various imaging sequences such as the spin echo, inversion recovery and gradient echo sequences, with these three sequences being modifiable to yield different variants (Brown & Semelka, 1999). For vascular imaging, sequences are classified as dark or bright blood variants depending on the contrast between the lumen and the surrounding structures. Dark blood sequences are good for examining the vessel wall while bright blood sequences are good for flow quantification or fast imaging (Kimura et al., 2009).

#### 2.4.3.1 Spin echo sequence

This is a dark blood sequence in which a  $180^\circ$  refocusing RF pulse is introduced after the initial  $90^\circ$  RF pulse as shown in figure 2-7. Application of a refocusing RF pulse results in the rephasing of the spins and an increase in the received signal (Pooley, 2005).  $T_1$  weighted spin-echo sequences are obtained using a short TR and short TE, while  $T_2$  weighted spin-echo sequences employ long TR and long TE. With  $T_1$  weighting water appears dark while it appears bright on  $T_2$  weighted images (Blink, 2004). Proton density imaging is obtained by using a long TR and short TE (Lipton, 2008).

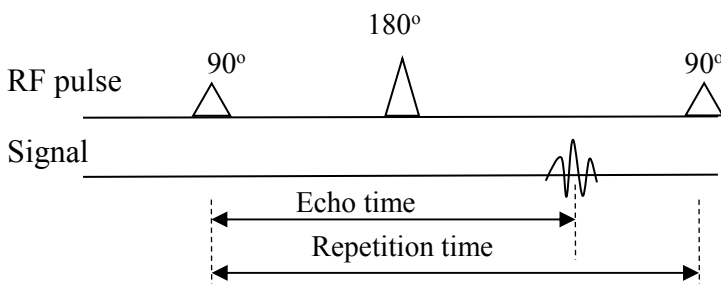


**Figure 2-7. A spin echo sequence comprising of a 90° pulse followed by a 180° refocusing pulse.** The repetition time (TR) is the interval between two 90° RF pulses while the echo time (TE) is the interval between a 90° RF pulse and the peak echo detected by the receiver coil.

### 2.4.3.2 Inversion recovery sequence

This is another black blood imaging technique and it is similar to the spin echo sequence. In this case, an initial 180° RF pulse is used to invert the net magnetization (Figure 2-8a). The extra pulse is included in order to suppress signals from a particular tissue. After the 180° RF pulse is turned off, the longitudinal magnetization begins to re-grow. When the longitudinal magnetization of the tissue to be suppressed re-grows up to zero, a 90° RF pulse is applied that flips all signals from all the other tissues into the transverse plane (Figure 2-8b). However, since the tissue of interest has no signal at this point nothing is rotated into the transverse plane. Another 180° RF pulse is then applied just like with the spin echo sequence. This method can be used to suppress water or fat when visualizing the vessel wall.

The inversion time (TI) is the time between the initial 180° RF pulse and the 90° RF pulse (Pooley, 2005; Bitar et al., 2006). Examples include fluid-attenuated inversion recovery (FLAIR) and short-tau inversion recovery (STIR) sequences which are used to suppress water and fat respectively (Brix et al., 2008). The dual echo fast spin echo is a variant of the T<sub>2</sub> weighted spin echo sequence. In this case, two images are obtained within one acquisition period. The first one could be a proton density image obtained with a short TE and the second image is obtained with a longer TE (Elster 2015).

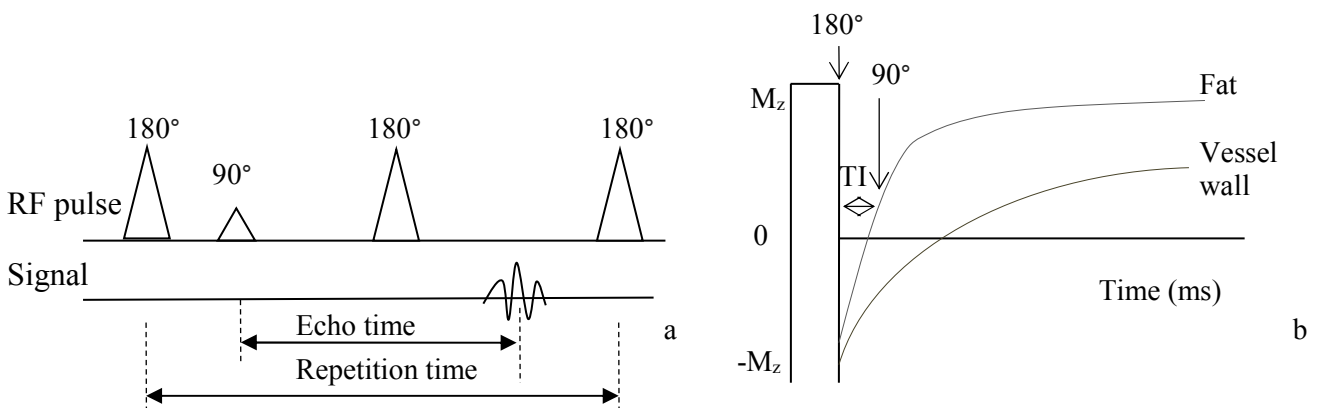


**Figure 2-8. Inversion recovery sequence** (a) An initial 180° RF pulse inverts the longitudinal magnetization. Subsequently, a 90° RF pulse and another 180° RF pulse are applied just like the spin echo sequence. (b) When the longitudinal magnetization of the tissue for suppression recovers up to 0, the 90° RF pulse is applied.

### 2.4.3.3 Gradient recalled echo (GRE) sequence

This is a bright blood imaging technique. The difference between a GRE sequence and a spin echo sequence is that the flip angle for the initial RF pulse may be less than 90° and there is no 180° refocusing RF pulse (Pooley, 2005). Rather, gradients are used to dephase and rephase the transverse magnetization (Pooley, 2005). With this sequence, when the flip angle is less than 90° the net magnetization is incompletely rotated into the transverse plane. Therefore, less time is needed for the longitudinal magnetization to return back to equilibrium ( $M_0$ ) in comparison with a spin echo sequence. This makes it possible to shorten the TR and imaging time. Many vascular imaging sequences are modifications of the GRE sequence and the vascular contrast is partly or entirely due the time of flight (TOF) effect. The TOF effect shall be explained in a subsequent section of this chapter.

### 2.4.3.4 Signal intensity equations

The signal intensity of an imaged voxel can be calculated using the sequence specific equations listed below (Hornak, 2006b; Brix et al., 2008).

Spin echo sequence

$$S = k\rho (1 - e^{-TR/T_1})e^{-TE/T_2} \quad (2.18)$$

Inversion recovery sequence

$$S = k\rho (1 - 2e^{-TI/T_1}) + e^{-TR/T_1} \cdot e^{-TE/T_2} \quad (2.19)$$

Gradient echo sequence

$$S = \frac{k\rho(1 - e^{-TR/T_1})\sin\theta \cdot e^{-TE/T_2}}{1 - e^{-TR/T_1}\cos\theta} \quad (2.20)$$

where S is the amplitude of the signal in the frequency domain, k is a constant specific to the scanner,  $\rho$  is the proton density of the tissue,  $T_1$  is the longitudinal relaxation time of the tissue,  $T_2$  is the transverse relaxation time of the tissue, TR is the repetition time, TE is the echo time, TI is the inversion time and  $\theta$  is the flip angle.

#### 2.4.4 Image formation

Frequency and phase encoding gradients are used to determine what location within the imaged volume that the signal received originated from. This involves applying two short temporary gradients after the initial RF pulse. The two gradients are applied one step at a time, in perpendicular directions (x, y or z planes) thereby creating a two dimensional matrix which comprises of a phase-encoding and a frequency encoding direction (van Geuns et al., 1999). The phase encoding gradient is applied orthogonally to the imaged slice and it causes a shift in the phase of only protons within a selected portion of the imaged slice. The frequency encoding gradient is then applied in a perpendicular direction and the signal is measured during the frequency encoding phase. Frequency encoding is a means of distinguishing between portions of the slice that have the same phase encoding. The process of phase and frequency encoding are repeated several times until the all portions of the slice have been encoded in both directions (van Geuns et al., 1999; MMcRobbie et al., 2006). The raw data obtained comprises of spatial frequencies that are within a specific bandwidth. In addition to the actual signals containing useful information on the imaged tissue, the bandwidth also contains electronic noise. The noise is due to arbitrary variations in the values assigned to each pixel. Some of the noise is caused by the currents within the patient due to the inductive effects of the magnetic field (Hoult & Lauterbur, 1979). Magnetic field inhomogeneities and thermal noise from the RF coils also contribute to the noise (Weishaupt et al., 2006).

Both the random noise and the actual signal within the bandwidth are stored on an abstract grid called k-space, which comprises of three coordinates  $k_x$ ,  $k_y$  and  $k_z$  (Mezrich, 1995). The k-space grid is filled along the directions of its three coordinates with each data point in k-space contains some details on the entire MR image (Mezrich, 1995). The central part of k-space contains details on the image contrast while the outer portion contains details on the spatial resolution of the image. The k-space data is subsequently transformed into an image using an algorithm called fast Fournier's transform (FFT) (Chen et al., 1999). The resultant image comprises of several picture elements or pixels. Each pixel is a 2-dimensional representation of the signals emanating from a small volume (volume element or voxel) within the object imaged. In addition to the signal, each pixel also contains the background noise included during image acquisition. The

relationship between the signal and the background noise is expressed as the signal to noise ratio or SNR (McRobbie et al., 2006). SNR is calculated as the ratio of the mean signal intensity of a region of interest to the standard deviation (SD) of the background air (Firbank et al., 1999).

### 2.4.5 Effects of sequence parameters on SNR, temporal resolution and/or spatial resolution

Image acquisition is a trade-off between signal-to-noise ratio (SNR), temporal and spatial resolution (Oelhafen et al., 2006). These three factors are affected by MRI scan parameters in differing and sometimes opposing degrees as shown in figure 2-9.

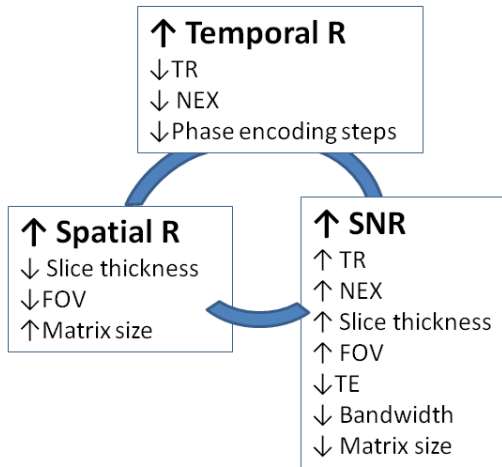



**Figure 2-9. A trade-off exists between SNR, temporal and spatial resolution and the three variables are affected by various scan parameters.**

The scan parameters can be modified by the operator based on which factor(s) out of SNR, temporal and/or spatial resolution is/are important. Scan parameters that increase SNR include the repetition time (TR), the number of excitations (NEX) and slice thickness; while those that decrease SNR include echo time (TE), receiver bandwidth and matrix size. SNR can also be affected by hardware specific parameters such as the magnetic field strength and the type of RF coils used (McRobbie, et al. 2003).

The relationship between SNR and the scan parameters is summarized in equation 2.21 (McRobbie, et al. 2003).

$$\text{SNR} = K \times S \left( \frac{\text{FOV}_{\text{PE}}}{N_{\text{PE}}} \times \frac{\text{FOV}_{\text{FE}}}{N_{\text{FE}}} \times L \right) \sqrt{\frac{\text{Scan time factors}}{BW}} \quad (2.21)$$



Voxel size factors

where  $FOV_{PE}$  and  $FOV_{FE}$  are the phase and frequency directions of the field of view respectively,  $N_{PE}$  and  $N_{FE}$  are the number of encoding steps in the phase and frequency direction,  $L$  is the slice thickness,  $NEX$  is the number of excitations and  $BW$  is the bandwidth.  $K$  comprises of hardware specific factors like the magnetic field strength and the RF coil and  $S$  is the signal value obtained from the signal intensity equation

Equations for the signal intensity are sequence-specific and the equations for various sequences were given in section 2.4.3. The pixel length in each direction is the quotient of the corresponding field of view and number of encoding steps. Therefore, the first half of equation 2.21 represents the size of the imaged voxel. The scan time is a product of  $NEX$ ,  $TR$  and  $N_{PE}$  (McRobbie et al., 2006a). Two of these parameters ( $NEX$  and  $N_{PE}$ ) are part of the second half of the equation 2.21. Therefore,  $SNR$  is proportional to the voxel size and square root of the acquisition time (Macovski, 1996).

$$SNR \propto \text{voxel size} \times \sqrt{(\text{scan time})}$$

Some of the scan parameters also affect spatial and temporal resolution as depicted in figure 2-9 and these will be discussed in more detail below.

#### 2.4.5.1 Slice thickness, field of view and matrix size

The image data is usually displayed as a matrix (McRobbie et al., 2006b). As mentioned earlier, frequency encoding and phase encoding are techniques for spatial location of received signals within the matrix using the spatial frequency and phase of magnetization of each proton. The rows and columns of the matrix represent the frequency and phase encoding directions respectively (McRobbie et al., 2006b). Since the pixel size is calculated by dividing the field of view by the matrix size, the spatial resolution improves with increasing matrix size and a decreasing field of view. The spatial resolution also improves as the slice thickness decreases, thereby preventing partial volume averaging of the boundary pixels and making it easier to define the luminal boundary (Weishaupt et al., 2006; Jackson et al., 2009). However, a large slice thickness, high field of view and low matrix size are required for adequate  $SNR$  because as the voxel size increases, the proportion of signal to the random noise emanating from the voxel increases (Weishaupt et al., 2006).

### 2.4.5.2 Number of phase encoding steps

The matrix size in the phase direction determines how many times the sequence is repeated (number of phase encoding steps) and therefore affects scan time (McRobbie et al., 2006b). Reducing the number of phase encoding steps by limiting the field of view to the region of interest, improves the temporal resolution (Weishaupt et al., 2006). In this situation, spatial resolution is not compromised because the spatial resolution will still be calculated based on the actual field of view. The only challenge is that there could be phase wrapping artifact, a situation where signal originating from outside the region of interest are mapped onto a wrong location in the image (Weishaupt et al., 2006).

### 2.4.5.3 TR, TE and Flip angle

SNR increases with TR due to greater longitudinal magnetization recovery (Bushberg et al., 2011). On the other hand, SNR decreases with TE due to increased transverse magnetization decay (Weishaupt et al., 2006). Unfortunately, increasing TR also increases temporal resolution.

### 2.4.5.4 Number of excitations (NEX)

A strategy used to reduce image noise involves scanning the imaging slice repeatedly and averaging the signals obtained (Bushberg et al., 2011). As the number of excitations increase, the sum of the signal increase by the same factor. However, the noise only increases by the square root of the factor (Hashemi et al., 2010). This is because the signal obtained from each excitation is relatively constant while the noise has more variance (Hashemi et al., 2010). Therefore, SNR increases by the square root of the NEX (Bushberg et al., 2011). However, increasing the number of signal averages also increases the scan time (Weishaupt et al., 2006).

### 2.4.5.5 The Radiofrequency (RF) coils

Different types of RF coils are available to suit the body part imaged. These include volume coils, surface coils and phase array coils (Welker et al., 2001; Weishaupt et al., 2006). RF coils could be used for transmission and/or reception of the RF signal. The closer the RF coil is to the region of interest, the greater the SNR (Weishaupt et al., 2006). Volume coils can be used to transmit or receive RF signals. The coil circumscribes the imaged volume and provides homogenous signals. It is commonly used for neuroimaging, but the SNR is limited (Welker et



al., 2001). Surface coils are receiver coils with excellent SNR for volumes near a surface coil but they have poorer SNR for volumes at a distance from the coil. Reducing the coil diameter improves SNR because of a decrease in the sample size and invariably the background noise (Hayes & Axel, 1985; Darrasse, 2003).

However, the field of view (FOV) is half the diameter of the coil (Antonio et al., 2004).

Therefore, as the coil size reduces, depth sensitivity also reduces. For example, a superficial coil of 4 cm diameter, produces optimal signal up to 2 cm away from the coil (Antonio et al., 2004). Surface coils are used for MRI-FMD studies because the conduit arteries such as the brachial and popliteal arteries are superficially located at the elbow and knee respectively. Phase array coils contain features of both volume and surface coils (Welker et al., 2001). Phased array coils consist of multiple coils and when data from all these coils are summed up, SNR increases (Bushberg et al., 2011).

#### **2.4.5.6 Magnetic field strength**

Higher magnetic field strengths produce greater SNR (Kuhl et al., 2008), but high magnetic field strengths are also associated with susceptibility artifacts (Oshinski et al., 2010). Susceptibility artifacts are common with cardiac imaging. An example is signal loss at tissue interfaces that have a large difference in their magnetic susceptibility (Oshinski et al., 2010). As the magnetic field strength increases, greater RF absorption and heating effects occur (Bushberg et al., 2011).

#### **2.4.6 MR angiography**

Different flow dependent bright blood imaging techniques may be used for cardiovascular imaging. Electrocardiographic (ECG) gating is employed for cardiac imaging devoid of motion artifacts. This is done by acquiring data at a specific period in the cardiac cycle. One cardiac cycle is often insufficient for capturing all data required to create the image, therefore imaging occurs over several heart beats (Nacif et al., 2012). For contrast enhanced MRA of peripheral arteries and their smaller branches, systolic gating is used to time image acquisition during peak blood flow in order to improve vascular contrast especially in areas of slower flow (Hartung et al., 2011). However, imaging during diastole may be preferable for luminal area measurements because the arterial size varies with the cardiac cycle and maximal distension occurs during the forward flow of late systole (Chuang et al., 2002). With ultrasonography, ECG gating allows for

end-diastolic measurements at the R wave (Chuang et al., 2002). Diastolic trigger delay techniques have also been used with non-contrast based bright blood imaging techniques to obtain still images of an artery for accurate luminal area measurements (Sorensen et al., 2002; Leeson, 2006). There are two main types of non-contrast based bright blood imaging techniques: Time-of-flight and phase contrast MR angiography (Laub et al., 1998).

#### 2.4.6.1 Phase contrast imaging

Phase contrast imaging can be used to measure the flow velocity and direction (Bitar et al., 2006). The technique measured changes in the phase of transverse magnetization of excited spins in the blood relative to magnetic gradients (McRobbie et al., 2006c). Three flow encoding bi-polar gradients are used to encode the flow in the x, y and z directions. One part of the bi-polar gradient is sensitive to flow while the other is not. The flow sensitive data from each bi-polar gradient is subtracted from non-flow sensitive data so that signals from stationary tissues are eliminated (Laub et al., 1998). The difference in the phase depends on the spin's velocity, therefore, the blood velocity can be derived from the phase data and the magnitude data can be used to construct an image of the lumen (Laub et al., 1998).

The phase of the MR signal increases as blood flow increases. However, the maximum phase shift that can be detected is  $180^\circ$  (Laub et al., 1998). Therefore, a maximum value for the expected velocities within the vessel of interest is determined and this value is called *venc* (McRobbie et al., 2006c). Encoding in the three directions increases the scan time because each bi-polar gradient is applied after a separate  $90^\circ$  RF pulse, introduced at the repetition time (TR). So the time it takes to encode in all directions will be three-fold of the TR (McRobbie et al., 2006c). Although phase contrast imaging has good vascular contrast and it is excellent for measuring flow direction and rate, its poor temporal resolution can be a limitation to MRI-FMD applications (Pai, 2007).

#### 2.4.6.2 Time-of-flight imaging

Gradient recalled echo sequences produce bright vessel lumina due to a phenomenon that occurs when an RF pulse and then a refocusing gradient are repeatedly applied to an imaging slice using a short TR and short TE (McRobbie et al., 2006c). This phenomenon, called the time of flight (TOF) effect, was first reported by Suryan in 1959 and it was subsequently demonstrated in the

blood vessels of the wrist (Hinshaw *et al.*, 1977; Kim & Parker, 2012). TOF imaging utilizes the relative difference in longitudinal magnetization between flowing blood and adjacent stationary tissues after repeated RF pulses (Kim & Parker 2012b). What happens is that stationary tissue experiences several RF pulses and becomes saturated, while flowing blood experiences fewer RF pulses and becomes only partially saturated. With TOF imaging, pixels from areas with saturated spins appear dark because only a few signals are detected in the region, while those from partially magnetized spins are grey and those from fully magnetized spins appear very bright because of the associated high signals produced (Hashemi *et al.*, 2010). Only flow that is perpendicular to the imaging plane produces signals, which is why the amount of signal detected decreases with turbulent flow and signal void may occur in tortuous vessels when the imaging plane is no longer perpendicular to the vessel (Brix *et al.*, 2008; Chiewvit *et al.*, 2011).

The signals produced from an intraluminal voxel of blood are not uniform, rather the signal decreases as the flow advances into the slice. Assuming that the volume of blood within the imaging slice at a given time is divided into segments as shown in Figure 2-10a, the first segment will contain fresh unsaturated spins that just entered into the slice with full equilibrium magnetization ( $M_0$ ) so will produce high signals (Laub *et al.*, 1998). The other segments will contain flowing spins at different degrees of saturation, with the amount of saturation increasing as the flow advances further and further into the imaging slice because of exposure to increasing number of RF pulses (Kim & Parker 2012b).

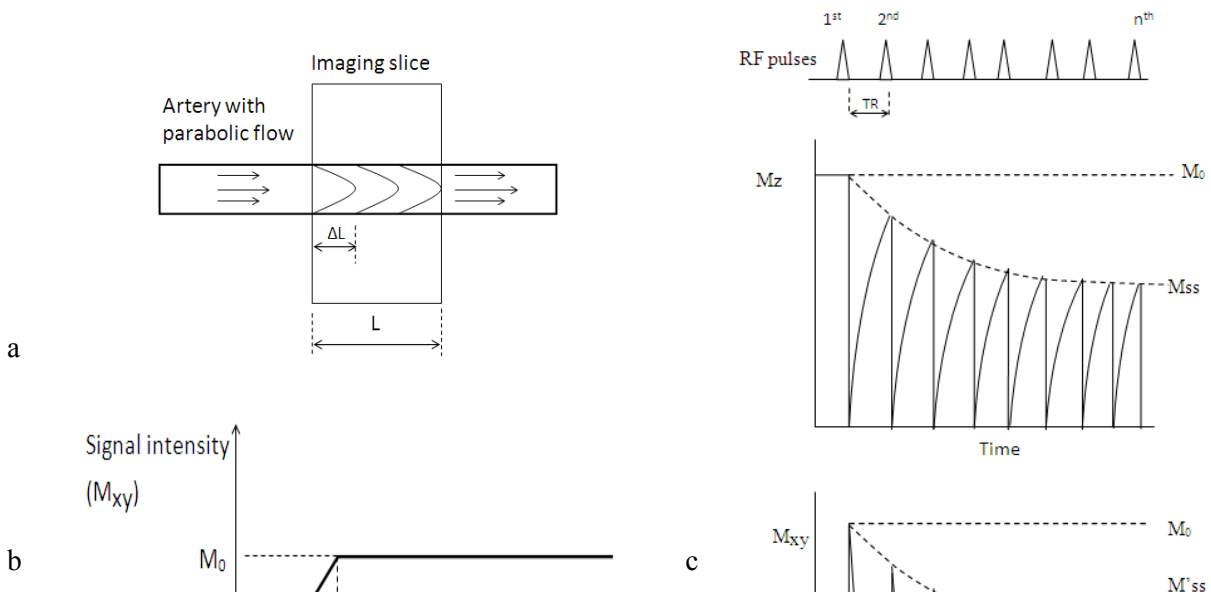


**Figure 2-10. Effects of velocity on signal intensity** (a) When the blood velocity is less than the threshold, there will be segments of flow within the slice that are at different levels of saturation. The length of each segment ( $\Delta L$ ) depends on the blood velocity. (b) The transverse magnetization ( $M'_{ss}$ ) increases with velocity until it gets to  $M_0$ . The velocity at this point is the threshold velocity and it is the quotient of  $L$  &  $TR$ . (c) If the velocity is slow, some segments within the lumen will receive multiple RF pulses, with their longitudinal and transverse magnetizations decreasing as the number of RF pulses increases until a steady state is achieved.

With repeated RF pulses, the amount of recovery in longitudinal magnetization gradually decreases until it gets to a steady state ( $M_{ss}$ ) therefore the amount of transverse magnetization (signal detected) also gradually decreases until it gets to a steady state ( $M'_{ss}$ ) as shown in Figure 2-10c (Elster 2015). The velocity of the blood determines how far the fresh spins advance into the slice ( $\Delta L$ ) before they experience an RF pulse and  $\Delta L$  determines the number of segments that the volume of blood within the slice can be divided into. If the velocity is high up to the point where  $\Delta L$  becomes  $L$ , then all of the saturated blood would exit the slice before the next  $TR$  meaning that there will be only one segment and the segment will only contain fresh blood at equilibrium magnetization ( $M_0$ ).

A similar result is seen with very small slice thicknesses or long  $TR$  values. In these cases, the slice will be completely filled up with fresh fully magnetized blood each time so it will produce maximal signal intensity. It is important to mention that although a long  $TR$  will produce high signals in the lumen, the vascular contrast may not be satisfactory because of associated recovery in longitudinal magnetization of the adjacent tissues (Kim & Parker 2012b). GRE sequences with long echo times are  $T2^*$  weighted. With  $T2$  weighting, susceptibility artifacts may occur because the rate of signal decay due to inhomogeneity of the external magnetic field differs between tissues (Bitar et al., 2006; Brix et al., 2008).

#### 2.4.6.2.1 Types of GRE sequences

During GRE imaging, by the time the next RF pulse flips the longitudinal magnetization into the transverse plane, there is usually some residual transverse magnetization and it contributes to the

signal detected if it is not removed (Elster, 1993). There are different types of GRE sequences based on what is done with the residual transverse magnetization. The first types are the steady state GRE sequences. With the coherent or partially refocused steady state GRE sequence, a rewind gradient is used to rephase the  $T_2^*$  magnetization (Bitar et al., 2006). An example is the segmented (FLASH) technique which was used for the first MRI-FMD study (Sorensen et al., 2002). With the fully refocused or balanced steady state GRE sequences the RF pulse phase is alternated between  $0^\circ$  and  $180^\circ$  and all the transverse magnetization is refocused therefore high signals are produced and the TR can be very short. A short TR makes rapid image acquisition possible, which is why the technique is suitable for cardiac imaging (Bitar et al., 2006). However, the technique is susceptible to inhomogeneities in the magnetic field and banding artifacts (Bitar et al., 2006; Chavhan et al., 2008). Examples include the true FISP, FIESTA and balance FFE techniques that have been used for FMD studies (Wiesmann et al., 2004; Leeson et al., 2006; Chavhan et al., 2008; Shan et al., 2012). A second type of GRE sequence is the in-phase and out-of-phase sequence which consists of paired GRE sequences within the same TR but at separate echo times. It is often used to assess fat containing lesions (Ramalho et al., 2012). With the spoiled GRE sequence, the residual transverse magnetization is removed before the next RF pulse (Elster 2015b).

The transverse magnetization is the measured MR signal intensity and it depends on the associated longitudinal magnetization. Removal of the residual transverse magnetization before the next RF pulse ensures that with the spoiled GRE sequence, any measured signal originates from fresh longitudinal magnetization (Elster, 2015b). The longitudinal magnetization depends on the blood velocity, slice thickness (L) and repetition time (TR).

#### 2.4.6.2.2 Relationship between velocity and signal intensity on a spoiled GRE sequence

The relationship between velocity and signal intensity on a spoiled GRE sequence is linear until a threshold velocity ( $V_{\text{thresh}}$ ) that is defined by the quotient of L and TR. After this point, the graph plateaus as depicted in Figure 2-10b (Hashemi et al., 2010). The linear aspect of the graph can be expressed as equation 2.22 (Hashemi et al., 2010).

$$\text{Signal intensity} = M_{\text{SS}} + (M_0 - M_{\text{SS}}) \frac{\text{TR}}{L} v \quad (2.22)$$

where  $M_{SS}$  is the signal intensity of blood at steady state,  $v$  is the velocity and  $\frac{TR}{L}$  is the inverse of the threshold velocity.

If the flow is parabolic and the threshold velocity is not exceeded, then the integrated signal intensity of a lumen with flowing fluid can be calculated as equation 2.23 (Gao & Liu, 2012)

$$\text{IntSI} = (M_{SS} \cdot L \cdot A) + (M_0 - M_{SS})TR \cdot A \cdot \bar{v} \quad \text{where } \bar{v} \leq \frac{L}{2 \cdot TR} \quad (2.23)$$

With spoiled GRE sequences, the longitudinal magnetization after an amount of RF pulses ( $n^-$ ), before steady state is achieved is calculated as (Kim & Parker, 2012)

$$M_z(n^-) = M_{z,ss} + (e^{-TR/T_1} \cos\theta)^{n-1} (M_0 - M_{z,ss}) \quad n \geq 1 \quad (2.24)$$

The time of flight sequence is a spoiled GRE sequence that is optimized to provide good vascular contrast. The sequence is optimized by using a short repetition time (TR) and a high flip angle in order to enhance flow related enhancement (FRE) and saturate stationary tissue (Kim & Parker, 2012). A long TR ensures that there is only fresh blood within the slice during each image acquisition (Hashemi et al., 2010). Small voxel sizes and short echo times are used to minimize loss of signal, due to loss of phase coherence between spins in the voxel (Kim & Parker, 2012). Other strategies for improving vascular contrast during TOF arteriography include using fat saturation pulse and venous saturation band to remove adjacent fat and venous signals (Chen et al., 1999). A magnetization transfer contrast (MTC) pulse could be used to improve contrast between the vessel and the background (Graham & Henkelman, 1997) although, these additional pulses add to the scan time. Temporal resolution can be improved using segmented k-space technique (Chen et al., 1999).

Flow compensation may be used to decrease flow related artifacts, but it results in a longer TE and decreased signal (Jeong et al., 2002). Ghosting artifacts may occur in the phase encoding direction with pulsatile flow and this artifact may blur the boundary of the lumen (Leeson *et al.*, 2006; Kim & Parker, 2012). The artifact can be decreased by adding another lobe to the phase-encoding gradient but this leads to an increase in the echo time (Kim & Parker, 2012).

## 2.5 Thesis Aims and Hypotheses

### 2.5.1 Thesis Aims

Hyperemia induced flow mediated dilatation is transient, therefore serial area measurements with high sampling frequency is required for detecting the peak dilatation. Ultrasound FMD is the current gold standard for assessment but it is operator dependent with a steep learning curve. MRI is less operator dependent but it is limited by the trade-off between temporal and spatial resolution. The primary aim of this thesis is to develop an MRIFMD technique that is more repeatable than ultrasound-FMD. The MRI-FMD technique should be able to obtain rapid, reliable serial area measurements. A secondary aim is to use the MRI-FMD technique to qualitatively assess reactive hyperemia.

### 2.5.2 Hypotheses

1. Reliable, rapid, serial measurements of the luminal area can be obtained in phantoms using an MRI integrated signal intensity approach
2. There is agreement between popliteal artery measurements' obtained using an MRI integrated signal intensity approach on moderate resolution images and that obtained by pixel counting of high resolution images.
3. Popliteal MRI-FMD using an MRI integrated signal intensity (IntSI) approach for serial area measurements is more repeatable than US-FMD.

---

**Chapter 3    Developing an MRI integrated signal intensity (IntSI) technique for measuring the luminal area and testing it in a flow phantom**

---



### 3.1 Abstract

**Objective:** To develop a semi-automated MRI technique for measuring the luminal area that offers better temporal resolution than the conventional pixel counting approach.

**Background:** Current methods of measuring the luminal area during studies such as flow-mediated dilatation rely on high spatial resolution but this entails a trade off involving temporal resolution and SNR. High temporal sampling frequency is however required to detect the peak dilatation.

**Methods:** A method for measuring luminal area was derived based on the integrated signal intensity of the luminal pixels and the central pixel intensity. This integrated signal intensity (IntSI) technique was derived using hemodynamic principles and the time of flight equation. The equation was based on the assumption that the luminal signal intensity has a parabolic profile when the velocity has a fully formed parabolic profile and the maximal velocity did not exceed the threshold velocity. Another assumption was that the ratio of the pixel area to the luminal area was very small. Using a flow phantom with 12 known luminal areas of different sizes and a small pixel area ( $0.4 \text{ mm}^2$ ), the effect of velocity and its profile on the accuracy of areas measured using this equation was assessed.

The effect of the pixel-to-luminal area ratio on the accuracy of areas measured using the technique was also assessed. Then the reliability of the IntSI and conventional pixel counting techniques for measuring luminal area was compared at different pixel sizes using the mean bias and coefficient of repeatability (CR) obtained from Bland Altman's plots. Finally, non-inferiority testing between pixel counting at  $0.4 \text{ mm}^2$  pixels and the IntSI technique (at  $0.4 \text{ mm}^2$  and  $1.4 \text{ mm}^2$  pixels respectively) was performed with a two one-sided test (TOST) for non-inferiority.

**Results:** The IntSI technique had greater measurement error when there was a mismatch between velocity and the entrance length for parabolic flow as opposed to when the velocity and entrance length were compatible for a fully formed velocity profile and the difference was statistically significant. When the pixel-to-luminal area ratio did not exceed 0.1, the difference in area measurement was at most 10%. The reliability of the IntSI technique at a pixel area of  $1.4 \text{ mm}^2$  (Mean bias  $\pm$  CR:  $0.22 \pm 1.43 \text{ mm}^2$ , ICC: 0.998) was non-inferior to that using pixel counting at  $0.4 \text{ mm}^2$  pixel area (Mean bias  $\pm$  CR:  $-0.07 \pm 1.12 \text{ mm}^2$ , ICC: 0.998).

**Conclusion:** The IntSI technique provides a reliable means of measuring the luminal area provided the assumptions are not violated.

## 3.2 Introduction

### 3.2.1 Limitations of current FMD measurement techniques

As discussed in chapter 2, ultrasound based methods measure FMD as change in the luminal diameter, while MRI-based methods measured FMD as change in luminal cross-sectional area (Leeson et al. 2006). Like other groups who have measured FMD as a function of change in area, I believe that area measurements are more appropriate because it captures multi-directional vessel dilatation unlike longitudinal imaging with US, thereby adequately measuring changes in vessel caliber (Chaudhry et al. 2007). However, area measurements using pixel counting may over/under estimate the vessel size because only pixels above a specific signal intensity threshold are included in the measured area (Chia, 1999). The pixels at the edge experience partial volume averaging because more than one tissue is responsible for the signal within the pixel (Khademi et al. 2014). These edge pixels that partially contain luminal signals may or may not be included in the luminal area measurements based on whether their signal intensity values are above or below the threshold. Therefore, area measurement by pixel counting is prone to both over-estimation and under-estimation measurement errors.

In order to minimize the measurement errors associated with pixel counting, the pixel size can be reduced as much as possible. Pixel sizes as low as 0.3 mm × 0.3 mm have been used for phase contrast imaging but this required a scan time of 25 s (Silber et al., 2001), which is long considering the dynamic changes in arterial size during FMD. Oliver et al (2012) used an SSFP sequence to achieve a pixel size of 0.2 mm × 0.2 mm and with a scan time as low as 15 s using a 3T scan but they did not specify the slice thickness used. Further decrease in the pixel size will improve the vessel boundary definition, but at the cost of either SNR or temporal resolution or both.

The low FMD response observed in patients at risk for cardiovascular disease, may be due in part to impairment of the microvasculature (Gibbs et al., 2011). This is because when there is distal microvascular disease, these resistant peripheral vessels no longer dilate in response to ischemia and accumulation of vasoactive metabolites. Therefore, there is an absence of the normal pressure gradient that is expected between the conduit arteries and the resistant vessels when the cuff is released during an FMD study. This leads to a poor hyperemic response, less

shear stress on the endothelium and a smaller FMD (Lauer et al., 2008). Ultrasound based methods for FMD can measure the blood velocity in order to assess the hyperemic response and estimate how much shear stress is applied to the endothelium (Gibbs et al., 2011). MRI-FMD studies using phase contrast imaging can demonstrate changes in velocity (Silber et al., 2001). Other studies using SSFP did not comment on the velocity (Sorensen et al., 2002; Leeson et al., 2006). An ideal MRI-FMD technique is one that can obtain reliable area measurements with a high temporal frequency and also demonstrate changes in velocity.

### 3.2.2 Another approach for measuring area

In view of the limitations of area measurement by pixel counting, a different approach for measuring FMD with MRI is suggested. This method uses the signal intensity of the lumen to estimate the luminal area and it provides a means of overcoming some of the constraints of SNR, spatial resolution and temporal resolution. Assuming that it is possible to image an artery using a pixel size that is larger than the cross-sectional area of the artery and there are no adjacent structures nearby, then the integrated signal intensity (IntSI) of that pixel will be based on only luminal signal. If the artery increases in size, the measured signal intensity will also increase. The integrated signal intensity of a lumen with flowing blood is also affected to some extent by velocity (McRobbie et al., 2006c). Therefore area and velocity affect the integrated signal intensity (IntSI) of the lumen as depicted in figure 3-1a.

If smaller pixels are used for imaging, the luminal IntSI will be the sum of all luminal pixel intensities. If the cross-sectional area of the lumen increases as shown in figure 3-1b and 3-1c, while all other parameters remain constant, then the signals produced will be spread over more pixels in the image and the luminal IntSI will increase. Since luminal integrated signal intensity (IntSI) increases with cross-sectional area, the luminal IntSI can be used as a surrogate measure of the luminal area and provided other factors remain constant, any increase in the integrated signal intensity of a lumen with static blood can be ascribed to an increase in the luminal cross-sectional area.

A benefit of this technique is that the edge pixels will contribute to the measured signal intensity and their contribution will be proportional to the partial volume fraction of the corresponding voxel.

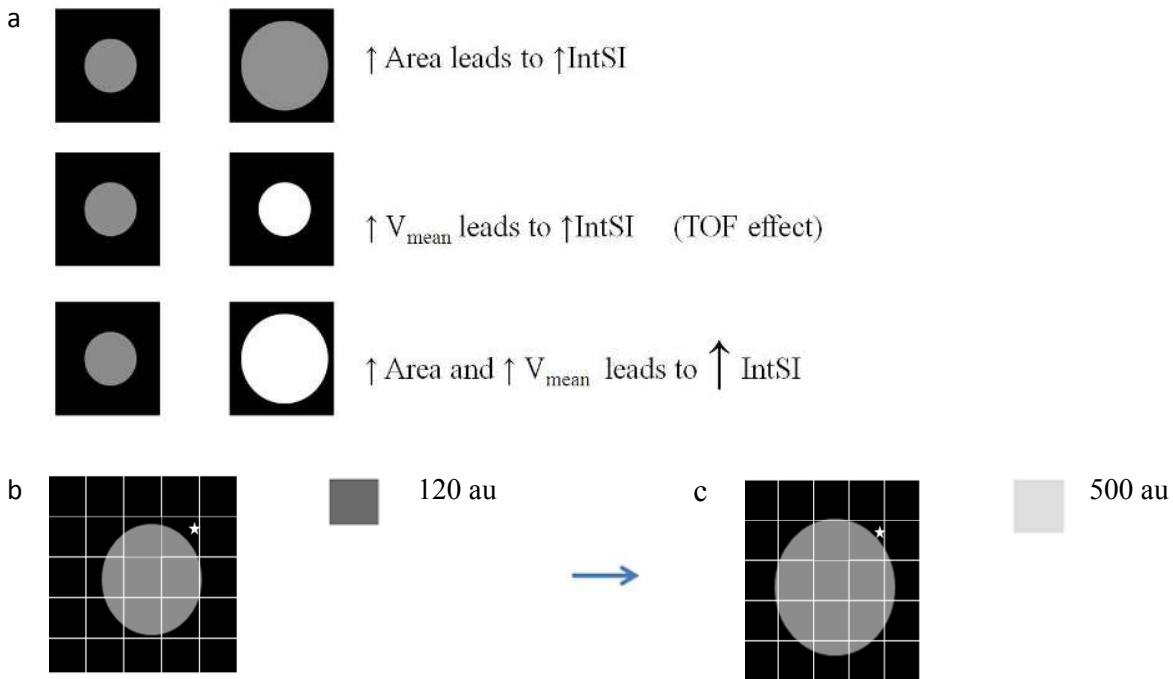


**Figure 3-1. An illustration of the effect of increases the luminal area and velocity on signal intensity.** (a) The artery is imaged with a pixel that encloses the arterial lumen. As area or velocity increase, IntSI also increases. When both area and velocity increase, there is a combined increase in IntSI. (b and c) When the lumen is imaged with smaller pixels, the intensity of the starred pixel in (c) is higher than that of (b) because the partial volume of the lumen in (c) is higher.

Therefore, regardless of the pixel size, the partial contribution of the luminal signals within the edge pixels will be included in measurements of the luminal IntSI. In view of the decreased need for high spatial resolution, the pixel size can be increased resulting in a decrease in scan time and consequently an improved temporal sampling frequency.

### 3.2.2.1 Adjusting for the effects of velocity on the integrated Signal intensity

As discussed in chapter 2, the TOF effect is the increase in luminal signal intensity due to fresh blood flowing into the imaging slice during data acquisition. The TOF effect is more profound during the hyperemic phase of an FMD study due to the high velocities that occur at this point. This increase in luminal signal intensity is useful because it provides evidence that the hyperaemic response is adequate and the distal microvasculature is healthy but it may obscure the more subtle increase in signal intensity due to the increase in the luminal area. Using certain

assumptions of hemodynamics and the TOF effect, a technique has been derived to adjust for the effects of velocity when measuring the luminal area using the integrated signal intensity of the luminal pixels.

### 3.2.3 Hypothesis

Reliable, rapid, serial measurements of the luminal area can be obtained in phantoms using an MRI integrated signal intensity approach

The aims of this chapter were:

- 1) to determine a suitable bright blood imaging technique that provides high vascular contrast, improved temporal resolution compared with previous MRI-FMD techniques and the ability to demonstrate flow information;
- 2) to derive a method for measuring area that adjusts for the contribution of the TOF effect to the luminal integrated signal intensity;
- 3) to test the reliability of the IntSI technique using a phantom; and 4) to compare the IntSI technique with a conventional high resolution, pixel counting approach.

### 3.3 Materials and Methods

#### 3.3.1 Effects of the sequence on the vascular contrast and scan time

Various bright blood imaging techniques were considered for imaging with the IntSI technique. These included phase contrast imaging, spoiled GRE sequence, SSFP sequence and arterial spin labeling. SSFP was not used because the associated banding artifacts may lead to an unpredictable decrease in the integrated signal intensity (Chavhan et al., 2008) and this will add variability to the measured area. Arterial spin labeling was not used because it has low SNR and temporal resolution (Borogovac & Asllani, 2012). Only phase contrast and spoiled GRE sequences were compared for scan efficiency.

A volunteer was scanned with these two cardiac gated bright blood techniques using a 3T Skyra Siemens scanner at St Michael's hospital. Ethical approval for the study and informed consent were obtained prior to the study. A volunteer was scanned rather than a phantom in order to include the effects of cardiac gating on the scan time. For convenience, the popliteal artery was scanned since it is a relatively large artery and can be imaged with the volunteer's head free from the magnet, a position acceptable to those with claustrophobia. The volunteer was positioned supine on the examination table and the right knee was placed within a knee coil. ECG leads were placed on the chest. The table was advanced feet first into the bore of the magnet. Ten axial 2D images of the knee were obtained using the two sequences. A flip angle of 90° was used for both sequences since SNR is maximal at this flip angle if the TR is very long (Bushberg et al., 2011). For both techniques, the number of excitations (NEX) used was 1 in order to reduce the scan time.

Other sequence parameters were also optimized in order to obtain a reasonable spatial and temporal resolution. For phase contrast imaging, the other sequence parameters were TR: 888.4 ms slice thickness: 5 mm, FOV: 222 mm × 83 mm, matrix: 128 × 34, pixel area: 3.0 mm<sup>2</sup>, TE: 4.0 ms. A fat saturation pulse was also applied in order to suppress signal from fatty tissue surrounding the lumen. For the spoiled GRE sequence, the scan parameters were group TR: 752ms, number of segments: 17, pixel area: 1.9mm<sup>2</sup>, slice thickness: 3.5 mm, FOV: 350mm × 153 mm, matrix: 256 × 112, TE: 3.7 ms. In addition to fat saturation and flow compensation, segmented k-space and magnetization transfer constant (MTC) were used to optimize the spoiled

GRE sequence. The phase contrast and spoiled GRE sequences were compared based on their vascular contrast and CNR efficiency (Edelstein et al., 2011).

The vascular contrast to noise ratio (CNR) was calculated as equation 3.1 (Magnotta & Friedman, 2006).

$$\text{CNR} = \frac{S_L - S_M}{\sigma} \quad (3.1 \text{ a})$$

where  $S_L$  and  $S_M$  are mean signal intensities of ROIs placed over the lumen and adjacent muscle respectively and  $\sigma$  is the standard deviation of the background noise.

Scan efficiency was calculated as equation 3.1b (Edelstein et al., 2011).

$$\text{CNR efficiency} = \frac{\text{CNR}}{\text{scan time}} \quad (3.1 \text{ b})$$

The CNR efficiency per unit volume was also calculated by dividing the CNR efficiency with the voxel volume.

### 3.3.2 Deriving the integrated signal intensity equation for measuring luminal area on a spoiled gradient recalled echo (GRE) sequence

The equilibrium magnetization ( $M_0$ ) is the value of the longitudinal magnetization when the net magnetization vector aligns with the applied magnetic field (Hornak, 2006a). At a flip angle of  $90^\circ$ , the net magnetization lies in the transverse plane and it is equal to the equilibrium magnetization ( $M_0$ ) (Hornak, 2006a). When stagnant blood experiences a single RF pulse in a spoiled GRE pulse sequence, the transverse magnetization is at a maximal value ( $M_{\text{peak}}$ ). The maximal value is attained because all the spins were unsaturated prior to application of the RF pulse (Hashemi et al., 2010). The magnitude of  $M_{\text{peak}}$  depends on the flip angle, with the highest value of  $M_0$  attained when a  $90^\circ$  RF pulse is applied. With repeated RF pulses and incomplete relaxation, the transverse magnetization gradually decreases to a steady state ( $M_{\text{SS}}$ ).

When the lumen contains flowing blood and the imaged slice experiences several RF pulses, the resultant transverse magnetization of the spins in the lumen will vary depending on the blood velocity. If the velocity is high enough for the slice to be completely re-filled with fresh blood after each RF pulse then the transverse magnetization of the fresh blood will be at the peak value ( $M_{\text{peak}}$ ). However, if the velocity is not high enough to completely refresh the slice with blood,

then only a portion of blood within the slice will be at the peak magnetization ( $M_{\text{peak}}$ ) while the other portion of blood will be partially saturated (Kim & Parker, 2012). If  $M_{\text{Sat}}$  represents the magnetization of the partially saturated blood, then the total signals emanating from the lumen or the integrated signal intensity of the lumen (IntSI) can be calculated as equation 3.2 (Gao & Liu, 2012).

$$\text{IntSI} = K\rho [(M_{\text{Sat}} \cdot A \cdot L) + K\rho(M_{\text{Peak}} - M_{\text{Sat}})A \cdot \text{TR} \cdot \bar{v}] \quad (3.2)$$

where  $K$  is the gain of the scanner,  $\rho$  is the proton density,  $A$  is luminal area,  $L$  is slice thickness,  $\bar{v}$  is mean blood velocity, and  $\bar{v} \leq \frac{L}{2 \cdot \text{TR}}$

Averaging  $M_{\text{Sat}}$  over all the RF pulses in order to quantify the IntSI involves complex equations that might not be readily applicable in the clinical setting. However,  $M_{\text{Sat}}$  can be calculated easily if the flip angle is  $90^\circ$ . When the flip angle is  $90^\circ$ ,  $M_{\text{Sat}}$  will be the steady value ( $M'_{\text{ss}}$ ) because steady state is achieved after the first RF pulse. In addition, the magnetization of fresh blood ( $M_{\text{peak}}$ ) after the first RF pulse will be the equilibrium magnetization ( $M_0$ ). The reasons for these are explained in section 3.3.2.1 and 3.3.2.2 below.

### 3.3.2.1 Calculating the transverse magnetization of static blood after a single $90^\circ$ RF pulse

For a spoiled GRE sequence, the longitudinal magnetization of stagnant blood at steady state ( $M_{\text{ss}}$ ) is given as equation 3.3a (Kim & Parker, 2012)

$$M'_{\text{ss}} = \frac{M_0(1 - e^{-\text{TR}/T_1})}{1 - e^{-\text{TR}/T_1} \cdot \cos\theta} \quad (3.3 \text{ a})$$

while the transverse magnetization of stagnant blood at steady state detected by the receiver coil ( $M'_{\text{ss}}$ ) is given as equation 3.3b (Kim & Parker, 2012)

$$M'_{\text{ss}} = \frac{M_0(1 - e^{-\text{TR}/T_1})\sin\theta \cdot e^{-\text{TE}/T_2}}{1 - e^{-\text{TR}/T_1} \cdot \cos\theta} \quad (3.3 \text{ b})$$

where  $\text{TR}$  is the repetition time,  $\text{TE}$  is the echo time,  $T_1$  is the longitudinal relaxation time of blood,  $T_2$  is the transverse relaxation time of blood and  $\theta$  is the flip angle.

( $M'_{\text{ss}}$ ) is a product of  $M_{\text{ss}}$  and ( $\sin\theta \cdot e^{-\text{TE}/T_2}$ ). The greater the flip angle, the greater the detected signal (Bushberg et al., 2011). The longitudinal magnetization for a spoiled gradient



echo sequence immediately after n RF pulses , before steady state is achieved is expressed in equation 3.3c (Kim & Parker, 2012)

$$M_Z(N) = M_{SS} + (e^{-TR/T_1} \cos \theta)^{n-1} (M_0 - M_{SS}) \quad n \geq 1 \quad (3.3 \text{ c})$$

where  $M_Z(n)$  is the longitudinal magnetization after nRF pulses,  $M_{SS}$  is the longitudinal magnetization at steady state and  $\theta$  is the flip angle.

Using equation 3.3c, when the flip angle used for imaging is  $90^\circ$ , the longitudinal magnetization at the first RF pulse can be calculated as equation 3.3d.

$$M_Z(1) = M_{SS} + (e^{-TR/T_1} \cos 90^\circ)^{1-1} (M_0 - M_{SS}) \quad (3.3 \text{ d})$$

$\cos 90^\circ$  is zero therefore

$$M_Z(1) = M_{SS} + (0)^0 (M_0 - M_{SS}) \quad (3.3 \text{ e})$$

and x raised to the power of zero is 1, therefore

$$M_Z(1) = M_{SS} + (1)(M_0 - M_{SS}) \quad (3.3 \text{ f})$$

$$M_Z(1) = M_0 \quad (3.3 \text{ g})$$

### 3.3.2.2 Calculating the transverse magnetization of static blood after two successive $90^\circ$ RF pulses

The longitudinal magnetization at the second RF pulse can be calculated as follows using equation 3.3c

$$M_Z(1) = M_{SS} + (e^{-TR/T_1} \cdot \cos 90^\circ)^{2-1} (M_0 - M_{SS}) \quad (3.4 \text{ a})$$

$$M_Z(2) = M_{SS} + (0)^1 (M_0 - M_{SS}) \quad (3.4 \text{ b})$$

and x raised to the power of one is x, therefore

$$M_Z(2) = M_{SS} \quad (3.4 \text{ c})$$

Therefore the transverse magnetization after the first RF pulse equals  $M_0$ , while steady state magnetization ( $M'_{SS}$ ) is achieved after the second RF pulse.

### 3.3.2.3 Calculating the luminal integrated signal intensity of a vessel with flowing blood when the flip angle is $90^\circ$

When stationary fluid experiences  $90^\circ$  RF pulses, the contrast of the image produced will vary depending on the k-space trajectory. This is because image contrast information which is encoded in the center of k-space (Bitar et al., 2006), has a magnitude that is affected by the trajectory used to fill k-space. If a radial or spiral trajectory is used, then the bright signal from the first RF pulse will be included in the contrast data that is stored in the center of k-space. In this case, the image contrast of the stationary fluid will be an average of the bright first signal and a number of steady state signals used to fill k-space. On the other hand, if a Cartesian trajectory is used and k-space is filled from top to bottom then the bright signal associated with the first RF pulse, will be at the periphery and the center of k-space will be filled by only steady state signals. In this situation, equation 3.2 can be re-written as 3.5a

$$\text{IntSI} = K\rho(M'_{ss} \cdot A \cdot L) + K\rho[(M_0 - M'_{ss})A \cdot \text{TR} \cdot \bar{v}] \quad \text{where } \bar{v} \leq \frac{L}{2 \cdot \text{TR}} \quad (3.5 a)$$

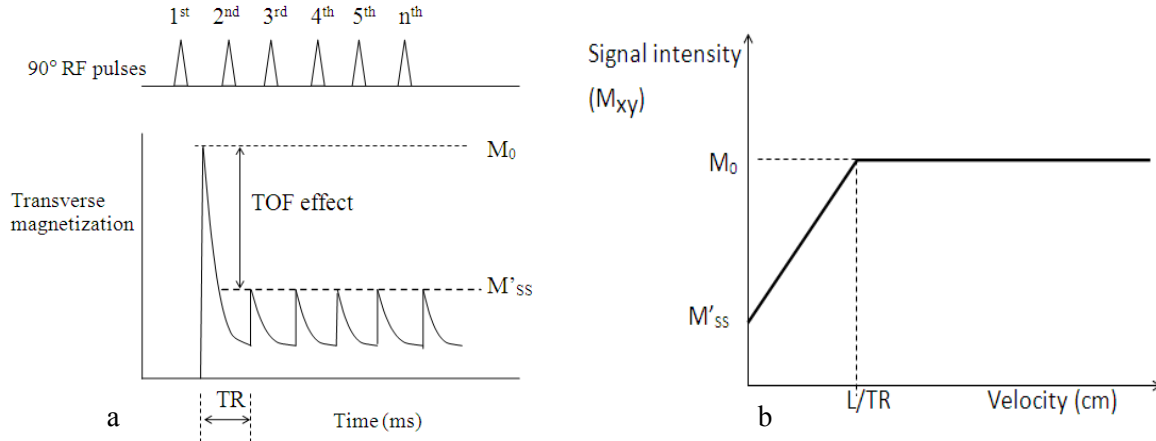


**Figure 3-2. Illustrations of the relationships between transverse magnetization, the number of RF pulses and blood velocity.** (a) When the flip angle is  $90^\circ$ , the transverse magnetization after the first RF pulse is at  $M_0$  while steady state is achieved by the second RF pulse. Therefore, the TOF effect is easily quantified as the difference between  $M_0$  and  $M'_{ss}$ . (b) There is a linear increase of signal intensity with velocity until the threshold velocity defined by the quotient of the slice thickness ( $L$ ) and TR.

The time of flight effect is the difference between the equilibrium magnetization and the steady state magnetization as illustrated in Figure 3-2a.

$$\text{TOF effect} = M_0 - M'_{ss} \quad (3.5 \text{ b})$$

As the velocity increases, the signal intensity increases because there is relatively more fresh blood than saturated blood within the slice. The linear relationship between velocity and the pixel intensity persists until a threshold velocity ( $L/TR$ ) beyond which no further increase occurs, as illustrated in 3-2b.

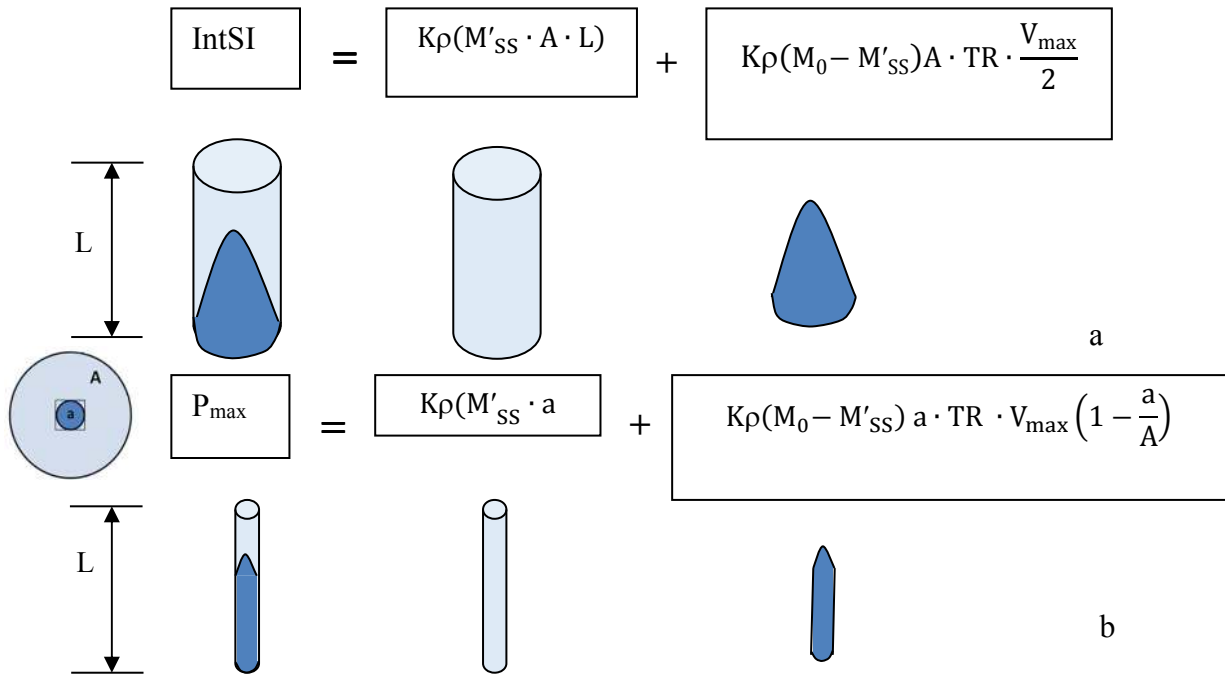


**Figure 3-3. The TOF effect within the lumen and that within a small central voxel** (a) shows the volumetric contribution of fresh spins and saturated spins to the integrated signal intensity of the lumen. (b) shows the volumetric contribution of the spins within the central voxel with cross-sectional area denoted by  $a$ .  $V_{max}(1-a/A)$  is the mean velocity within a radius from the centre of the lumen to the boundary of the central voxel as explained in the supplementary methods.

Equation 3.5a can be graphically illustrated by assuming that the arterial lumen has a cylindrical volume, with cross-sectional area ( $A$ ) and height equal to slice thickness ( $L$ ). When there is stagnant blood in the lumen, the integrated signal intensity of the lumen will be the product of the steady state signal intensity ( $M'_{ss}$ ) and the luminal volume. If there is blood flowing in the lumen with a parabolic velocity profile and the threshold velocity is not exceeded, the integrated

signal intensity of the lumen will contain an extra paraboloidal volume of signal due to the TOF effect from fresh blood that has just entered the slice. The height of the paraboloid ( $\Delta L$ ) will be a product of the TR and the mean blood velocity ( $V_{\text{mean}}$ ). Due to the parabolic nature of the flow,  $V_{\text{mean}}$  will be half of the maximal velocity ( $V_{\text{max}}$ ).

### 3.3.2.4 Deriving the luminal area from the integrated signal intensity equation

Assuming that the flow is parabolic, then the mean luminal velocity ( $\bar{v}$ ) is half of the maximal velocity. Substituting  $\bar{v}$  with half of  $V_{\text{max}}$  in equation 3.5 yields:

$$\text{IntSI} = K\rho(M'_{\text{SS}} \cdot A \cdot L) + K\rho \left[ (M_0 - M'_{\text{SS}}) \cdot A \cdot \text{TR} \frac{V_{\text{max}}}{2} \right] \quad (3.6 \text{ a})$$

Multiplying both sides by 2

$$2 \cdot \text{IntSI} = 2 \cdot K\rho (M'_{\text{SS}} \cdot A \cdot L) + K\rho [(M_0 - M'_{\text{SS}}) \cdot A \cdot \text{TR} \cdot V_{\text{max}}] \quad (3.6 \text{ b})$$

Solving for the luminal area

$$2 \cdot \text{IntSI} = A \cdot \{2 \cdot K\rho (M'_{\text{SS}} \cdot L) + K\rho [(M_0 - M'_{\text{SS}}) \cdot \text{TR} \cdot V_{\text{max}}]\} \quad (3.6 \text{ c})$$

$$A = \frac{2 \cdot \text{IntSI}}{2 \cdot K\rho (M'_{\text{SS}} \cdot L) + K\rho [(M_0 - M'_{\text{SS}}) \cdot \text{TR} \cdot V_{\text{max}}]} \quad (3.6 \text{ d})$$

The luminal area can be calculated with equation 3.6d if  $V_{\text{max}}$  is known. However, if  $V_{\text{max}}$  is unknown, it can be determined from the maximal pixel intensity ( $P_{\text{max}}$ ) since velocity affects the fractional contributions of fresh spins to the  $P_{\text{max}}$  as illustrated in figure 3-3. The mean velocity within a radius defined by the central voxel ( $V_{\text{p}}$ ) can be used as an approximation of  $V_{\text{max}}$  if the pixel to luminal area ratio ( $a/A$ ) is small as explained in Supplementary Methods at the end of this chapter.

$$V_{\text{p}} \sim V_{\text{max}} \quad (3.6 \text{ e})$$

Based on Figure 3-3b,  $V_{\text{p}}$  can be determined from  $P_{\text{max}}$  using equation 3.6g which is a modification of equation 3.6a

$$P_{\text{max}} = K\rho(M'_{\text{SS}} \cdot a \cdot L) + K\rho[(M_0 - M'_{\text{SS}}) a \cdot \text{TR} \cdot V_{\text{p}}] \quad (3.6 \text{ f})$$

where  $a$  is the pixel area.

Solving for  $V_P$  gives the value for  $V_{\max}$

$$V_P = \frac{P_{\max} - K\rho(M'_{SS} \cdot a \cdot L)}{K\rho[(M_0 - M'_{SS}) \cdot a \cdot TR]} = V_{\max} \quad (3.6 g)$$

Replacing  $V_{\max}$  in equation 3.6d with the approximated value obtained in equation 3.6g gives equation 3.7a

$$A = \frac{2 \cdot \text{IntSI}}{2 \cdot K\rho(M'_{SS} \cdot L) + K\rho[(M_0 - M'_{SS}) \cdot TR \cdot V_{\max}]} \quad (3.6 d)$$

$$A = \frac{2 \cdot \text{IntSI}}{2 \cdot K\rho(M'_{SS} \cdot L) + K\rho[(M_0 - M'_{SS}) \cdot TR] \frac{P_{\max} - K\rho(M'_{SS} \cdot a \cdot L)}{K\rho[(M_0 - M'_{SS}) \cdot a \cdot TR]}} \quad (3.7 a)$$

Cancelling out  $K\rho[(M_0 - M'_{SS}) \cdot TR]$

$$A = \frac{2 \cdot \text{IntSI}}{2 \cdot K\rho(M'_{SS} \cdot L) + \frac{P_{\max} - K\rho(M'_{SS} \cdot a \cdot L)}{a}} \quad (3.7 b)$$

Simplifying the equation

$$A = \frac{2 \cdot \text{IntSI} \cdot a}{2 \cdot K\rho(M'_{SS} \cdot a \cdot L) + P_{\max} - K\rho(M'_{SS} \cdot a \cdot L)} \quad (3.7 c)$$

Subtracting  $K\rho(M'_{SS} \cdot a \cdot L)$

$$A = \frac{2 \cdot \text{IntSI} \cdot a}{K\rho(M'_{SS} \cdot a \cdot L) + P_{\max}} \quad (3.7 d)$$

Since  $K\rho(M'_{SS} \cdot a \cdot L)$  is the central pixel's intensity at steady state when there is no flow ( $P_{SS}$ ), therefore equation 3.7d can be written as

$$A = \frac{2 \cdot \text{IntSI} \cdot a}{P_{SS} + P_{\max}} \quad (3.7 e)$$

### 3.3.2.5 Summary of the assumptions made while deriving the IntSI technique for measuring luminal area with a spoiled gradient echo sequence

1. The TOF effect increases with the velocity up to a threshold velocity beyond which no further increase in the TOF effect occurs.
2. When the flip angle is  $90^\circ$ , spins in the slice will either be completely fresh spins or completely saturated spins.
3. When stationary fluid experiences  $90^\circ$  RF pulses and a Cartesian trajectory is used to fill k-space, that the image contrast will be based solely on the steady state signals.
4. The imaged arterial lumen has a cylindrical volume, with a circular cross-sectional area (A) and height of slice thickness (L).
5. All velocities within the slice are less than the threshold velocity.
6. The velocity has a fully formed parabolic profile in which the mean velocity is half of the maximal velocity.
7. The mean velocity within the most central pixel ( $V_p$ ) can be used as an approximation for  $V_{max}$  provided the pixel-to-luminal area ratio is small.

Assumptions 1, 2 and 3 are based on basic MRI physics, as discussed in chapter 2. Assumption 4 may be violated if the imaging plane is not perpendicular to the long axis of the artery.

Assumption 5, 6 and 7 may be violated depending on the velocity during imaging, the pixel area and the luminal area of the vessel imaged. A phantom study was designed to test the reliability of the IntSI technique when assumptions 6 and 7 no longer hold true.

### 3.3.3 The phantom study

A 3D printed model fabricated by the machine shop of the Sunnybrook Research Institute was used. The model consisted of 12 rigid tubes (A to L) connected in series and attached to a flow pump (Mityflex peristaltic pump model no 913-24127, FL, USA), that had an adjustable flow rate (range 0.47-13.33cc/s). The cross-sectional areas of the tubes were 4.91mm<sup>2</sup>, 7.07 mm<sup>2</sup>, 9.62 mm<sup>2</sup>, 12.6 mm<sup>2</sup>, 15.9 mm<sup>2</sup>, 19.6 mm<sup>2</sup>, 23.8 mm<sup>2</sup>, 26 mm<sup>2</sup>, 28.3 mm<sup>2</sup>, 33.2 mm<sup>2</sup>, 35.8 mm<sup>2</sup> and 38.5 mm<sup>2</sup>. The areas were comparable to the brachial and popliteal luminal areas.

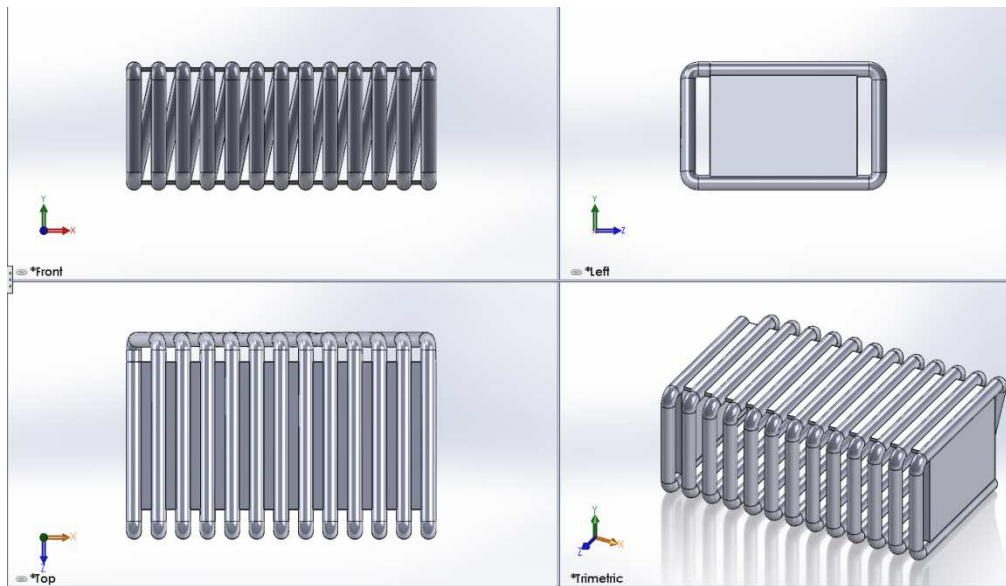
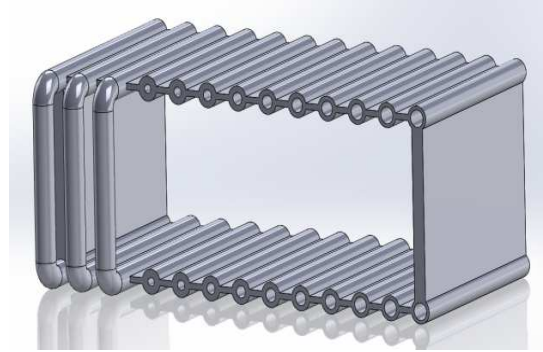
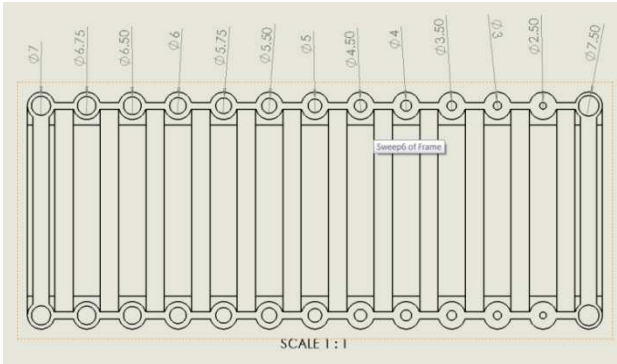


**Figure 3-4. The phantom set-up. (a) An image of the 3D printed model. (b) An image of the pump.**

There was a smooth transition in diameter between the tubes and the tubes had 7 mm spacing between them in order to prevent flow artifacts from one tube overlapping on the image of another tube. The width of the phantom was 12 cm and this defined the length of the tubes.

The required entrance length for fluid to establish a fully developed parabolic profile was taken into consideration. The entrance length for a fully developed parabolic flow profile ( $l_e$ ) was calculated with the formula (Tongpun et al., 2014).

$$l_e = 0.06 \cdot Re \cdot D \quad (3.8 a)$$

where  $l_e$  is the entrance length for fully developed laminar flow in cm,  $Re$  is Reynolds number, and  $D$  is the luminal diameter in cm. Reynolds number was calculated using the formula (Mott, 2006).

$$Re = \frac{\bar{v} \cdot D}{k_v} \quad (3.8 b)$$

where  $\bar{v}$  is the mean velocity in cm/s,  $D$  is the luminal diameter in cm,  $k_v$  the kinematic viscosity of water in  $\text{cm}^2/\text{s}$ .

The smallest tube (Tube A) had a luminal diameter of 0.25 cm. If the kinematic viscosity of water at 20°C is 0.01  $\text{cm}^2/\text{s}$ , (Vanoni, 2006) and the mean velocity was 25 cm/s in this smallest tube, then the Reynolds number and entrance length for tube A were calculated as 625 and 9.38 cm respectively. At a mean velocity of 25 cm/s within Tube A, the mean velocity within the largest tube (Tube L) will be 3.19 cm/s because velocity is inversely proportional to the luminal area when the flow rate is constant. Therefore, the Reynolds number and entrance length for Tube L will be 223.3 and 9.38 cm respectively.

The tubes were filled with water using the flow pump and the water was recycled through the tubes. Although recycling of fluid during imaging may result in heating and affect the kinematic velocity, we did not expect any significant increase in temperature because the room temperature was controlled. All air bubbles were expelled before imaging commenced. Imaging was performed with a 3T Siemens MRI scanner and a surface coil. The imaging slice was located perpendicular to the tubes and at a distance of 9.5 cm from the origin of the tubes, so that water in the imaging slice would have had a fully developed parabolic flow profile at this point.

### 3.3.3.1 The effect of velocity on area measurements

A spoiled GRE sequence was used for testing the effect of velocity on area measurements. The scan parameters were flip angle: 90°, TR: 20 ms, TE: 4.6 ms, slice thickness: 10 mm, NEX: 1, FOV: 280 mm × 280 mm, matrix: 448 × 448, pixel area: 0.4  $\text{mm}^2$ , scan time: 9.0 s. Based on the



TR and slice thickness, the threshold velocity was 50 cm/s. The upper limit for the range of velocities used for imaging was calculated from a predetermined entrance length and the luminal diameter using equation 3.8c, a derivative of equations 3.8a and 3.8b.

$$V_{\max} = \frac{2 \cdot k_v \cdot l_e}{0.06 \cdot D^2} \quad (3.8 \text{ c})$$

Equation 3.8c was used to calculate the highest mean velocity that when combined with an entrance length of 9.5 cm will accommodate a fully formed parabolic flow profile. The number 2 in the equation was included in order to obtain  $V_{\max}$  from the mean velocity since  $V_{\max}$  is twice the mean velocity.

During the experiments, the tube velocities were varied by adjusting the flow rate in incremental steps and in order to ensure that the data acquisition was at a defined flow rate, a five-second pause was introduced between each image acquisition and the flow rate was adjusted during this period.

#### **3.3.3.1.1 Effect of velocities compatible with full formed parabolic flow on the IntSI technique**

The first experiment was performed to test the effect of velocity on the IntSI technique when the tube velocities were compatible with the entrance length required for parabolic flow and the TOF threshold velocity was not exceeded. Two separate image acquisitions were obtained at different flow rates. The flow rates were values at which the associated tube velocities were compatible with the entrance length of 9.5 cm. The tube velocities did not exceed the threshold of 50 cm/s, a value that was calculated as the quotient of the slice thickness and TR. To determine the steady state pixel intensity ( $P_{SS}$ ), two images were acquired without flow and the maximal luminal pixel intensity from these images was obtained. An average obtained from analysis of the two images of the static fluid was used for  $P_{SS}$  as described subsequently in the post processing section.

#### **3.3.3.1.2 The effect of velocity/entrance length mismatch on the IntSI technique (assumption 5)**

The second experiment was designed to assess the effect of violating assumption 5, a situation in which the velocity has a blunted parabolic profile because the entrance length is insufficient for the development of a fully formed parabolic profile. Therefore, the mean velocity is greater than

half of the maximal velocity. This will make areas calculated with the IntSI technique unreliable since one of the assumptions made while deriving the equation is that the velocity has a fully formed parabolic profile. For this phase, the flow rate was increased so that the tube velocities were higher than that compatible with a fully developed parabolic flow as calculated with equation 3.8c at the given entrance length and tube diameter. Two images were obtained at different high flow rates.

### 3.3.3.1.3 Post processing of the MR images

The images were post processed with imageJ ( (National Institutes of Health, Bethesda, USA). The display contrast and ambient light were kept constant throughout the study. For measuring luminal area using the IntSI technique, a polygonal ROI was used to enclose all pixels that appeared to contain any amount of luminal signals. A polygonal ROI was used rather than a circular ROI because a polygonal ROI offers the operator more flexibility when enclosing luminal pixels. The integrated signal intensity (IntSI) of the ROI was measured by summing the intensities of all the pixels.  $P_{max}$  was determined as the maximal pixel intensity obtained from a polygonal ROI placed within the lumen.  $P_{SS}$  was the value of  $P_{max}$  when the velocity was zero. Each image was processed by the same observer five times and the average of five area measurements was recorded. The luminal areas were calculated using the IntSI technique.

$$A = \frac{2 \cdot \text{IntSI} \cdot a}{P_{SS} + P_{max}} \quad (3.7 e)$$

The difference in area measurement between the observed and the known area was calculated as

$$\text{Relative error in area measurment}(\%) = \left[ \frac{(\text{Observed area} - \text{Known area})}{\text{Known area}} \cdot 100 \right]$$

To see the effect of velocity on the accuracy of the IntSI technique based area measurements, the relative error between the observed and expected luminal areas was plotted against the velocity. The mean value of the two images per flow rate was used.

### 3.3.3.2 The effect of the pixel to luminal area ratio on the measured area (Assumption 7)

To test for the effect when the area ratio is not small and therefore the averaged velocity within the most central pixel ( $V_p$ ) cannot be assumed to be very close to  $V_{max}$ , other experiments were

performed using larger pixel areas. Firstly, the pixel area was increased to 1.4 mm<sup>2</sup> using a matrix size of 256 × 256 and a FOV of 300 mm × 300 mm, while the FOV, flip angle, NEX and TE remained unchanged. This reduced the scan time to 5.6 s. Subsequently, the experiment was repeated a second time using a larger FOV (500 mm × 500 mm) while all other parameters remained constant in order to increase the pixel area further to 3.8 mm<sup>2</sup>. The images were post processed as described previously and the area measurement errors obtained by comparing the observed luminal area and the known area was also calculated as described previously for each pixel size. The images were not anonymous because the reader could guess the pixel size by visual inspection.

### 3.3.3.2.1 Post processing of the MR images

IntSI, P<sub>max</sub> and P<sub>SS</sub> were obtained with the method described in section 3.3.3.4.1. Different pixel-to-luminal area ratios were generated using the three pixel sizes (0.4 mm<sup>2</sup>, 1.4 mm<sup>2</sup> and 3.8 mm<sup>2</sup>) and the twelve luminal areas. In order to determine when the area ratio has negligible effect on the calculated area, the area measurement error at each point was plotted against the corresponding area ratio.

### 3.3.3.3 The reliability of area measurements using the IntSI technique versus a pixel counting approach.

In order to determine the reliability of the IntSI technique, areas measured with the IntSI technique were compared with the known luminal areas of the tubes in the flow phantom and also compared with values obtained by the pixel counting approach. For area measurements by pixel counting, an average of five area measurements was recorded.

### 3.3.4 Statistical analyses

The results were expressed as mean ± SD. The intraclass correlation coefficient (ICC) was used to test for agreement between the observed luminal area and the known luminal area. The ICC was calculated for luminal areas measured with the IntSI technique and areas obtained via thresholding and pixel counting respectively. Bland Altman plots were used to assess the presence of systemic bias. The coefficient of repeatability (CR), which is two standard deviations from the mean difference between the observed and known luminal areas was used to estimate

the measurement reliability of each method (Vaz et al., 2013). A sample size of 10 tubes with 5 observations per subject achieves 80% power to detect an intraclass correlation (ICC) of 0.9 under the alternative hypothesis when the null hypothesis is an ICC of 0.7 using an F-test with a significance level of 0.05 (Walter et al., 1998). Therefore, a sample size of 12 tubes was sufficient to meet the sample size requirement for testing the reliability of the IntSI technique. The mean value obtained from five measurements was used for precision. All calculations were carried out using the R Project for Statistical Computing version 3.1.3 (by R Foundation for Statistical Computing, Vienna, Austria).

Lin's concordance correlation coefficient ( $\rho_c$ ) was used as a measure of the strength of agreement between each measurement technique and the known luminal areas. As the reduced major axis of the data gets closer to the line of perfect concordance,  $\rho_c$  increases (Huang et al., 2015). The strength of agreement criteria for  $\rho_c$  were as follows:  $>0.99$  for almost perfect agreement;  $0.95-0.99$  for substantial agreement;  $0.90-0.95$  for moderate agreement;  $<0.90$  for poor agreement (McBride, 2005).

A two-one-sided t-test (TOST) using the function `rTOST` in the equivalence package of R was used to test for non-inferiority between areas measured with high resolution at  $0.4 \text{ mm}^2$  pixels and those with the IntSI technique ( $0.4 \text{ mm}^2$  and  $1.4 \text{ mm}^2$  pixels) at an alpha of 0.1 and power of 0.8. The null hypothesis was that the IntSI technique (at  $0.4 \text{ mm}^2$  and  $1.4 \text{ mm}^2$  pixels respectively) was inferior to pixel counting at  $0.4 \text{ mm}^2$  pixels, while the alternative hypothesis was that the IntSI technique (at  $0.4 \text{ mm}^2$  and  $1.4 \text{ mm}^2$  pixels respectively) was non-inferior to pixel counting at  $0.4 \text{ mm}^2$  pixels. The margin of similarity was the CR for the mean difference between the known luminal area and areas measured by pixel counting at  $0.4 \text{ mm}^2$  pixels.



**Figure 3-5. An image of the lower half of the flow phantom using a spoiled GRE sequence.** The image was acquired with pixel area of  $1.4 \text{ mm}^2$ . The 12 lumina appear bright against a dark background on the spoiled GRE sequence.

## 3.4 Results

### 3.4.1 Effects of the sequence on the vascular contrast and scan time

Despite using pixels as large as  $3.0 \text{ mm}^2$ , the scan time for phase contrast imaging was still 24s (Table 3-1). The contrast to noise ratio (CNR) was highest with phase contrast. Although the spoiled GRE sequence had a CNR that was a bit lower than that of phase contrast imaging, the pixel area used for the spoiled GRE sequence was lower than that of phase contrast and the associated scan time was one-third that of the phase contrast sequence (Table 3-1). The spoiled GRE sequence had higher CNR efficiency. It also had a higher CNR efficiency per unit volume, despite the fact that the slice thickness used for the spoiled GRE sequence was smaller than that of the phase contrast sequence (Table 3-1). Therefore, the spoiled GRE sequence was the more suitable technique to use for area measurements with the IntSI technique.

**Table 3-1. Pixel areas, CNRs and scan times of the two bright blood sequences in a volunteer.**

	Phase contrast sequence	spoiled GRE sequence
Pixel area ( $\text{mm}^2$ )	3.0	1.9
CNR	727	677
Scan time (s)	24	7.1
CNR efficiency ( $\text{s}^{-1}$ )	30.3	95.4
Slice thickness (mm)	5	3.5
Voxel volume ( $\text{mm}^3$ )	15	6.7
(CNR efficiency)/volume ( $\text{s}^{-1} \cdot \text{mm}^{-3}$ )	2.02	14.24

### 3.4.2 Effect of the velocity and entrance length mismatch on the IntSI technique.

When the velocities were compatible with the entrance length of 9.5 cm (velocity range: 0.7 -27 cm/s), the difference in area measurement using the IntSI technique was within  $\pm 10\%$  of the known area of the tubes (Figure 3-6). When the velocities were incompatible with the entrance length of 9.5 cm (velocity range: 6.9 - 42 cm/s), the difference in the area measurement was significantly higher (Figure 3-6). In all cases, the velocities did not exceed the threshold of 50cm/s.

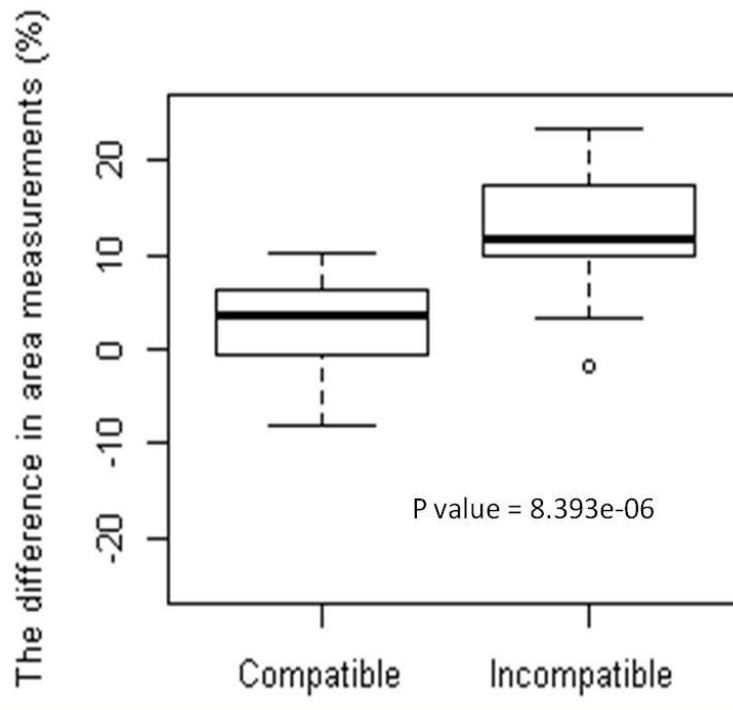


**Figure 3-6. Box plot showing the effects of velocity and entrance length mismatch on area measurements obtained with the IntSI technique.** (a) When the velocities during imaging were compatible with the entrance length, the difference in area measurements obtained with the IntSI technique was between -10% and 10%. (b) When the velocities were incompatible with the entrance length, the difference in area measurement was significantly higher.

### 3.4.3 Effects of pixel-to-luminal area ratio on the IntSI technique

Figure 3-7 is a plot of various pixel-to-luminal area ratios against the difference in area measurements when the velocities within the tubes were compatible with parabolic flow. There was a linear relationship between the pixel-to-luminal area ratio and the difference in the area measurements. When the pixel-to-luminal area ratio was less than 0.1, the difference between areas calculated with the IntSI technique and the known area was within 10%. As the area ratio increased beyond 0.1, the difference between the known and expected area measurements increased.

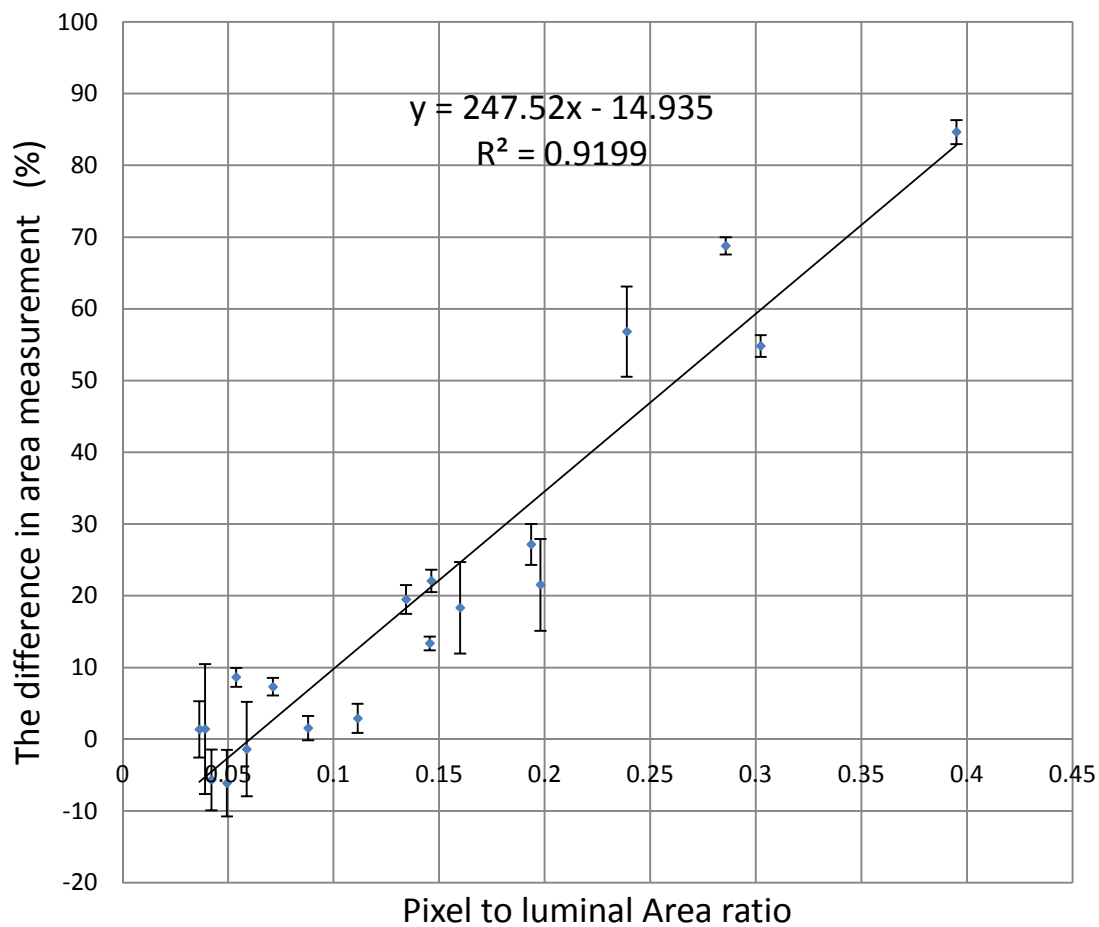


**Figure 3-7. A scatter plot of the relative difference between observed and expected luminal area measurements versus the area ratio with the line of best fit shown.** The error bars are  $\pm 1$ SD). For area ratios less than 0.1, the average difference in area measurement was  $3.0 \pm 7.5$  %

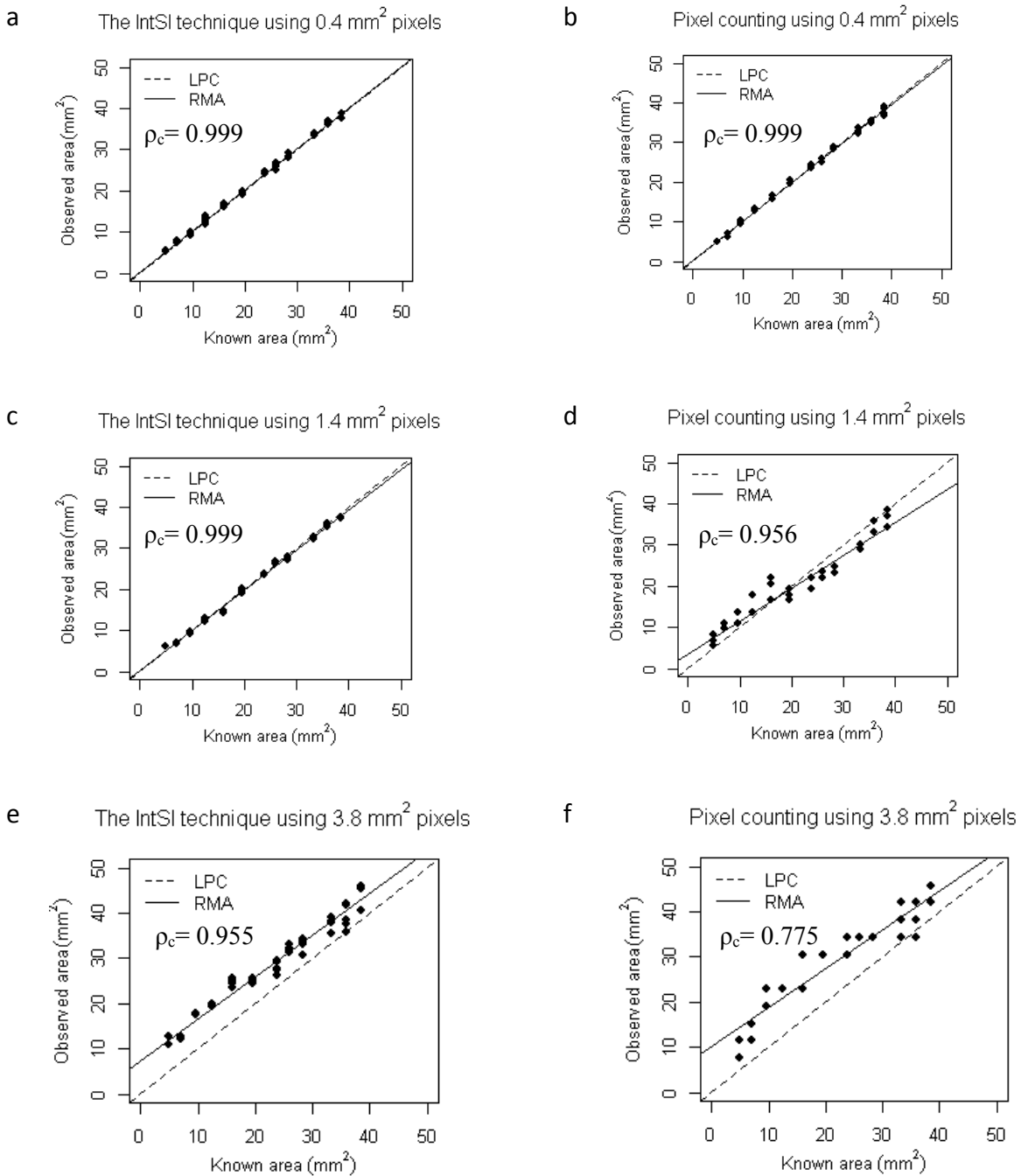
### 3.4.4 Reliability of area measures using the IntSI technique versus the pixel counting approach

Figure 3-8 consists of scatter plots of the observed luminal area (IntSI and pixel counting) against the known luminal area, with a reduced major axis included in each graph. The mean difference and coefficients of repeatability (CR) are presented with the Bland-Altman plots and ICCs in figure 3-9. Both area measurement techniques showed poorer values for the CR and ICC as the pixel area increased. When the pixel area used for imaging was  $0.4 \text{ mm}^2$  measurements obtained by IntSI technique were in agreement with the known values (Figure 3-9a; mean difference  $\pm$  CR:  $0.34 \pm 1.17 \text{ mm}^2$ , ICC: 0.998) and they were comparable to that obtained by pixel counting (Figure 3-9b; mean difference  $\pm$  CR:  $-0.07 \pm 1.12 \text{ mm}^2$ , ICC: 0.998). When the pixel area increased to  $1.4 \text{ mm}^2$ , areas measured with the IntSI technique (Figure 3-9c) (mean difference  $\pm$  CR:  $-0.22 \pm 1.43 \text{ mm}^2$ , ICC: 0.998) were comparable to the IntSI and pixel counting methods at  $0.4 \text{ mm}^2$  pixels. Using Lin's concordance correlation coefficient ( $\rho_c$ ) to test for accuracy and precision, pixel counting at  $0.4 \text{ mm}^2$  pixels was not better than IntSI technique at  $0.4 \text{ mm}^2$  and  $1.4 \text{ mm}^2$  pixel areas respectively (Figure 3-8). The pixel counting approach at  $1.4 \text{ mm}^2$  pixels was less reliable than the methods mentioned above (Figure 3-9d; mean difference  $\pm$  CR:  $0.69 \pm 6.15 \text{ mm}^2$ , ICC: 0.971). When the luminal area was less than  $15 \text{ mm}^2$ , measurements obtained by pixel counting at  $1.4 \text{ mm}^2$  pixel size were overestimated, with a shift in the reduced major axis to the left from the line of perfect concordance, while the measurements were underestimated when the luminal area was greater than  $15 \text{ mm}^2$ , with a shift of the reduced major axis to the right (Figure 3-8d).

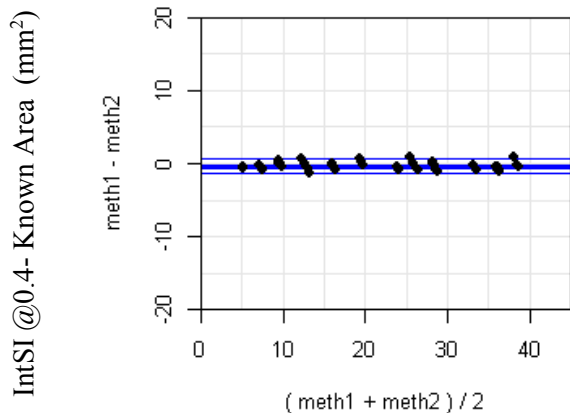
When the pixel area was  $3.8 \text{ mm}^2$ , the IntSI technique was less reliable (Figure 3-9e; mean difference  $\pm$  CR:  $5.86 \pm 3.93 \text{ mm}^2$ , ICC: 0.916,  $\rho_c=0.955$ ) with a shift to the left of the line of perfect concordance (Figure 3-8e). Areas measured with pixel counting at  $3.8 \text{ mm}^2$  pixel size were also less reliable (mean difference  $\pm$  CR:  $7.34 \pm 6.77 \text{ mm}^2$ , ICC: 0.854,  $\rho_c=0.775$ ) than that obtained using smaller pixels (Figure 3-9f).

Non-inferiority testing at an alpha of 0.1 showed that the IntSI technique (at  $0.4 \text{ mm}^2$  and  $1.4 \text{ mm}^2$  pixel areas respectively) was non-inferior to pixel counting at  $0.4 \text{ mm}^2$  pixels (Table 3-2). The margin of similarity for non-inferiority testing was the CR of the known luminal area versus pixel counting at  $0.4 \text{ mm}^2$  pixels.

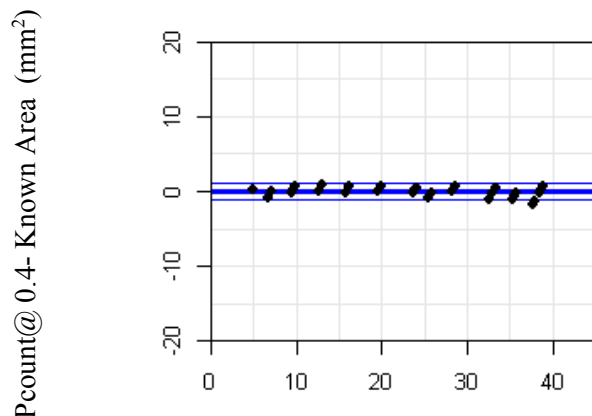




**Figure 3-8. Scatter plots of observed area versus the known area using the pixel counting approach and the IntSI technique.** (a) and (b) are plots of the known luminal area versus the IntSI technique and pixel counting approaches respectively using  $0.4 \text{ mm}^2$  pixels. (c) and (d) are plots of the known luminal area versus the IntSI technique and pixel counting approaches respectively using  $1.4 \text{ mm}^2$  pixels. (e) and (f) are plots of the known luminal area versus the IntSI technique and pixel counting approaches respectively using  $3.8 \text{ mm}^2$  pixels. LPC is the line of perfect concordance while RMA is the reduced major axis.

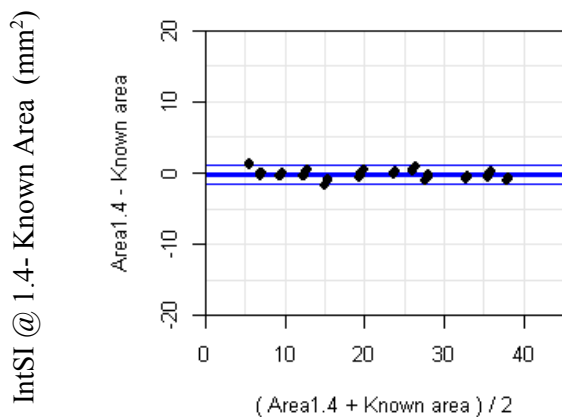


(IntSI @0.4 + Known Area)/2 (mm<sup>2</sup>)

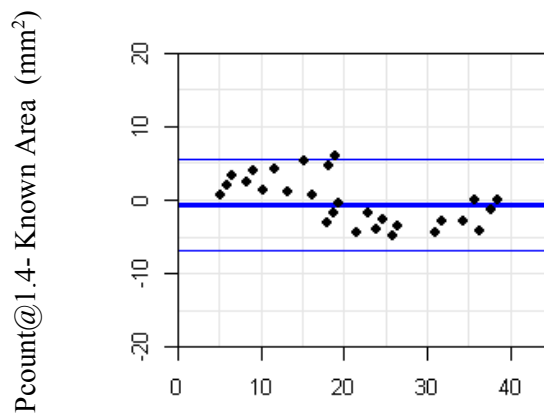


(Pcount@0.4 + Known Area)/2 (mm<sup>2</sup>)

Mean bias ± CR (mm <sup>2</sup> )	ICC	Mean bias ± CR (mm <sup>2</sup> )	ICC
0.36 ± 1.04	0.998 ( 0.997 - 0.999)	-0.07±1.12	0.998 (0.998-0.999)

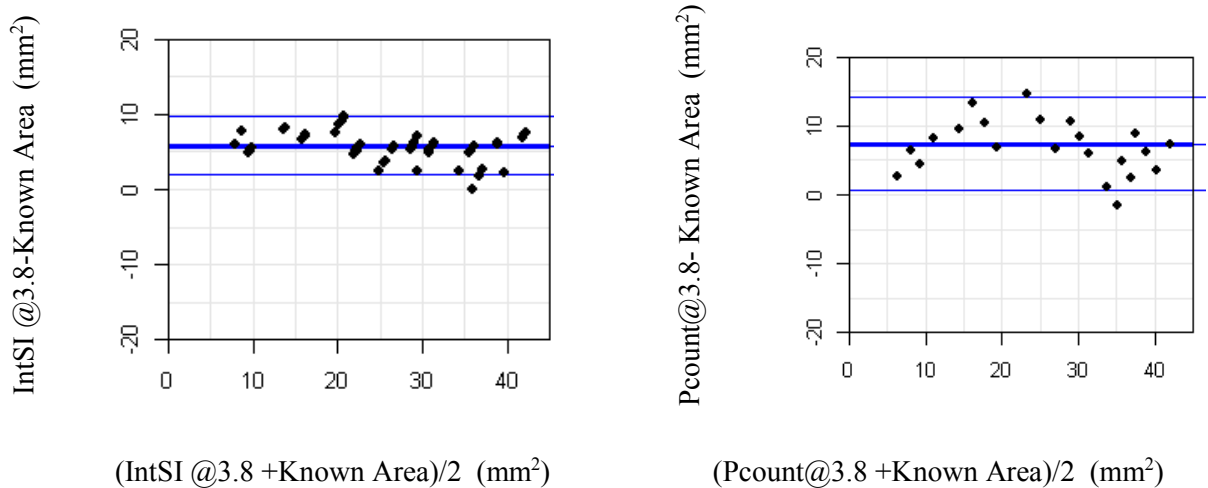


(IntSI @1.4 + Known Area)/2 (mm<sup>2</sup>)



(Pcount@1.4 + Known Area)/2 (mm<sup>2</sup>)

Mean bias ± CR (mm <sup>2</sup> )	ICC	Mean bias ± CR (mm <sup>2</sup> )	ICC
-0.22 ± 1.43	0.998 (0.997-0.999)	0.69 ± 6.15	0.971 (0.940-0.990)



Mean bias $\pm$ CR (mm <sup>2</sup> )	ICC	Mean bias $\pm$ CR (mm <sup>2</sup> )	ICC
5.86 $\pm$ 3.93	0.916 (0.837-0.970)	7.34 $\pm$ 6.77	0.854 (0.731-0.946)

**Figure 3-9. Bland-Altman plots and ICCs (with 95% confidence intervals) of the known luminal area versus area obtained with the IntSI technique (IntSI) and the high resolution/pixel counting approach (Pcount) respectively.** (a) and (b) are results for the known luminal area versus the IntSI technique and pixel counting approaches respectively using 0.4 mm<sup>2</sup> pixels. (c) and (d) are results for the known luminal area versus the IntSI technique and pixel counting approaches respectively using 1.4 mm<sup>2</sup> pixels. (e) and (f) are results for the known luminal area versus the IntSI technique and pixel counting approaches respectively using 3.8 mm<sup>2</sup> pixels.

**Table 3-2. Testing for non-inferiority between the pixel counting (Pcount) technique at 0.4 mm<sup>2</sup> pixels and those of the IntSI technique (at 0.4 mm<sup>2</sup> and 1.4 mm<sup>2</sup> pixels respectively).**

	Mean difference and confidence intervals (mm <sup>2</sup> )	Se.diff	P value
0.4 IntSI vs 0.4 Pcount	-0.43 (-0.56 to -0.31)	0.10	9.98e-11
1.4 IntSI vs 0.4 Pcount	0.15 (0.0001 to 0.30)	0.12	1.62e-13

## 3.5 Discussion

In this chapter, an area measurement technique was developed that does not require spatial resolution as high as that needed for measuring via pixel counting. This alternative approach therefore allows for improved temporal resolution. This method, termed the IntSI technique, measures the luminal area using the integrated signal intensity of the luminal pixels. The technique uses the maximal pixel intensity to adjust for effects of velocity on the integrated signal intensity.

### 3.5.1 Choosing an appropriate bright blood sequence

Features that were considered when choosing an appropriate bright blood sequence for measuring luminal area with the IntSI technique included temporal resolution, vascular contrast and velocity information. A high temporal resolution is required to enable rapid serial area measurements during FMD studies. Vascular contrast is necessary in order to ensure that signals from adjacent structures like the muscle and fat do not contribute to the integrated signal intensity and result in overestimation of the luminal area. Although the SSFP sequence is routinely used for MRI-FMD, it is unsuitable for measuring area with the IntSI technique because of associated banding artifacts that occur due to field inhomogeneity (Chavhan et al., 2008). These low signal artifacts will confound the linear relationship between velocity and signal intensity, making it difficult to use the signal intensity as an indirect measure of reactive hyperemia. The sequences that were considered included a phase contrast sequence and a spoiled GRE sequence. Phase contrast imaging had good vascular contrast and it contained velocity information but despite using large pixels for imaging, the acquisition time was as long as 24s. Other authors have also noted this limitation of phase contrast imaging (Silber et al., 2005). The spoiled GRE sequence on the other hand had good vascular contrast and the scan time was three times less than that of the phase contrast sequence.

### 3.5.2 The IntSI technique and assumptions

The IntSI technique for area measurements was derived from an equation that calculates the total MRI signal within the artery on a spoiled GRE sequence (Gao & Liu, 2012). The technique was based on some MRI physics concepts, such as the TOF effect increasing with velocity up to a threshold value beyond which there is no further increase in velocity (Hashemi et al., 2010).

Another concept is that when a tube with flowing spins is subjected to repeated RF pulses on a spoiled GRE sequence using a  $90^\circ$  flip angle, the spins within the slice will either be completely saturated spins or fresh spins that are at equilibrium magnetization (Kim & Parker, 2012). Therefore, it is important that  $90^\circ$  RF pulses are used for imaging with the IntSI technique. In addition, a Cartesian k-space trajectory ensures that the  $P_{SS}$  is solely based on the steady state signals. These can be incorporated as part of the protocol for area measurements with the IntSI technique. It is also assumed that the imaged arterial lumen has a cylindrical volume, with a circular cross-sectional area ( $A$ ) and height of slice thickness ( $L$ ). The other assumptions made while deriving the IntSI equation are not as straightforward as those mentioned above. These include the presence of a parabolic velocity profile (Zierler & Sumner, 2014) with the velocities being less than the threshold velocity (Hashemi et al., 2010) and the assumption that the mean velocity of the central pixel can be used as a substitute for the maximal velocity provided that the pixel-to-luminal area ratio is small. These other assumptions were tested in a phantom study.

### 3.5.3 Effect of the velocity profile on the IntSI technique

The fifth assumption made while deriving the IntSI technique was that the velocity profile was a fully formed parabolic type in which the mean velocity is half of the maximal velocity. A parabolic velocity profile is not attained immediately after fluid enters a tube. Rather, the fluid has to travel a distance within the tube before a fully formed parabolic flow profile develops and this distance depends on the tube velocity (Mott, 2006; Tongpun et al., 2014). The flow phantom had a finite length, just like vivo situations where the imaged artery has a finite length. Therefore to test for the effect of a velocity/entrance length mismatch, the tube velocity was varied. The difference in area measurement between the known area and that obtain with the IntSI technique was within the range of -10% to 10%, when the mean velocities in the tubes during imaging were compatible with that requirement for an entrance length of 9.5 cm. When the mean velocity was higher than that compatible with the given entrance length for the development of a fully formed parabolic flow, the difference in the area measurement varied from -2% to 42% (Figure 3-6b).

It was observed that the difference in area measurements increased as the velocity increased. This can be ascribed to a gradual change in the velocity profile from parabolic flow to plug flow at high velocities and it highlights the importance of ascertaining the velocity profile of an artery

when using the IntSI technique to calculate the luminal area. If the velocity profile is a blunted parabola or closer to plug flow, then the calculated luminal area will be overestimated. This is because the mean luminal intensity will be less than expected. Spectral Doppler ultrasound can be used to determine the velocity profile of peripheral arteries (Ade et al., 2012).

#### 3.5.4 Effect of exceeding the threshold velocity on the IntSI technique

The sixth assumption is that the velocities during imaging do not exceed the threshold velocity associated with the TOF effect. When the velocities exceed the threshold there is no further increase in signal intensity with velocity. Therefore, all velocities beyond the threshold velocity are assigned the maximal signal intensity and then the TOF effect no longer has a parabolic profile like the corresponding velocity profile. Rather the profile becomes blunted and this leads to overestimation of the area measurements as shown in Figure 3-6b. When maximal velocity within the slice was higher than the threshold velocity of 50 cm/s, the difference in the area measurement was greater than 10%. This makes it important to ensure when an artery is measured with the IntSI technique, a suitable combination of the slice thickness and TR should be selected for imaging in order to arrive at threshold velocity that can accommodate the maximal possible arterial velocity.

#### 3.5.5 Effect of the pixel-to-luminal area ratio on the IntSI technique

The seventh assumption is that the averaged velocity within the most central pixel ( $V_p$ ) can be used as a substitute for the maximal velocity ( $V_{max}$ ), provided that the pixel-to-luminal area ratio is small. When the pixel-to-luminal area ratio was varied with all other assumptions upheld, then provided that the pixel-to-luminal area ratio did not exceed 0.1, the difference in luminal area measurements was less than 10% (Figure 3-7). The effect of the pixel-to-luminal area ratio on the IntSI technique was further highlighted with the scatter plots (Figure 3-8). When the pixel size was as large as 3.8 mm<sup>2</sup> the luminal area was over-estimated, with a shift to the left from the line of unity (Figure 3-8e). The overestimation is because when the pixel area is large, the average velocity in the central pixel ( $V_p$ ) is no longer representative of  $V_{max}$ . The minimum baseline diameters of the brachial and popliteal arteries are 2.6 mm and 3.9 mm respectively as seen with ultrasound in children who are at least 8 years old (Ostrem et al. 2014, Sandgren et al. 1998). These correspond to minimum area values of 5.31 mm<sup>2</sup> and 11.95 mm<sup>2</sup> respectively.

Therefore, provided that the pixel areas used for imaging these arteries do not exceed  $0.531 \text{ mm}^2$  and  $1.195 \text{ mm}^2$  respectively, the difference in the measured areas will not exceed 10%.

Interestingly, it is difficult to measure vasodilatation with ultrasound when the vessel diameter is less than 2.5 mm (Sorensen et al., 1995), which means that even in the hands of a skilled sonographer, ultrasound has no advantage over MRI for diameters less than 2.5 mm. However, the likelihood of scanning an artery that small is slim, since the smallest brachial artery should be 2.6 mm in diameter (Ostrem et al. 2014). Although it is preferable to use smaller pixels in order to minimize the difference in area measurement, the use of smaller pixels may compromise temporal resolution and SNR.

### 3.5.6 Reliability of the IntSI technique

Area measurements using the IntSI technique were semi-automated, without a need to define the luminal boundary. The ROI for intensity measurements was located at a position where there was no luminal signal, so that all the boundary pixels were included in the ROI. This approach provides a means of reducing the effect of partial volume on area calculations. This is unlike the pixel counting approach in which the entire pixel is either included or excluded in the calculated luminal area, leading to measurement errors.

Other automated methods for area measurement have reported measurement error as low as 0.9% using phase contrast imaging (Oyre et al., 1998). Just like the IntSI technique, the authors defined the luminal boundary with three-dimensional paraboloid modeling of the velocity based on assumptions of laminar flow and a circular lumen area (Oyre et al., 1998). Velocity encoding was used to determine  $V_{\max}$  and the velocities within pixels at the luminal boundary and a second degree polynomial function was used to calculate the x and y co-ordinates for the circular luminal area. The low measurement error observed using this technique is expected because the pixel area used for imaging was  $0.25 \text{ mm}^2$  and the imaged phantom had an internal diameter of 8 mm. If the imaged phantom had a circular lumen, then the luminal area will be  $50 \text{ mm}^2$  and the area ratio 0.01. The authors did not specify the required scan time and acknowledged that for smaller luminal areas, a higher resolution will be required to achieve similar results. However, a higher resolution will require a longer scan time. Unlike Oyre et al (1998) the luminal areas used to test IntSI technique were between  $4.9 \text{ mm}^2$  to  $38.5 \text{ mm}^2$  which are representative of the

brachial and popliteal luminal areas (Sandgren et al., 1998; Ostrem et al., 2014). In another study, that used a pulsatility-based segmentation (PUBS) technique for defining the luminal boundary, the measurement error of a tube with internal diameter of 8 mm was at most 4.8%, while a smaller tube with internal diameter of 5 mm tube was overestimated by 28% (Alperin & Lee, 2003). The author ascribed the high error observed with the smaller tube to partial volume averaging. Despite the wide range of tube sizes used to assess the IntSI technique, the difference in area measurement with the technique did not exceed 10%, even when the luminal diameter was 5 mm or less, provided that area ratio was below 0.1 (Figure 3-7). This shows that partial volume averaging has less effect on area measurement with the IntSI technique as opposed to the pixel counting approach. With the IntSI technique, the partial volume of the edge pixels are included in the area calculations unlike with pixel counting where edge pixels are included or excluded from the area measurements based on whether their signal intensity values are above or below the threshold.

### 3.5.7 Comparing the IntSI technique with pixel counting

The accuracy and precision of the IntSI technique were compared with a pixel counting method for area measurements using different spatial resolutions. This was done in order to demonstrate that for a given pixel area, the IntSI technique is more reliable than pixel counting for a pixel area. It was also of interest to determine how large the pixel area can be when measuring the lumen with the IntSI technique and still obtain results comparable with pixel counting, so that the scan time could be shortened using moderately sized pixels for imaging. The reliability of area measurements using the IntSI technique at a pixel area of  $1.4\text{mm}^2$  ( $\rho_c= 0.999$ ) was comparable with that of pixel counting at the higher resolution of  $0.4\text{mm}^2$  pixel area ( $\rho_c= 0.999$ ) (Figure 3-8). Increasing the pixel area from  $0.4\text{mm}^2$  to  $1.4\text{mm}^2$  led to a decrease in scan time from 9.0 seconds to 5.6 seconds. This decrease in scan time provides an opportunity to improve the temporal resolution during an FMD study.

This chapter demonstrates that it is possible to obtain reliable luminal area measurements with the IntSI technique using moderately sized pixels. The lower spatial resolution provides an opportunity to improve the temporal sampling frequency.



### 3.6 Supplementary Methods

This section explains why the mean velocity within a radius defined by the central pixel ( $V_p$ ) can be substituted for  $V_{max}$  when the pixel to luminal area ratio is small, as referred to on page 14.

If the luminal radius is  $R$  and the maximal velocity is  $V_{max}$ , then the velocity at a point with radius ( $r$ ) from the center of the lumen is given below (Cengel & Cimbala, 2006).

$$V_r = V_{max} \left( 1 - \frac{r^2}{R^2} \right) \quad (S3 - 1)$$

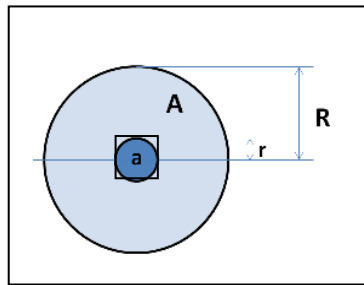


**Figure 3-10. An illustration of the luminal area (A) with radius (R) and a small circular area (a) with radius (r).**

If  $r$  is the radius from the center of the lumen to the boundary of a central voxel's cross-section, then the velocity at radius ( $V_r$ ) can be calculated using equation S3-1 above.

If the central pixel defines the radius of interest, the mean velocity within the central pixel ( $V_p$ ) can be obtained by integrating all the velocities within that radius.

Equation S3-1 can also be expressed as a ratio of the central voxel's cross-sectional area ( $a$ ) to the cross-sectional area of the lumen ( $A$ ) by multiplying with  $\pi$ .

$$V_r = V_{max} \left( 1 - \frac{a}{A} \right) \quad (S3 - 2)$$

As  $a$  gets smaller,  $V_r$  gets closer to  $V_{max}$ .

---

**Chapter 4    Popliteal artery spectral Doppler  
waveform analysis for in vivo adaptation  
of the IntSI technique**

---

## 4.1 Abstract

**Objective:** To adapt the IntSI technique for in vivo measurements by assessing the spectral Doppler waveform of the artery.

**Background:** The IntSI technique measures luminal area as a function of the integrated signal intensity of the luminal pixels. This technique was shown in Chapter 3 to produce accurate results in a controlled setting using flow phantoms. Before applying this method in vivo, it is important to consider whether the assumptions made while deriving the technique hold true for arterial flow. Spectral Doppler analysis provides a means of assessing the assumption that the velocity profile is parabolic. It also makes it possible to determine  $V_{\max}$  during the low flow rates of diastole and at different physiological states. Once  $V_{\max}$  is known, the TOF threshold velocity can be calculated by modifying the slice thickness and TR so that we do not violate the assumption that  $V_{\max}$  is less than the threshold value. The pixel intensity at steady state ( $P_{SS}$ ) is required for measurements with the IntSI technique. Spectral Doppler analysis provides an opportunity to assess the time averaged velocity during diastole in an unperturbed artery. If this is close to zero, and the flip angle used for MR imaging is  $90^\circ$ , then data acquired during this period can be used as  $P_{SS}$ .

**Methods:** To assess if the popliteal artery has a parabolic velocity profile, spectral Doppler analysis of the popliteal artery was performed on 10 healthy volunteers at rest, during distal occlusion and during reactive hyperemia. To determine what the TOF threshold velocity should be, the time averaged maximal velocity ( $TAV_{\max}$ ) during diastole was calculated.

To assess if MRI data acquired during diastole in an unperturbed artery can be used as  $P_{SS}$ , the diastolic time averaged mean velocity ( $TAV_{\text{mean}}$ ) at baseline was obtained.

**Results:** Spectral Doppler analysis showed that the popliteal artery had a blunted parabolic flow profile with a  $V_{\text{mean}}/V_{\max}$  ratio of 0.6 when averaged over diastole. The highest velocities at diastole occurred during hyperemia with a  $TAV_{\max}$  up to 23.55 cm/s. In unperturbed arteries  $TAV_{\text{mean}}$  during diastole was  $-1.07 \pm 1.05$  cm/s.

**Conclusion:** The IntSI technique may be used to measure the luminal area of the popliteal artery if adjustments are made for the blunted parabolic profile. MRI data acquired during diastole in an unperturbed artery ( $P_B$ ) can be used as the steady state pixel intensity ( $P_{SS}$ ) if signals from the first RF pulses of each segment are excluded from data used to determine the image contrast and adjustments are made for the small net retrograde flow that occurs during data acquisition.

## 4.2 Introduction

In Chapter 3, the integrated signal intensity (IntSI) technique was demonstrated as an accurate method for obtaining the luminal area in flow phantoms. The technique measures the luminal area as a function of the integrated signal intensity of luminal pixels. It adjusts for the effect of velocity on the signal intensity using the most central pixel's intensity (with and without flow). The technique is based on certain assumptions and it is necessary to test if these assumptions hold true in peripheral arteries. The assumptions include:

- 1) The arterial velocity has a fully formed parabolic profile in which the mean velocity is half of the maximal velocity;
- 2) The maximal velocity ( $V_{\max}$ ) during data acquisition is less than the TOF threshold velocity; and
- 3) The averaged velocity within the most central pixel ( $V_p$ ) can be used as a substitute for  $V_{\max}$  provided the pixel-to-luminal area ratio is small.

The popliteal artery was used to test the IntSI technique in vivo rather than the brachial artery which is the commonly used artery for ultrasound FMD function (Deanfield et al., 2007; Stoner et al., 2013). Reasons for using the popliteal artery include its anatomic advantage. The artery lies close to the midline therefore is expected to produce homogeneous MR signals when placed within the bore of the magnet since local field inhomogeneities increase with distance from the center of the magnet (Brix et al., 2008). Popliteal imaging offers a means of scanning patients with claustrophobia because the patient can be placed feet first into the bore and the head will be free of the confined space. Another reason for testing the IntSI equation with the popliteal artery is that atherosclerosis is seen more often in the lower limbs (Laredo & Lee, 2008). Therefore, developing an MRI-FMD technique that can identify dysfunction in the artery before structural damage occurs may be useful in those at risk for atherosclerosis.

### 4.2.1 The assumption of parabolic flow in the popliteal artery

The IntSI technique is based on an assumption that peripheral arteries have parabolic flow profiles with the mean velocity ( $V_{\text{mean}}$ ) being half of the corresponding maximal velocity ( $V_{\max}$ ) at each time point (Ade et al. 2012). However, it is not clear if this is the case with the popliteal artery. As discussed in Chapter 2, the blood has to travel a distance from the origin of an artery before the velocity profile becomes a fully formed parabolic type. This distance called the

“entrance length” increases with the Reynolds number, the luminal diameter and blood velocity. Apart from the viscous forces that explain the parabolic flow profile, arterial flow also experiences inertial forces because arterial flow is pulsatile in nature (Womersley, 1955). The Womersley number ( $\alpha$ ) is a dimensionless number used to define the relationship between these two forces and characterize the flow profile (Womersley, 1955).

If the length of the popliteal artery is less than the required entrance length, the flow profile in the artery will not develop into a fully formed parabolic type; rather, the velocity profile will be blunted with the  $V_{\text{mean}}/V_{\text{max}}$  ratio greater than 0.5 (Zierler & Sumner, 2014). Since the TOF effect varies with velocity, if the velocity profile is blunted, the TOF effect will have a blunted parabolic profile also and the areas calculated using the IntSI technique will be overestimated. This is because the central pixel intensity, which is the denominator in the IntSI equation, will be less than it should be. Spectral Doppler ultrasound can be used to determine the velocity profile of the popliteal artery (Ade et al., 2012).

#### **4.2.2 The assumption that the maximal velocity in the popliteal artery does not exceed the TOF threshold velocity**

Unlike the phantom study in which the flow is continuous, flow within an unperturbed peripheral artery is triphasic, with a high forward flow in the first phase, which corresponds to late systole. The second phase occurs during early diastole and consists of retrograde flow due to distal peripheral resistance while the third phase in mid diastole shows anterograde flow following the closure of the aortic valve (Scissons, 2008). The arterial size also varies with the cardiac cycle, with maximal distension occurring during the forward flow of late systole (Chuang et al., 2002). To reduce the effect of cardiac cycle-related variations on the arterial size, conventional MRI-FMD studies use ECG gating with diastolic trigger delay (Sorensen et al., 2002; Leeson et al., 2006). These studies acquire data during a diastolic window and several cardiac cycles are required to fill up all the lines in k-space. Imaging during diastole is also suitable for area measurement with the IntSI technique, partly to avoid cardiac cycle based variations in the luminal area as highlighted above. Diastolic gating is also important because of the assumption made while deriving the IntSI technique that the threshold velocity associated with the TOF effect is not exceeded (Hashemi et al., 2010). With diastolic gating, the high velocities of systole are avoided during MR data acquisition and imaging occurs during the slower velocities of

diastole. Diastolic gating is also useful during hyperemia because the average diastolic velocity during hyperemia is usually much lower than the averaged systolic velocity (Osada & Radegran, 2005).

Once the threshold velocity is exceeded, any additional increase in velocity will not lead to an increase in the signal intensity of centrally located pixels. However, with a parabolic velocity profile, flow close to the vessel wall will not attain the threshold velocity as fast as the central flow does, due to frictional forces. This means that luminal pixels close to the vessel wall will still show increased signal intensity with velocity. Therefore, the integrated TOF effect in the lumen will become a blunted paraboloid and the mean luminal TOF effect will be greater than half of the maximal value. This is undesirable because area measurements using the IntSI technique will then be overestimated since the method assumes that the mean TOF effect is half of the maximal value. Spectral Doppler analysis can be used to determine the highest possible velocity that may occur during diastole in order to select a slice thickness that will result in an appropriate threshold velocity (Kim & Parker, 2012).

#### 4.2.3 The pixel intensity when there is no flow during imaging

When stagnant fluid in the phantom is imaged with a spoiled GRE sequence using a 90° flip angle, the signal detected after the first RF pulse will be at the maximal value ( $M_0$ ) and signals detected after subsequent RF pulses will be at the lowest value ( $M'_{ss}$ ). Unlike the phantom study, central pixel intensity during arterial imaging may not be at steady state even when there is no flow during image acquisition. This is because the data is obtained over several cardiac cycles. During the systolic phase of each cardiac cycle, there will be a forward flow of fully magnetized spins into the slice. If the diastolic trigger delay is long enough, the slice will be completely re-filled with fresh blood and the first RF pulse at each new cardiac cycle will produce signals at  $M_0$ . The center of k-space contains image contrast information and the bright signal from the first RF pulse may or may not contribute to the image contrast, depending on the trajectory used to fill k-space (Perrin, 2013). If a radial or spiral trajectory is used to fill k-space and image contrast is determined from more than two or more cardiac cycle segments, then the bright signals from the first RF pulse of the second and subsequent cardiac cycle segments will make the pixel intensity when there is no flow higher than  $P_{ss}$ . This increase in signal intensity can be avoided if a Cartesian trajectory is used for filling k-space and data from each segment is

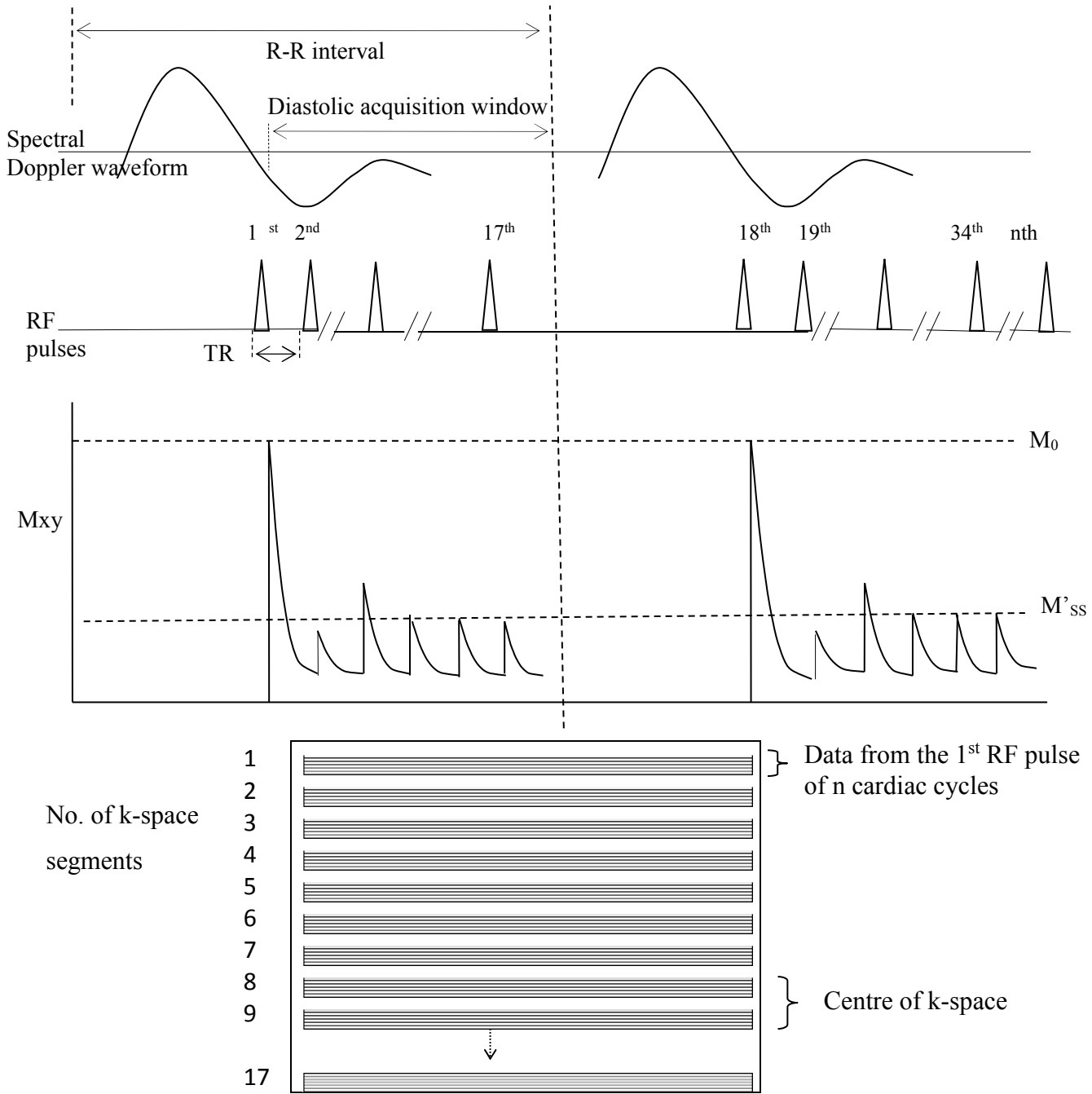


**Figure 4-1. Cardiac gating with a diastolic trigger delay ensures that imaging does not occur during the high velocities of systole.** However, if the R-R interval is long enough, the slice is completely refilled with fresh blood and the signal produced after the first RF pulse in each cardiac cycle will be at the highest value ( $M_0$ ). When there is retrograde diastolic flow, the measured signal will be less than  $M'_{ss}$  due to the effect of the venous suppression band and during anterograde diastolic flow, it will be higher than  $M'_{ss}$  due to fresh blood in the slice. Therefore, the intensity of the central pixel will depend on the direction of flow when the center of k-space is filled since the center of k-space contains contrast information.

spaced out at intervals in k-space. In this situation, all the bright signals at  $M_0$  will be at the periphery and steady state signals will be at the center of k-space. So the image contrast will be based on the steady state signal and image contrast will not be affected by the number of lines required to fill the center of k-space because each line at the center of k-space will be filled by signals at steady state.

Another challenge with arterial imaging is that there is flow during diastole, with a brief period in which there is no flow just before the next cardiac cycle. Since the diastolic period within which there is no flow is very brief, depending on the TR, this period may be insufficient for MR data acquisition. The data acquisition window may be widened to include the back and forth diastolic flow but this may lead to inaccuracy in estimating  $P_{ss}$ . If a Cartesian trajectory is used to fill k-space with the lines filled up at intervals within k-space, and the center of k-space happens to be filled during the retrograde portion of the cardiac cycle, the central pixel's intensity will be less than  $P_{ss}$  due to the presence of a venous saturation band. This saturation band is usually placed distal to the imaging plane during MR angiography in order to saturate adjacent venous signals, but this may also lead to saturation of signals from the retrograde blood entering the slice.

The presence of saturated blood within the central voxel will reduce the intensity of signals detected from the voxel. Conversely, if the center of k-space is filled during the antegrade diastolic flow, the central pixel's intensity will be higher than  $P_{ss}$ , because of the entrance of fresh blood into the slice during imaging. Therefore, depending on the phase(s) of the cardiac cycle during which the center of k-space is filled and the amount of lines in k-space used to determine the image contrast, the central pixel's intensity may be less than or greater than  $P_{ss}$ . Spectral Doppler analysis may be used to estimate the duration of the different phases of diastole.

The aims of this chapter were:

- 1) to determine if the velocity profile of the popliteal artery is parabolic;
- 2) to determine the time averaged mean velocity during hyperemia in order to determine the threshold velocity given a fixed slice thickness and repetition time (TR);
- 3) to determine the time averaged velocity during diastole in an unperturbed artery.



## 4.3 Materials and Methods

### 4.3.1 Theoretical calculation for the highest velocity compatible with a given entrance length for parabolic flow in the popliteal artery

In chapter 2, the entrance length for parabolic flow in a pulsatile artery ( $l_e$ ) was calculated as

$$l_e = 0.3 \cdot Re \cdot \frac{R}{\alpha} \quad (4.1)$$

Where  $Re$  is Reynolds number,  $R$  is the radius of the arterial lumen and  $\alpha$  is the Womersley number of the specific artery. The Reynolds number can be calculated as (Mott, 2006)

$$Re = \frac{V_{max} \cdot (2R)}{2 \cdot k_v} \quad (4.2)$$

where  $V_{max}$  is the maximal velocity in cm/s,  $R$  is the luminal radius in cm,  $k_v$  the kinematic viscosity of water in  $cm^2/s$ .

Substituting for  $Re$  in equation 4.1 with equation 4.2 and solving for  $V_{max}$  gives equation 4.3, which can be used to calculate the maximal velocity compatible with a given entrance length for parabolic flow.

$$V_{max} = \frac{l_e \cdot k_v \cdot \alpha}{0.3 \cdot R^2} \quad (4.3)$$

The popliteal artery has a Womersley number of 4 (Hoskins & Hose, 2017). The artery measures  $19.11 \pm 3.47$  cm (Ozgun et al., 2009) from its origin at the adductor hiatus to its termination at the origin of the anterior tibial artery, while the maximum diameter of the popliteal artery is 9.6 mm (Sandgren et al., 1998). To avoid turbulent flow during imaging, if the velocity profile is sampled 2 cm above the termination of the popliteal artery, then the entrance length for parabolic flow profile will be an average of 17.11 cm. At an arterial diameter of 9.6 mm, the highest velocity compatible with an entrance length of 17.11 cm was calculated as 11.33 cm/s using equation 4.3. At a more realistic diameter of 6 mm (Sandgren et al., 1998), the highest velocity compatible with the entrance length of 17.11 mm is 25.18 cm/s. Therefore, depending on the arterial diameter, blood velocity and required entrance length for parabolic flow, the velocity profile may not be parabolic in the popliteal artery.

### 4.3.2 Subject selection and control of factors that affect reactive hyperemia

Ten young adult male volunteers with ages ranging between 19-27 years had their popliteal arteries assessed with spectral Doppler ultrasound. Informed consent was obtained from each volunteer and ethics approval was obtained from the Sunnybrook Health Sciences Centre Research Ethics Board. In order to ensure that the hyperemic velocities measured were reflective of the normal values expected in the popliteal artery; potential volunteers at risk for microvascular dysfunction were excluded from the study. These include those with a history of cardiovascular disease, dyslipidemia or diabetes. Smokers were not included in the study given that smoking is associated with microvascular dysfunction (Fujii et al., 2013).

Subjects were scanned in a temperature controlled room after a period of rest because reactive hyperemia is lessened in cold environments (Widlansky et al., 2007).

### 4.3.3 The Ultrasound technique

A Philips iU22 Ultrasound system (Philips Healthcare, Andover, MA, USA) at the Diagnostic Imaging Department of Sunnybrook Health Sciences Centre was used for the ultrasound study. Each subject was positioned prone on an examination couch with the pneumatic cuff of an aneroid sphygmomanometer (D.E. Hokanson Inc., Bellevue, WA USA) placed on just above the ankle for distal occlusion. A linear array 9-3 MHz transducer was used to image the artery. The ultrasound probe was positioned in the popliteal fossa behind the knee. Spectral Doppler imaging was performed using pulse wave Doppler at an insonation angle of  $60^\circ$  and a frequency of 3.5MHz. The sonographer manipulated the transducer using the heel-to-toe technique to ensure the ultrasound beam was at an angle of  $60^\circ$  to the long axis of the popliteal artery (Lee, 2014). The area had an average depth of 3.4 cm from the skin surface. To avoid turbulent flow, the sample volume was positioned 2 cm above the origin of the anterior tibial artery (Tindall et al., 2006).

The sample volume was expanded from wall-to-wall in order to include all velocities within the lumen. The average length of the Doppler sampling volume was 6 mm. In cases of aliasing, a wrap-around artifact that occurs when the maximum velocity in the imaging plane exceeds the velocity scale, the scale was adjusted so that high velocities were correctly represented above the

baseline (Pozniak et al., 1992). To assess the velocity profile at baseline, a spectral Doppler tracing of the unperturbed artery was obtained and then the cuff was inflated to 240 mmHg for 5 minutes. To assess the velocity profile when there is distal occlusion, another spectral Doppler tracing was obtained one minute before the cuff was released. Then a final tracing was obtained when the cuff was released in order to assess the velocities during reactive hyperemia. For each stage, data was acquired over three cardiac cycles.

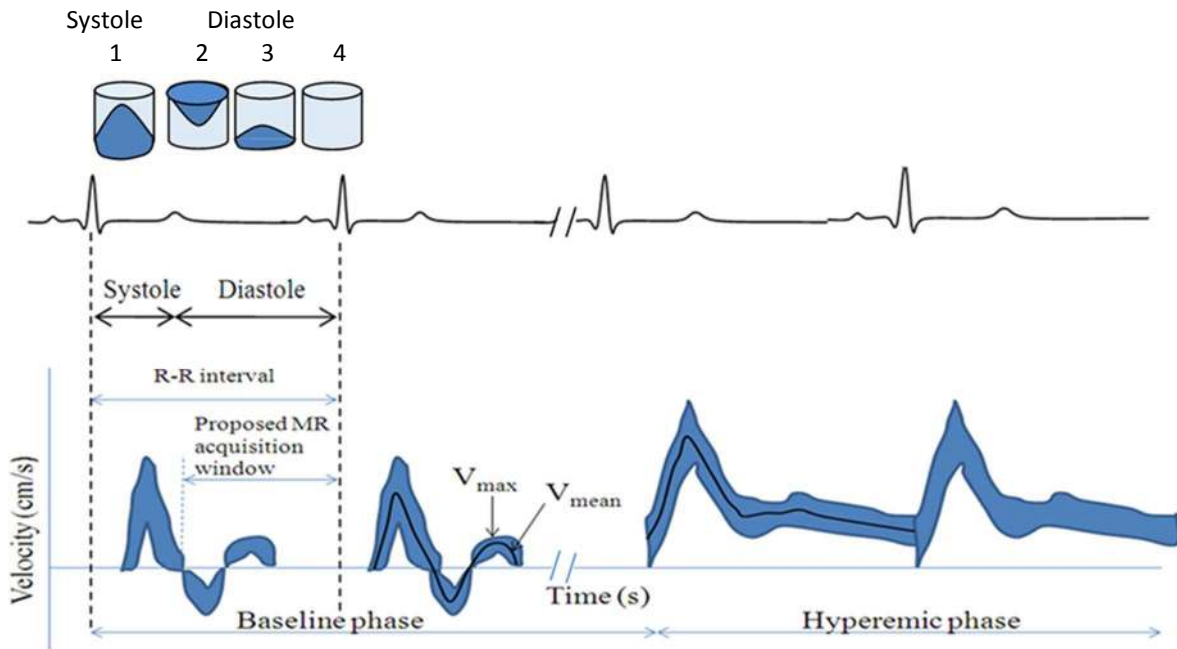


**Figure 4-2. A schematic drawing of the spectral Doppler tracing at baseline and during hyperemia respectively.** The ECG tracing lies above the Doppler waveform, while the direction of flow in the vessel is illustrated above the ECG tracing. For velocities above the zero baseline,  $V_{max}$  is represented by the upper bound of the Doppler waveform envelope while it is represented by the lower bound for velocities less than zero. The black line represents  $V_{mean}$ . The proposed MR signal acquisition window is the diastolic phase of the cardiac cycle. At baseline, diastole includes a retrograde phase (2), an anterograde phase (3) and a phase in which there is no flow (4).

#### 4.3.4 Post processing

The vessel diameter was measured with electronic callipers provided with the scanner. The callipers were placed at the luminal intima boundaries of the near and far walls of the artery and the average of three measurements was recorded. The spectral Doppler waveforms at different hemodynamic states were analyzed to obtain the time averaged velocities (TAV) and velocity

profiles at the different states. The time averaged maximal velocity ( $TAV_{max}$ ) of a given cardiac cycle was calculated as the integral of the magnitude of  $V_{max}$  over the cardiac cycle divided by the R-R interval (Ade et al., 2012). For anterograde velocities,  $V_{max}$  at each time point was defined by the upper boundary of the spectral envelope as shown in figure 4-2, while for retrograde velocities,  $V_{max}$  at each time point was defined by the lower boundary of the spectral envelope. To calculate  $TAV_{max}$ , the spectral Doppler waveform was converted to a binary image in ImageJ (US National Institutes of Health, Bethesda, MD, USA) and the area under the curve for positive velocities and the area above the curve for negative velocities were summed and then divided by the R-R interval (Ballyns et al., 2011) as shown in figure 4-3a.

The time averaged intensity weighted mean velocity ( $TAV_{mean}$ ) of the cardiac cycle (Evans et al., 1989; Young, 2011) is represented by the black line in Figure 4-2 and it was obtained as follows: a matrix of the intensities of all velocities over the entire cardiac cycle was exported into an excel spreadsheet (Figure 4-3b) using a macro in imageJ (Rasband, 2005). The pixel intensities were representative of the amount of blood particles moving at that velocity. The total number of particles moving at a given time point was calculated by summing up all the pixels at that time point. The sum of the velocities of all particles at a given time point was obtained by multiplying each pixel value by the corresponding velocity and the average velocity at each time point was calculated. Subsequently,  $TAV_{mean}$  was calculated by dividing the sum of the average velocity at each time point in a cardiac cycle by the R-R interval.  $TAV_{max}$  and  $TAV_{mean}$  were also computed for the anterograde and retrograde portion of the tracing as well as the entire diastolic period. The  $TAV_{mean}$  and  $TAV_{max}$  values were calculated as the mean of three cardiac cycles and the corresponding  $TAV_{mean}/TAV_{max}$  ratios were also calculated. A parabolic profile was one in which the velocity ratio was 0.5. Ratios greater than 0.5 but less than 1.0 were termed blunted parabolic profiles (Ade et al., 2012).

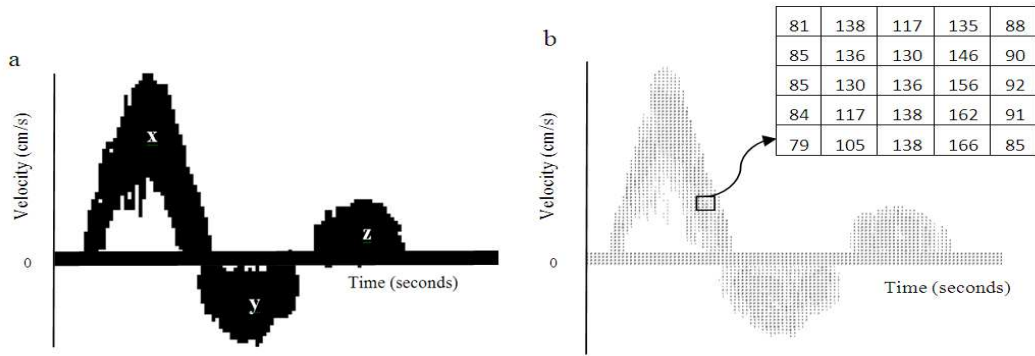


**Figure 4-3. Post processing to obtain  $TAV_{max}$  and  $TAV_{mean}$ .** (a) is a binary image of a spectral Doppler waveform.  $TAV_{max}$  was calculated by adding the area under the curve for positive velocities (x and z) with the area above the curve for negative velocities (y) and then divided by the R-R interval. (b) is a matrix of the pixel intensities of all velocities over a cardiac cycle. The  $TAV_{mean}$  was calculated from this matrix. The pixel intensities representing the x-axis were not included in the calculations.

#### 4.3.5 Statistical analyses

The waveforms of three cardiac cycles were analyzed on each spectral Doppler tracing obtained at baseline, during distal occlusion and during reactive hyperemia. The data obtained was presented as mean $\pm$ SD.  $TAV_{mean}$  was plotted as a function of  $TAV_{max}$  during the various portions of the cardiac cycle and at the three physiological states. To compare  $TAV_{mean}/TAV_{max}$  ratio during the three physiological states with the values of 0.5, expected for fully developed parabolic flow, an independent one- tailed t-test was used.

## 4.4 Results

In the resting state, the popliteal artery had a triphasic waveform: forward flow occurred during systole, while retrograde flow followed by anterograde flow occurred at diastole. Then there was an intervening pause with little to no flow before the next waveform (Figure 4-3a). Sometimes retrograde flow occurred again after the anterograde diastolic flow, giving a quadriphasic waveform which may be seen in lower extremity arteries at rest (Hussain et al., 1996). This second retrograde flow during diastole was in two volunteers at baseline and in five volunteers at the distal occlusion phase (Figure 4-3b). This second retrograde flow was included when calculating the time averaged velocities during diastole and during the entire cardiac cycle. During hyperemia, the flow velocities increased, and waveform changed from triphasic to monophasic with continuous anterograde flow (Figure 4-3c). The baseline diameter was  $5.56 \pm 0.67$  mm, while the maximal diameter post reactive hyperemia was  $5.84 \pm 0.69$ mm.

### 4.4.1 The velocity profile of the popliteal artery

At baseline the  $TAV_{\text{mean}}/TAV_{\text{max}}$  ratio was 0.60 during diastole which is the proposed MR signal acquisition window, while it was 0.68 for the entire cardiac cycle (Table 4.1). During cuff inflation, the  $TAV_{\text{mean}}/TAV_{\text{max}}$  ratio was 0.62 for the proposed MR signal acquisition window and 0.68 for the entire cardiac cycle (Table 4.1). During hyperemia, the velocity ratio was 0.61 within the proposed MR signal acquisition window while it was 0.67 for the entire cardiac cycle. The  $TAV_{\text{mean}}/TAV_{\text{max}}$  ratios during the proposed MR signal acquisition window were different from the expected ratio of 0.5 with p values less than 0.05.

### 4.4.2 The maximum time averaged velocity for the threshold value

The maximal velocities occurred during hyperemia. The  $TAV_{\text{max}}$  and  $TAV_{\text{mean}}$  during the diastole were  $17.51 \pm 6.04$  cm/s and  $10.87 \pm 4.10$  cm/s respectively, with upper limits for the  $TAV_{\text{max}}$  and  $TAV_{\text{mean}}$  being 26.26 cm/s and 18.38 cm/s respectively.  $TAV_{\text{max}}$  and  $TAV_{\text{mean}}$  during the entire cardiac cycle were  $22.96 \pm 6.36$  cm/s and  $14.37 \pm 6.17$  cm/s, with 31.38 cm/s and 24.35 cm/s being the upper limit for  $TAV_{\text{max}}$  and  $TAV_{\text{mean}}$  during entire cardiac cycle respectively.

#### 4.4.3 The time averaged velocity at baseline for the steady state value

The  $TAV_{max}$  and  $TAV_{mean}$  of the unperturbed artery averaged over diastole were  $-1.60 \pm 1.56$  cm/s and  $-1.07 \pm 1.04$  cm/s respectively while the  $TAV_{max}$  and  $TAV_{mean}$  averaged over the cardiac cycle were  $5.06 \pm 2.07$  cm/s and  $3.43 \pm 1.40$  cm/s respectively (Table 4-1).

Spectral Doppler analysis showed that in an unperturbed artery, the interval between the R wave and the onset of the spectral waveform was  $202.13 \pm 6.37$  ms. The systolic flow lasted  $229.58 \pm 8.79$  ms, the retrograde diastolic phase lasted about  $188.80 \pm 7.46$  ms and the anterograde diastolic phase lasted  $253.52 \pm 15.53$  ms (Table 4-2).

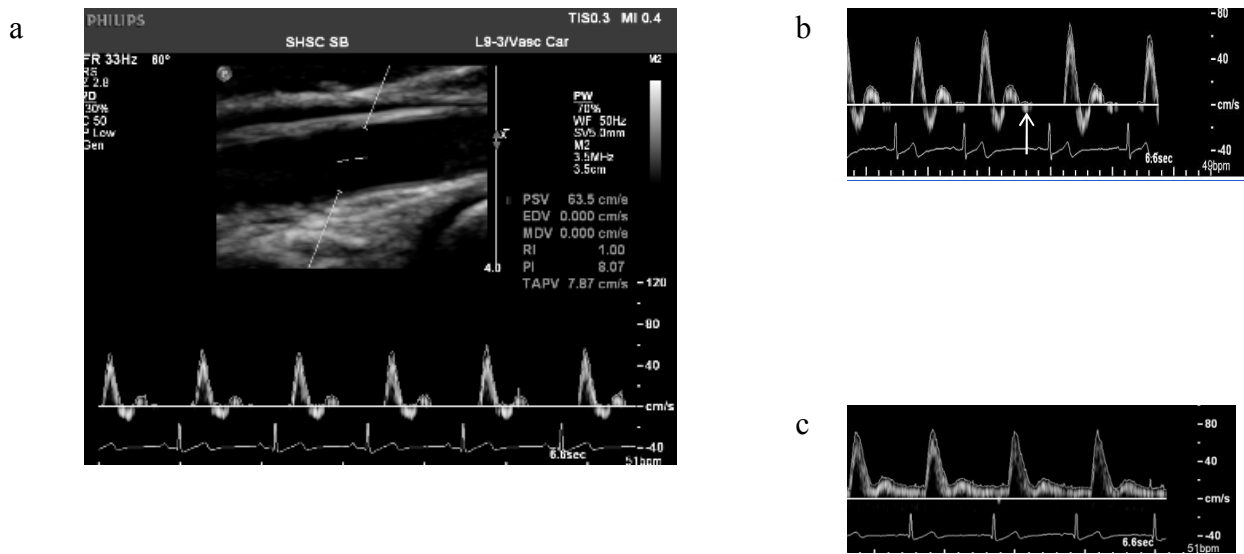


**Figure 4-3. Spectral Doppler ultrasound of the popliteal artery.** (a) is a duplex ultrasound image showing a pulsatile popliteal spectral Doppler tracing in an unperturbed artery. The sample volume was placed within the lumen at an insonation angle of  $60^\circ$  (b) shows an uncommon second retrograde diastolic flow (white arrow) that is sometimes seen during cuff inflation. (c) is the hyperaemic phase during which there is forward flow in throughout the entire cardiac cycle.

**Table 4-1. Velocities for different phases of the cardiac cycle at baseline, during cuff inflation and during reactive hyperemia.**

	<b>TAV<sub>max</sub> [cm/s]</b> <b>mean ± SD</b>	<b>TAV<sub>mean</sub> [cm/s]</b> <b>mean ± SD</b>	<b>V<sub>mean</sub>/V<sub>max</sub></b>
<b>At Baseline</b>			
Systolic flow	25.06 ± 6.92	16.01 ± 7.02	0.77 ± 0.050
Diastolic retrograde flow	-12.12 ± 3.80	-6.79 ± 3.73	0.60 ± 0.03
Diastolic anterograde flow	6.66 ± 2.02	3.74 ± 1.11	0.60 ± 0.07
2 <sup>nd</sup> retrograde diastolic flow*	-4.57 ± 1.62	-3.24 ± 0.96	0.62 ± 0.07
Averaged over diastole	-1.60 ± 1.56	-1.07 ± 1.05	0.60 ± 0.14
Averaged over the cardiac cycle	5.06 ± 2.07	3.43 ± 1.40	0.68 ± 0.07
<b>During cuff inflation</b>			
Systolic flow	24.16 ± 7.44	15.91 ± 5.02	0.66 ± 0.09
Diastolic retrograde flow	-13.99 ± 3.95	-8.31 ± 1.92	0.48 ± 0.12
Diastolic anterograde flow	6.49 ± 3.50	3.74 ± 2.06	0.58 ± 0.05
2 <sup>nd</sup> retrograde diastolic flow**	-4.79 ± 2.36	-3.05 ± 1.81	0.62 ± 0.24
Averaged over diastole	-2.98 ± 0.10	-1.83 ± 0.62	0.62 ± 0.15
Averaged over the cardiac cycle	15.91 ± 5.02	1.92 ± 1.31	0.68 ± 0.12
<b>During Hyperemia</b>			
Systolic flow	33.01 ± 7.20	23.25 ± 5.25	0.70 ± 0.07
Averaged over diastole	17.51 ± 6.04	10.87 ± 4.09	0.61 ± 0.08
Averaged over the cardiac cycle	22.95 ± 6.36	14.47 ± 6.05	0.67 ± 0.16

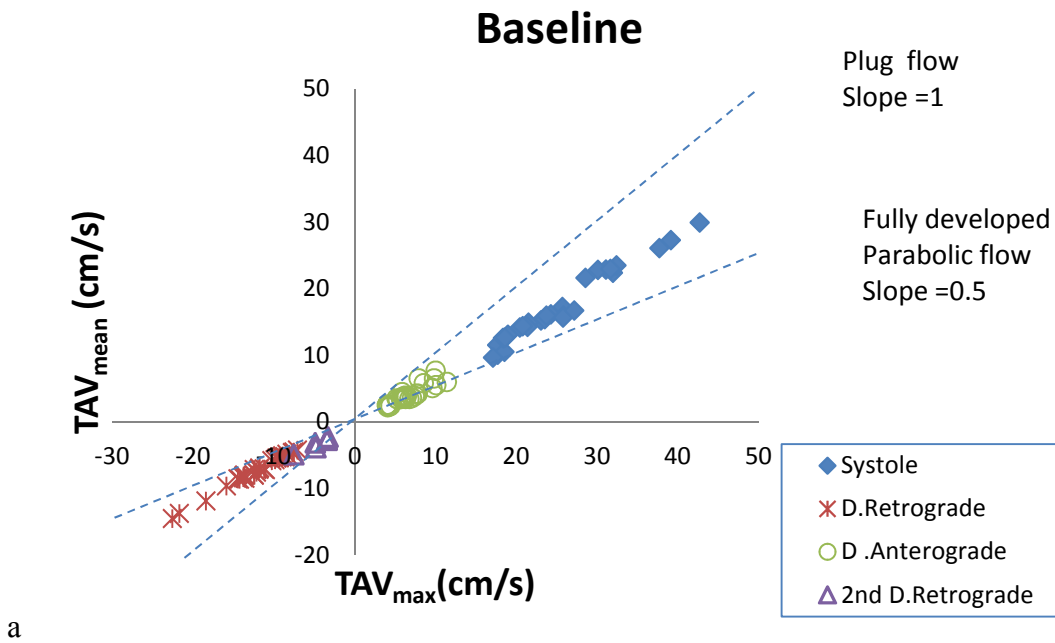
\*Only 3 volunteers had 2<sup>nd</sup> retrograde diastolic flow when the artery was at rest

\*\*Only 5 volunteers had a 2<sup>nd</sup> retrograde flow during distal occlusion



**Table 4-2. Duration of the different phases of the popliteal waveform in an unperturbed artery**

	Time [ms]
From R wave to start of systolic flow	202.13 ± 6.37
Duration of systolic flow	229.58 ± 8.79
From R wave to the start of diastolic flow	447.35 ± 17.58
Duration of diastolic retrograde flow	188.80 ± 7.46
Duration of diastolic anterograde flow	253.52 ± 15.53
Duration of diastole	699.16 ± 25.87
Duration of the entire cardiac cycle	928.75 ± 33.32



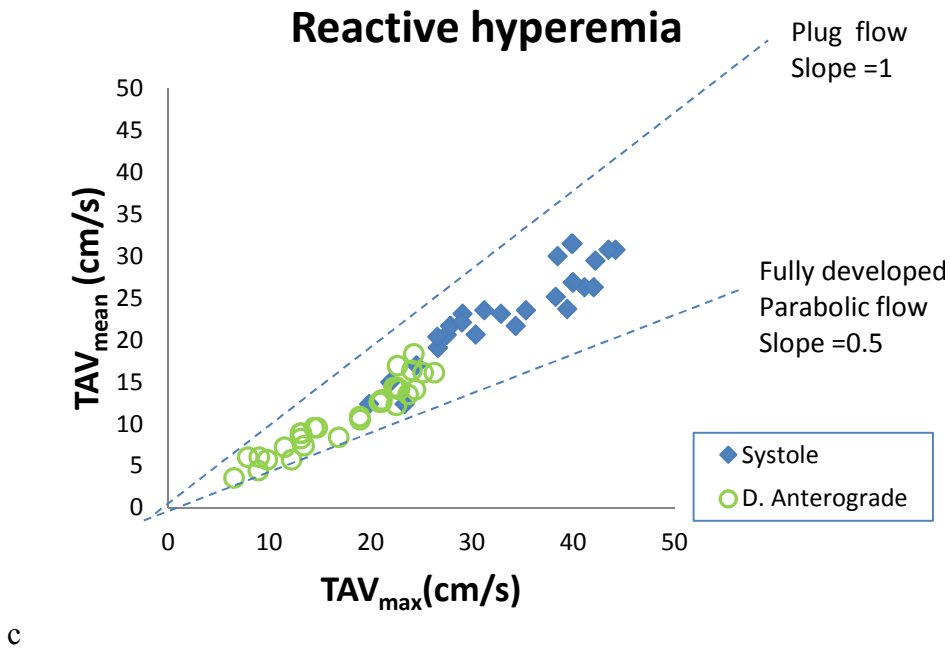
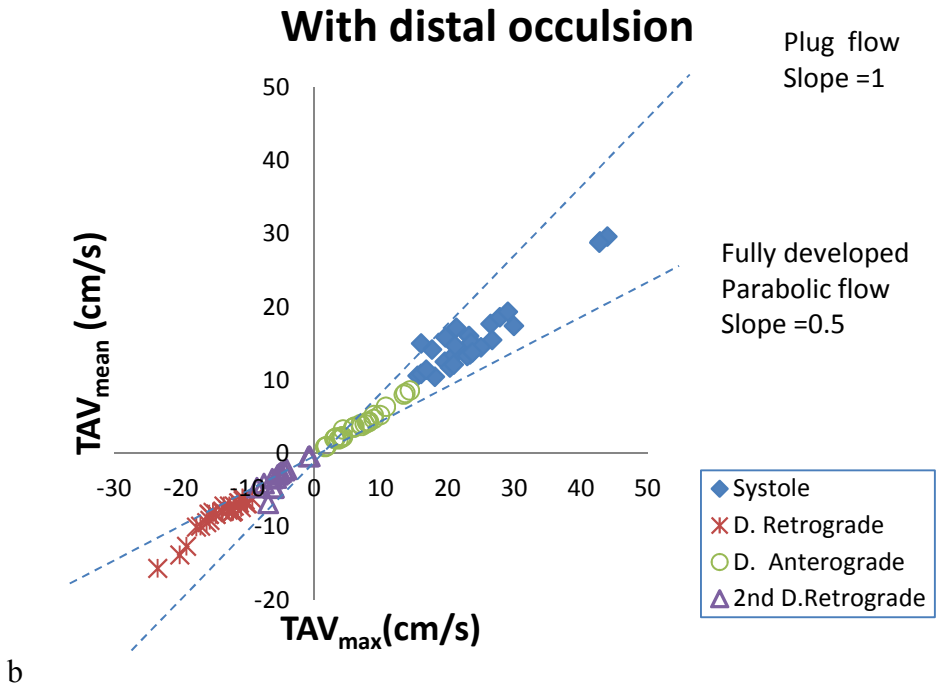


**Figure 4-4. Scatter plots of TAV<sub>mean</sub> against TAV<sub>max</sub> at baseline (a), during distal occlusion (b) and during reactive hyperemia (c). The dataset in each graph was divided into the systolic phase, the retrograde portion of diastole (D. Retrograde), the anterograde portion of diastole (D. Anterograde) and the second retrograde portion of diastole (2<sup>nd</sup> D. Retrograde). A line of unity was included for plug flow (slope =1) and another line was included for fully developed parabolic flow (slope=0.5)**

## 4.5 Discussion

This chapter explores whether some of the assumptions made while deriving the IntSI technique for measuring the luminal area hold true in vivo. Spectral Doppler analysis provided an opportunity to test the assumptions that: 1) the velocity profile in the popliteal artery is parabolic with the mean velocity being half of the maximal velocity, and 2) the maximal velocity ( $V_{\max}$ ) during data acquisition is less than the TOF threshold velocity. In addition, with spectral Doppler, it was possible to determine whether MR data obtained during diastole in an unperturbed artery can be used as the steady state MR signal intensity value.

### 4.5.1 The assumption of parabolic flow in the popliteal artery

From theoretical calculations, the highest velocity compatible with the entrance length of 17.11 cm in an artery 6 mm in diameter was 25.18 cm/s. The entrance length was based on the assumption that the velocity profile was sampled at a distal location just 2 mm above the termination of the popliteal artery, in order to get the longest possible entrance length and avoid turbulence at the bifurcation. Baseline and maximal post hyperemic measurements of the popliteal arterial diameter in this present study agreed with the theoretical value of 6mm. The  $TAV_{\max}$  during the diastolic phases of the waveform did not exceed the theoretical upper limit of 25.18 cm/s at baseline during distal occlusion or post reactive hyperemia. The velocity ratio was calculated at rest, during cuff inflation and during reactive hyperemia using the quotient of the time averaged mean velocity ( $TAV_{\text{mean}}$ ) and the time averaged maximal velocity ( $TAV_{\max}$ ). When parabolic flow is present, the TAV ratio should be 0.5. In an unperturbed artery, the velocity ratio was  $0.77 \pm 0.050$  at systole and  $0.60 \pm 0.14$  when averaged over diastole, the proposed data acquisition period. Similar results were observed during distal occlusion and during reactive hyperemia despite imaging away from the bifurcation of the popliteal artery.

A reason for the blunted parabolic profile may be that distance from the arterial origin to the imaging site was not up to the entrance length required for fully developed parabolic flow. Another reason could be that the popliteal artery has small muscular branches and the presence of turbulence at these locations leads to a blunted parabolic velocity profile. The higher velocity ratio during systole may be because of the inverse relationship between velocity and the entrance length required for parabolic flow (Mott, 2006; Tongpun et al., 2014). Systole is associated with

high velocities. At such high velocities, the distance from the origin of the popliteal artery to the site of imaging may be shorter than the required entrance length for parabolic flow, due to limitations in the length of the popliteal artery.

The  $TAV_{\text{mean}}/TAV_{\text{max}}$  ratio during the three different physiologic states differed significantly from the expected ratio of 0.5. The systolic velocity ratio of 0.77 and diastolic ratio of 0.60 in unperturbed popliteal arteries in this present study agree with the systolic and diastolic ratios of 0.76 and 0.57 respectively reported in the femoral artery (Osada & Radegran, 2005). However, they differ from another study that showed a systolic ratio of 0.57 and a diastolic ratio of 0.48 (Ade et al., 2012) in the femoral artery. In the second study by Ade et al (2012) only the first retrograde portion of diastole was considered without the antero-grade diastolic flow or the occasional second retrograde portion, which might explain why their study differed from both this present study and also that by Osada & Radegran (2005). The implication of a blunted velocity profile is that area measurements using the IntSI equation will be overestimated. Equation 4.4 is a step during the derivation of the IntSI equation. The value 2 in equation 4.4 is because with parabolic flow,  $V_{\text{max}}$  is twice  $V_{\text{mean}}$ .

$$A = \frac{2 \cdot \text{IntSI}}{\left[ \frac{2P_{\text{SS}} + P_{\text{max}} - P_{\text{SS}}}{a} \right]} \quad (4.4)$$

However, spectral Doppler analysis of the popliteal waveform showed that  $V_{\text{mean}}$  was  $0.6 V_{\text{max}}$  or  $V_{\text{max}}/1.67$ . When the value of 1.67 replaces 2 in equation 3.7d, the IntSI technique becomes equation 4.5, as shown in the supplementary section.

$$A = \frac{\text{IntSI} \cdot a}{[0.4P_{\text{SS}} + 0.6P_{\text{max}}]} \quad (4.5)$$

#### 4.5.2 The assumption that the maximal velocity in the popliteal artery does not exceed the TOF threshold velocity

With reactive hyperemia, there is a large amount of forward flow within the imaged slice during data acquisition. If the velocities are higher than the threshold velocity that occurs with the TOF effect, then there will no longer be an increase in the signal intensity with velocity. Therefore, the TOF profile will not be of the fully formed parabolic type, rather the profile will be blunted. This means that  $P_{\text{max}}$  will be less than it should be and areas calculated with the IntSI technique

will be overestimated. With the time averaged maximal velocities of  $15.35 \pm 6.71$  cm/s, averaged over diastole during hyperemic flow, a threshold velocity above the higher value in the range (22.06 cm/s) will prevent threshold based measurement errors when using the IntSI technique to measure the popliteal area. When optimizing the spoiled GRE sequence for area measurements with the IntSI technique, the slice thickness and repetition time (TR) can be modified accordingly since the threshold velocity is the quotient of these two variables.

### 4.5.3 The pixel intensity when there is no flow during imaging

Assuming that in an unperturbed artery, the imaging slice is refilled with fresh blood at each cardiac cycle and imaging occurs over several cardiac cycles, there will be high signals at the first RF pulse of each new cardiac cycle. If this high signal is used to fill the center of k-space, the image contrast will be high and the central pixel's intensity will be higher than  $P_{SS}$ . However, if a Cartesian trajectory is used to fill k-space with the periphery filled first, then the central pixel's intensity will be  $P_{SS}$  if there is no flow during data acquisition. In this present study, spectral Doppler analysis showed that in an unperturbed artery the magnitude of  $TAV_{mean}$  during the retrograde portion of diastole ( $-6.79 \pm 3.73$  cm/s) was much greater than the magnitude of  $TAV_{mean}$  during the anterograde part of diastole ( $3.74 \pm 1.11$  cm/s) although  $TAV_{mean}$  averaged over the whole of diastole was  $-1.07 \pm 1.05$  cm/s. This value was inclusive of the portion in which there was no flow. The greater retrograde flow compared with anterograde flow suggests that if a venous suppression band is used during MR imaging, the suppressed retrograde flow into the slice during diastole will be greater than the fresh high signal anterograde flow entering the slice. This means that the central pixel's intensity during the diastolic window in an unperturbed artery may be lower than  $P_{SS}$  and this could lead to overestimation of the luminal area. The central pixel intensity when the artery is unperturbed ( $P_B$ ) can be obtained from the baseline image of an FMD study and the equation for area measurement with the IntSI technique can then be rewritten for in vivo arterial imaging as equation 4.6 when  $P_B$  is used as a surrogate for  $P_{SS}$ .

$$A = \frac{\text{intSI. a}}{0.6 P_B + 0.4 P_{\max}} \quad (4.6)$$

Subsequent MRI experiments in vivo may explore whether a correction factor may be added to the measured  $P_B$  in order to adjust for area measurement errors due to the suppressed retrograde signals.

#### 4.5.4 Conclusion

This chapter demonstrates that the popliteal artery has a blunted parabolic flow; therefore, the equation for area calculations with the IntSI technique was modified accordingly. The chapter also shows that a threshold velocity as low as 23.55 cm/s is suitable for imaging the popliteal artery and it suggests that the central pixel intensity obtained when the artery is at rest ( $P_B$ ) can be used in place of the steady state intensity ( $P_{SS}$ ). However, this value may be lower than expected due to a greater amount of retrograde flow of blood with suppressed signals entering the slice during image acquisition. A solution to this is to avoid using a venous saturation band during imaging. But the saturation band is necessary because the vein is very close to the artery and with the moderately sized pixels used for imaging, voxels at the luminal edge may contain partial volumes of venous and arterial signals. Therefore, the presence of venous signals will elevate the integrated signal intensity and the area will be overestimated.

## 4.6 Supplementary

The value 2 in the IntSI equation is based on  $V_{\text{mean}}$  being 0.5 of  $V_{\text{max}}$  or  $V_{\text{max}}/2$ . However spectral Doppler analysis shows that  $V_{\text{mean}}$  is 0.6 of  $V_{\text{max}}$  or  $V_{\text{max}}/1.67$ , instead of  $V_{\text{max}}/2$  during diastole.

Equation S4-1 is one of the steps for deriving the IntSI equation in Chapter 3.

$$A = \frac{2 \cdot \text{IntSI}}{\left[ \frac{2P_{\text{SS}} + P_{\text{max}} - P_{\text{SS}}}{a} \right]} \quad (\text{S4-1})$$

With popliteal imaging, 1.67 can replace 2 in equation 3.7d,

$$A = \frac{1.67 \cdot \text{IntSI}}{\left[ \frac{1.67 P_{\text{SS}} + P_{\text{max}} - P_{\text{SS}}}{a} \right]} \quad (\text{S4-2})$$

or

$$A = \frac{1.67 \cdot \text{IntSI} \cdot a}{[1.67P_{\text{SS}} + P_{\text{max}} - P_{\text{SS}}]} \quad (\text{S4-3})$$

Dividing the numerator and denominator by 1.67

$$A = \frac{\text{IntSI} \cdot a}{[0.4P_{\text{SS}} + 0.6P_{\text{max}}]} \quad (\text{S4-4})$$

---

**Chapter 5    Measuring the area of the popliteal artery with the IntSI technique**

---



## 5.1 Abstract

**Objective:** To test the reliability of the IntSI technique for popliteal area measurements.

**Background:** FMD requires rapid reliable serial measurements of the artery's cross-sectional area in order to detect the maximal dilatation. In view of the trade-off between spatial and temporal resolution, sequence optimization is required for area measurements with the IntSI technique to ensure that the pixel-to-luminal area ratio is as small as possible while the temporal sampling frequency is as high as possible. A vessel segmentation technique is also required to remove adjacent extra-luminal signals. It is unclear whether adjustments to the IntSI technique are needed for in vivo applications of this area measurement technique because the IntSI equation requires the maximal pixel intensity when there is no flow ( $P_{SS}$ ) but this value is difficult to obtain in vivo. Imaging an unperturbed artery during a diastolic data acquisition period provides a pixel intensity value ( $P_B$ ) that is close to ( $P_{SS}$ ). Testing the reliability of the IntSI technique against high resolution imaging provides a means of assessing if further adjustments are needed to account for  $P_B$  being used instead of  $P_{SS}$ .

**Methods:** Mathematical modeling was used to optimize the scan parameters. A sliding paraboloid technique was used to identify luminal pixels and the luminal area was calculated with the IntSI technique using the IntSI equation at  $V_{mean}$  being 0.6 of  $V_{max}$ . The results obtained were compared with high resolution imaging with pixel counting as a gold standard. Numerical optimization was used to determine a correction factor to account for  $P_B$  being lower than  $P_{SS}$ , due to suppression by a venous saturation band of the net retrograde flow that enters the slice during data acquisition. The results were also compared with high resolution imaging.

**Results:** IntSI technique required a shorter scan time (6-9s,) than the high resolution imaging (180-240s) and there was agreement between the IntSI technique and high resolution imaging. However measurements with the IntSI technique were larger than those of high resolution/ pixel counting (mean difference  $\pm$  RC:  $3.05 \pm 2.55 \text{ mm}^2$ ). Using a correction factor, the reliability of the IntSI technique improved. (ICC: 0.98 (0.97-0.99), mean difference  $\pm$  RC:  $0.14 \pm 2.32$ ).

**Conclusion:** This study shows that the IntSI technique with a correction factor can be applied in vivo to obtain rapid serial area measurements.

## 5.2 Introduction

The IntSI technique for measuring area assumes that all the pixels within the region of interest contain only luminal signals. If some pixels within the ROI contain signals from other structures, then the luminal area will be overestimated. Luckily, requirements for the IntSI technique such as the use of  $90^\circ$  RF pulses and a short TR (needed for a high threshold velocity), also reduce the background signal. To further ensure that only luminal signals are included in the area measurements, a vessel segmentation technique is required. It is also important to optimize the IntSI technique for application during FMD studies because FMD requires rapid reliable serial measurements of the artery's cross-sectional area in order to detect the maximal dilatation. Rapid measurements need high temporal resolution while reliable measurements require a small pixel size due to the assumption that pixel-to-luminal area ratio is small. However, a trade-off exists between spatial and temporal resolution. Sequence optimization is essential to ensure that the pixel-to-luminal area ratio is as small as possible while the temporal sampling frequency is as high as possible. The baseline pixel intensity ( $P_B$ ) may be used as the pixel intensity when there is no flow during image acquisition ( $P_{SS}$ ) if measurements obtained by substituting  $P_{SS}$  with  $P_B$  in the IntSI equation are reliable.

### 5.2.1 Vascular contrast and vessel segmentation

Unlike the phantom study, the lumen of the popliteal artery has adjacent structures that may contribute to the measured signal from the ROI if their signals are not suppressed, with resultant over-estimation of the luminal area. Therefore apart from the venous saturation pulse for removing signals from the adjacent vein, a fat saturation pulse is also applied to remove the perivascular fat signals (Chen et al., 1999). Fat saturation may provide a rim of dark pixels around the lumen if the pixel size is small enough to prevent signal averaging of the fat and adjacent tissues and the rim of dark pixels may provide contrast for definition of the luminal boundary. A magnetization transfer contrast (MTC) pulse could also be included to improve contrast between the vessel and the background (Graham & Henkelman, 1997). However, these preparatory pulses add to the scan time.

To prevent adjacent extraluminal signals from contributing to the integrated signal intensity, an appropriate post-processing background subtraction technique must be employed to segment the

lumen. There are different post-processing vessel segmentation techniques (Lesage et al., 2009); some depend on the appearance of the vessel and surrounding structures. For example, the region of interest (ROI) background correction method in imageJ (Collins, 2012) can be used to segment the lumen based on the knowledge that the intensity of a lumen with flowing blood is usually higher than that of stationary adjacent muscle. The method involves selecting an ROI in the background e.g. adjacent muscle and subtracting the mean intensity of this ROI from the slice (Collins, 2012). However, this option might not be suitable because of the possibility that some luminal pixels might also be subtracted if their intensity is close to that of muscle. The geometrical approach for vessel segmentation uses surface models, centerlines and cross-sectional models to segment the vessel (Lesage et al., 2009). For example, the sliding paraboloid background correction technique in imageJ (Castle & Keller, 2007) selects pixels based on whether they fit in a paraboloidal surface. With this technique, all pixels containing luminal pixels can be selected and then a mask created and applied to the original image. This will preserve the original signal intensities of luminal pixels while removing background signals.

### 5.2.2 The pixel intensity when there is no flow ( $P_{SS}$ ) versus $P_B$

The IntSI equation requires the central pixel's intensity when there is no flow ( $P_{SS}$ ), but this value is difficult to obtain in vivo because during the diastolic data acquisition period, blood moves in and out of the imaged slice. Imaging an unperturbed artery during a diastolic data acquisition period may provide a pixel intensity ( $P_B$ ) that is close to ( $P_{SS}$ ) but if  $P_B$  differs from  $P_{SS}$  then the calculated area will be inaccurate.

### 5.2.3 Sequence optimization

To obtain reliable serial area measurements in an artery undergoing rapid changes in size as occurs with FMD, the pixel-to-luminal area and temporal sampling frequency are important. However, there are challenges with obtaining the ideal pixel-to-luminal area and temporal sampling frequency because of the trade-off between spatial resolution and temporal resolution as discussed below. Sequence optimization is therefore required. Sequence optimization also enables a slice thickness and TR combination for a threshold velocity that can accommodate all velocities that occur in the popliteal artery. A short TR increases the threshold velocity and it is a useful technique to minimize background signal intensity. Other techniques to minimize the background signal intensity are also important considerations during sequence optimization.

### 5.2.3.1 The trade-off between spatial and temporal resolution

The IntSI technique assumes that the averaged velocity within the most central pixel ( $V_p$ ) can be used as a substitute for  $V_{max}$  provided the pixel-to-luminal area ratio is small. As observed in chapter 3, as the pixel-to-luminal area ratio increases the measurement error associated with the IntSI technique increases. The use of high spatial resolution for imaging provides a low pixel-to-luminal area ratio but there is a limit to increasing the spatial resolution because with high spatial resolution, the time required to fill all the lines in k-space increases and the scan time increases. However to allow high sampling frequency during rapid changes in the vessel diameter that occur when performing an FMD study, a short scan time is required. The maximal dilatation during an FMD study usually occurs within 45-60 seconds, but it may sometimes be as early as 15 seconds or as late as 180 seconds. Apart from the constraints that spatial resolution places on the scan time, cardiac gating also adds to the scan time. However, a segmented k-space technique can be used to improve temporal resolution because the technique involves filling out several lines in k-space per heart beat thereby shortening the scan time (Chen et al., 1999).

### 5.2.3.2 Ensuring an adequate threshold velocity

Intensity increases with velocity up to a threshold, beyond which no further increase occurs and the threshold velocity is the quotient of the slice thickness and TR. These two variables can be adjusted to ensure that the threshold velocity is adequate for the maximal possible velocity that may occur during imaging. Decreasing the TR increases the threshold velocity and reduces the scan time but there is a limit to which the TR can be shortened because reducing the TR decreases the amount of signal detected and vascular contrast. The slice thickness, on the other hand, can be increased as much as possible; however, efforts must be made to ensure that the imaging plane is perpendicular to the artery because the imaged vessel segment is assumed to be a cylinder whose base is the luminal cross-sectional area.

Mathematical modeling of the sequence parameters provides an opportunity to optimize the IntSI based area measurement technique for the popliteal artery, ensuring that the best possible scan time, pixel size and threshold velocity are used for imaging.

## 5.2.4 Hypothesis

There is agreement between popliteal artery measurements' obtained using an MRI integrated signal intensity approach on moderate resolution images and that obtained by pixel counting of high resolution images.

The aims of this chapter are:

- 1) to optimize the sequence parameters for reliable and rapid serial area measurements with the IntSI technique;
- 2) to develop a suitable technique for vessel segmentation; and
- 3) to test for agreement between popliteal luminal areas measured using the IntSI technique (with  $P_B$  representing  $P_{SS}$ ) and those obtained from pixel counting of high resolution images in order to validate that the in vivo modified IntSI technique is a suitable method for measuring luminal area during FMD.

## 5.3 Materials and Methods

### 5.3.1 Optimizing the MRI sequence

Mathematical modeling was used to optimize the MRI sequence parameters for area measurements with the IntSI technique. Different signal intensity values ( $M'_{ss}$ ) were simulated using the GRE signal equation (McRobbie et al. 2003)

$$M'_{ss} = \frac{k\rho(1 - e^{-TR/T_1}) \text{Sin}\theta \cdot e^{-TE/T_2^*}}{1 - e^{-TR/T_1} \cdot \text{Cos}\theta} \quad (5.1)$$

where  $k$  is a proportionality constant specific to the scanner (Hornak, 2006b),  $T_1$ , and  $T_2^*$  of arterial blood using a 3T MRI scanner are 1664 ms and 47.3 ms respectively (Lu et al., 2004; Lu & van Zijl, 2005) and  $\rho$  for arterial blood is 0.8533 g of water/ml (Herscovitch & Raichle, 1985).

Short TR values were used improve vascular contrast by saturating stationary tissue (Kim & Parker, 2012). The TR values ranged from 12-52 ms. A short TE of 3.7 ms was employed in order to minimize loss of signal due to loss of phase coherence between spins in the voxel (Kim & Parker, 2012). The flip angle was kept at  $90^\circ$ , as this is an assumption on which the IntSI technique is based. At a flip angle of  $90^\circ$ , steady state is achieved after the first RF pulse (Kim & Parker, 2012). Another benefit of a high flip angle is that the stationary tissues are saturated and vascular contrast improves (Kim & Parker, 2012). A large slice thickness of 10 mm was used to help with optimization of threshold velocity against TR.

Different SNR values were calculated using the relationship between SNR, temporal resolution, spatial resolution as depicted in equation 4.2 (McRobbie, et al. 2003)

$$\text{SNR} = M'_{ss} \left( \frac{\text{FOV}_{PE}}{N_{PE}} \cdot \frac{\text{FOV}_{FE}}{N_{FE}} \cdot \Delta z \right) \sqrt{\frac{N_{FE} \cdot N_{PE} \cdot \text{NEX}}{\text{BW}}} \quad (5.2)$$

where  $\text{FOV}_{PE}$  and  $\text{FOV}_{FE}$  are the field of view in the phase and frequency direction respectively,  $N_{PE}$  and  $N_{FE}$  are the number of encoding steps in the phase and frequency direction,  $\Delta z$  is the slice thickness, NEX is the number of excitations, BW is the bandwidth and  $M'_{ss}$  is the signal value obtained from the GRE signal equation.

For the modeling, the values for FOV, bandwidth and slice thickness were kept constant. Parameters used for modeling were; slice thickness = 10 mm, NEX = 1, Bandwidth = 815Hz, K=24, FOV = 280 mm × 280 mm and matrix = 512 × 256. The matrix size was varied by adjusting the  $N_{PE}$  and  $N_{FE}$  using factors 1, 1.6, 2, 2.6 and 4. This produced in-plane pixel areas of 0.3 mm<sup>2</sup>, 0.77 mm<sup>2</sup>, 1.2 mm<sup>2</sup>, 2.13 mm<sup>2</sup> and 4.88 mm<sup>2</sup> respectively. These values were chosen to access the effect of increasing pixel area on the scan time. As  $N_{PE}$  decreased, the scan time also decreased while the SNR and pixel area increased. The percent phase field of view was 50%.

In order to make the threshold velocity as large as possible to accommodate the high velocities associated with hyperemia, a large slice thickness of 10 mm was used for imaging. An added benefit of a large slice thickness is that it improves SNR. Although a disadvantage of using a thick imaging slice is that overestimation of the diameter might occur in tortuous vessels or any other situation when the imaging plane is not exactly perpendicular to the vessel.

With cardiac gating, imaging occurs over several cardiac cycles. The scan time was calculated as follows: The number of lines in k-space that are filled in one cardiac cycle (termed the number of lines per segment (nLPS)), was first calculated as the quotient of the data acquisition window (DAW) and the TR.

$$nLPS = DAW / TR \quad (5.3)$$

Then the number of cardiac cycles over which imaging occurs was calculated as the quotient of the number of phase encoding steps ( $N_{PE}$ ) and the number of lines per segment (nLPS) since  $N_{PE}$  is the maximum number of lines in k-space filled during imaging. The number of cardiac cycles required for imaging was shortened by assuming that only a percentage of the  $N_{PE}$  will be employed for data acquisition. The number of cardiac cycles required for data acquisition using 50% of the  $N_{PE}$  was calculated.

$$\text{number of cardiac cycles} = (N_{PE} / nLPS) \times 50\% \quad (5.4)$$

The scan time was calculated from the number of cardiac cycles and the R-R interval.

$$\text{Scan time (s)} = \text{number of cardiac cycles} \times (R - R \text{ interval}) \quad (5.5)$$

At a given heart rate of 60 beats per minute, and an R-R interval of 1000 ms, if a trigger delay of 450ms is applied in order to avoid imaging during systole, then the diastolic data acquisition

window (DAW) will be 550 ms. At a TR of 12ms, the number of lines per segment (nLPS) will be 45. Since the number of phase encoding steps or the total number of lines in k-space is 256 then 6 cardiac cycles will be required for imaging (i.e. 256/45) and the scan time will be 6 seconds.

At a TR of 52 ms, 10 lines in k-space can be filled per cardiac cycle, 26 cardiac cycles will be required for imaging and the scan time will be 26 seconds.

A graph of SNR versus scan time was plotted using the various scenarios.

### 5.3.2 Reliability of area measurements obtained with the IntSI technique

Ten healthy volunteers were included in the study out of which five were male and five were female. Their age range was  $27 \pm 8.36$  years. Ethical approval was obtained from the institution and a written informed consent was obtained from each volunteer. A 3T MRI Siemens scanner and a knee coil were used to image the right knee. The patient was positioned supine with the feet advanced first into the scanner. In order to obtain images of an unperturbed popliteal artery, data acquisition commenced after 10 minutes of rest (Peretz et al., 2007). Images were obtained at rest so that the central pixel intensity when the vessel is unperturbed ( $P_B$ ), can represent the central pixel intensity at steady state ( $P_{SS}$ ). I had noted previously in section 5.2.2, that the pixel intensity of static blood at steady state ( $P_{SS}$ ) cannot be obtained in vivo because imaging occurs over several cardiac cycles and considered using the pixel intensity of an unperturbed artery ( $P_B$ ) as the steady state intensity because in Chapter 4 it was observed that during diastole, there is minimal net retrograde flow when the popliteal artery is at rest.

Spoiled GRE sequences with a venous saturation pulses were used for imaging. Venous saturation pulses were applied to remove adjacent signals from the popliteal vein. However, it is possible that the presence of a venous saturation band may lead to suppression of the minimal net retrograde flow that occurs in an unperturbed popliteal artery during the diastolic data acquisition period. The first image was obtained with a high-resolution spoiled GRE sequence in order to provide a measure of the luminal area using a pixel counting approach. The sequence parameters were flip angle  $90^\circ$ , matrix =  $1024 \times 992$ , FOV =  $134 \text{ mm} \times 129 \text{ mm}$ , pixel area =  $0.02 \text{ mm}^2$ , slice thickness = 3 mm, TE = 14 ms TR = 1180 ms, NEX = 4, percent phase field of view: 43.75%, acquisition time = **180-240 s** (depending on the heart rate). The second image was



obtained with moderately sized pixels, in order to measure the luminal area via the IntSI technique. In this case, the sequence parameters were, flip angle =  $90^\circ$ , matrix =  $320 \times 140$ , FOV =  $350 \text{ mm} \times 153 \text{ mm}$ , pixel area =  $1.2 \text{ mm}^2$ , slice thickness = 10 mm, NEX = 1, TE = 3.5 ms, TR = 24 ms, acquisition time = **6-9 s** (depending on the heart rate), nLPS = 17. Imaging was ECG gated and a trigger time of 435ms was applied. Five out of the ten volunteers had repeat studies using both methods. Therefore, fifteen popliteal area measurements were obtained per MR imaging sequence.

### 5.3.2.1 Post processing

The MR images were post processed with imageJ (ImageJ, 2003). The sliding paraboloid technique (Castle & Keller, 2007) was used for vessel segmentation. The technique assumes that the MR image is transformed into a 3D surface with the z-axis represented by the pixel intensity, such that each structure within the image appears as an elevation of the surface.

The algorithm attempts to fit a paraboloid onto each elevation of the 3D surface. At each point of elevation, a paraboloid was defined from 4 parabolae along the x, y and the two 45-degree directions. When attempting to segment the lumen using the sliding paraboloid technique the luminal pixel intensity decreases with the distance from the center of the lumen partly due to the effect of parabolic flow and also because the boundary pixels have lower signals as a result of partial volume averaging with the juxtaluminal tissues which produce little or no signal. Boundary pixels that experience partial volume averaging fit in the paraboloid while extraluminal pixels do not. When the paraboloid intersected zero in the middle of a pixel, that pixel was included as a luminal pixel. Each paraboloid had an apical radius of curvature which defined the width of the paraboloid. The radius of curvature at the apex will vary during the baseline and hyperemic phases of FMD. As the velocities increase during hyperemia, the intensity values will increase making the fitted paraboloid steeper and the radius of curvature smaller as shown in Figure 5-1. The widest paraboloid that was acceptable for fitting into the 3D elevations of the images was defined based on that which could fit into the 3D elevation of the lumen of an unperturbed artery as shown in Figure 5-2. The 3D elevations of juxtaluminal tissues will have wider radiuses of curvature so they will be subtracted from the image.

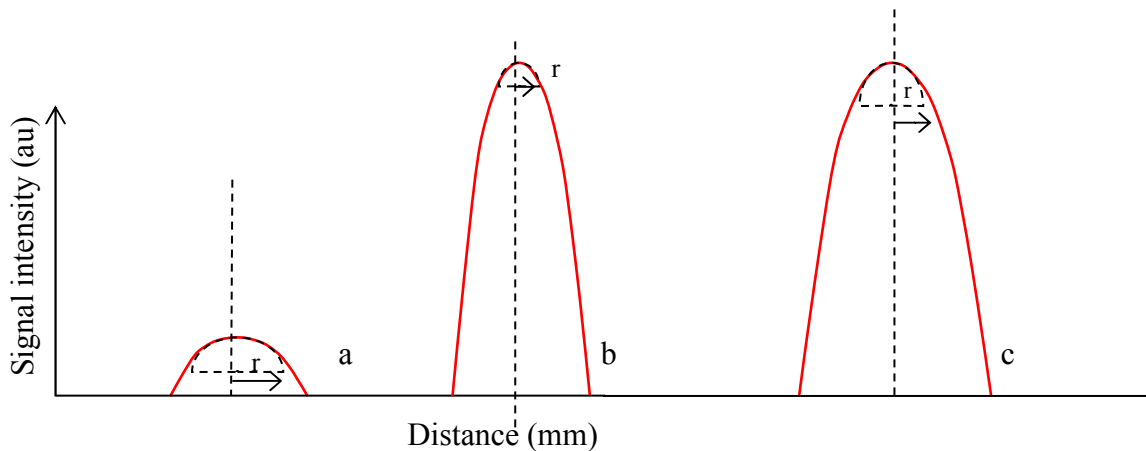


**Figure 5-1. As the luminal pixel intensities increase, the fitted paraboloid becomes steeper and the radius of curvature ( $r$ ) becomes smaller.** Paraboloid a represents the baseline, when the pixel intensities are relatively low and the radius of curvature is relatively wide. Paraboloid b represents hyperemia without vasodilatation. In this case, the pixel intensities are higher resulting in a smaller radius of curvature. Paraboloid c represents hyperemia and vasodilatation. In this case, because the pixel intensities are still high, the radius of curvature will still be smaller than that of the baseline image.

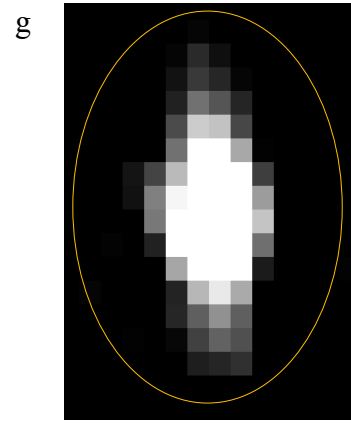
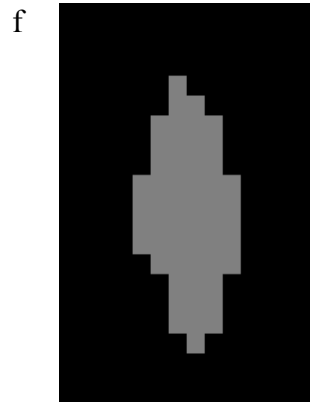
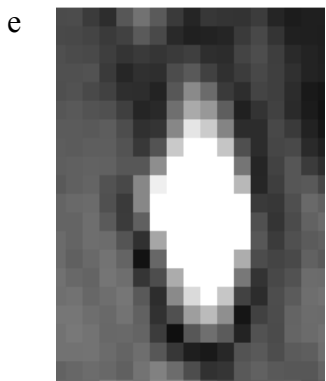
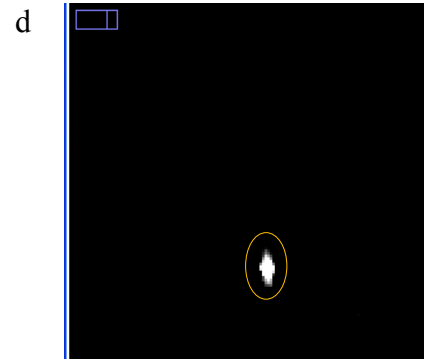
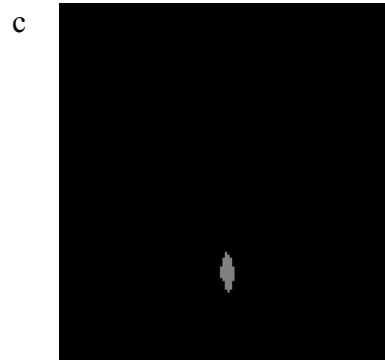
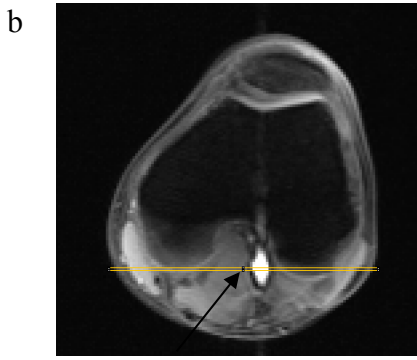
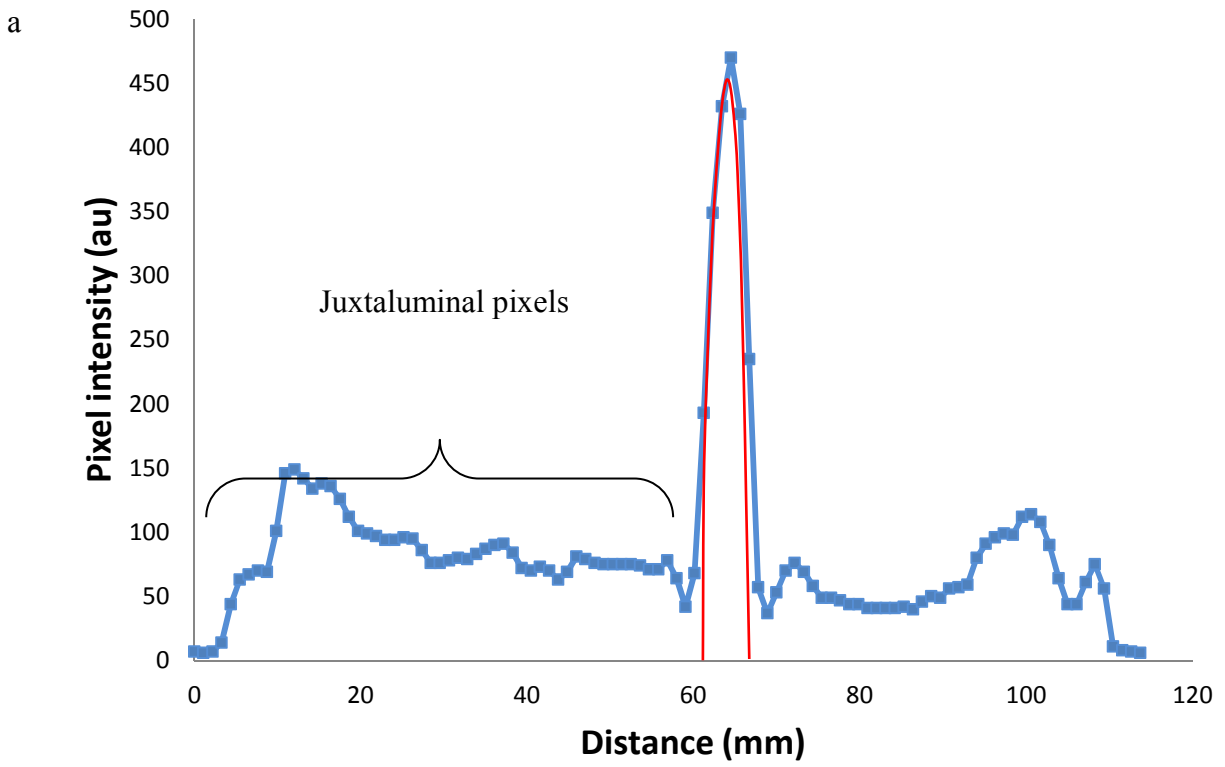
The disable smoothing option in the sliding paraboloid dialog box was selected so that pixels at the edge of the lumen will not be filtered out of the image. The apical radius of curvature for the paraboloid ranged from 0.05 to 0.10 of the pixel length. After applying the sliding paraboloid technique as described above, juxtaluminal pixels had intensities of 0 au while the luminal pixels had values that were assigned based on the fitted paraboloid. To restore the intraluminal pixels to their native values, a mask was first created using a built-in macro function called Change value in ImageJ (ImageJ, 2003). The macro converted the intensities of luminal pixels in figure 5-2b to 1 au, therefore the image produced was binary with luminal pixel assigned 1 au, while the surrounding pixels had a value of 0 au. The calculator plus plug-in (Rasband & Landini, 2004) was used to multiply the mask with the unprocessed image which had native pixel values. A new image was produced in which the luminal pixels had their native intensity values while surrounding pixels had intensity values of zero. To measure the integrated signal intensity of the lumen, a region of interest (ROI) was placed over the lumen. As long as the ROI enclosed the lumen, its size was not of importance since the surrounding pixels had signal intensity values of 0 au, The integrated signal intensity (IntSI) and the maximal pixel intensity ( $P_{max}$ ) of the luminal

ROI were obtained in each image using the multi-measure plugin in imageJ (Rasband et al., 2006).

In view of the blunted parabolic flow profile of the popliteal artery, a modified IntSI equation for popliteal imaging (equation 5.5) was used to calculate the luminal area. As mentioned in section 5.3.2, for an unperturbed artery,  $P_{\max}$  was assumed to be the central pixel's intensity at rest ( $P_B$ ). This is because the central pixel is expected to be the brightest pixel, even if there is no flow in the lumen since the pixel contains only luminal signals unlike more peripherally located pixels that may experience partial volume averaging with the surroundings.

$$A = \frac{\text{intSI. a}}{0.4 P_B + 0.6 P_{\max}} \quad (5.6)$$

In situations where there is little or no flow during imaging, a paraboloid can still be fit on the 3D surface of the lumen for vessel segmentation because the edge pixels that experience partial volume averaging will have lower signal intensities than the more centrally located pixels.



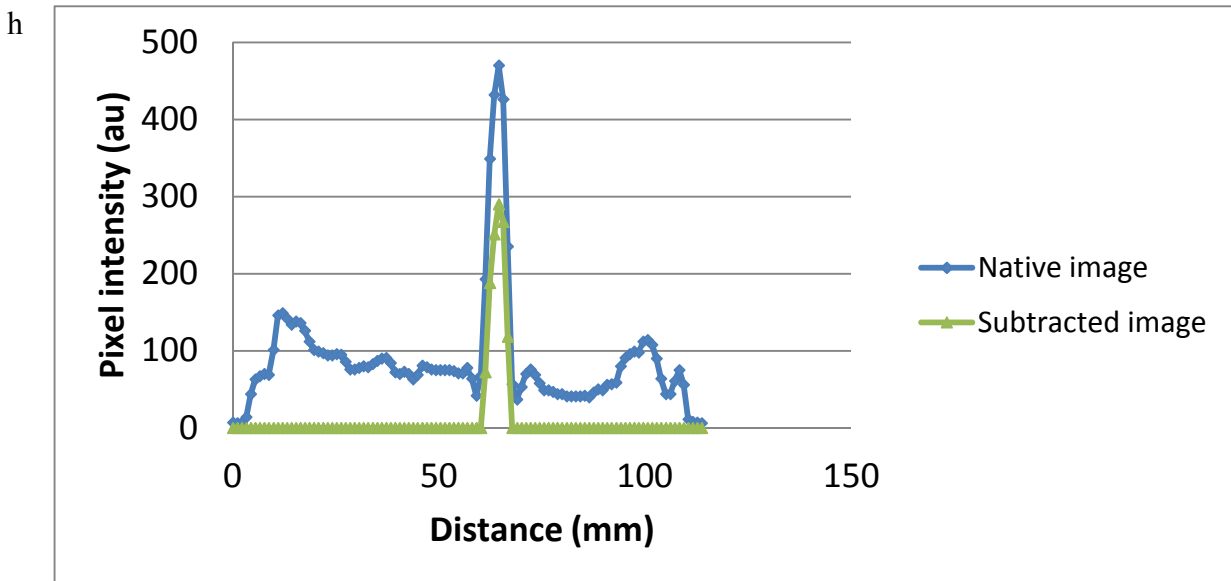


**Figure 5-2. Application of the sliding paraboloid background subtraction technique in vivo.** (a) shows a red colored parabola fitted into a plot profile of the lumen and juxtaluminal tissues. Luminal pixel intensities fit within the parabola while juxtaluminal pixels lie outside the parabola. (b) shows the span of the plot profile on an image of the knee. The popliteal artery is arrowed. (c) shows the mask that was obtained after applying the sliding paraboloid technique and the change value algorithm. (d) shows the final image produced as a product of the native and the masked image. (e), (f) and (g) are zoomed out images of (b), (c) and (d) respectively. An ovoid ROI is showed enclosing the lumen in (d) and (f). The size of the ROI was not of importance since the surrounding pixels had a signal intensity of zero. (h) shows the plot profile before and after the background is subtracted.

The luminal area of the high resolution images was measured by thresholding and pixel counting. The area measurements obtained with the IntSI equation (equation 5.5) were compared with those from the high resolution pixel counting method.

### 5.3.3 The correction factor

When  $P_B$  is used as a substitute for  $P_{SS}$ , there is an assumption that there is no flow during the diastolic data acquisition period. However, there is some retrograde and anterograde flow during diastole. Spectral Doppler analysis shows that the  $TAV_{max}$  during the retrograde phase is 12.1 cm/s (0.12 mm/ms). In the presence of a distal venous suppression band, the retrograde flow will have no signals. When the TR is 24 ms, the average distance that the retrograde flow will move

within the central voxel will be  $[0.12 \times 24 = 2.9 \text{ mm}]$  and a signal void column will lie within the voxel. Subsequent anterograde flow will lead to a reduction in the signal void column.

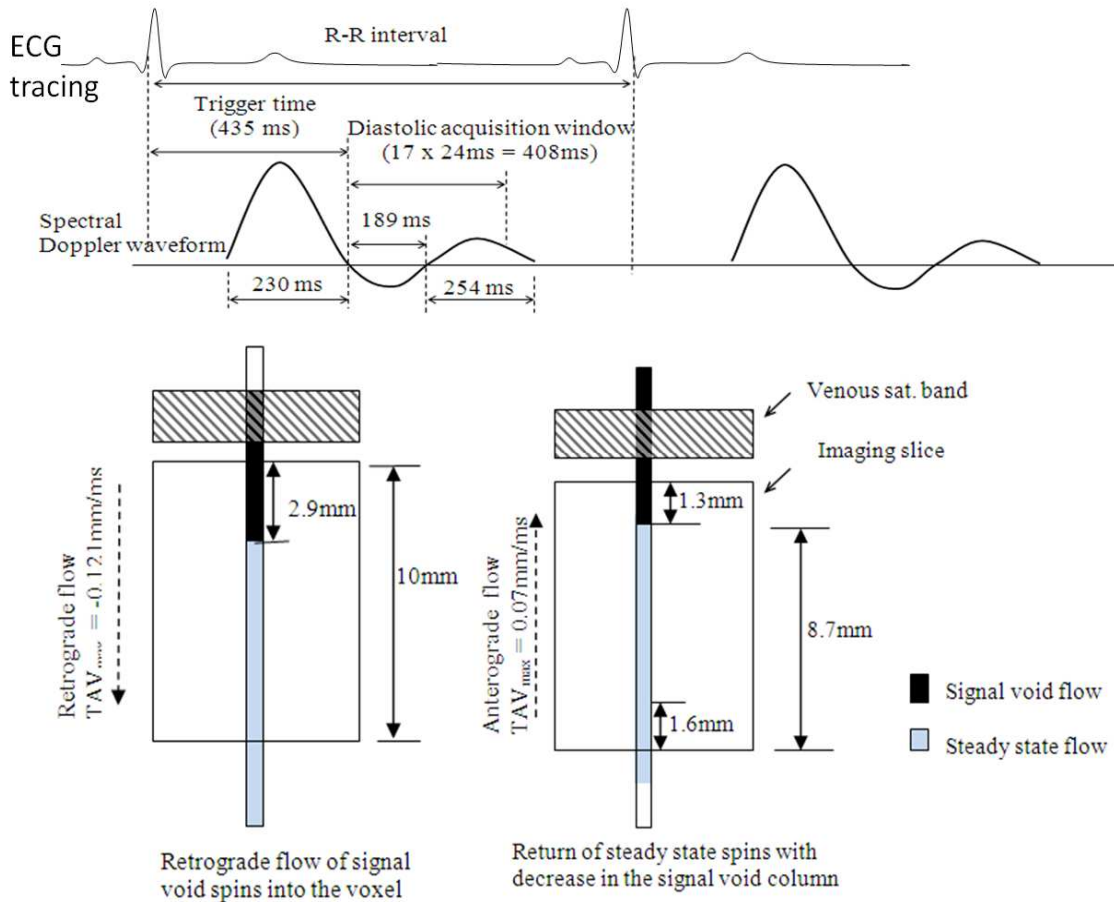
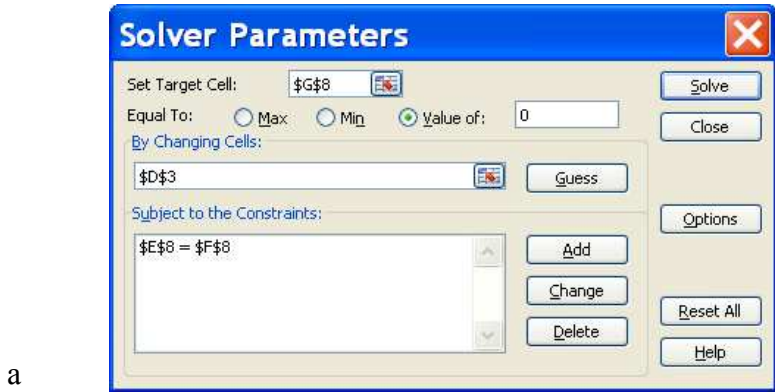


**Figure 5-3. The effects of retrograde and anterograde flow on the partial volume of signal void and saturated spins within the central voxel are illustrated. Retrograde flow leads to signal void spins entering into the voxel while anterograde flow restores saturated spins into the voxel and expels some of the signal void spins from the slice.**

From spectral Doppler analysis, the TAV<sub>max</sub> during the anterograde diastolic flow was 6.7 cm/s (0.07 mm/ms). At a TR of 24 ms, the anterograde flow will return steady state spins that were previously moved out of the voxel slice back in and this forward flow will also push some of the signal void column out of the slice, thereby reducing the signal void column by a distance of  $[0.07 \times 24 = 1.6 \text{ mm}]$ . Therefore the residual signal void column will be  $(2.9 - 1.6 = 1.3 \text{ mm})$  and only a length of  $(10 - 1.3 = 8.7 \text{ mm})$  within the slice will contain signals at the steady state. If

$P_{SS}$  is obtained from steady state spins over a length of 10 mm (which is the slice thickness) and  $P_B$  is obtained from steady state spins at a length of 8.7 mm, then the ratio of  $P_B$  to  $P_{SS}$  can be determined as  $10/8.7 = 1.15$ . Therefore if  $P_B$  is known,  $P_{SS}$  can be calculated as  $1.15P_B$ , as shown in Figure 5-3.



a

	A	B	C	D	E	F	G
1	IntSI*a	$P_{max} * 0.6$	$P_B * 0.4$	Variable cell	Area (IntSI)	Area (High res.)	
2							
3	15381.6	213	160	1.25	37.23	30.41	
4	21626.4	442.8	273.2		27.57	30.41	
5	8218.8	173.4	116.9		25.71	24.7	
6	13596	227.4	131.6		34.68	35.77	
7	14221.2	247.8	172.24		30.70	34.6	Target cell
8				Mean	31.18	31.18	0.00
9							

b

**Figure 5-4. Using the solver function in excel to numerically optimize the correction factor.** (a) shows a dialog box that requires three sets of information: the target cell, the variable cell and the constraint. (b) shows an excel spreadsheet that illustrates how the solver is used to calculate the correction factor. The target cell is G8, the variable cell is D3 and the constraint placed on the solver is that E8 equals F8.

To test if the correction factor of 1.15 was reasonable, another approach was also used to estimate the correction factor. What-if analysis was performed with the excel 2007 solver add-in tool (Dodge & Stinson, 2007). The solver has a dialog box that requires three sets of information: the target cell, the variable cell and the constraint as shown in Figure 5-4a. Application of the solver function is illustrated in Figure 5-4b below. The target cell is G8, the variable cell is D3, while the constraint placed on the solver was that areas calculated with the IntSI equation should be equal to that obtained by high resolution imaging. The variable cell (D3) contained a

modifiable correction factor that can be used to multiply  $P_B$  in order to make the value closer to  $P_{SS}$ . Only 5 datasets were used to estimate the correction factor in Figure 5-4b. However, data from the fifteen volunteers were used for the actual calculations.

Based on the correction factor obtained, the IntSI equation was adjusted. Area measurements with the adjusted IntSI equation were compared with those from high resolution pixel counting. Figure 5-5a and 5-5b are representative images obtained with high resolution imaging and the IntSI technique respectively, in the same volunteer. To determine the inter-rater reliability of the IntSI technique, data from the 15 volunteers was processed by another rater and area measurements were calculated with the adjusted IntSI equation.

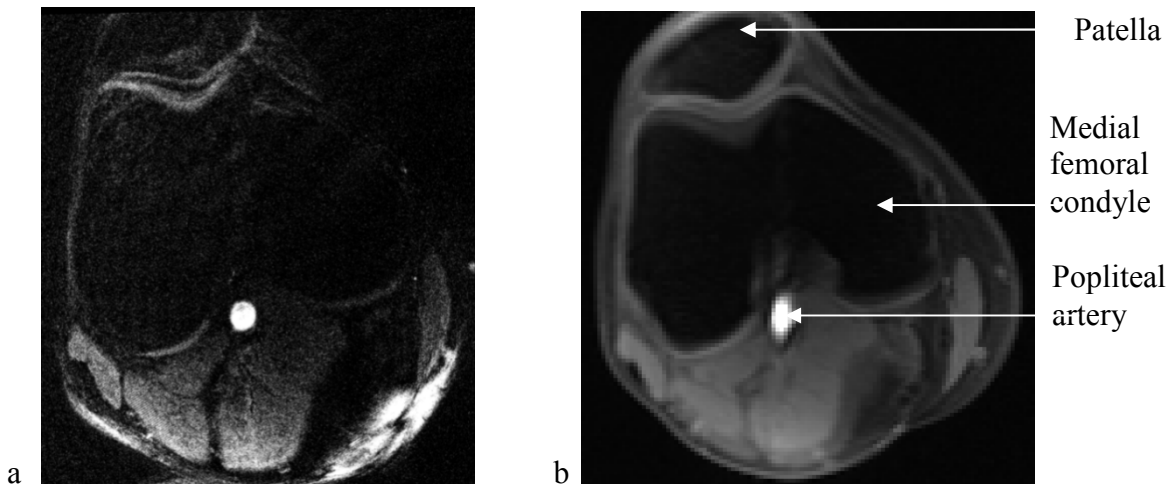


**Figure 5-5. Images of the knee, with the popliteal artery lying posterior to the femoral condyles.** (a) is a high-resolution image (pixel area:  $0.02 \text{ mm}^2$ , scan time: 180-240 s) while (b) was obtained with a lower resolution (pixel area:  $1.2 \text{ mm}^2$ , scan time: 6-9s), for area measurements with the IntSI technique. The shape of the lumen in figure b appears more oblong than figure a due to a phase artifact.

### 5.3.4 Statistical analyses

Each image was processed five times. The results were expressed as mean  $\pm$  SD. Bland Altman plot and Lin's concordance correlation coefficient were used to test for agreement between areas measured using the IntSI technique and areas measured by pixel counting of high resolution images. The intraclass correlation coefficient (ICC) and the mean difference between the two methods were calculated (Vaz et al., 2013). The inter-rater reliability was assessed with the intraclass correlation coefficient. All calculations were carried out using the R Project for



Statistical Computing version 3.1.3 (by R Foundation for Statistical Computing, Vienna, Austria).

## 5.4 Results

### 5.4.1 Mathematical modeling for optimizing the MRI sequence

The mathematical modeling aimed to achieve the smallest pixel size, TR and scan time that can be used for the IntSI technique. It also aimed to obtain the highest possible threshold velocity ( $V_T$ ). The smallest pixel area used for modeling was  $0.3 \text{ mm}^2$ . Figure 5-6 shows that at a pixel area of  $0.3 \text{ mm}^2$ , the TR was 52 ms and the scan time was 25 s. With a moderate pixel area of  $1.2 \text{ mm}^2$ , at a TR of 52 ms, the scan time decreased to 12 s. To achieve a scan time of 10 s or less, at a relative SNR of 1, a TR of 28 ms or less is required.

Using a TR of 24 ms, and a moderate pixel area of  $1.2 \text{ mm}^2$ , the scan time was as low as 6 s at a relative SNR of 1. This provides a sampling frequency of 10 images/min or less depending on the heart rate. At a TR of 24 ms and a slice thickness of 10 mm, the threshold velocity required for the velocity profile to fit within the slice is 42 cm/s.

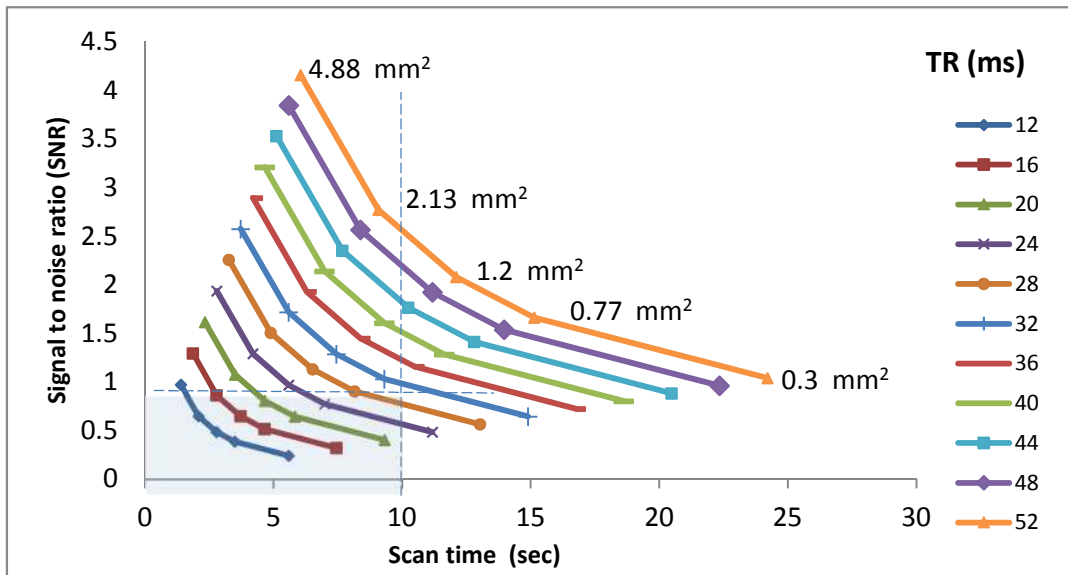


**Figure 5-6. A plot of SNR versus scan time.** As the scan time increased due to a decrease in the pixel size, the SNR decreased. Eleven lines were plotted using TR ranging from 12-52 ms. TR was kept constant in each line.

### 5.4.2 Reliability of area measurements with the IntSI technique

Area measurement using high resolution and pixel counting required 180-240 seconds for data acquisition, while the IntSI technique required just 6-9 seconds. The mean luminal area was  $29.42 \pm 5.35 \text{ mm}^2$  for high resolution imaging and  $32.46 \pm 5.61 \text{ mm}^2$  for the IntSI technique (Table 5.1). There was agreement between popliteal areas obtained from pixel counting of high resolution images and that obtained using the IntSI technique (Figure 5-7a). The ICC for high resolution imaging and the IntSI technique was 0.91(0.82-0.96). The data points lay towards the left of the line of unity (Figure 5.7a) with the areas measured using the IntSI technique being  $3.05 \pm 2.55 \text{ mm}^2$  larger than the high resolution method (Figure 5.8a).

### 5.4.3 Effects of adding a correction factor to the IntSI equation

Numerical optimization gave a value of 1.36 for the correction factor. This is larger than the value of 1.15 obtained from spectral Doppler analysis. Application of a correction factor of 1.15 obtained from spectral Doppler analysis in the IntSI equation gives equation 5.7

$$A = \frac{\text{IntSI. a}}{1.15 P_B + 0.6[P_{\max} - 1.15 P_B]} = \frac{\text{IntSI. a}}{0.46 P_B + 0.6 P_{\max}} \quad (5.7)$$

Application of a correction factor of 1.36 obtained from numerical optimization gives equation 5.8

$$A = \frac{\text{IntSI. a}}{1.36 P_B + 0.6[P_{\max} - 1.36 P_B]} = \frac{\text{IntSI. a}}{0.54 P_B + 0.6 P_{\max}} \quad (5.8)$$

Averaging the values  $0.46 P_B$  and  $0.54 P_B$  in equations 5.7 and 5.8 gave  $0.5 P_B$  and this was applied to the IntSI equation. Therefore, the denominator in the IntSI equation became  $0.5 P_B + 0.6 P_{\max}$ . Using this adjusted IntSI equation, the mean luminal area decreased to  $29.56 \pm 5.26 \text{ mm}^2$  (Table 5.1), with an increase in the ICC between the high resolution/pixel counting and the IntSI technique to 0.98 (0.97-0.99) while the mean difference decreased to  $0.14 \pm 2.32 \text{ mm}^2$  (Figure 5-8b). The inter-rater ICC using the adjusted IntSI equation was 0.92 (0.89- 0.95).

**Table 5-1. Luminal area measurements of the popliteal artery obtained by high resolution imaging and the IntSI technique without (0.4P<sub>B</sub>) and with (0.5P<sub>B</sub>) the correction factor respectively.**

n = 15	High resolution imaging	IntSI technique @0.4P <sub>B</sub>	IntSI technique @0.5P <sub>B</sub>
Mean ± SD (mm <sup>2</sup> )	29.42 ± 5.35	32.46 ± 5.61	29.56 ± 5.26

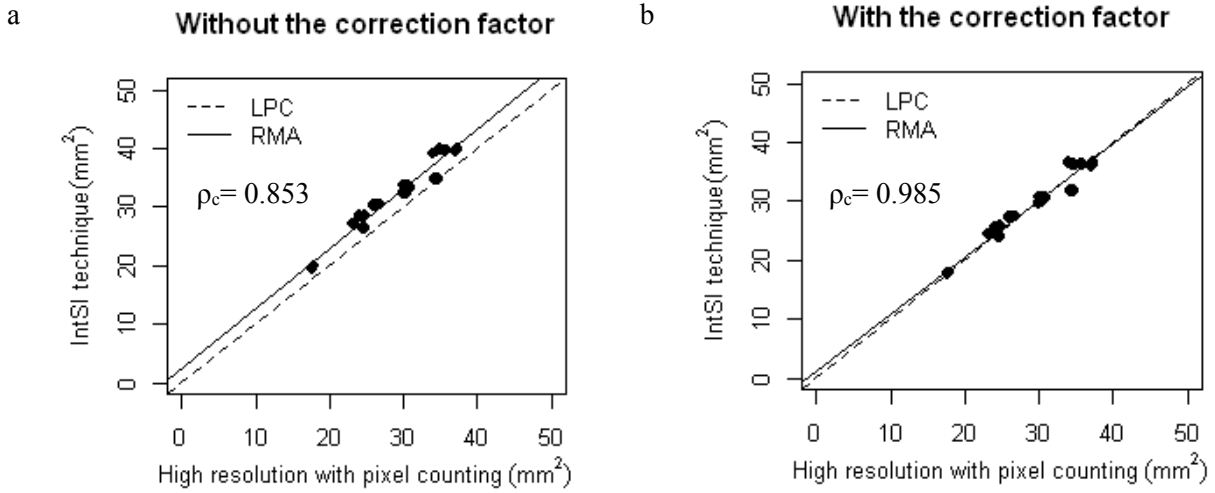
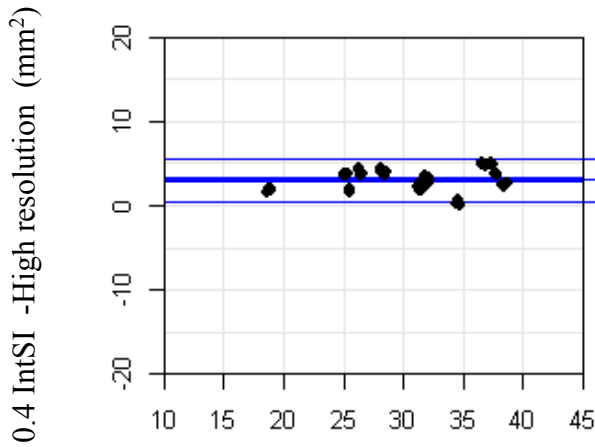
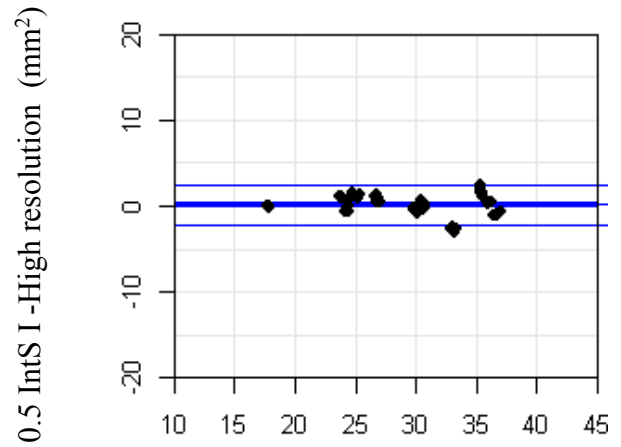


**Figure 5-7. The scatter plots for comparison between the IntSI technique and the high resolution imaging approaches for measuring the luminal area. (a) When the IntSI equation was used without the correction factor, there was a shift of the reduced major axis (RMA) to the left of the line of perfect concordance (LPC). (b) When the IntSI equation was used with the correction factor, the reduced major axis overlay the line of perfect concordance.**



(0.4 IntSI + High resolution)/2 (mm<sup>2</sup>)



(0.5 IntSI + High resolution)/2 (mm<sup>2</sup>)

Mean bias ± CR (mm <sup>2</sup> )	ICC	Mean bias ± CR (mm <sup>2</sup> )	ICC
3.05 ±2.55	0.91(0.82-0.96)	0.14±2.32	0.98 (0.97-0.99)

**Figure 5-8. Bland Altman's plots for comparison between the IntSI technique and the high resolution imaging approaches for measuring area.** (a) using the IntSI equation without the correction factor, (b) using IntSI equation with the correction factor. There was agreement between high resolution imaging and the IntSI technique. However, the ICC was higher and the mean difference lower, when the correction factor was used (n=15).

## 5.5 Discussion

FMD requires rapid serial area measurements because the time to peak dilatation is variable and the peak dilatation is transitory. To optimize the IntSI technique for area measurement during FMD, sequence optimization is required due to the constraints of temporal resolution and spatial resolution. Mathematical modeling provided a means to optimize the sequence parameters for imaging with the IntSI technique. The designed sequence was then applied in vivo. Area measurements with the IntSI technique were compared with high resolution and pixel counting.

### 5.5.1 Mathematical modeling

The sequence parameters for the IntSI technique were optimized for rapid serial area measurements in vivo using mathematical modeling. The modeling results show that, with a TR of 24 ms, and a moderate pixel area of  $1.2 \text{ mm}^2$ , the scan time can be as low as 6 seconds at a relative SNR of 1. A scan time of 6 seconds allows a sampling frequency of 10 images per minute. The modeling was based on an assumption of a heart rate of 60 beats per minute. However, the average heart rate for healthy adults greater than 18 years is 72 beats per min with a range of 60-100 beats per min (Khurana 2007). Therefore in those with higher heart rates, the scan time would be shorter, resulting in a higher sampling frequency while the scan time will be longer for those with slower heart rates such as athletes or some patients with cardiac disease (Khurana 2007).

Using a large slice thickness for the modeling helped to improve the SNR, in addition, a large slice reduces the chances that the blood velocity will exceed the threshold velocity. With a slice thickness of 10 mm and a TR of 24 ms, the threshold velocity will be 41.7 cm/s. This value can be used for imaging the popliteal artery during diastole with low likelihood that the threshold velocity will be exceeded. This is because spectral Doppler analysis showed in chapter 4 that the time averaged maximal velocity ( $TAV_{\max}$ ) of the popliteal artery during the diastolic data acquisition window was less than 42 cm/s, even in the presence of reactive hyperemia. To avoid the high velocities of systole, ensure that data is acquired during diastole and improve the chances of the blood velocity being less than the threshold value, a diastolic trigger delay should be used during data acquisition. With a diastolic trigger delay, imaging commences at a specific time from the onset of the R wave. An adaptive trigger delay technique may be useful in those

with variable heart rate to ensure that imaging always commences at a specific point in the cardiac cycle (Roes et al., 2008; Fernandez et al., 2009).

A pixel area of  $1.2 \text{ mm}^2$  was used for imaging, with the scan time ranging from 6-9 s depending on the heart rate. This scan time is an improvement on those attained when fast sequences like the SSFP sequence were used to obtain high resolution images ( $0.3 \text{ mm} \times 0.3 \text{ mm}$ ) for area measurement by pixel counting (Leeson et al., 2006; Oliver et al., 2012). The scan times with the SSFP sequence range from 15 seconds to greater than 30 seconds depending on whether the field strength of the magnet is 1.5T or 3T with the shorter scan times associated with higher fields strengths (Leeson et al., 2006; Oliver et al., 2012). Recently, a new black blood technique using water-selective 3D SSFP-echo and a 3T scanner has been used to achieve acquisition times less than 12 seconds during FMD studies. However, the authors did not specify how much the acquisition time was lower than 12 seconds (Langham et al., 2013).

As discussed in chapter 3, provided the area ratio is at most 0.1, the relative error in area measures using the IntSI technique will be less than 10%. Since the smallest possible baseline area for the popliteal artery is  $11.95 \text{ mm}^2$  (Sandgren et al. 1998), the pixel area of  $1.2 \text{ mm}^2$  used for imaging the popliteal arteries should be associated with an error less than 10%. The addition of background signals to the measured IntSI could also lead to errors in the calculated area. The ability to segment pixels containing luminal signals with the aid of a mask created with the sliding paraboloid background subtraction technique reduced the chances of adding juxtaluminal signals to the integrated SI and overestimating the luminal area.

### 5.5.2 Comparison between the IntSI technique and high resolution imaging

There was agreement between the areas measured with the IntSI technique and the high resolution/pixel counting method with an intraclass correlation of 0.91 (Figure 5-7a), which supports the ability of the IntSI technique to measure area in vivo. However, the Bland Altman plot showed that measurements using the IntSI technique were an average of  $3 \text{ mm}^2$  larger than that by high resolution and pixel counting (Figure 5-8a). A possible reason why the area measures using the IntSI technique were higher than the high resolution imaging could be the presence of a venous saturation band. This is because if the retrograde flow that enters the slice during image acquisition has no signal, having been completely saturated by the venous

saturation band, then the  $P_B$  will be lower than expected; therefore the mean signal intensity will be less than it should be and the calculated area using the IntSI technique will be elevated since there is a reduction in the denominator of the IntSI equation for area measurements due to  $P_B$  being lower than  $P_{SS}$ . However, under conditions of hyperemic flow, there may be a need to decrease or remove the correction factor. This is because retrograde flow is reduced or eliminated during hyperemia. If the correction applied for calculating the luminal area of an unperturbed artery is also applied during hyperemia, the maximal area of the artery may be underestimated and the FMD also underestimated. The oval shape of luminal images acquired with the IntSI technique (Figure 5.5b) was ascribed to phase encoded motion artifact rather than the effect of partial volume averaging of the thick slices imaged. Changing the phase encoding direction from up-down to left-right resulted in a corresponding change in the direction of the artifact.

### 5.5.3 Effects of adding a correction factor to the IntSI equation

When a correction factor was added by assuming that  $P_{SS}$  is  $1.2 P_B$  the difference between the IntSI equation and high resolution imaging decreased to  $0.14 \pm 2.32 \text{ mm}^2$ , with an improvement of the ICC to 0.95 (0.91-0.98) as shown in Figure 5-8b. If the minimal detectable change in area during an FMD study is 5% and the minimum baseline diameter of the popliteal artery is 3.9 mm (Sandgren et al. 1998), which corresponds to minimum area of  $11.95 \text{ mm}^2$  assuming that the cross-sectional area is circular, then 5% FMD will be associated with an absolute area increase of  $0.6 \text{ mm}^2$ , which is larger than the  $0.14 \pm 2.32 \text{ mm}^2$  and therefore can be regarded as a real change.

### 5.5.4 Conclusion

This chapter shows that the IntSI technique can be applied in vivo; however, a correction factor needs to be included to account for  $P_B$  being less than  $P_{SS}$  and thereby preventing measurement overestimation. The technique enables improved temporal sampling frequency increasing the chances of detecting the peak dilatation during an FMD study.



## 5.6 Supplementary methods

### 5.6.1 An outline of the background subtraction technique

1. The images were open as a stack in imageJ
2. A plot profile of luminal pixels spanning the center of the lumen was obtained from the baseline image. (Analyze -> plot profile)
3. The apical radius of curvature in pixel length was estimated from the steepness of the apex.
4. This value was inserted in the Subtract Background dialog box. The sliding paraboloid function in the dialog box was clicked and the images were processed as a stack. (Process -> subtract background)
5. The disable smoothing option in the sliding paraboloid dialog box was selected so that pixels at the edge of the lumen will not be filtered out of the image.
6. To restore the intraluminal pixels to their native values, a mask of the images was created using the Change Value function, with the luminal pixel assigned 1 au and the surrounding pixels assigned 0 au.
7. Then a new stack of the images was opened and these unprocessed images were multiplied with the mask using the Calculator Plus function in order to get a new stack of images in which luminal pixels have their native intensity values while surrounding pixels have intensity values of zero.
8. A region of interest (ROI) was placed over the lumen and the Multi Measure function was used to obtain the  $P_{\max}$  and IntSI (called Max and IntDen respectively in imageJ) from the stack of images.
9. A spreadsheet was created in excel using the results and the luminal area of each image was calculated using the IntSI equation.

---

**Chapter 6    Comparing popliteal MRI-based FMD  
using the IntSI technique with brachial  
US-FMD in healthy volunteers**

---

## 6.1 Abstract

**Objectives:** To demonstrate that MRI-FMD using the IntSI technique is more repeatable than US-FMD.

**Background:** Ultrasound based flow mediated dilatation of the brachial artery is used to assess macrovascular function. However, US-FMD is operator dependent and technically challenging; this limits the use of FMD as a means of assessing endothelial function in multi center research. MRI is less operator dependent, but it is constrained by spatial and temporal resolution. The IntSI technique provides an opportunity to reliably obtain rapid serial area measurements during an FMD study so that the peak dilatation can be detected. To rule out microvascular disease, the IntSI technique is explored as a surrogate means of quantifying blood flow and reactive hyperemia. This is because the integrated signal intensity (IntSI) of the lumen increases with the luminal area and mean velocity and these factors also affect blood flow. If the IntSI based MRI-FMD technique is more repeatable than the current ultrasound technique, the IntSI technique can be easily applied for multi-center FMD studies.

**Methods:** Brachial US-FMD was compared with popliteal US-FMD in 19 healthy volunteers. The IntSI technique was also used to perform an MRI-FMD study. The test-retest repeatability of popliteal MRI-FMD using the IntSI technique was compared with that of the brachial US-FMD and popliteal US-FMD. The coefficient of repeatability from Bland Altman plots, intraclass correlation coefficient (ICC) and the within subject coefficient of variability ( $CV_w$ ) were used to test for repeatability of each method. The Pearson's correlation coefficient was used to test for agreement between the FMD techniques. A two-one-sided t-test (TOST) was used to test for non-inferiority between the  $CV_w$  of the FMD techniques. Reactive hyperemia was qualitatively graded as poor or adequate using the maximum IntSI to baseline IntSI ratio. Those in which the maximum /baseline IntSI ratio was 1.2 or less were classified as demonstrating poor reactive hyperaemic response, while those in which the ratio was greater than 1.2 were classified as having adequate reactive hyperaemic response.

**Results:** There was moderate agreement between brachial US-FMD and popliteal US-FMD ( $r$ : 0.59). The mean difference between the baseline areas of the popliteal artery using MRI versus US was  $4.76 \pm 5.19 \text{ mm}^2$ , which is a difference of 19 % relative to the US baseline area. The mean difference between popliteal US-FMD and MRI-FMD was 5.07%. The within subject coefficient of variability of the popliteal MRI-FMD technique at 24% was non-inferior to both

the brachial ultrasound and popliteal ultrasound FMD techniques at 23% and 26% respectively. The poor hyperaemic response group had lower hyperemic values during brachial US-FMD than the adequate hyperemic response group ( $4.01 \pm 2.52$  versus  $5.14 \pm 2.56$ ). Similar findings were observed with popliteal US-FMD ( $2.91 \pm 0.94$  versus  $3.56 \pm 1.45$ ). However, the difference was not significant at  $p > 0.05$  in both cases.

**Conclusion:** MR-FMD using IntSI technique for measuring FMD is non-inferior to both popliteal US-FMD and brachial US-FMD. This technique has the potential to be a reliable method of measuring macrovascular endothelial dysfunction in disease states and qualifying the microvascular dependent reactive hyperemia.

## 6.2 Introduction

Endothelial dysfunction is a precursor of atherosclerosis and its associated complications such as heart attack and stroke (Chhabra, 2009). It is also said to be an underlying factor in other disease conditions (Mohandas et al., 1985; Bagg et al., 2001; Yinon et al., 2010; Westman et al., 2013). Endothelial function assessment of peripheral arteries is used to indirectly estimate atherosclerotic risk and coronary endothelial dysfunction (Rakobowchuk et al., 2008).

### 6.2.1 Flow mediated dilatation and reactive hyperemia

As reviewed in Chapter 2, flow mediated dilatation (FMD) is a means of assessing macrovascular endothelial function. The technique measures the response of healthy conduit arteries to reactive hyperemia (Celermajer et al. 1992). Reactive hyperemia is the increased blood flow that occurs following ischemia-induced microvascular dilatation. Reactive hyperemia results from a pressure gradient between the dilated microvasculature and the conduit artery. The surge of blood through the conduit artery during reactive hyperemia causes shear stress on the endothelial lining. This triggers nitric oxide production by the endothelium, relaxation of the adjacent vascular smooth muscle and macrovascular vasodilatation. The degree of reactive hyperemia gives an indication of how healthy the microvasculature is. For a given arterial cross-sectional area, the higher the reactive hyperemia, the greater the shear stress and the higher the FMD response will be. Therefore, it is important to quantify reactive hyperemia in order to determine if a poor FMD response is due to endothelial dysfunction in the conduit artery, or due to underlying microvascular disease. Reactive hyperemia is usually quantified as a ratio of the

maximal blood flow recorded after the cuff deflation to the baseline blood flow (Celermajer et al., 1992).

### 6.2.2 Limitations of ultrasonography

Ultrasound is commonly used to measure the FMD, however, operator dependence remains a big limitation (Corretti et al., 2002). It is recommended that personnel undergo rigorously supervised training before being allowed to independently perform ultrasound-based FMD. They are also expected to maintain competency by completing 100 scans annually (Corretti et al., 2002). In a regular hospital or clinical setting, sonographers may not have the opportunity to perform the recommended number of scans annually depending on the number of patients referred for the procedure. Since the procedure is time consuming, spending time scanning volunteers annually in order to maintain competency may not be a feasible alternative because sonographers are a limited resource and their time may be required for other clinically referred ultrasound procedures (Alley et al., 2014). In view of the strict requirements for maintaining competency for US-FMD studies, application of ultrasound FMD has yet to proceed beyond sophisticated research laboratories partly due to these not easily attainable guidelines (Hamilton et al., 2011).

Another limitation of ultrasonography is that it measures vasodilatation as an increase in the longitudinal diameter of the lumen and the cross-sectional area is calculated based on the assumption that the lumen has a circular area; however if the lumen is rendered elliptical due to pressure from the overlying ultrasound transducer the calculated area will be less than it should be (Leeson et al., 2006). In addition, longitudinal imaging will not adequately capture multi-dimensional vessel dilatation during FMD and if there is an inadvertent shift in the imaging plane during the FMD study, then an error will be introduced.

### 6.2.3 Pros and cons of MRI-FMD

MR imaging has the advantage of cross-sectional imaging and it is possible to use the same imaging plane throughout multiple data acquisitions, provided the limb is immobilized during imaging, thereby reducing operator dependence (Silber et al., 2005; Leeson et al., 2006). With phase contrast imaging, reactive hyperemia can be quantified because the blood velocity can be measured (Silber et al., 2005) and the blood flow calculated as a product of the mean velocity and luminal area (Zierler & Sumner, 2014). However, unlike ultrasonography, MR imaging is

limited by the trade-off between spatial and temporal resolution (Leeson et al., 2006). This limitation of MRI is more severe with phase contrast imaging compared to other MRI sequences (Silber et al., 2005). However, the faster sequences such as SSFP that are used for MRI-FMD studies do not provide velocity information (Sorensen et al., 2002; Leeson et al., 2006). For accurate measurements of FMD, the Nyquist sampling interval should be less than  $\frac{1}{2}$  the time to peak (Luke, 1999). The time to peak may be as low as 25.8 seconds (Fernandes et al., 2014). Therefore, the sampling interval during MRI-FMD should be less than 13 seconds. In chapter 5, a scan time of 6-9 seconds was achieved with the IntSI technique. This provides an opportunity to overcome the limitation of temporal resolution during MRI-FMD. The IntSI may also be able to qualitatively demonstrate reactive hyperemia.

Cost is another limitation of MRI-FMD. MRI has a higher cost per unit time compared with ultrasonography. However, if MRI is more repeatable than ultrasonography, then a cost effectiveness analysis may show MR-FMD to be relatively cheaper than ultrasound because the MRI cost may be offset by decreasing the sample size required in experimental groups. In addition, if the time required to perform MR-FMD is short enough for the study to be included in time already earmarked for a comprehensive cardiovascular MRI study, then there will be no added cost for performing the study.

#### **6.2.4 Assessing FMD and reactive hyperemia with the IntSI technique**

The IntSI technique for measuring the luminal area on MR images was derived in Chapter 3. It uses an equation that requires the integrated signal intensity of the lumen and the central pixel intensity to calculate the luminal area. The technique is based on a spoiled gradient echo (GRE) sequence. With a spoiled GRE sequence, residual magnetization from previous RF pulses are “spoiled” or abolished, so that any signal detected from the lumen after the application of an RF pulse can be ascribed entirely to that particular RF pulse. The technique was described in detail in Chapter 3. This area measurement approach offers higher temporal sampling frequency because it does not depend on a high spatial resolution for measurement accuracy. Therefore the peak dilatation may be captured and the FMD calculated.

Reactive hyperemia is a ratio of two flow quantities (Celermajer et al., 1992), with quantity of flow being a product of the mean blood velocity and the luminal area (Zierler & Sumner, 2014).

Since the integrated signal intensity of the lumen (IntSI) increases with both the mean blood velocity and the luminal area, IntSI could possibly be used to qualitatively demonstrate reactive hyperemia. In this case, reactive hyperemia may be expressed as a ratio of the peak IntSI recorded after the cuff was deflated to the baseline IntSI. It is anticipated that the IntSI technique will provide repeatable measurements of vascular dilatation during FMD studies and demonstrate reactive hyperemia without the limitations associated with ultrasonography or phase contrast MR imaging.

#### 6.2.5 Choice of the artery for measuring MRI- FMD using the IntSI technique

FMD has been demonstrated in various peripheral arteries such as the radial (Joannides et al., 1995), brachial (Doshi et al., 2001), femoral (Kooijman et al., 2008) and popliteal (Nishiyama et al., 2007) arteries. Although brachial FMD is suggested as the non-invasive gold standard for assessing macrovascular endothelial function (Deanfield et al., 2007; Stoner et al., 2013) and it will be expected that the IntSI technique will be tested for brachial, we choose the popliteal artery instead because testing the MR-FMD IntSI technique because it is larger than the brachial artery. In a larger artery, there is lower likelihood that pixel-to-luminal area ratio will affect area measurements with the IntSI technique. In addition, as mentioned in chapter 4, the popliteal artery is closer to the midline than the brachial artery, therefore, will produce more homogenous MR signals when placed within the bore of the magnet (Brix et al., 2008). Imaging the popliteal artery may also be more acceptable to patients with claustrophobia because they can be placed caudo-cranially into the magnet, leaving the head free from the confined space. The popliteal artery was preferable for the MRI-FMD technique because atherosclerosis is seen more often in the lower limbs (Laredo & Lee, 2008) and there is some suggestion that ED may occur earlier in the lower limbs compared with the upper limbs (Sanada et al., 2005). Therefore assessing lower limb hemodynamic response with MRI might be a more appropriate marker of vascular health. However, there is a need to establish an association between popliteal ultrasound FMD and the gold standard (brachial FMD) and then determine if popliteal MRI-FMD using the IntSI technique is at least as reproducible as US-FMD.

## 6.2.6 Hypothesis

Popliteal MRI-FMD using the IntSI technique is more repeatable than brachial US-FMD

The aims of this chapter were:

- 1) to test for agreement between brachial ultrasound FMD and popliteal ultrasound FMD;
- 2) to test for agreement between popliteal ultrasound FMD and popliteal MRI-FMD using the IntSI technique;
- 3) to demonstrate that MRI-FMD using the IntSI technique is more repeatable than US-FMD;  
and
- 4) to demonstrate that the IntSI technique is able to qualitatively assess reactive hyperemia.



## 6.3 Materials and Methods

### 6.3.1 Subject selection and control of factors that affect FMD

Ethical approval for the study was obtained from both Sunnybrook Health Sciences Centre and St. Michael's Hospital. Informed consent was also obtained from 19 healthy adults who volunteered for the study. Based on the recommended guidelines for FMD studies (Corretti et al., 2002), various external factors that may affect the measured FMD were taken into consideration. Volunteers were required to have no history of cardiovascular disease, dyslipidemia or diabetes because these are risk factors for endothelial dysfunction. Subjects were scanned in a temperature controlled room after a period of rest because temperature and exercise increase FMD (Widlansky et al., 2007; Tinken et al., 2008). The scan was done in the morning after an overnight fast because ingestion of coffee and fatty food may contribute to variability in FMD measurements (Buscemi et al., 2010; Koulouris et al., 2010). The test-retest scans were done within a short interval in order to prevent any diurnal variation in FMD (Harris et al., 2006). Smokers were not included in the study because smoking is associated with a poor FMD response (Findlay et al., 2013).

Volunteers were requested not to take vitamin C, E or multivitamin preparations (Taddei et al., 1998) and those that had used vasoactive medication within the previous 3 months were not included in the study (Corretti et al., 2002). None of the volunteers were on any weight loss or special diet and they were requested to avoid strenuous exercise for 48 hours before the study (Black et al., 2009; Hwang et al., 2012). However, their diets and physical activity were not standardized. Female subjects were scanned during the pre-ovulatory phase of their cycle because endogenous estradiol which has a vasodilatory effect is low during this phase (Hashimoto et al., 1995; Corretti et al., 2002). In view of the peculiarities of MRI scanning, other exclusion criteria included the presence of metallic implants, etc. or conditions which were considered unsuitable for MRI such claustrophobia.

Volunteers had test-retest studies of the brachial and popliteal ultrasound scans at Sunnybrook Hospital on the same day, with an interval of 30 minutes between each test and retest. On a separate day, volunteers had test-retest Popliteal MRI-FMD studies using either a 3T Siemens scanner available at St Michael's hospital or at Sunnybrook hospital. The test-retest MRI scans

also had 30 minutes interval between them. The age, gender, height, weight, BMI, blood pressure and heart rate of each volunteer were recorded. Each FMD study comprised of serial measurements of the vessel lumen. Flow information was also obtained in order to assess reactive hyperemia, as shown in Figure 6-1.

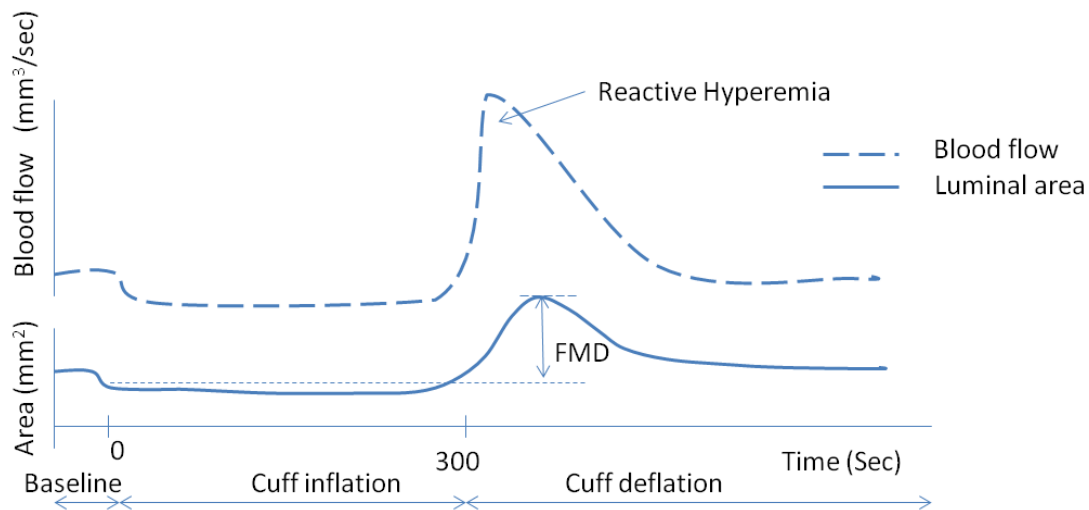


**Figure 6-1. A schematic representation of the changes in the cross-sectional area of the vessel lumen and the blood velocity over time.** Once the cuff is released, reactive hyperemia occurs followed by a slower onset of vasodilatation.

### 6.3.2 Brachial ultrasound FMD technique

For brachial US-FMD, a Philips iU22 Ultrasound system (Philips Healthcare, Andover, MA, USA) available at the Diagnostic Imaging Department at Sunnybrook Health Sciences Centre was used. All scans were performed by an experienced operator certified in vascular technology by the American Registry of Diagnostic Medical Sonography (ARDMS). The investigator had trained for FMD procedures using feasibility studies and prior to this current study, the operator had independently performed FMD ultrasound studies for a separate research project. Scans were done at the same time of the day. Cine images were saved on the scanner and transferred to a CD for offline analysis. Each subject was positioned supine on an examination couch and allowed to rest for about 10 minutes during which ECG leads were positioned on the chest wall to enable image acquisition at end diastole. Subsequently, the right arm was abducted and placed on an armrest with the pneumatic cuff of an aneroid sphygmomanometer (D.E. Hokanson Inc., Bellevue, WA USA) positioned on the forearm to provide distal occlusion.

The wrist was slightly elevated with the aid of a small cushion so that the proximally placed cuff could inflate and deflate without causing any displacement of the limb or distortion of the imaging plane. The cuff was positioned distal to the imaged arterial segment as shown in Figure 6-2a. This is because distal occlusion of the artery produces more reproducible results than proximal occlusion and it is said to be specific for nitric oxide dependent vasodilatation unlike proximal occlusion (Doshi et al., 2001; Peretz et al., 2007). Most of the volunteers were imaged with an L12-5 MHz linear high frequency transducer, but in cases where the brachial artery was located less superficial, an L9-3 MHz linear transducer was used instead. The transducer was placed in a probe holder and positioned 2 cm above the antecubital fossa. Some adjustments were made until a longitudinal image of the brachial artery was visualized with the near and far walls clearly defined. The gain of the scanner was also adjusted so that the lumen was clear of any artifacts after which the transducer was immobilized with the probe holder in order to retain the imaging plane.

Four baseline grey scale longitudinal images of the brachial artery were obtained. Then spectral Doppler imaging was performed using an insonation angle of 60°. The sample volume was expanded from wall-to-wall in order to include all velocities within the lumen and the scanner automatically calculated the time averaged maximal velocity of the artery ( $TAV_{max}$ ). Although the scanner had an option for simultaneously obtaining B-mode images and spectral Doppler data, this option was not utilized because the insonation angle required for optimal B-mode images is 90°, while that for spectral Doppler should be less than 60° (Thijssen et al., 2011a). Therefore, each image was obtained separately but the drawback was that the sampling lasted up to 10 seconds or more. Subsequently, the blood pressure cuff was inflated to 50 mmHg above the systolic pressure for 5 minutes. When the cuff was deflated, measurements of vessel diameter and blood velocity were performed at an average interval of 10 seconds and the measurements continued up to 5 minutes post-deflation. The magnification, focus, depth and gain were kept constant throughout the examination period.

### 6.3.3 Popliteal ultrasound FMD technique

For the popliteal US-FMD, the protocol was similar to that of brachial ultrasound; however, the subject was positioned prone with the inflatable cuff placed on the leg, slightly below the bulk of

the calf muscles as shown in Figure 6-2b. This is because the placement of the cuff around the bulk of the calf muscles was intolerable to the volunteers. The L9-3 MHz transducer was used for imaging the popliteal artery because the popliteal artery was relatively less superficial than the brachial artery. The ultrasound probe was positioned in the popliteal fossa which lies behind the knee, in order to image the popliteal artery. A cushion was placed under the ankle so that the imaging plane would not be distorted by movements of the limb when the cuff was inflated or deflated. Similar to the brachial ultrasound study, four baseline images were obtained and the time averaged maximal velocity ( $TAV_{max}$ ) was recorded. The cuff was inflated up to 240 mmHg in order to occlude the underlying artery and produce limb ischemia. Arterial occlusion was confirmed by an absence of a pulse in the region of posterior tibial and dorsalis pedis arteries. Increasing the pressure beyond 240 mmHg was associated pain that most volunteers found intolerable. The occluding blood pressure cuff was deflated after a period of 5 minutes. Once the occlusion was relieved, serial B-mode and spectral Doppler images were obtained for the vessel diameter and  $TAV_{max}$  measurements respectively. The serial images were recorded over 5 minutes at an average sampling rate of 1 image every 10 seconds.

The popliteal US-FMD study was performed right after the brachial FMD since the arteries of interest are located in separate regions of the body. and although FMD is a marker for systemic bioavailability of nitric oxide (Pyke & Tschakovsky, 2005), the immediate vasodilatory response is due local release of nitric oxide by the endothelium of the conduit artery (Corretti et al., 2002). Popliteal US FMD lasted about 30 minutes, by which time it was expected that the brachial artery would have returned to its original size (Harris et al., 2006). At this point, we repeated the brachial FMD, followed by another popliteal FMD for test-retest repeatability, since repeating the reactive hyperemic stimulus after an interval of 30 minutes does not affect the sensitivity of the vasodilator response of the endothelium (Harris et al., 2006).

A



b



**Figure 6-2. Positioning for US-FMD.** (a) is the positioning for the brachial study while (b) is the positioning for the popliteal study.

### 6.3.3.1 US Post processing for vessel segmentation and measurement

The images were post processed with imageJ (ImageJ, 2003). To reduce cardiac cycle based variations in the area, end diastolic B mode images were used for the diameter measurements (Chuang et al., 2002). Each image was converted to a binary form. The Default (IsoData) auto threshold algorithm in imageJ was used for thresholding. It uses an iterative approach to define the threshold. First, it divides the image into object and background using an initial threshold that is mid way between the two peaks on the histogram. After calculating the mean intensity for the object and the mean intensity for the background, it adds these two values and gets an average which is used as the new threshold value. This process is performed repeatedly until the threshold is larger than the average of the two clusters of intensities (Ridler & Calvard, 1978).

$$\text{i.e., threshold} = (\text{average background} + \text{average objects})/2.$$

The diameter was calculated from the area of a rectangular as follows. A rectangular ROI with a width of 20 mm was placed over a horizontal segment of the lumen. The location of the ROI was saved in ROI manager. In the rare instances where there was a shift in the relative location of the ROI on a subsequent image, then an anatomical landmark in the image was used to reposition the ROI. The area of the “rectangular” portion of the thresholded lumen within the ROI is measured. Since the width and area of the defined lumen were known, the length (luminal diameter) was calculated using the formula for the area of a rectangle. The average baseline diameter

measurement was determined from the four pre-occlusion images and the baseline luminal area was determined from this value based on the assumption that the luminal area is circular.

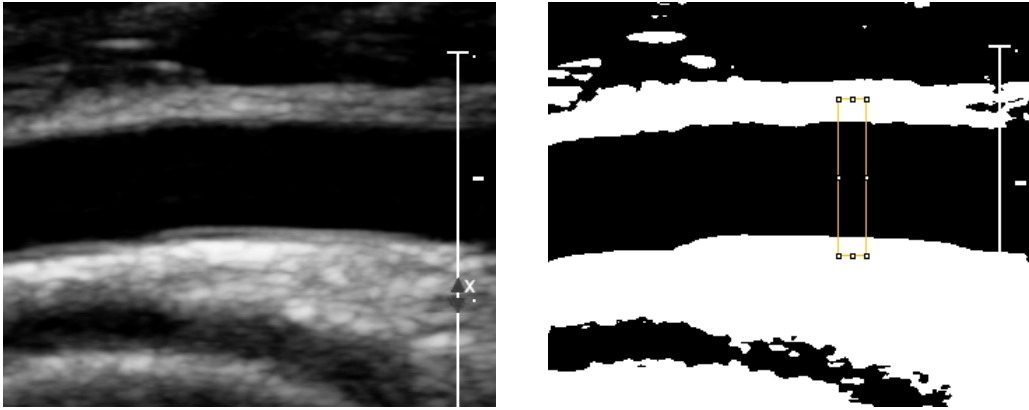


**Figure 6-3. An ultrasound image of the popliteal artery, before and after being converted to a binary form.** A rectangular ROI is placed on the binary image so that the luminal diameter can be obtained from the area of the ROI.

### 6.3.3.2 Indices of peak vasodilatation (FMD and time to peak)

Similar to the approach by (Pyke & Tschakovsky, 2007), the maximal diameter was defined as the maximum y-value obtained from a fitted curve. A double Richards curve was fit to the data using an 8 parameter flexible logistic function in R called FlexParamCurve (version 1.5-3) whose equation was given as 6.1 below (Oswald et al., 2012). The fitted double Richards curve derived from the positive and negative curves is illustrated in Figure 6.4.

$$y = \frac{\text{Asym}}{\left(\left[1 + m \cdot \exp(-k(t-i))\right]1/m\right)} + \frac{\text{Asym}'}{\left(\left[1 + m' \cdot \exp(-k'(t-i'))\right]1/m'\right)} \quad (6.1)$$

where

- Asym is the value for the asymptote of the positive (increasing) curve
- k is the value for the rate parameter of the positive (increasing) curve
- i is the value for the point of inflection of the positive (increasing) curve
- m is the value for the shape parameter of the positive (increasing) curve
- Asym' is the value for the asymptote of the negative (decreasing) curve
- k' is the value for the rate parameter of the negative (decreasing) curve
- i' is the value for the point of inflection of the negative (decreasing) curve
- m' is the value for the shape parameter of the negative (decreasing) curve

The maximal y-value was obtained by serially adjusting the x-value of the fitted curve using a code in the FlexParamCurve package in R (Oswald, 2015) while the time to peak (TTP) was its

corresponding x-value. The maximal area was calculated from the diameter with the assumption of a circular area. The maximal change in diameter and area were calculated by subtracting the maximal value from the baseline values respectively. The FMD was calculated in two different ways. It was calculated using the traditional method as the percent change in diameter from the baseline diameter and it was also calculated as the percent change in area.

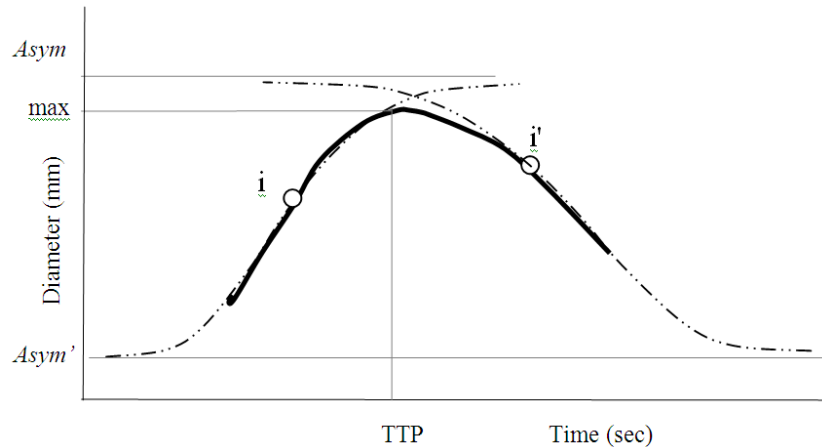


**Figure 6-4. Positive and negative generalized logistic curves are illustrated in broken lines, with a double Richards curve superimposed as a thick line.** The maximal diameter (max) is the peak of the double Richards curve. Depending on the point of intersection of the two curves, max may be less than the asymptote of the positive curve (Asym). The asymptote of the negative curve (Asym') and the time to peak (TTP) are also illustrated.

### 6.3.3.3 Reactive hyperemia and Hyperemic velocity

The blood flow was calculated as a product of the mean blood velocity and the luminal cross-sectional area of the conduit artery (Zierler & Sumner, 2014) while reactive hyperemia was calculated as the ratio of the maximal blood flow recorded after the cuff deflation to the baseline blood flow (Celermajer et al., 1992).

### 6.3.4 Popliteal MRI-FMD technique

Nineteen volunteers were scanned using a 3T MRI scanner and a knee coil. Twelve of them were tested at St Michael's hospital using a 3T Skyra Siemens scanner while seven had their examination at Sunnybrook hospital using a 3T Prisma Siemens scanner. The scan protocol used at St Michael's hospital was imported into the Sunnybrook scanner so the same sequence parameters were used on both scanners. In this case, each volunteer was positioned supine on an imaging table, unlike the popliteal US-FMD study in which the patients were positioned prone. It

was not expected that the positioning will have an effect on FMD since the stroke volume index and cardiac output index are not affected by a change in position from supine to prone (Toyota & Amaki, 1998). The procedure was performed in a temperature-controlled room. The right knee was placed within the knee coil and the limb was immobilized using cushions and sandbags. Distal occlusion was achieved with an MRI compatible sphygmomanometer (Gamma G5, Heine Germany). The blood pressure cuff was placed around the leg, slightly below the bulk of the calf muscles and a cushion was placed under the ankle so that the imaging plane will not be distorted due to movements of the limb when the cuff was inflated or deflated. MRI compatible ECG leads were placed on the chest and the examination commenced after a period of rest. A spoiled gradient echo sequence was used for imaging.

Nineteen volunteers were scanned and rescanned using a 3T MRI scanner and a knee coil. Twelve of them were tested at St Michael's hospital using a 3T Skyra Siemens scanner while seven had their examination at Sunnybrook hospital using a 3T Prisma Siemens scanner. The scan protocol used at St Michael's hospital was imported into the Sunnybrook scanner so the same sequence parameters were used on both scanners.

First, the popliteal artery was identified using a 3 plane localizer, then a series of axial slices spanning the popliteal fossa was obtained with the imaging plane perpendicular to the popliteal artery. Out of the series of slices, a suitable one was selected in which no branches were coming off the popliteal artery. This slice was imaged using the IntSI sequence developed in chapter 4. The sequence parameters were flip angle  $90^\circ$ , matrix =  $320 \times 140$ , FOV =  $350 \text{ mm} \times 153 \text{ mm}$ , pixel area =  $1.2 \text{ mm}^2$ , slice thickness = 10 mm, acquisition time = 6-9 seconds depending on the heart rate, TE = 3.5 ms TR = 24 ms. Imaging was ECG gated and a trigger time of 435 ms was applied in order to avoid the high velocities of systole. The trigger time was measured from the onset of systole, since the duration of systole is usually constant compared to diastole, even in those with irregular heart rates (Wallis et al., 1986). The trigger time value of 435 ms was determined from Spectral Doppler analysis of the popliteal artery in chapter 4. Spectral Doppler analysis showed that the time from the R wave to the onset of diastolic flow in the popliteal artery is  $447.35 \pm 17.58 \text{ ms}$ . Four baseline MR images of the popliteal artery were obtained, for calculation of the baseline luminal area as described in Chapter 5. Then, the blood pressure cuff was inflated up to 240 mmHg for 5 minutes. Imaging continued throughout the cuff inflation



period and for five minutes after the cuff was deflated. The re-scan MRI was done after an interval of 30 minutes in order to assess the test-retest reproducibility of the IntSI area measurement technique.



**Figure 6-5. The set up for the popliteal MRI-FMD.** The knee was immobilized within the knee coil and the pneumatic cuff was placed distal to the popliteal artery.

#### 6.3.4.1 Post processing for vessel segmentation and measurement

The MR images were post-processed with imageJ (ImageJ, 2003). The sliding paraboloid background subtraction algorithm in imageJ (Castle & Keller, 2007) was used to segment the luminal pixels. The technique was explained in detail in Chapter 5. The sliding paraboloid technique involved identifying luminal pixels based on a fitted paraboloid. A binary image or mask was then created by assigning the value 1 to pixels that fit in the paraboloid and 0 to those that did not. The created mask was used to multiply the native image using the calculator plus plugin (Rasband & Landini, 2004). The luminal pixels of each resultant image retained their native signal intensities while the adjacent background pixels had signal intensities of zero. A region of interest was defined using the pixels at the boundary which had zero pixel intensity. The multi-measure function (Rasband et al., 2006) was used to save the ROI and apply it to the other images, ensuring that the ROI encircled the luminal pixels in all the images. The IntSI was measured as the sum of the pixel intensities within the defined ROI and the maximal pixel intensity was also recorded ( $P_{\max}$ ) in each image.

#### 6.3.4.2 Luminal area determination

As discussed in Chapter 5, the IntSI equation was adapted for imaging the popliteal artery, because 1) the artery has a blunted parabolic flow profile, 2) arterial blood is not completely static during data acquisition, as imaging occurs over several cardiac cycles, but there is minimal flow during diastole in an unperturbed artery. Therefore, the central pixel intensity of an unperturbed artery ( $P_B$ ) was used in place of  $P_{SS}$ , 3) minimal retrograde flow entering the slice during data acquisition may be suppressed a venous saturation pulse used to remove adjacent signals from the popliteal artery, leading to  $P_B$  being lower than it should be. Therefore a correction factor was also included in the modified IntSI equation and the luminal area ( $A$ ) was calculated using the IntSI technique as expressed as equation 6.2.

$$A = \frac{\text{intSI} \cdot a}{0.5 P_B + 0.6 P_{\max}} \quad (6.2)$$

where IntSI is the integrated signal intensity of the luminal pixels,  $a$  is the pixel area,  $P_B$  is the baseline pixel intensity and  $P_{\max}$  is the maximal pixel intensity of the image being processed.

As mentioned in section 5.3.2, the central pixel's intensity of the unperturbed artery ( $P_B$ ) was determined as an average of  $P_{\max}$  obtained from the three baseline images. This is because the central pixel is expected to be the brightest pixel, even if there is no flow in the lumen since the pixel contains only luminal signals unlike more peripherally located pixels that may experience partial volume averaging with the surroundings. Subsequently, time-plots were drawn using the area measurements obtained from equation 5.7.

#### 6.3.4.3 Indices of peak vasodilatation (FMD and time to peak)

Similar to the ultrasound approach for determining the peak dilatation, a curve was fitted into the post deflation MR data using the 8 parameter flexible logistic function called FlexParamCurve (version 1.5-3) algorithm in the R statistics software (Oswald, 2015) described previously.

The maximal area was defined as the maximal y-value of the fitted curve as shown in Figure 6-6 and the corresponding x-value was the time to peak (TTP). The FMD was determined as the maximum percentage change in arterial cross-sectional area (Lee et al., 2007). The total dilatatory response of the vessel was calculated by integrating the area under the curve.

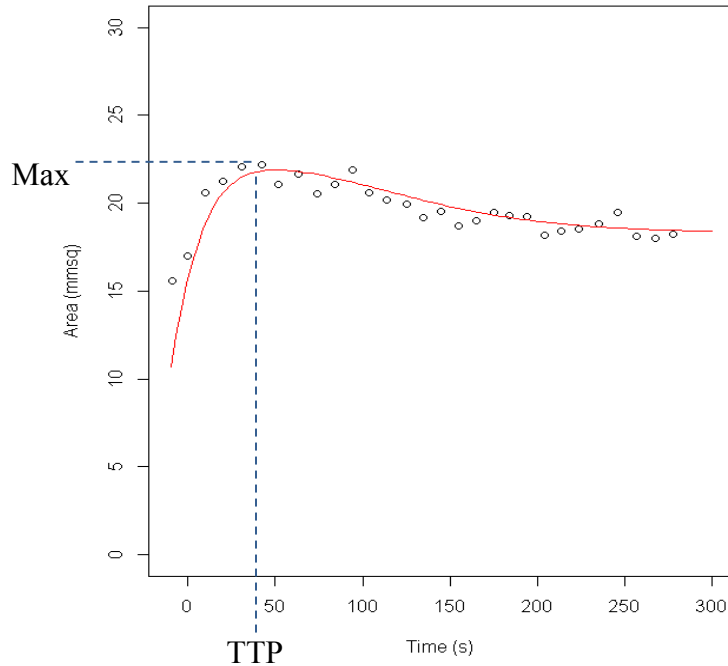


**Figure 6-6. A fitted curve (red) in the post cuff deflation data of a volunteer.** The curve was obtained with the FlexParamCurve algorithm in R. The maximal dilatation (Max) is the maximal y-value of the fitted curve while the time to peak (TTP) is the corresponding x-value.

#### 6.3.4.4 Reactive hyperemia

Reactive hyperemia was qualitatively graded as poor or adequate using the maximum IntSI to baseline IntSI ratio. Those in which the maximum /baseline IntSI ratio was 1.2 or less were classified as demonstrating poor reactive hyperaemic response, while those in which the ratio was greater than 1.2 were classified as having adequate reactive hyperaemic response.

#### 6.3.5 Statistical analysis

The results were expressed as the mean  $\pm$  standard deviation. The Pearson correlation coefficient and intraclass correlation coefficient were used to test for agreement between brachial ultrasound FMD and popliteal ultrasound FMD, bearing in mind that the brachial artery might have a larger FMD than the popliteal artery due to the relationship between vessel size and FMD (Charakida et al., 2010). Bland Altman's plots were used to determine the mean difference and limits of agreement between brachial ultrasound FMD, popliteal ultrasound FMD and popliteal MR-FMD. The limits of agreement were two standard deviations from the mean difference (Bland & Altman, 1986).

The within subject coefficient of variation ( $CV_w$ ), intraclass correlation coefficient (ICC) and the coefficient of repeatability (CR) on Bland Altman plots were used to assess the test–retest reliability of the brachial US-FMD, popliteal US-FMD and popliteal MRI-FMD. The minimum sample size required for test-retest repeatability of FMD was calculated as sixteen. Details of how this value was arrived at are also in the supplementary methods. The technical error of measurement (TEM) was used to quantify the measurement error (Lewis, 1999; Charakida et al., 2010). Details of the formulas used for the  $CV_w$  and TEM are in the supplementary methods. The CR represents the limits of agreement and it was twice the standard deviation of the mean difference (Bland & Altman, 1986; Vaz et al., 2013). The ICC was calculated using the R statistics software. The Pearson’s correlation coefficient was used to test for correlation between the indices of peak vasodilatation (FMD and TTP) and various parameters such as height, BMI, pulse rate, baseline luminal area etc.

A two-one-sided t-test (TOST) using the function `rTOST` in the `equivalence` package in R (Robinson, 2016) was used to test for non-inferiority between the  $CV_w$  of the FMD techniques. The null hypothesis was that the  $CV_w$  of popliteal MR-FMD is inferior to that of brachial US-FMD while the alternative hypothesis was that there is no significant difference between their  $CV_w$ . The margin of similarity was the confidence interval (CI) of CV for the test retest data of brachial US-FMD. Reactive hyperemia was qualitatively graded as using a fold change in IntSI from baseline to the maximal value during FMD. Those in which the fold change in IntSI was 1.2 or less were classified as demonstrating poor reactive hyperaemic response, while those in which the fold change was greater were classified as having adequate reactive hyperaemic response. The data was analyzed using the R project for statistical computing (version 3.1.3), which is a freely available, open-source statistics software (Chambers, 2009).

## 6.4 Results

### 6.4.1 Imaging and post processing duration

The period from which the patient was positioned on the couch to obtaining the baseline scans was longer with ultrasound (3-12 minutes for ultrasound versus 4-5 minutes for MRI). However, data acquisition was approximately 11 minutes for both techniques, comprising of 1 minute or less for baseline data acquisition, 5 minutes of cuff inflation and 5 minutes of data additional data collection post-cuff deflation. Therefore, US-FMD required 14 – 23 minutes while MRI-FMD was completed in 15-16 minutes. Post processing for each US-FMD study lasted  $23.1 \pm 2.2$  min, while the IntSI MRI-FMD technique required  $11.3 \pm 1.6$  min.

### 6.4.2 Characteristics of the volunteers

Table 1 shows the general characteristics of the volunteers. Nineteen young and healthy volunteers were scanned out of which eleven were male and eight were female. The average age for the study population was  $25.8 \pm 8.3$  years. The overall mean heart rate was  $59.7 \pm 7.0$  beats/min. The mean BMI for the males was  $25.7 \pm 4.2 \text{ kg/m}^2$ , which is considered overweight. The females, on the other hand, had a mean BMI of  $22.3 \pm 2.0 \text{ kg/m}^2$ , which is considered healthy. Both groups had a low mean blood pressure with an overall mean blood pressure of  $110.0 \pm 8.2$  mmHg.

**Table 6-1. General characteristics of the study population.**

	Male	Female	All
Sex	11	8	19
Age (years)	$24.4 \pm 8.6$	$27.4 \pm 8.1$	$25.8 \pm 8.3$
Height (cm)	$179.6 \pm 10.5$	$170.4 \pm 8.8$	$175.2 \pm 10.5$
Weight (kg)	$82.4 \pm 10.3$	$65.3 \pm 11.4$	$74.3 \pm 13.7$
BMI ( $\text{kg/m}^2$ )	$25.7 \pm 4.2$	$22.3 \pm 2.0$	$24.1 \pm 3.7$
Systolic blood pressure (mmHg)	$113.6 \pm 8.1$	$105.0 \pm 5.4$	$110.0 \pm 8.2$
Diastolic blood pressure (mmHg)	$72.9 \pm 9.2$	$63.8 \pm 7.4$	$69.1 \pm 9.5$
Heart rate (beats/min)	$58.5 \pm 8.0$	$61.1 \pm 5.8$	$59.7 \pm 7.0$

### 6.4.3 Agreement between brachial US-FMD and popliteal US-FMD

The overall mean baseline area of the brachial artery was  $10.73 \pm 3.60 \text{ mm}^2$ , and while the overall mean brachial FMD was  $16.59 \pm 5.31\%$  (Table 6-3 in the supplementary results). The popliteal artery, on the other hand, had an overall mean baseline area of  $24.51 \pm 5.70 \text{ mm}^2$  and an overall mean FMD of  $10.93 \pm 4.53 \%$  (Table 6-4 in the supplementary results).

There was moderate agreement between brachial FMD and popliteal FMD with a Pearson's correlation coefficient of 0.59 (Figure 5-6a). The ICC was 0.31 (0.09-0.58) with a mean difference of  $5.66 \pm 4.54\%$  (Figure 5-6b).

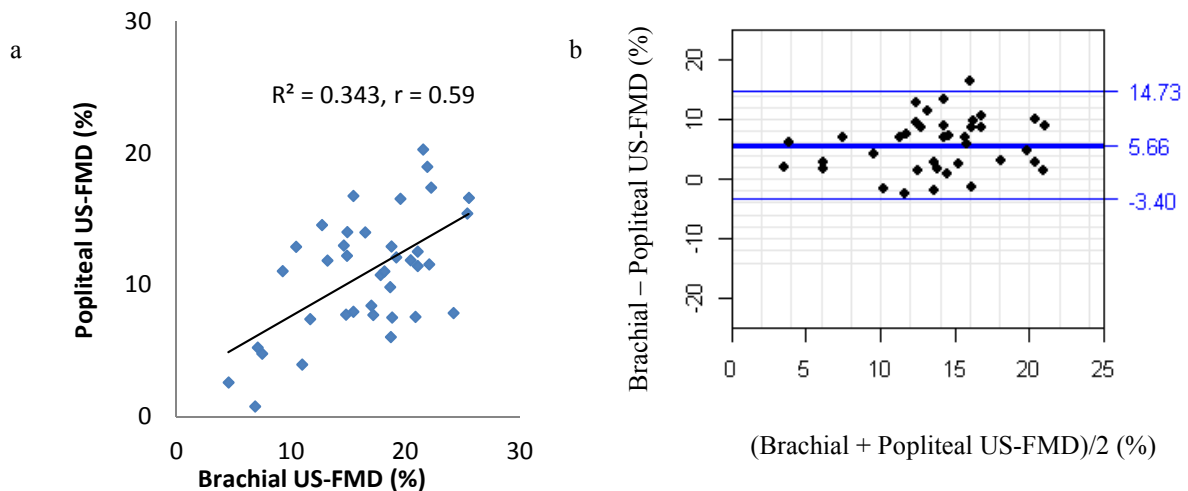


**Figure 6-7. A comparison between brachial US-FMD and popliteal US-FMD.** (a) Scatter plot for US-FMD measurements in the brachial and popliteal artery respectively. (b) Bland Altman plot of brachial US-FMD versus popliteal US-FMD. FMD was calculated as a percent change in the luminal area. The two blue horizontal lines in this figure and subsequent ones represent the limits of agreement and they are two standard deviations from the mean difference.

## 6.4.4 Popliteal Ultrasound FMD study

### 6.4.4.1 Repeatability of the popliteal US baseline area measurements

The popliteal artery had an overall mean baseline area of  $24.51 \pm 5.70 \text{ mm}^2$ . There was agreement between the test and retest baseline ultrasound measurements of the popliteal area (ICC = 0.92, [0.80-0.97]), ( $r = 0.93$ ), with the trend line lying on the line of equality (Figure 6-8a). The test-retest baseline area measurements for the popliteal artery had a  $CV_w$  of 5%, the TEM was  $1.65 \text{ mm}^2$ , while the CR was  $4.59 \text{ mm}^2$  as shown on the Bland Altman plot (Figure 6-8b).

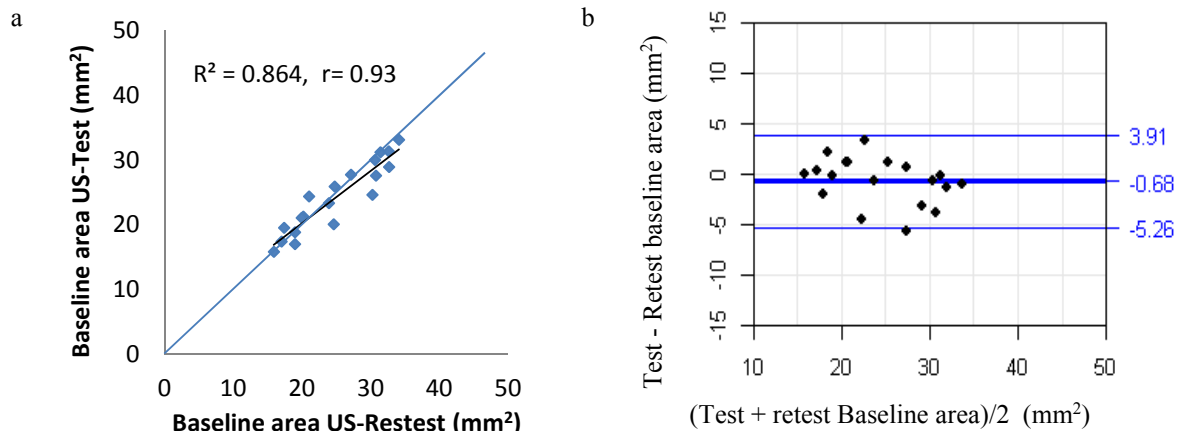


**Figure 6-8. A comparison between test and retest measurements of the baseline popliteal area using ultrasonography.** (a) Scatter plot with a line of equality, for test-retest repeatability of US-based measurements of the baseline area of the popliteal artery. (b) Bland Altman's plot for the test-retest repeatability of US-based measurements of the baseline area of the popliteal artery.

### 6.4.4.2 Repeatability of the popliteal US-FMD measurements

There was agreement between test-retest FMD measurements of the popliteal area (ICC = 0.62, [0.24-0.83]), ( $r = 0.61$ ), (Figure 6-9a). The test-retest measurements for popliteal US-FMD had a  $CV_w$  of 18%. The TEM was 2.83%, while the CR was 8.16% as shown on the Bland Altman plot (Figure 6-9b).

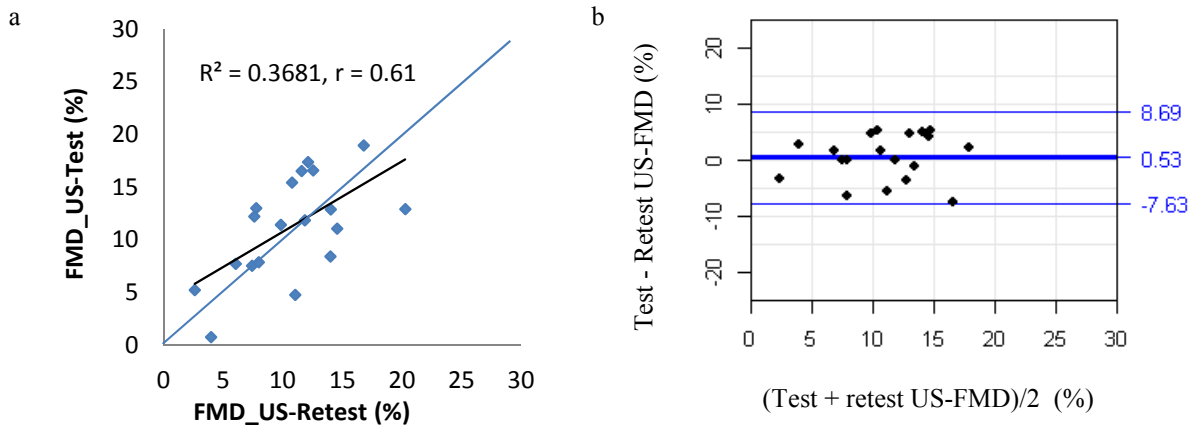


**Figure 6-9. A comparison between test and retest measurements of popliteal FMD using ultrasonography.** (a) Scatter plot with a line of equality, for test-retest repeatability of popliteal US-FMD. (b) Bland Altman's plot for the test-retest repeatability of popliteal US-FMD. FMD was calculated as a percent change in the luminal area.



## 6.4.5 Popliteal MRI-FMD study

### 6.4.5.1 Repeatability of popliteal MRI-based baseline area measurements

The overall mean value for MRI-based popliteal baseline areas measurements was  $29.26 \pm 6.65$  mm<sup>2</sup>. There was agreement between the test-retest baseline MRI-based measurements of the popliteal area (ICC = 0.91 [0.90-0.98]), ( $r = 0.96$ ), with the trend line lying on the line of equality (Figure 6-10a). The CV<sub>w</sub> was 3%, the TEM was 1.32 mm<sup>2</sup>, while the CR was 3.74 mm<sup>2</sup> as shown on the Bland Altman plot (Figure 6-10b).

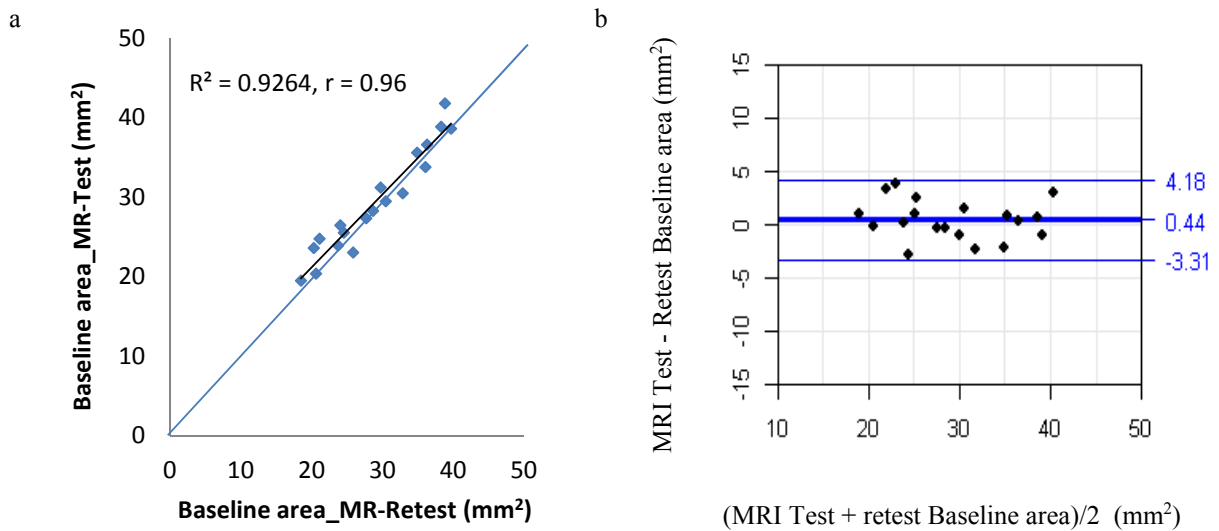


**Figure 6-10. A comparison between test and retest measurements of the baseline popliteal area using MRI.** (a) Scatter plot with a line of equality, for test-retest repeatability of popliteal baseline area measurements obtained with MRI. (b) Bland Altman's plot for the test-retest repeatability of popliteal baseline area obtained with MRI.

### 6.4.5.2 Repeatability of the popliteal MRI-FMD measurements

The overall mean MRIFMD was  $15.55 \pm 7.47\%$ . There was agreement between test-retest FMD measurements of the popliteal area (ICC = 0.72, [0.43-0.89]), ( $r = 0.72$ ), (Figure 6-11a). The test-retest FMD measurements had a  $CV_w$  of 17%, the TEM was 3.78%, while the CR was 10.99% as shown on the Bland Altman plot (Figure 6-1b).

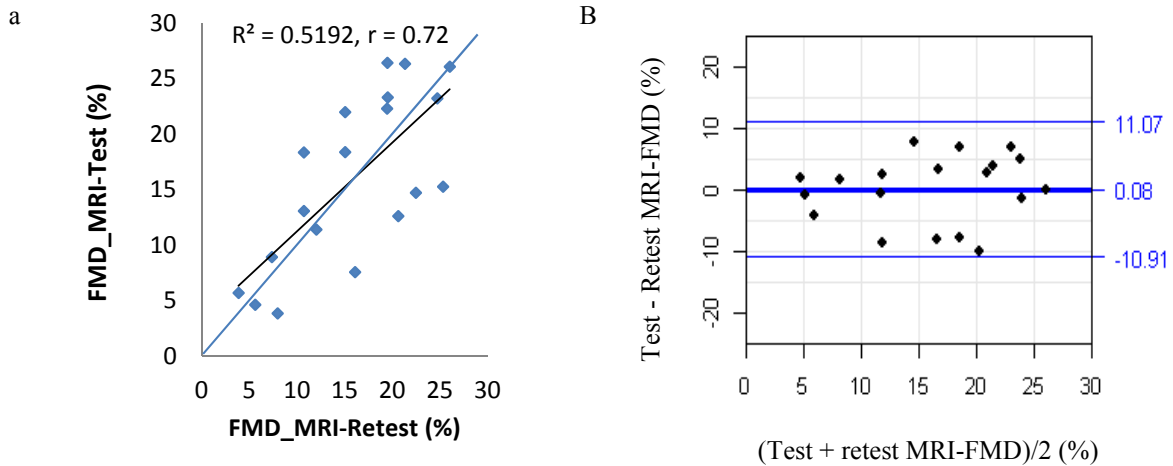


**Figure 6-11. A comparison between test and retest measurements of popliteal FMD using MRI.** (a) Scatter plot with a line of equality, for test-retest repeatability of popliteal MRI-FMD. (b) Bland Altman's plot for the test-retest repeatability of popliteal MRI-FMD. FMD was calculated as a percent change in the luminal area.

## 6.4.6 Agreement between the ultrasound and MRI based measurements

### 6.4.6.1 Popliteal US baseline area versus popliteal MRI baseline area measurements

There was agreement between baseline area measurements obtained with US and MRI. (ICC = 0.75, [0.59-0.88]). However, the MRI measurements were greater than US measurements resulting in a shift of the trend line towards the left of the line of equality (Figure 6-12a). The mean difference was  $4.75 \pm 2.60\text{mm}^2$  (Figure 6-12b), which is 19% increase relative to the US baseline area.

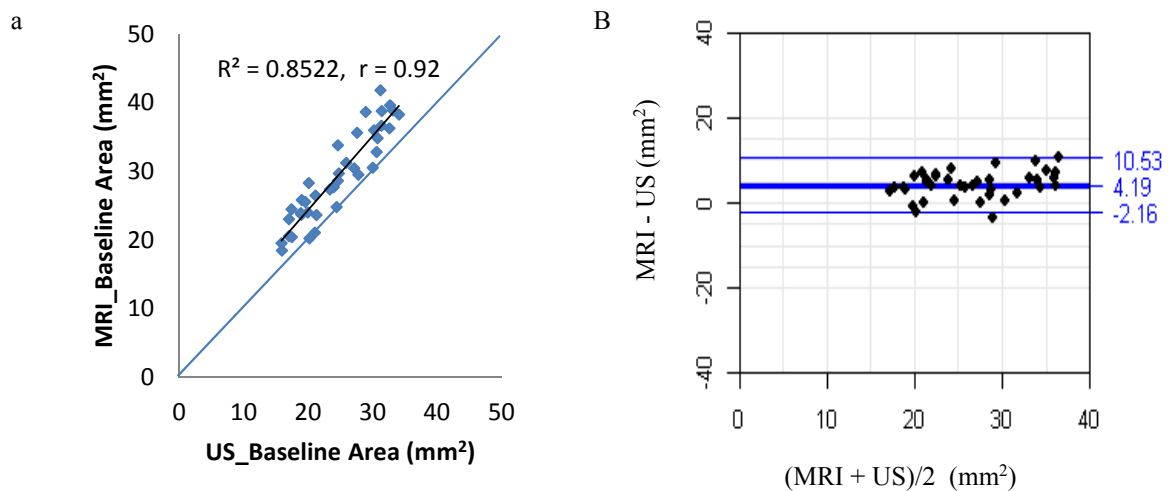


**Figure 6-12. A comparison between popliteal FMD baseline area measurements using US versus MRI in 19 subjects.** Each subject was scanned twice. (a) Scatter plot with a line of equality, for popliteal baseline area measurements using US versus MRI. (b) Bland Altman's plot for the difference between baseline areas measurements via US versus MRI.

### 6.4.6.2 Popliteal US-FMD versus popliteal MRI-FMD

There was agreement between popliteal FMD measurements obtained with both ultrasonography and MRI (ICC=0.61, [0.24-0.83]). However, the MRI-FMD values were higher than US-FMD with a bias of 5.07% (Figure 6-13a). The coefficient of variability of the popliteal MRI-FMD was comparable with both brachial ultrasound and popliteal ultrasound FMD (All were within the range of 23 - 26%) (Table 6-2). There was no significant difference in their ICC since there was an overlap in the confidence intervals (Table 6-2).

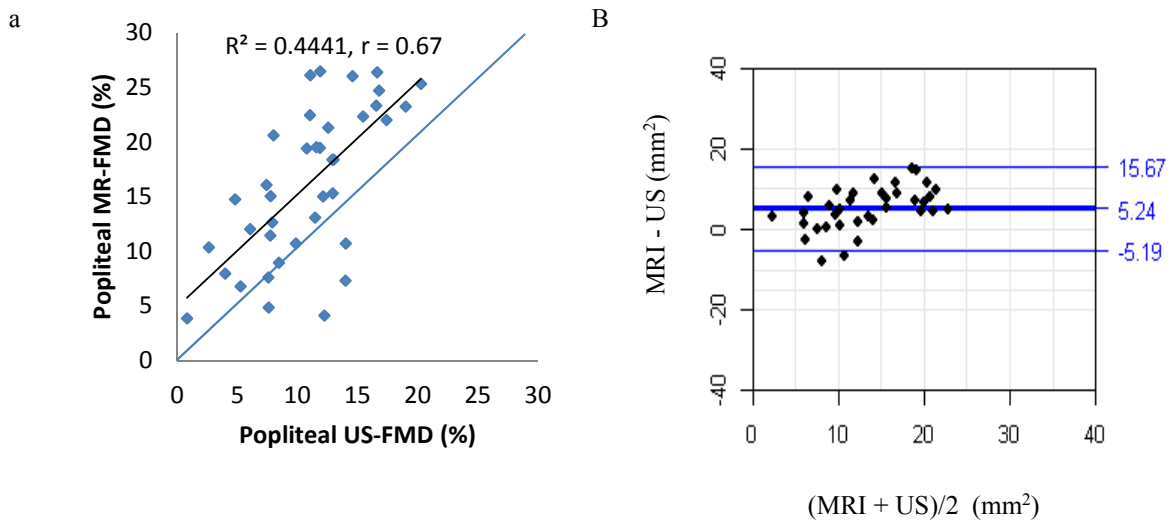


**Figure 6-13. A comparison between popliteal US-FMD and popliteal MRI-FMD in 19 subjects.** Each subject was scanned twice. (a) Scatter plot with a line of equality, for popliteal FMD using MRI versus ultrasound. (b) Bland Altman's plot for the difference between FMD measurements via ultrasound and MRI. FMD was calculated as a percent change in the luminal area.

### 6.4.6.3 Brachial US-FMD versus popliteal MRI-FMD

There was fair agreement between brachial US-FMD and popliteal MRI-FMD ( $r = 0.33$ ), (Figure 6-14a). The mean difference  $\pm$  CR between brachial US-FMD and popliteal MRI-FMD was  $0.42 \pm 14.50 \text{ mm}^2$  (Figure 6-14b).

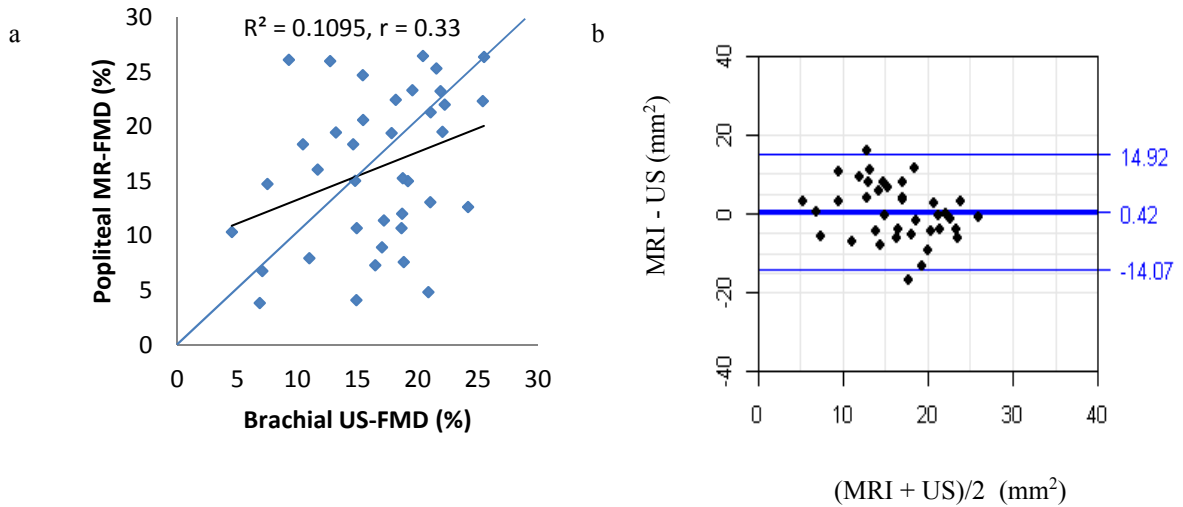


**Figure 6-14. A comparison between brachial US-FMD and popliteal MRI-FMD in 19 subjects.** Each subject was scanned twice. (a) Scatter plot with a line of equality, for brachial US-FMD versus popliteal MRI-FMD. (b) Bland Altman's plot for the difference between FMD measurements via brachial ultrasound and popliteal MRI. FMD was calculated as a percent change in the luminal area.

### 6.4.7 Variability of the ultrasound and MRI based measurements

There was an overlap in the confidence intervals of the  $CV_w$  for the three FMD techniques and also an overlap in the confidence intervals of their ICCs (Table 6-2). The  $CV_w$  of popliteal MRI-FMD was non-inferior to that of brachial US-FMD and popliteal US-FMD (Table 6-3). Non-inferiority testing was done using the confidence interval of  $CV_w$  for brachial US-FMD as the margin of similarity.

**Table 6-2. Summary of the test-retest repeatability of brachial US-FMD, popliteal US-FMD and popliteal MRI-FMD**

% change in area	Overall Mean $\pm$ SD (%)	Mean diff. $\pm$ CR (%)	$CV_w$ and CI	TEM (%)	ICC and CI
Brachial US-FMD	16.59 $\pm$ 5.31	0.76 $\pm$ 10.80	0.23 (0.21 to 0.25)	3.76	0.51 [0.09-0.77]
Popliteal US-FMD	10.93 $\pm$ 4.53	0.53 $\pm$ 8.16	0.26 (0.24 to 0.28)	2.83	0.62 [0.24-0.83]
Popliteal MRI-FMD	16.0 $\pm$ 7.20	0.08 $\pm$ 10.99	0.24 (0.22 to 0.26)	3.78	0.72 [0.43-0.89]

**Table 6-3. Testing for non-inferiority between the intrasubject coefficient of variability ( $CV_w$ ) of the FMD techniques**

	Mean difference between the $CV_w$ and the CI (mm <sup>2</sup> )	P value
Brachial US-FMD vs Popliteal US-FMD	-0.0002 (-0.12 to 0.12)	3.00e-4
Brachial US-FMD vs Popliteal MRI-FMD	0.04 (-0.05 to 0.14)	2.43e-4

CI = Confidence interval

### 6.4.8 Qualitative assessment of reactive hyperemia with the IntSI technique

The adequate hyperaemic response (HR) group had higher hyperemic values during brachial US-FMD than the poor RH group ( $5.14 \pm 2.56$  versus  $4.01 \pm 2.52$ ). Similar findings were observed with popliteal US-FMD ( $3.56 \pm 1.45$  versus  $2.91 \pm 0.94$ ). However, the difference was not statistically significant at  $p < 0.05$  in both cases.

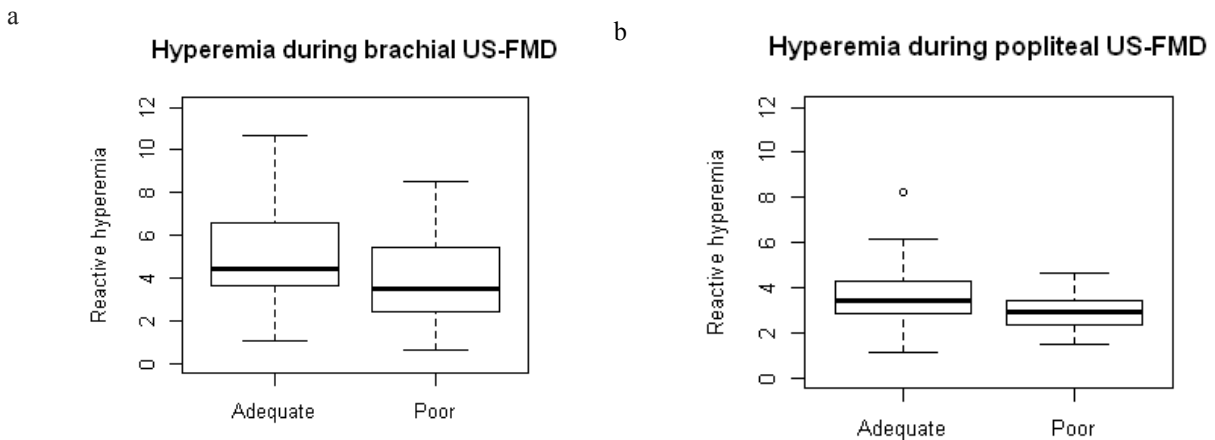


**Figure 6-15. Box plots showing the ultrasound based hyperemic response in the two groups qualitatively classified with the IntSI technique as having poor or adequate hyperemic response respectively. (a) shows the hyperemic response during brachial US-FMD while (b) shows the hyperemic response during popliteal US-FMD**

### 6.4.9 Box plot for the TTP using each FMD technique

There was no significant difference between the TTP using the three FMD techniques at  $p < 0.05$ . In some cases, brachial US-FMD, popliteal US-FMD and popliteal MRI-FMD had TTP as low as 31.42 seconds, 30.66 seconds and 25.96 seconds respectively.

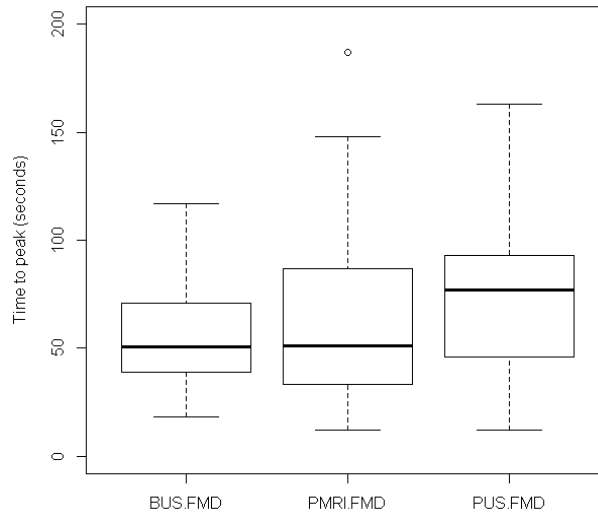


Figure 6-16. Box plots showing the TTP using the three FMD techniques. BUS.FMD = Brachial US-FMD, PUS.FMD = Popliteal US-FMD, PMRI-FMD = Popliteal MRI-FMD



#### 6.4.10 Indices of peak vasodilatation and various parameters.

FMD and time to peak (TTP) were the indices of peak vasodilatation that were examined. The TTP for brachial US-FMD was  $56.21 \pm 24.79$  seconds. The TTP for popliteal FMD were  $74.32 \pm 43.66$  seconds and  $72.97 \pm 47.01$  seconds using the ultrasonography and the MRI based IntSI technique respectively. The indices of peak vasodilatation measured in the popliteal artery were compared with various parameters. There was moderate correlation between MRI based reactive hyperemia and MRI-FMD ( $r = 0.54$ ). However, ultrasonography did not show a similar result ( $r = 0.18$ ), (Table 6-3). There was moderate correlation between diastolic BP and US-FMD ( $r = 0.51$ ), however, there was weak correlation between diastolic BP and MRI-FMD ( $r = 0.38$ ), (Table 6-3). Other variables such as age, BMI and pulse rate etc correlated weakly or very weakly with FMD and TTP, using both US and MRI

**Table 6-4. Summary of the association between FMD and TTP in the popliteal artery with general characteristics of the volunteers.**

General Characteristics	FMD				TTP			
	US		MRI		US		MRI	
	R <sup>2</sup>	r	R <sup>2</sup>	r	R <sup>2</sup>	R	R <sup>2</sup>	R
Age	0.004	0.06	0.024	0.05	0.004	0.07	0.066	0.26
BMI	0.006	0.08	0.045	0.21	0.15	0.39	0.051	0.23
Pulse rate	0.017	0.13	0.011	0.11	0.0004	0.02	0.0467	0.21
Systolic blood pressure	0.14	0.38	0.09	0.30	0.06	0.24	0.03	0.06
Diastolic blood pressure	0.26	0.51	0.14	0.38	0.06	0.24	0.03	0.18
Baseline luminal area	0.10	0.31	0.004	0.06	0.03	0.18	0.001	0.02
TTP	0.0001	0.01	0.15	0.39				

R<sup>2</sup> is the coefficient of determination, r is the Pearson's correlation coefficient

## 6.5 Discussion

The repeatability of FMD may be affected by three sources of error. The imaging technology, the patient's physiology and the post processing technique may contribute to poor repeatability of FMD studies. US-FMD is technically challenging and ultrasonography in general, is operator dependent (Corretti et al., 2002). Although MRI does not have these limitations, conventional MRI-FMD techniques are limited by a tradeoff between spatial and temporal resolution. The IntSI technique has advantages over previous MRI methods of measuring FMD. It offers a higher temporal sampling frequency which improves the chances of detecting the transitory peak dilatation during FMD. Area measurement with the IntSI technique requires a scan time of 6-9 seconds whereas measurements by pixel count of high resolution images using a fast sequence such as the SSFP sequence and a 3T scanner requires up to 15 seconds (Oliver et al., 2012). Another advantage of the IntSI technique is its ability to qualitatively demonstrate reactive hyperemia. Phase contrast imaging is capable of demonstrating hyperemia but it has a limitation of low temporal resolution (Pai, 2007).

The IntSI technique for MRI-FMD can be incorporated into a comprehensive protocol for MRI based evaluation of vascular health because if a patient is already positioned on the examination table for an MRI, including an FMD study in the examination protocol will only add a few more minutes to the total examination time. This is because the imaging plane for MR imaging is easy to define and maintain. In the present study, it took 4-5 minutes to position the patient, fix the imaging plane and obtain baseline MR images. Then distal occlusion was applied for 5 minutes with imaging continuing for another 5 minutes post-occlusion. Therefore an MRI-FMD study will only add 15 minutes to the total examination time. This is unlike ultrasound where technical challenges may increase the time required to define the imaging plane, stabilize the transducer and obtain the baseline images. It took 3 to 12 minutes to set up the ultrasound study and obtain baseline images in this present study. Other authors reported that it took them 1 to 10 minutes to obtain high quality baseline scans (Raitakari & Celermajer, 2000).

Post processing for MRI-FMD using the IntSI technique was shorter than US-FMD ( $11.3 \pm 1.6$  min versus  $23.1 \pm 2.2$  min). Automated post-processing methods for US-FMD such as the Brachial analyzer and FMD Studio have been designed to reduce the analysis time (Faita *et al.*, 2011*b*). Authors have reported a mean analysis time  $21 \pm 1$  min with Brachial analyzer and  $14 \pm$

1 min with FMD Studio (Faita *et al.*, 2011b). In view of the advantages of the IntSI technique for MRI-FMD over the more established ultrasound approach, a test-retest repeatability study of the IntSI technique was compared with that of ultrasound-FMD.

### **6.5.1 Agreement between brachial ultrasound FMD and popliteal ultrasound FMD**

Brachial ultrasound FMD is the gold standard for assessing endothelial function (Deanfield *et al.*, 2007; Stoner *et al.*, 2013). However, the popliteal artery was chosen to test the IntSI technique, partly due to its anatomical advantage. It lies close to the center of the magnet and will produce more homogenous MR signals than the brachial artery which lies more peripherally (Brix *et al.*, 2008). The moderate agreement between brachial US-FMD and popliteal US-FMD in this chapter shows that popliteal FMD can also be used as a marker of endothelial function. Although brachial FMD was larger in magnitude than popliteal FMD, this may be explained by the observation that smaller arteries have higher wall shear stress, which triggers a higher FMD response in smaller arteries (Celermajer *et al.*, 1992).

### **6.5.2 Agreement between popliteal US-FMD and popliteal MRI-FMD**

#### **6.5.2.1 Popliteal baseline area (ultrasound versus MRI)**

The smaller popliteal baseline area measurements recorded with ultrasonography when compared with MRI (Figure 6-12), may be because unlike MRI that measures the luminal area from cross-sectional images, the ultrasound data is obtained from longitudinal images due to the poor lateral resolution of ultrasound. The luminal area is then calculated from the diameter based on the assumption that the lumen has a circular cross section. However, if the lumen is oval then the calculated area will be inaccurate. A study comparing brachial intravascular ultrasound measurements with extravascular ultrasound found that intravascular measurements were larger and the vessel was oval (Ong *et al.*, 2002). Pressure from the ultrasound transducer may also compress an artery making the lumen oval (Triboulet *et al.*, 2006; Cary *et al.*, 2014). Therefore when the ultrasound area is derived from the diameter by assuming that the area is circular, the calculated area will be less than it should be. However, the popliteal artery lies deep within the popliteal fossa, therefore, it is possible that this may not be affected by the US transducer pressure. Other authors observed larger brachial luminal area measurements with ultrasound

compared to MRI (Sorensen et al., 2002; Leeson et al., 2006) and they ascribed it to their ultrasound measurement being from the intima media boundary while MRI measured the from the lumen intima interface. In this present study, ultrasound measurements were from the lumen-intima interface.

#### 6.5.2.2 Popliteal FMD (US-FMD versus MRI-FMD)

An acceptable reproducibility for FMD studies is a mean difference of 2% to 3% (Corretti et al., 2002). Both popliteal US-FMD and popliteal MRI-FMD in my study had mean differences below this range. Therefore, either technique is acceptable as a means of assessing FMD. However, MRI detected a larger FMD response than ultrasound. The mean difference between popliteal US-FMD and MRI-FMD was 5.07%. This differs from a similar study on the brachial artery in which the mean difference between US-FMD and MRI-FMD was 0.14% (Leeson et al., 2006). The reason why our US and MRI popliteal FMD studies showed less agreement compared to that by Leeson et al (2006) may be because they measured FMD at 60 second which might not be the point of maximal dilatation as our MRI study had time-to-peak values as early as 11s. Another reason for the difference is that the maximal dilatation may not be detected by ultrasonography if the time to peak is short, this is because the immediate post-cuff deflation period is sometimes associated with a slight shift in the ultrasound imaging plane, despite the use of a probe holder. Therefore, the peak dilatation might not be detected.

A third reason may due to the ability of MRI to demonstrate multi-directional vessel dilatation unlike longitudinal imaging with ultrasound which can only capture dilatation in the longitudinal plane. A final reason may be because the MRI and US studies were performed on separate days. Although this may not be a good enough reason since Leeson et al (2006) also performed the test-retest repeatability studies for ultrasound and MRI respectively, on separate days. In this present study, efforts were made to make the dates for the tests as close together as possible. The patients were scanned at the same period in the day for both scans to avoid the diurnal variations in FMD and female volunteers were scanned during the same phase of their menstrual cycle. However, diet and exercise were not strictly controlled over the intervening days.

### **6.5.3 Agreement between brachial US-FMD and popliteal MRI FMD**

#### **6.5.3.1 Popliteal FMD (US-FMD versus MRI-FMD)**

It was observed that the mean difference between brachial US-FMD and popliteal MRI-FMD was smaller than that between popliteal US-FMD and popliteal MRI-FMD. This may be attributed to brachial FMD having a larger FMD response than popliteal FMD. The large difference between popliteal US-FMD and popliteal MRI-FMD may be ascribed to the inability to capture multi-directional increase in the arterial lumen on longitudinal ultrasound images. However the larger FMD response that usually occurs in the brachial artery results in a large difference between brachial US-FMD and popliteal US-FMD, but a smaller difference between brachial US-FMD and popliteal MR-FMD

#### **6.5.3.2 Repeatability of Popliteal MRI-FMD versus brachial US-FMD**

The focus of my research was to demonstrate that popliteal MRI-FMD was more repeatable than brachial US-FMD. Although I was not able to show that the within subject coefficient of variability of the popliteal MRI-FMD technique was better than either the brachial ultrasound or popliteal ultrasound US-FMD techniques, it was non-inferior to both US-FMD techniques. The within subject coefficients of variability for the ultrasound and MRI studies were greater than the values of 7.6% to 11.9% reported for same day brachial ultrasound repeatability (Ghiadoni et al., 2012) and the value of 9-10% for different day brachial ultrasound repeatability (Donald et al., 2008). The values were closer to that of 23% observed in a previous brachial ultrasound repeatability study (Sorensen et al., 2002). Despite not being able to demonstrate the superiority of popliteal MRI-FMD over brachial US-FMD, in view of the technical and anatomical advantages of popliteal FMD, the approach should still be considered as an alternative means of measuring macrovascular endothelial function since it is non-inferior to brachial US-FMD.

### **6.5.4 Qualitative assessment of reactive hyperemia with the IntSI technique**

FMD depends on macrovascular shear stress and reactive hyperemia is not a good estimate of shear stress. This is because the reactive hyperemia increases as the baseline diameter increases while the shear stress decreases as the baseline diameter increases (Pyke & Tschakovsky, 2005). However, it is still useful to quantify reactive hyperemia in order to assess macrovascular function

and to determine if a poor FMD response is due to an underlying microvascular disease. Although the group classified as having a poor hyperemic response using the IntSI technique showed lower hyperemic response during brachial US-FMD and popliteal US-FMD, the difference was not statistically significant in both cases. This may be because the study comprised of healthy volunteers. It is possible that the difference between the groups may be statistically significant in those with or at risk for endothelial dysfunction.

#### **6.5.5 Adequacy of the sampling interval of the MRI-FMD using the IntSI technique**

The mean TTP had lower standard deviations of 31.42 seconds, 30.66 seconds and 25.96 seconds using brachial US-FMD, popliteal US-FMD and popliteal MRI-FMD respectively (Figure 6.16). Therefore, a sampling interval of 6-9 seconds with the MRI IntSI technique is good for FMD, because according to the Nyquist sampling theorem (Luke, 1999), this sampling interval can accommodate TTP as low as 20 seconds.

#### **6.5.6 Correlation between indices of peak vasodilatation and various parameters**

This study was not primarily designed to assess the effects of various general characteristics of the volunteers on the indices of vasodilatation (FMD and the time to peak). However, preliminary efforts were made to examine if there was any correlation between the volunteer characteristics and these indices of vasodilatation. The moderate correlation between diastolic BP and popliteal US-FMD was not found with popliteal MR-FMD. The ultrasound finding agrees with a previous brachial US study in which lower FMD was associated with lower diastolic BP during sub-maximal exercise (Lambiase et al., 2014). Other variables such as age, BMI and pulse rate correlated weakly or very weakly with FMD and TTP, using both ultrasonography and MRI. A larger and more diverse sample is required to adequately assess effects of the different variables on MRI-FMD using the IntSI approach.

#### **6.5.7 Study limitations**

Application of the IntSI technique for reliable area measurements during an MRI-FMD study has various limitations. Some of the limitations are due to assumptions made while deriving the IntSI equation. These assumptions have been discussed in detail in Chapter 3. The technique assumes

that the TOF effect increased with the blood velocity and that the threshold velocity at which this linear relationship stops is neither attained nor exceeded. In hyperdynamic states or possible situations where the imaged segment of the conduit artery is narrow with a resultant increase in the maximal velocity beyond the threshold, the IntSI will no longer give a reliable estimate of the luminal area. In those with small arterial lumina, if the pixel-to-luminal area is greater than 0.1, then it will be wrong to assume that the mean velocity within the most central pixel ( $V_p$ ) can be used as an approximation for  $V_{max}$ .

Another limitation is that the popliteal artery has a blunted parabolic velocity profile, which does not conform to the IntSI technique's assumption that the velocity has a fully formed parabolic profile in which the mean velocity is half of the maximal velocity. The IntSI equation was modified for the popliteal artery using a value 0.6 instead of 0.5 for the ratio of  $V_{mean}$  to  $V_{max}$  in order to accommodate the blunted parabolic flow profile of the artery. However, in situations where the  $V_{mean}$  to  $V_{max}$  ratio differs from 0.6, the modified equation becomes an unreliable means of calculating the luminal area. The correction factor for suppressed retrograde flow that was introduced into the modified IntSI equation for popliteal imaging may lead to underestimation of area measurements during reactive hyperemia and subsequently FMD underestimation. This is because retrograde flow is reduced or eliminated during hyperemia, unlike an unperturbed artery that has triphasic flow.

Other limitations to the applicability of the technique are that only 90° spoiled gradient RF pulses can be used for imaging and that k-space should be filled using a Cartesian trajectory. Failure to comply with these requirements will introduce error into the MRI-FMD study. When performing a repeatability study for MRI-FMD using the IntSI technique, if different segments of the artery are imaged during the test and re-test phases respectively, or if in one instance, the imaging plane is not positioned perpendicular to the long axis of the vessel, then error will be introduced with resultant poor repeatability of the technique.

A final limitation of this study is that an adaptive trigger delay was not used during MR imaging. With a diastolic trigger delay, imaging commences at a specific time from the onset of the R wave. An adaptive trigger delay technique may be useful in those with variable heart rate to ensure that imaging always commences at a specific point in the cardiac cycle (Roes et al.,

2008). It may also be helpful where systole is longer than the predetermined diastolic delay or in those with faster heart rate with R-R intervals that cannot accommodate the predetermined diastolic delay and image acquisition period (Fernandez et al., 2009).

### 6.5.8 Conclusion

IntSI approach for measuring the popliteal area provides a means of improving the sampling frequency during MRI-FMD. It offers a reliable method of measuring macrovascular endothelial dysfunction and qualifying macrovascular dependent reactive hyperemia. Although this study was not able to demonstrate popliteal MRI-FMD as superior to brachial US-FMD, it was non-inferior to brachial US-FMD.



## 6.6 Supplementary

### 6.6.1 Supplementary methods

#### 6.6.1.1 The technical error of the measurement (TEM)

The technical error of the measurement (TEM) was calculated using equation S6-1 (Lewis, 1999).

$$\text{TEM} = \sqrt{\frac{\sum_{i=1}^n (d_i^2)}{2n}} \quad (\text{S6-1})$$

where  $d_i$  is the difference between the paired FMD measurements obtained from the  $i$ th volunteer and  $n$  is the sample size.

#### 6.6.1.2 The within subject variability ( $S_w$ )

The within subject variability ( $S_w$ ) for the paired data was obtained by squaring the standard deviation of each paired difference ( $S_i^2$ ), finding the mean of the squared standard deviations and calculating the square root of this mean value (Rodbard, 1974; Bland, 2006).

$$S_w = \sqrt{\frac{\sum_{i=1}^n (S_i^2)}{n}} \quad (\text{S6-2})$$

#### 6.6.1.3 The within subject coefficient of variation ( $CV_w$ )

The within subject coefficient of variation ( $CV_w$ ) was calculated by dividing the within subject variability with the overall sample mean ( $\bar{x}$ ) and then by  $\sqrt{2}$  (Hopkins, 2000; Donald et al., 2006).

$$CV_w = \frac{S_w}{\bar{x}\sqrt{2}} \quad (\text{S6-3})$$

The confidence interval for the coefficient of variation was used as the equivalence margin for the non-inferiority test. They were obtained by calculating  $CV_w$  using the root mean square approach. In this approach, the root mean square of the mean difference of all paired data was divided by  $\sqrt{2}$  (Bland, 2006).

$$CV_w = \sqrt{\frac{\sum_{i=1}^n (D_i)^2}{2n}} \quad (\text{S6-4})$$

where  $D_i$  is the mean difference of the paired FMD measurements obtained from the  $i$ th volunteer and  $n$  is the sample size.

#### 6.6.1.4 Percentage change

Percentage change was calculated as a quotient of the test-retest difference in FMD ( $D$ ) and the overall sample mean ( $\bar{x}$ ) of the two FMD values.

$$PC = \frac{D}{\bar{x}} \quad (S6-5)$$

#### 6.6.1.5 The minimum sample size

The minimum sample size required for test-retest repeatability of FMD was calculated using equation 6.6 (van Belle, 2011).

$$n = \frac{16(CV)^2}{(PC)^2} \quad (S6-6)$$

where  $CV$  is the same day coefficient of variation for brachial US-FMD and  $PC$  is the test-retest percentage change in FMD.

For the sample size calculation, the values for the same day  $CV$ , difference in FMD and the arithmetic average of the two values were 10%, 0.97% and 9.79% respectively (Leeson et al., 2006). Therefore, the minimum sample size was calculated as 16.

A sample size of 18 was calculated as sufficient to test for inferiority using the `sampleN.noninf` function in R (Labes, 2016) assuming the  $CV$  is up to 0.20, at a target power of 0.8 and alpha at 0.1.

## 6.6.2 Supplementary results

**Table 6-5. Test-retest reliability results for brachial US-FMD**

Brachial artery	Test Mean (SD)	Retest Mean (SD)	Overall Mean (SD)	Mean diff. ± CR*	Coefficient of Variability(CV)	TEM
Baseline values						
Area (mm <sup>2</sup> )	10.81± 3.79	10.65 ±3.50	10.73 ±3.60	-0.15 ± 3.25	0.07	1.13
Diameter (mm)	3.65 ± 0.65	3.64 ±0.60	3.65 ± 0.62	-0.02 ± 0.57	0.04	0.20
Post hyperemic values						
Area (mm <sup>2</sup> )	12.56 ± 4.48	12.51 ±4.37	12.54 ± 4.36	-0.05 ± 3.77	0.07	1.30
Diameter (mm)	3.94 ± 0.71	3.94 ± 0.69	3.94 ± 0.69	-0.00 ± 0.61	0.04	0.21
FMD						
Δ Area (%)	16.21± 4.39	16.98 ±6.20	16.59 ± 5.31	0.76 ±10.80	0.16	3.76
Δ Diameter (%)	7.78 ± 2.05	8.12 ±2.88	7.95 ± 2.47	0.34 ± 5.01	0.15	1.74
Time to peak	56.42 ±21.61	56.01 ±28.21	56.21 ± 24.79	-0.42 ± 44.14	0.19	14.9

**Table 6-6. Test-retest reliability results for popliteal US-FMD**

Popliteal artery	Test Mean (SD)	Retest Mean (SD)	Overall Mean (SD)	Mean diff. ± CR*	Coefficient of Variability (CV)	TEM
Baseline values						
Area (mm <sup>2</sup> )	24.85 ± 6.14	24.17 ± 5.36	24.51± 5.70	-0.67 ± 4.58	0.05	1.65
Diameter (mm)	5.58 ±0.70	5.54 ± 0.65	5.56 ± 0.67	-0.05 ± 0.56	0.03	0.19
Post hyperemic values						
Area (mm <sup>2</sup> )	27.41 ± 6.62	27.06 ± 6.24	27.24 ± 6.35	-0.35 ± 5.3	0.05	1.84
Diameter (mm)	5.86 ± 0.73	5.83± 0.68	5.83± 0.69	-0.03 ± 0.59	0.02	0.20
FMD						
Δ Area (%)	10.66± 4.36	11.20± 4.80	10.93 ± 4.53	0.53 ± 8.16	0.18	2.83
Δ Diameter (%)	5.00 ± 2.01	5.42 ± 2.28	5.21 ± 2.13	0.42 ± 3.74	0.18	1.32
Time to peak	72.74 ±29.66	75.89 ±43.16	74.32 ±43.66	3.16 ± 189.79	0.29	30.98

**Table 6-7. Test-retest reliability results for popliteal MRI-FMD**

Popliteal artery	Test Mean (SD)	Retest Mean (SD)	Overall Mean (SD)	Mean diff. ± CR*	Coefficient of Variability (CV)	TEM
Baseline values						
Area (mm <sup>2</sup> )	29.05± 6.90	29.48 ± 6.57	29.26 ±6.65	0.44 ± 3.74	0.03	1.32
Diameter (mm)	6.04 ± 0.73	6.09 ± 0.68	6.07 ±0.69	0.05 ± 0.41	0.02	0.14
Post hyperemic values						
Area (mm <sup>2</sup> )	33.67 ± 8.23	34.10 ±7.41	33.89 ± 7.73	0.43 ± 4.77	0.03	1.67
Diameter (mm)	6.50±0.80	6.55 ± 0.71	6.53 ±0.75	0.05 ± 0.50	0.02	0.18
FMD						
Δ Area (%)	15.96 ±6.91	16.04 ±7.67	16.0 ±7.20	0.08 ± 10.99	0.17	3.78
Δ Diameter (%)	7.67±3.28	7.64±3.66	7.65 ± 3.43	0.46 ± 5.68	0.17	1.86
Time to peak	73.20± 35.61	72.74±57.21	72.97 ± 47.01	-0.46 ± 92.45	0.31	31.8

---

**Chapter 7    Concluding Summary, General  
Discussion and Future Directions**

---

## 7.1 Concluding Summary

### 7.1.1 Summary of the Literature Review

The literature review comprises of three sections that explored vascular biology, hemodynamics methods of evaluating vascular function and MRI physics. The first section reviewed vascular anatomy and physiology. It also focused on the pathophysiological processes that underlie vascular dysfunction in general and endothelial dysfunction in particular. In this section hemodynamic principles were considered. The second part considered various methods used to assess endothelial function such as plethysmography, peripheral arterial tonography and flow mediated dilatation and it also considered the limitations of each method. The third part explores the basic concepts in MR physics in order and possible methods of optimizing MRI-FMD. The IntSI technique for measuring area with MRI is based on concepts in hemodynamics and MRI physics, so it was useful to review the concepts in detail.

### 7.1.2 Summary of the Original Research

Ultrasound based flow mediated dilatation of the brachial artery is used to assess macrovascular endothelial function. However, the operator dependency of ultrasound makes US-FMD unsuitable for routine clinical applications or multi centre studies. MRI, on the other hand, is less operator dependent, but it is constrained by spatial and temporal resolution. High spatial resolution is needed for reliable area measurements and high temporal resolution is required in order not to miss the transient peak dilatation. This thesis involves designing a reliable MRI method of measuring the luminal area that affords a high sampling frequency during MRI-FMD studies and the technique was based on the integrated signal intensity (IntSI) of the luminal pixels. The IntSI technique provides an opportunity to reliably obtain rapid serial area measurements during an FMD study so that the peak dilatation can be detected.

The dissertation consists of three studies. In the first study (Chapter 3), the IntSI technique was derived using hemodynamic principles and the time of flight equation. As mentioned above, MR imaging is limited by a trade-off between spatial and temporal resolution. Therefore, the main objective of the thesis was to design a reliable MRI area measurement technique that does not require very high spatial resolution so that the temporal resolution can be increased when performing serial area measurements. The equation was based on certain assumptions. 1) The

TOF effect increases with the velocity up to a threshold velocity beyond which no further increase in the TOF effect occurs. 2) When the flip angle is  $90^\circ$ , spins in the slice will either be completely fresh spins or completely saturated spins. 3) When stationary fluid experiences  $90^\circ$  RF pulses and a Cartesian trajectory is used to fill k-space, that the image contrast will be based solely on the steady state signals. 4) The imaged arterial lumen has a cylindrical volume, with a circular cross-sectional area (A) and height of slice thickness (L). 5) The velocity has a fully formed parabolic profile in which the mean velocity is half of the maximal velocity. 6) The maximal velocity ( $V_{\max}$ ) is less than the threshold velocity. 7) The mean velocity within the most central pixel ( $V_p$ ) can be used as an approximation for  $V_{\max}$  provided the pixel-to-luminal area ratio is small.

The assumptions were tested using a flow phantom and it was found that the IntSI technique over-estimated the luminal area when the maximal tube velocity exceeded the threshold velocity. The areas measures were also overestimated when the velocity did not have a fully formed parabolic profile. When the pixel-to-luminal area ratio did not exceed 0.1, the difference in area measurement was at most 10%. The reliability of area measurements using the IntSI technique at a pixel area of  $1.4 \text{ mm}^2$  (Mean bias  $\pm$  CR:  $0.22 \pm 1.43 \text{ mm}^2$ , ICC: 0.998) was comparable to that obtained using pixel counting at  $0.4 \text{ mm}^2$  pixel area (Mean bias  $\pm$  CR:  $-0.07 \pm 1.12 \text{ mm}^2$ , ICC=0.998). Therefore provided the pixel-to-luminal area ratio is approximately 0.1, the velocity profile is parabolic and the threshold velocity is not exceeded, the IntSI technique can be used to obtain reliable area measurements.

In the second section of the thesis (chapter 4), spectral Doppler analysis of the popliteal artery was employed to assess if assumptions made while deriving the IntSI technique hold true in vivo. Spectral Doppler analysis was also used to determine a suitable data acquisition period within the cardiac cycle, such that the threshold velocity will not be exceeded and the pixel intensity at steady state ( $P_{SS}$ ) may be obtained. Imaging during diastole was considered since the velocities at diastole are less than those at systole and cardiac cycle based variations the luminal area are also less at diastole (Chuang et al., 2002). The popliteal artery was the vessel of choice due to its anatomical advantages. Spectral Doppler analysis showed that the popliteal artery had a blunted parabolic flow profile with a  $V_{\text{mean}}/V_{\text{max}}$  ratio of 0.6. The highest velocities at diastole occurred during hyperemia with a maximal  $TAV_{\text{max}}$  of 23.55 cm/s. In unperturbed arteries,  $TAV_{\text{max}}$  during

diastole was  $-1.07 \pm 1.05$  cm/s, which means that there is a little quantity of retrograde flow during diastole. Therefore, the IntSI technique may be applied for measuring the luminal area of the popliteal artery when data acquisition is done during diastole provided that: 1) the IntSI equation is modified using a value of 0.6 for the  $V_{\text{mean}}/V_{\text{max}}$  ratio; 2) the slice thickness/TR combination provides a threshold velocity greater than 22 cm/s; 3) the steady state pixel intensity ( $P_{\text{SS}}$ ) is substituted with the pixel intensity of an unperturbed popliteal artery ( $P_{\text{B}}$ ) with adjustments being made for the small net retrograde flow that was observed in unperturbed popliteal arteries.

The third study (chapter 5), tested the reliability of the IntSI technique for popliteal area measurement against those obtained with a high resolution imaging and pixel counting approach. In view of the trade-off between spatial and temporal resolution, mathematical modeling was used to optimize the imaging sequence in order to ensure that the pixel-to-luminal area ratio was as small as possible while the temporal sampling frequency was as high as possible. The sliding paraboloid technique was used to segment the lumen. Area measurements were calculated using the IntSI technique with adjustments made for  $V_{\text{mean}}/V_{\text{max}}$  ratio of 0.6. Testing the reliability of the IntSI technique against high resolution imaging provided a means of assessing if further adjustments to the IntSI equation were needed to account for  $P_{\text{B}}$  being used in place of  $P_{\text{SS}}$ .

The IntSI technique required a shorter scan time (6-9s,) than the high resolution imaging (180-240s) and there was agreement between the IntSI technique and high resolution imaging. However, measurements with the IntSI technique were larger than those of high resolution/ pixel counting (mean difference  $\pm$  RC:  $3.05 \pm 2.55$  mm<sup>2</sup>). Numerical optimization was used to determine a correction factor to account for  $P_{\text{B}}$  being lower than  $P_{\text{SS}}$ . The difference between  $P_{\text{B}}$  and  $P_{\text{SS}}$  was ascribed to suppression of the net retrograde flow that enters the slice during data acquisition by a venous saturation band. With the correction factor, the reliability of the IntSI technique improved (ICC: 0.98 (0.97-0.99), mean difference  $\pm$  RC:  $0.14 \pm 2.32$ ). The study shows that the IntSI technique with a correction factor can be applied in vivo to obtain rapid serial area measurements.

The final study (chapter 6) aimed to demonstrate that MRI-FMD via the IntSI technique is more repeatable than US-FMD. The study also applied the IntSI technique for qualitative assessment



of reactive hyperemia, in order to be able to rule out microvascular disease. The rationale behind the approach was that since the integrated signal intensity (IntSI) of the lumen varies directly with the luminal area and mean velocity, then IntSI will increase with reactive hyperemia. The study compared the conventional brachial US-FMD with popliteal US-FMD in 19 healthy volunteers. Then the IntSI technique was used to perform an MRI-FMD study. The test-retest repeatability of popliteal MRI-FMD using the IntSI technique was compared with that of popliteal US-FMD. The maximum /baseline IntSI ratio during FMD was used as a measure of reactive hyperemia. Moderate agreement was observed between brachial US-FMD and popliteal US-FMD (r: 0.59). When ultrasound and MRI area measurements of the popliteal artery were compared, the MRI measurements were larger with a mean difference of  $4.76 \pm 5.19 \text{ mm}^2$ , which represents 19 % increase in MRI measurements relative to those of ultrasound. Popliteal MRI-FMD demonstrated higher values than Popliteal US-FMD with a mean difference of 5.07%. Various reasons were suggested for the increase in values obtained with MRI relative to US. The within subject coefficient of variability of the popliteal MRI-FMD technique at 24% was non-inferior to both the brachial ultrasound and popliteal ultrasound FMD techniques (23 % and 26% respectively). This chapter showed that the MR based IntSI technique for measuring FMD is non-inferior to neither popliteal US-FMD nor brachial US-FMD and it has a potential for qualitative assessment of reactive hyperemia when tested in those with at risk for endothelial dysfunction.

## 7.2 General Discussion

Endothelial dysfunction is a reversible process that occurs in blood vessels. Macrovascular endothelial function is predominantly nitric oxide dependent. Flow mediated dilatation is able to identify endothelial dysfunction in at risk groups so that early interventions can be applied to halt the disease progression. FMD can also be used to monitor the efficacy of therapies used to improve endothelial function. FMD is affected by various factors. These include physiological factors such as the menstrual cycle (Hashimoto *et al.*, 1995), exercise (Tinken *et al.*, 2008), viral illness, (Celermajer, 2008), coffee ingestion (Buscemi *et al.*, 2010), intake of antioxidants and fatty meals (Taddei *et al.*, 1998; Koulouris *et al.*, 2010; Findlay *et al.*, 2013). Environmental factors such as the ambient temperature or season of the year may also affect the FMD response (Widlansky *et al.*, 2007).

To reduce the effect of these physiological and environmental factors, patients are required to fast over night, refrain from vigorous exercises, be scanned in a temperature controlled room after a period of rest and preferably scanned in the morning to reduce the effect of the circadian rhythm on FMD (Corretti *et al.*, 2002; Stoner & McCully, 2012). The cuff duration, pressure and location may also affect the FMD response (Doshi *et al.*, 2001; Corretti *et al.*, 2002). In addition, the baseline diameter and shear rate also influence the FMD response (Pyke & Tschakovsky, 2007; Charakida *et al.*, 2010). Finally, the imaging technique also contributes to the variability of the technique, and that is the focus of this thesis.

### 7.2.1 Why the MRI-based IntSI technique for FMD?

The challenge with ultrasound based FMD is that the technique has a steep learning curve (Corretti *et al.*, 2002). In fact, to be certified as competent to independently conduct ultrasound based FMD studies, an operator must have performed 100 cases under supervision and is also expected to complete 100 scans annually in order to maintain a level of adequate expertise (Corretti *et al.*, 2002). MRI, on the other hand, is easier to perform and MR image acquisition is not as challenging as ultrasonography. However, previous MRI studies on 1.5T MRI scanners only sampled the luminal area once for the post hyperaemic vasodilatory response (Sorensen *et al.*, 2002; Leeson *et al.*, 2006). Sampling was at 60 seconds following the onset of reactive hyperemia but the peak dilatation may not necessarily occur at this fixed time point. This means

that the maximal dilatation may be missed. There are constraints with frequent sampling of the luminal area during FMD, because of the tradeoff between spatial resolution, SNR and temporal resolution. Application of a higher strength 3T scanner improves the SNR thereby allowing for scan times as short as 15 seconds (Oliver et al., 2012). This provides a sampling frequency of 4 images per minute.

The IntSI technique was developed and applied in this thesis in order to overcome the limitations of spatial and temporal resolution. It was based on several assumptions as mentioned earlier. Provided the assumptions are not violated, phantom studies show that the IntSI technique offers a reliable means of measuring luminal area. In view of the findings from the phantom study that in order to keep the area measurement error less than 10%, the pixel to luminal ratio should not exceed 0.1, a pixel area of  $1.2 \text{ mm}^2$  was considered suitable for measuring the popliteal artery with the IntSI technique because the minimum baseline area of the popliteal artery is  $11.95 \text{ mm}^2$  when calculated as a circular area using the luminal diameter obtained from ultrasonography (Sandgren et al. 1998). This corresponds to a pixel to luminal area ratio of 0.1. However, a smaller pixel area not greater than  $0.53 \text{ mm}^2$  will be required for brachial area calculations since the minimum baseline area of the brachial artery is  $5.31 \text{ mm}^2$  (Ostrem et al. 2014). When a pixel area as large as  $1.2 \text{ mm}^2$  was used to image the popliteal artery and the scan time improved to 6-9 seconds depending on the heart rate. This provided a sampling frequency of 6-10 images per second.

Another goal of this thesis was to develop an MRI technique that can assess reactive hyperemia. Phase contrast imaging can be used to assess reactive hyperemia but it is limited by low temporal resolution (Pai, 2007). Other MRI-FMD studies that used faster sequences such as the SSFP were not able to assess reactive hyperemia (Sorensen et al., 2002; Leeson et al., 2006). The IntSI technique applied in this thesis was used for qualitative assessment of reactive hyperemia. Volunteers were grouped as poor and adequate responders based on the maximum /baseline IntSI ratio during FMD. The difference between the groups was not statistically significant, this may be because the two groups comprised of healthy volunteers. A subsequent test in those with dysfunction may show a significant difference.

## 7.2.2 Adaptations that were required for in vivo application of the IntSI technique

Throughout the course of this thesis, it has been emphasized that the IntSI technique for area measurement is based on several assumptions and some of the assumptions may not hold in vivo. One of the assumptions made while deriving the IntSI equation was that arterial flow has a parabolic velocity profile, with the mean velocity being half of the maximal velocity. The finding in this thesis that the popliteal artery has a blunted parabolic profile with an average ratio of 0.6 at baseline, during distal occlusion and during reactive hyperemia agrees with the values of 0.57-0.76 reported in the femoral artery (Osada & Radegran, 2005) but differs from a similar study that had values of 0.48-0.57 (Ade et al., 2012). In the second study by Ade et al (2012) only the first retrograde portion of diastole was considered without the anterograde diastolic flow nor the occasional second retrograde portion. This might explain why their study differed from both this present study and also that by Osada & Radegran (2005). In view of the time averaged mean velocity ( $TAV_{\text{mean}}$ ) being 60% instead of 50% of the time averaged maximal velocity ( $TAV_{\text{max}}$ ), the IntSI equation was modified.

Using a spoiled gradient echo sequence, a linear relationship exists between velocity and signal intensity up to a threshold point beyond which further increases in velocity have no effect on the signal intensity, the threshold value being the quotient of slice thickness and TR (Hashemi et al., 2010). The IntSI technique assumes that the maximal blood velocity during image acquisition is less than the threshold. Based on the highest diastolic velocity of 22 cm/s recorded during hyperemia on spectral Doppler analysis, a slice thickness/TR combination of 10 mm/24 ms was used for imaging the popliteal artery. This was to ensure that the maximal velocity within the popliteal artery did not exceed the threshold.

The IntSI technique also requires the steady state intensity of the most central luminal pixel. In the phantom study, this value was easily obtained because a 90° RF pulse was applied and a Cartesian trajectory was used to fill k-space in an outer to inner approach. However, data acquisition when imaging the popliteal artery occurs over several cardiac cycles, with the imaged slice of the vessel being constantly re-filled with fresh blood at each new cardiac cycle even if there is no flow during the actual period of data acquisition. So the steady state pixel intensity ( $P_{\text{ss}}$ ) during in vivo imaging of a pulsatile artery will be higher than if there was no flow during

systole. Spectral Doppler was used to ascertain if the central pixel intensity obtained during diastole in an unperturbed artery ( $P_B$ ) can be used as the steady state value ( $P_{SS}$ ). It was discovered that there was net retrograde flow during diastole, therefore, the likelihood is that  $P_B$  may be lower than  $P_{SS}$  because a venous suppression band is used during imaging and it will lead to retrograde flow of blood with suppressed signals entering the slice during image acquisition.

### 7.2.3 Effect of $P_B$ on the reliability of area measurements with the IntSI technique

The possibility that  $P_B$  is lower than  $P_{SS}$ , might explain why popliteal area measurements using the IntSI technique were on an average of  $3 \text{ mm}^2$  larger than those by high resolution and pixel counting. This is because if  $P_B$  is lower than  $P_{SS}$ , the denominator in the IntSI equation will be smaller than it should be and that will lead to an overestimation in the calculated area. When a correction factor was added by assuming that  $P_{SS}$  is  $1.2 P_B$ , the difference between the IntSI equation and high resolution imaging decreased to  $0.14 \pm 2.32 \text{ mm}^2$ . If the minimal detectable change in area during an FMD study is chosen as 5% using a minimum baseline area of  $11.95 \text{ mm}^2$  for the popliteal artery (Sandgren et al. 1998), a 5% FMD will translate into an absolute area increase of  $0.6 \text{ mm}^2$ , which is larger than the  $0.14 \pm 2.32 \text{ mm}^2$  and therefore can be reliably detected and regarded as a real change.

### 7.2.4 MRI-FMD using the IntSI technique versus ultrasonography

Having established in phantoms that the IntSI technique for area measurements is reliable and demonstrated that it can be used to obtain repeatable area measurements in vivo that are comparable to high resolution MR imaging, the next step was to compare it with ultrasound. Considering the advantages of MR imaging via the IntSI technique over the commonly used ultrasonographic approach for serial area measurements, it was expected that the IntSI technique for FMD will have superior repeatability compared with US-FMD.

#### 7.2.4.1 Popliteal US-baseline area versus MRI-baseline area

This thesis found that popliteal baseline area measurements recorded with ultrasonography were smaller than MRI measurements. This is likely as a result of ultrasound area being obtained from the diameters measurements from longitudinal images, while MRI area measurements are

obtained from cross-sectional images. With ultrasound imaging, longitudinal ultrasound images are used rather than cross-sectional images, due to the poor lateral resolution of ultrasound. The area is calculated from the diameter with the assumption that the lumen has a circular area. However, if the arterial lumen is oval as seen in a brachial intravascular ultrasound study (Ong et al., 2002), then the calculated area will be inaccurate. The artery may also be rendered oval during extravascular studies due to pressure from the ultrasound transducer (Triboulet et al., 2006; Cary et al., 2014). Interestingly, some authors reported larger area measurements with ultrasound which they ascribed to measuring the diameter of the artery from the intima media boundary (Sorensen et al., 2002; Leeson et al., 2006). Their MRI measurements on the other hand, were from the lumen intima interface. In my thesis, ultrasound measurements were from the lumen-intima interface.

#### 7.2.4.2 US-FMD compared with MRI-FMD

Both popliteal US-FMD and popliteal MRI-FMD had acceptable test-retest repeatability (Corretti et al., 2002). However, MRI showed a larger FMD response than ultrasound. This differs from a similar study on the brachial artery in which the US-FMD and MRI-FMD responses were closer (Leeson et al., 2006). Unlike those authors, who measured FMD at 60 seconds, I obtained serial measurements over time to determine the maximal dilatation. This may explain why our US and MRI popliteal FMD studies showed less agreement compared to their study. In addition, if the time to peak is short, US may not capture the maximal dilatation, if there is a slight shift in the ultrasound imaging plane when the cuff is deflated. This sometimes happens, despite the use of a probe holder. Another explanation for the difference between FMD responses of both imaging modalities may be the fact that MRI detects multi-directional vessel dilatation unlike longitudinal imaging with ultrasound which only captures dilatation in the longitudinal plane. Although the MRI and US studies were performed on separate days, this may not be an appropriate explanation for the observed difference, since Leeson et al (2006) also performed their ultrasound and MRI respectively, on separate days. We made efforts to fix the dates for the tests as close together as possible. To avoid diurnal variations in FMD, the patients were scanned at the same period in the day for both scans. Female volunteers were scanned during the same phase of their menstrual cycle. However, diet and exercise were not strictly controlled over the intervening days.

#### **7.2.4.3 Repeatability of Popliteal MRI-FMD**

The main focus of my research was to design an MRI-FMD technique that is more repeatable than brachial US-FMD. However, I was not able to demonstrate that MRI-FMD using the IntSI technique was superior to US-FMD. Nevertheless, the popliteal MRI-FMD technique was non-inferior to both the brachial US-FMD and popliteal US-FMD techniques. The within subject coefficients of variability for the ultrasound and MRI studies were greater than the values of 7.6% to 11.9% reported for same day brachial ultrasound repeatability (Ghiadoni et al., 2012) and the value of 9-10% for different day brachial ultrasound repeatability (Donald et al., 2008). The values were closer to that of 23% observed in a previous brachial ultrasound repeatability study (Sorensen et al., 2002).

#### **7.2.4.4 Ability to qualitatively assess reactive hyperemia with the IntSI technique**

Although FMD assesses macrovascular function, if the microvasculature is impaired there will be poor FMD, despite the presence of a healthy macrovascular endothelium. Reactive hyperemia is often used to assess the microvasculature during FMD studies, but a study by Leeson et al (2006) used the SSFP sequence which is not able to assess reactive hyperemia. Despite the fact that phase contrast imaging can quantify reactive hyperemia, the SSFP sequence is commonly used for FMD studies instead because it provides a better temporal resolution (Sorensen et al., 2002; Silber et al., 2005; Leeson et al., 2006). This thesis intended that the designed MRI technique for measuring FMD will be able to qualify reactive hyperemia. Volunteers in the group classified as having a poor hyperemic response using the IntSI technique showed lower hyperemic response during brachial US-FMD and popliteal US-FMD, although the difference was not statistically significant in both cases. This is probably because the study comprised of healthy volunteers. It is possible that the difference between the groups may be statistically significant in those with or at risk for endothelial dysfunction.

#### **7.2.4.5 Cost effectiveness and potential utility of the IntSI technique**

Equipment required for the US-FMD technique are relatively affordable and available but ultrasonography in general, is operator dependent and ultrasound based FMD is technically challenging (Corretti et al., 2002). MRI does not share these limitations of ultrasonography

although it may have a higher cost per unit time. This thesis showed that MRI-FMD using the IntSI technique is non-inferior to brachial US-FMD and popliteal US-FMD in a single center study. If the MRI-FMD technique was shown to be more repeatable than US-FMD, it will have created an opportunity for smaller sizes during interventional studies. Nevertheless, the non-inferiority of the technique is of importance for multi center studies. This is because data acquisition with MRI is less operator dependent than ultrasonography, as a result, data from multiple sites can be captured with this MRI technique and sent to a central pool for post-processing.

The period from which the patient was positioned on the couch to obtaining the baseline scans was longer with ultrasound (3-12 minutes for ultrasound versus 4-5 minutes for MRI). However, data acquisition was approximately 11 minutes for both techniques, comprising of 1 minute or less for baseline data acquisition, 5 minutes of cuff inflation and 5 minutes of additional data collection after the cuff was deflated. Therefore, US-FMD required 14 – 23 minutes while MRI-FMD was completed in 15-16 minutes. For the study, the cost per unit time for ultrasound imaging was \$3.33/min, while MRI cost \$8.33/min, which corresponds to \$47-77 for US-FMD and \$125-133 for MR-FMD. Although MRI-FMD was more expensive, if the time required to perform MR-FMD is short enough for the study to be included in a block of time already earmarked for a comprehensive cardiovascular MRI study, then there will be no added cost for performing the study. This will make MRI-FMD more cost effective than US-FMD. Another advantage of the MRI-FMD technique is that it has a shorter post processing time compared with US-FMD ( $11.3 \pm 1.6$  min versus  $23.1 \pm 2.2$  min), which means that more MRI-FMD cases may be post-processed per day. In addition, since the MRI-post-processing technique is semi-automated, the technologist at the consul could process the data while other sequences are running.

The IntSI approach for measuring the popliteal area is reliable and it provides a means of improving the sampling frequency during MRI-FMD. It also shows potential for qualitative assessment of reactive hyperemia, unlike previous studies with the SSFP sequence (Sorensen et al., 2002; Leeson et al., 2006). This thesis showed that MRI-FMD using the IntSI technique is non-inferior to the more established ultrasound approach. The ability of the IntSI technique to qualify reactive hyperemia and the fact that the technique is not constrained by the usual trade-



off between spatial and temporal resolution makes it suitable for MRI-FMD. The technique can be incorporated into a comprehensive protocol for MRI based evaluation of vascular health.

## **7.3 Future Directions**

There are a number of ways to improve the IntSI technique for area measurements and its applicability for studies of FMD. Some of these methods are enumerated below. Considerations will also be made for other applications of the IntSI technique beyond FMD assessment.

### **7.3.1 Usage of an adaptive diastolic trigger delay**

As mentioned in chapter 6, one limitation of the IntSI technique applied in this thesis is that a predetermined diastolic trigger delay rather than an adaptive trigger delay was used to determine what point in the cardiac cycle that data acquisition commences. I intend to redesign the imaging sequence with a diastolic adaptive delay included. This will ensure that imaging commences at a specific time from the onset of the R wave (Roes et al., 2008). It will be helpful in those with variable heart rate to ensure that imaging always commences at a specific point in the cardiac cycle.

### **7.3.2 Effect of subject characteristics, diet and exercise on FMD**

I will use in a wider range of volunteers to test the effects of subject characteristics such as age, BMI, sex etc on FMD measurements obtained with the IntSI technique. I also intend to test the effect of dietary interventions and exercise on MRI-FMD, as some authors have demonstrated an association between diet, exercise and FMD, using ultrasonography. High fat meals are associated with endothelial dysfunction (Marinos et al., 2015) and in subjects who perform endurance exercise on the previous day, endothelial function after high-sugar food intake improves (Weiss et al., 2008).

### **7.3.3 Carotid endothelial function, carotid stiffness and aortic compliance,**

In addition to applying the IntSI technique for FMD assessment in peripheral arteries, a number of other experiments are being considered for further applications of the MRI IntSI technique. Possible applications include measuring endothelial function in the carotid artery and assessment other markers of vascular function such as arterial compliance. I will measure carotid endothelial function using hypercapnia as a stimulus for cerebral vasodilatation, increased cerebral blood flow and carotid endothelial shear stress. In this case, the area of the common carotid artery will be measured before and after a period of breath holding (Fierstra et al., 2013).

Although arterial stiffness may be measured with pulse wave velocity (PWV), a widely used marker of cardiovascular events (Laurent et al., 2006; Gkaliagkousi & Douma, 2009), PWV only provides a generalized assessment of arterial compliance. Local assessment for arterial compliance can be obtained by calculating the arterial distensibility (Laurent et al., 2006). This involves direct measurement of the luminal area during systole and diastole. Arteries change in size during the cardiac cycle with maximal distension occurring during the forward flow of late systole when a large volume of blood is pushed out of the heart into the arterial (Chuang et al., 2002). During diastole, the artery returns to its pre-systolic size. Arterial distensibility is calculated as the relative change in area divided by the pulse pressure (Kylintireas et al., 2011).

Capacitance arteries such as the carotid and aorta reduce the effect of pulsatile pressure and flow during the cardiac cycle on target organs such as the brain, kidneys and retina (Lefferts et al., 2014). Age and/or disease related arterial stiffness is associated with cardiovascular events such as stroke and myocardial infarction (Lefferts et al., 2014). It may also contribute to target organ damage such as renal dysfunction and retinal damage (Lefferts et al., 2014). The stiffness of superficial arteries like the carotid artery is often assessed with ultrasonography (Laurent et al., 2006) while MRI may be used to assess deep arteries like the aorta (Resnick et al., 1997). In patients with hypertension, remodeling of the vascular wall occurs, including hypertrophy of the vascular smooth muscle cells of the tunica media. This makes the vessel less compliant. Atherosclerosis also makes arteries less compliant. PWV and carotid stiffness are useful for assessing age related decline in arterial compliance, while aortic stiffness is useful in cases of hypertension and diabetes (Laurent et al., 2006).

Unlike FMD measurements in which a high sampling frequency is required to detect the time to peak dilatation, a high sampling frequency is not needed for arterial compliance studies since the artery maintains a constant systolic to diastolic size. However, application of the IntSI technique for measuring compliance of arteries such as the carotid artery and the aorta as part of a comprehensive protocol for MRI based evaluation of vascular health may result in a shorter total examination time. In addition, current techniques for measuring area during arterial compliance studies use the pixel counting and thresholding approach with in-plane resolutions as large as  $1.56 \times 1.17$  mm and slice thickness up to 6 mm (Shan et al., 2012). However, using such large pixels and thick slices may lead to partial volume averaging and poor estimation of the vessel

size if the imaging plane is not perpendicular to the artery. Therefore, subtle differences in size between systole and diastole may be missed.

The IntSI technique can be applied for measuring arterial distensibility by acquiring two images during the cardiac cycle, one image at systole and the other at diastole. The technique may be applicable for pulsatile arteries with high resistance such as the aorta or sometimes the common carotid artery, when there is little or no flow during diastole (Arger, 2004). However, it may not be applicable for low resistance arteries like the common carotid artery. This is because low resistance arteries have continuous flow during diastole and it may be incorrect to use the maximal pixel intensity of the diastolic image as  $P_{ss}$ . I intend to explore other methods to obtain  $P_{ss}$ , so that the IntSI technique can be applicable for assessing the distensibility of all arteries and hypothesize that the modified IntSI technique will be more repeatable as a means of measuring arterial stiffness compared with current MRI techniques.

The effect of exercise on arterial stiffness differs. Endurance (aerobic) exercise such as walking on a treadmill, swimming or bicycling and resistance exercise such as weight lifting affect vascular function. Regular endurance exercise has a positive effect on cardiovascular system. It slows down the age-related normal loss of elasticity and compliance in the common carotid and it improves FMD (Tanaka et al., 2000; Dawson et al., 2013). Resistance exercise, on the other hand, is said to increase arterial stiffness (Lefferts et al., 2014) and decrease FMD (Dawson et al., 2013). The decrease in FMD following resistance exercise is ascribed to associated increased blood pressure that occurs during resistance exercise (Dawson et al., 2013) but this decrease in FMD does not occur in those who regularly perform either aerobic or endurance exercises (Phillips et al., 2011). Interestingly in those with spinal cord injury, resistance exercise improved FMD (Stoner et al., 2007). Therefore, a concluding experiment I intend to perform is to demonstrate the effect of different types of exercise on arterial stiffness using the IntSI technique (Maczewski & Beresewicz, 1998).

## References

- Ade CJ, Broxterman RM, Wong BJ & Barstow TJ (2012). Anterograde and retrograde blood velocity profiles in the intact human cardiovascular system. *Exp Physiol* **97**, 849–860.
- Agatista PK, Ness RB, Roberts JM, Costantino JP, Kuller LH & McLaughlin MK (2004). Impairment of endothelial function in women with a history of preeclampsia: an indicator of cardiovascular risk. *Am J Physiol Heart Circ Physiol* **286**, H1389–H1393.
- Alderton WK, Cooper CE & Knowles RG (2001). Nitric oxide synthases: structure, function and inhibition. *Biochem J* **357**, 593–615.
- Alley H, Owens CD, Gasper WJ & Grenon SM (2014). Ultrasound assessment of endothelial-dependent flow-mediated vasodilation of the brachial artery in clinical research. *J Vis Expe* 52070.
- Alperin N & Lee SH (2003). PUBS: Pulsatility-based segmentation of lumens conducting non-steady flow. *Magn Reson Med* **49**, 934–944.
- Anderson TJ, Charbonneau F, Title LM, Buithieu J, Rose MS, Conradson H, Hildebrand K, Fung M, Verma S & Lonn EM (2011). Microvascular function predicts cardiovascular events in primary prevention: Long-term results from the firefighters and their endothelium (FATE) study. *Circulation* **123**, 163–169.
- Anon (2011). EFSA Panel on Dietetic Products, Nutrition and Allergies (NDA) Scientific Opinion on the substantiation of health claims related to walnuts and maintenance of normal blood LDL-cholesterol concentrations (ID 1156, 1158) and improvement of endothelium - depe. *EFSA J* **9**, 2074.
- Anon (n.d.). Statistics Canada. Mortality, Summary List of Causes 2008. Released October 18, 2011.
- Antonio GE, Griffith JF & Yeung DKW (2004). Small-field-of-view MRI of the knee and ankle. *AJR* **183**, 24–28.
- Archer SL, Huang JM, Hampl V, Nelson DP, Shultz PJ & Weir EK (1994). Nitric oxide and cGMP cause vasorelaxation by activation of a charybdotoxin-sensitive K channel by cGMP-dependent protein kinase. *Proc Natl Acad Sci USA* **91**, 7583–7587.
- Arger PH (2004). Blood Vessels: anatomy and Physiology. In *The complete guide to vascular ultrasound*, ed. Iyoob SD, pp. 1–5. Lippincott Williams & Wilkins, Philadelphia, PA.

- Armengol J, Calbó J, Pujol T & Roura P (2008). Bernoulli correction to viscous losses: Radial flow between two parallel discs. *Am J Phys* **76**, 730.
- Armstrong P & Keevil S (1991). Magnetic resonance imaging--1: Basic principles of image production. *BMJ Br Med J* **303**, 35–40.
- Arrebola-Moreno AL, Laclaustra M & Kaski JC (2012). Noninvasive Assessment of Endothelial Function in Clinical Practice. *Rev Española Cardiol (English Ed)* **65**, 80–90.
- Asher GN, Viera AJ, Weaver M a, Dominik R, Caughey M & Hinderliter AL (2012). Effect of hawthorn standardized extract on flow mediated dilation in prehypertensive and mildly hypertensive adults: a randomized, controlled cross-over trial. *BMC Complement Altern Med* **12**, 26.
- Atkinson G (2014). Shear rate normalization is not essential for removing the dependency of flow-mediated dilation on baseline artery diameter: past research revisited. *Physiol Meas* **35**, 1825–1835.
- Atkinson G & Batterham AM (2013). The percentage flow-mediated dilation index: a large-sample investigation of its appropriateness, potential for bias and causal nexus in vascular medicine. *Vasc Med* **18**, 354–365.
- Atkinson G & Batterham AM (2014). Response to: “Allometric scaling of endothelium-dependent vasodilation: Brachial artery flow-mediated dilation coming of age.” *Vasc Med* **19**, 142–143.
- Atkinson G, Batterham AM, Black M a, Cable NT, Hopkins ND, Dawson E a, Thijssen DHJ, Jones H, Tinken TM & Green DJ (2009). Is the ratio of flow-mediated dilation and shear rate a statistically sound approach to normalization in cross-sectional studies on endothelial function? *J Appl Physiol* **107**, 1893–1899.
- Atlas SA (2007). The renin-angiotensin aldosterone system: pathophysiological role and pharmacologic inhibition. *J Manag care Pharm* **13**, 9–20.
- Auld D. & Srinivas K (2005). Fundamentals of Fluid Mechanics in Aerodynamics for students. *Aerospace, Mech Mechatron Eng Univ Sydney*.
- Badeer H (2001). Hemodynamics for medical students. *Adv Physiol Educ* **25**, 44–52.
- Bagg W, Whalley GA, Gamble G, Drury PL, Sharpe N & Braatvedt GD (2001). Effects of improved glycaemic control on endothelial function in patients with type 2 diabetes. *Intern med J* **31**, 322–328.

- Ballyns JJ, Shah JP, Hammond J, Gebreab T, Gerber LH & Sikdar S (2011). Objective sonographic measures for characterizing myofascial trigger points associated with cervical pain. *J Ultrasound Med* **30**, 1331–1340.
- van Belle G (2011). Sample Size. In *Statistical Rules of Thumb*, pp. 27–51. John Wiley & Sons, Hoboken, NJ USA.
- Benjamin N, Calver A, Collier J, Robinson B, Vallance P & Webb D (1995). Measuring Forearm Blood Flow and Interpreting the Responses to Drugs and Mediators. *Hypertension* **25**, 918–923.
- Berger R, Stanek B, Hulsmann M, Frey B, Heher S, Pacher R, Neunteufl T, Hülsmann M, Frey B, Heher S, Pacher R & Neunteufl T (2001). Effects of endothelin a receptor blockade on endothelial function in patients with chronic heart failure. *Circulation* **103**, 981–986.
- Betik AC, Luckham VB & Hughson RL (2004). Flow-mediated dilation in human brachial artery after different circulatory occlusion conditions. *Am J Physiol Heart Circ Physiol* **286**, H442–H448.
- Binko J, Majewski H & Henry P (1998). endothelium-denuded rat aortas through inducible NOS. 853–859.
- Bitar R, Leung G, Perng R, Tadros S, Moody AR, Sarrazin J, McGregor C, Christakis M, Symons S, Nelson A & Roberts TP (2006). MR pulse sequences: what every radiologist wants to know but is afraid to ask. *Radiographics* **26**, 513–537.
- Björnberg J, Albert U & Mellande S (1990). Resistance responses in proximal arterial vessels , arterioles and veins during reactive hyperaemia in skeletal muscle and their underlying regulatory mechanisms. *Acta Physiol Scand* **139**, 535–550.
- Black M a, Cable NT, Thijssen DHJ & Green DJ (2009). Impact of age, sex, and exercise on brachial artery flow-mediated dilatation. *Am J Physiol Heart Circ Physiol* **297**, H1109–H1116.
- Black MA, Cable NT, Thijssen DHJ & Green DJ (2008). Importance of measuring the time course of flow-mediated dilatation in humans. *Hypertension* **51**, 203–210.
- Bland J (2006). How should I calculate a within-subject coefficient of variation? Available at: <https://www-users.york.ac.uk/~mb55/meas/cv.htm> [Accessed October 20, 2015].
- Bland JM & Altman DG (1986). Statistical methods for assessing agreement between two methods of clinical measurement. *Lancet* **1**, 307–310.

- Blink EJ (2004). Basic MRI physics. In, pp. 0–75. Available at: [mri-physics-en.pdf](#).
- Bliss MR (1998). Hyperaemia. *J Tissue Viability* **8**, 4–13.
- Borogovac A & Asllani I (2012). Arterial Spin Labeling (ASL) fMRI: advantages, theoretical constraints, and experimental challenges in neurosciences. *Int J Biomed Imaging* **2012**, 818456.
- Bots ML, Westerink J, Rabelink TJ & De Koning EJP (2005). Assessment of flow-mediated vasodilatation (FMD) of the brachial artery: Effects of technical aspects of the FMD measurement on the FMD response. *Eur Heart J* **26**, 363–368.
- Brewster S, Floras J, Zinman B & Retnakaran R (2013). Endothelial function in women with and without a history of glucose intolerance in pregnancy. *J Diabetes Res* **2013**, 382670.
- Brix G, Kolem H, Nitz WR, Bock M, Huppertz A, Zech CJ & Dietrich O (2008). Basics of Magnetic Resonance Imaging and Magnetic Resonance Spectroscopy. In *Magnetic Resonance Tomography*, 1st edn., ed. Maximilian F Reiser, Semmler W & Hricak H, pp. 3–167. Springer-Verlag, Berlin Heidelberg.
- Brown M a & Semelka RC (1999). MR imaging abbreviations, definitions, and descriptions: a review. *Radiology* **213**, 647–662.
- Buscemi S, Batsis JA, Arcoletto G & Verga S (2010). SHORT COMMUNICATION Coffee and endothelial function: a battle between caffeine and antioxidants? *Eur J Clin Nutr* **64**, 1242–1243.
- Bushberg JT, Seibert JA, Leidholdt EMJ & Boone JM (2011). *MR Image Characteristics. In the essential physics of medical imaging*, 3rd editio. Lippincott Williams & Wilkins. Available at: <https://www.inkling.com/read/essential-physics-medical-imaging-jerrold-bushberg-3rd/chapter-13/13-2-mr-image-characteristics>.
- Buxton RB (2009). Relaxation and contrast in MRI. *Introd to Funct Magn Reson imaging* 147–172.
- Cary TW, Reamer CB, Sultan LR, Mohler ER & Sehgal CM (2014). Brachial artery vasomotion and transducer pressure effect on measurements by active contour segmentation on ultrasound. *Med Phys* **41**, 022901.
- Casey DP & Joyner MJ (2009). NOS inhibition blunts and delays the compensatory dilation in hypoperfused contracting human muscles. *J Appl Physiol* **107**, 1685–1692.



- Castle M & Keller J (2007). Rolling Ball Background Subtraction (ImageJ). *Ment Heal Res Institute, Univ Michigan*. Available at: <http://imagej.net/plugins/rolling-ball.html> [Accessed July 15, 2014].
- Caughey GE, Cleland LG, Penglis PS, Gamble JR & James MJ (2001). Roles of Cyclooxygenase (COX)-1 and COX-2 in Prostanoid Production by Human Endothelial Cells: Selective Up-Regulation of Prostacyclin Synthesis by COX-2. *J Immunol* **167**, 2831–2838.
- Cavalcante JL, Lima JAC, Redheuil A & Al-Mallah MH (2011). Aortic stiffness: current understanding and future directions. *J Am Col Cardiol* **57**, 1511–1522.
- Celermajer DS (1997). Endothelial dysfunction: does it matter? Is it reversible? *J Am Coll Cardiol* **30**, 325–333.
- Celermajer DS (2008). Reliable endothelial function testing: at our fingertips? *Circulation* **117**, 2428–2430.
- Celermajer DS, Sorensen KE, Gooch VM, Spiegelhalter DJ, Miller OI, Sullivan ID, Lloyd JK & Deanfield JE (1992). Non-invasive detection of endothelial dysfunction in children and adults at risk of atherosclerosis. *Lancet* **340**, 1112–1115.
- Celermajer DS, Sorensen KE, Spiegelhalter DJ, Georgakopoulos D, Robinson J & Deanfield JE (1994). Aging is associated with endothelial dysfunction in healthy men years before the age-related decline in women. *J Am Coll Cardiol* **24**, 471–476.
- Cengel YA & Cimbala JM (2006). Flow in pipes. In *In: Fluid Mechanics, Fundamentals and Applications*, 1st edn., pp. 321–343. McGraw-Hill, New York, NY. Available at: [http://www.uio.no/studier/emner/matnat/math/MEK4450/h11/undervisningsmateriale/modul-5/Pipeflow\\_intro.pdf](http://www.uio.no/studier/emner/matnat/math/MEK4450/h11/undervisningsmateriale/modul-5/Pipeflow_intro.pdf).
- Chambers JM (2009). Facets of R. *R J* **1**, 5–8.
- Charakida M, De Groot E, Loukogeorgakis SP, Khan T, Lüscher T, Kastelein JJ, Gasser T & Deanfield JE (2013). Variability and reproducibility of flow-mediated dilatation in a multicentre clinical trial. *Eur Heart J* **34**, 3501–3507.
- Charakida M, Masi S, Lüscher TF, Kastelein JJP & Deanfield JE (2010). Assessment of atherosclerosis: The role of flow-mediated dilatation. *Eur Heart J* **31**, 2854–2861.
- Chaudhry FA, Bangalore S, Upadya S, Shah A, Eftekhari H, Pudupud D & Sehgal CM (2007). Cross-sectional imaging identifies flow-mediated vasodilatation more accurately compared with longitudinal imaging. *J Am Soc Echocardiogr* **20**, 1380–1385.

- Chavhan G, Babyn P & Jankharia B (2008). Steady-State MR Imaging Sequences: Physics, Classification, and Clinical Applications 1. *Radiographics* **8**, 1147–1161.
- Chen Q, Stock K, Prasad P & Hatabu H (1999). Fast magnetic resonance imaging techniques. *Eur J Radiol* **29**, 90–100.
- Chhabra N (2009). Endothelial dysfunction – A predictor of atherosclerosis. *Internet J Med Updat* **4**, 33–41.
- Chia YH (1999). *Monitoring changes in aortic diameter* (thesis). University of Toronto.
- Chiewvit P, Piyapittayanan S & Pongvarin N (2011). Cerebral venous thrombosis: diagnosis dilemma. *Neurol Int* **3**, e13.
- Chuang ML, Douglas PS, Bisinov EA & Stein JH (2002). Effect of cardiac cycle on ultrasound assessment of endothelial function. *Vasc Med* **7**, 103–108.
- Clark JF & Pyne-Geithman G (2005). Vascular smooth muscle function: The physiology and pathology of vasoconstriction. *Pathophysiology* **12**, 35–45.
- Collins T (2012). Image intensity Processing. *MBF "ImageJ Microsc Man*. Available at: [http://imagej.net/mbf/image\\_intensity\\_proce.htm#intensity\\_BG](http://imagej.net/mbf/image_intensity_proce.htm#intensity_BG).
- Conference (n.d.). Conference Board of Canada. The Canadian Heart Health Strategy: Risk Factors and Future Cost Implications. Feb 2010.
- Corretti MC, Anderson TJ, Benjamin EJ, Celermajer D, Charbonneau F, Creager M a, Deanfield J, Drexler H, Gerhard-Herman M, Herrington D, Vallance P, Vita J & Vogel R (2002). Guidelines for the ultrasound assessment of endothelial-dependent flow-mediated vasodilation of the brachial artery: a report of the International Brachial Artery Reactivity Task Force. *J Am Coll Cardiol* **39**, 257–265.
- Corretti MC, Plotnick GD & Vogel RA (1995). Technical aspects of evaluating brachial artery vasodilation using high-frequency ultrasound. *Am J Physiol* **37**, H1397–H1404.
- Crispi F, Domínguez C, Llurba E, Martín-Gallán P, Cabero L & Gratacós E (2006). Placental angiogenic growth factors and uterine artery Doppler findings for characterization of different subsets in preeclampsia and in isolated intrauterine growth restriction. *Am J Obstet Gynecol* **195**, 201–207.
- Cudmore S, de Groot E & O’Kennedy N (2012). Food Health Claims - Cardiovascular Health. *Atl Food Clin trials*.

- Cuzzocrea S, Mazzon E, Dugo L, Di Paola R, Caputi AP & Salvemini D (2004). Superoxide: a key player in hypertension. *Faseb J* **18**, 94–101.
- Darrasse L (2003). Perspectives with cryogenic RF probes in biomedical MRI. *Biochimie* **85**, 915–937.
- Dawson EA, Green DJ, Cable NT & Thijssen DHJ (2013). Effects of acute exercise on flow-mediated dilatation in healthy humans. *J Appl Physiol* **115**, 1589–1598.
- Dawson NS, Zawieja DC, Wu MH & Granger HJ (2006). Signaling pathways mediating VEGF165-induced calcium transients and membrane depolarization in human endothelial cells. *FASEB J* **20**, 991–993.
- Deanfield JE, Halcox JP & Rabelink TJ (2007). Endothelial function and dysfunction: testing and clinical relevance. *Circulation* **115**, 1285–1295.
- Dodge M & Stinson C (2007). Perform what if analysis with the excel 2007 solver tool. Available at: <https://support.office.com/en-us/article/Perform-What-If-Analysis-with-the-Excel-2007-Solver-Tool-dc81f136-dfd2-4933-9595-4bfe12aa419d>.
- Donald AE, Charakida M, Cole TJ, Friberg P, Chowienczyk PJ, Millasseau SC, Deanfield JE & Halcox JP (2006). Non-Invasive Assessment of Endothelial Function. Which Technique? *J Am Coll Cardiol* **48**, 1846–1850.
- Donald AE, Charakida M, Falaschetti E, Lawlor DA, Halcox JP, Golding J, Hingorani AD, Smith GD & Deanfield JE (2010). Determinants of vascular phenotype in a large childhood population: The avon longitudinal study of parents and children (ALSPAC). *Eur Heart J* **31**, 1502–1510.
- Donald AE, Halcox JP, Charakida M, Storry C, Wallace SML, Cole TJ, Friberg P & Deanfield JE (2008). Methodological Approaches to Optimize Reproducibility and Power in Clinical Studies of Flow-Mediated Dilatation. *J Am Coll Cardiol* **51**, 1959–1964.
- Doshi SN, Naka KK, Payne N, Jones CJ, Ashton M, Lewis MJ & Goodfellow J (2001). Flow-mediated dilatation following wrist and upper arm occlusion in humans: the contribution of nitric oxide. *Clin Sci (Lond)* **101**, 629–635.
- Dower JI, Geleijnse JM, Gijsbers L, Schalkwijk C, Kromhout D & Hollman PC (2015a). Supplementation of the Pure Flavonoids Epicatechin and Quercetin Affects Some Biomarkers of Endothelial Dysfunction and Inflammation in (Pre)Hypertensive Adults: A Randomized Double-Blind, Placebo-Controlled, Crossover Trial. *J Nutr* **145**, 1459–1463.

- Dower JI, Geleijnse JM, Gilsbers L, Zock PL & Kromhout D (2015b). Effects of the pure flavonoids epicatechin and quercetin on vascular function and cardiometabolic health: a randomized, double-blind, placebo-controlled, crossover trial. *Am J Clin Nutr* **101**, 914–921.
- Du T, Hu D & Cai D (2015). Outflow Boundary Conditions for Blood Flow in Arterial Trees. *PLoS One* **10**, e0128597. doi10.1371/journal.pone0128597.
- Dunn KM & Nelson MT (2010). Calcium and diabetic vascular dysfunction. Focus on “Elevated Ca(2+) sparklet activity during acute hyperglycemia and diabetes in cerebral arterial smooth muscle cells”. *AJP Cell Physiol* **298**, C203–C205.
- Edelstein WA, Mahesh M & Carrino JA (2011). MRI: Time Is Dose—and Money and Versatility. *J Am Coll Radiol* **18**, 1492–1501.
- EFSA Panel on Dietetic Products N and A (2012). Scientific Opinion on the substantiation of a health claim related to cocoa flavanols and maintenance of normal endothelium-dependent vasodilation pursuant to Article 13 ( 5 ) of Regulation ( EC ) No 1924 / 2006 1. *EFSA J* **10**, 1–21.
- Elahi MM, Kong YX & Matata BM (2009). Oxidative stress as a mediator of cardiovascular disease. *Oxid Med Cell Longev* **2**, 259–269.
- Elster AD (1993). Gradient-echo MR imaging: techniques and acronyms. *Radiology* **186**, 1–8.
- Elster AD (2015a). Dual-Echo FSE. *Quest answers MRI*. Available at: <http://mri-q.com/dual-echo-fse.html>.
- Elster AD (2015b). Multiple RF pulses. *Quest answers MRI*. Available at: <http://mri-q.com/4-or-more-rf-pulses.html> [Accessed February 25, 2016].
- Etsuda H, Takase B, Uehata A, Kusano H, Hamabe A, Kuhara R, Akima T, Matsushima Y, Arakawa K, Satomura K, Kurita A & Ohsuzu F (1999). Morning attenuation of endothelium-dependent, flow-mediated dilation in healthy young men: possible connection to morning peak of cardiac events? *Clin Cardiol* **22**, 417–421.
- Evans DH, Schlindwein FS & Levene ML (1989). The relationship between time averaged intensity weighed mean velocity and time averaged maximum velocity in neonatal cerebral arteries. *Ultrasound Med Biol* **15**, 429–435.
- Faber JE & Stouffer GA (2008). Introduction to Basic Hemodynamic Principles. In *Cardiovascular Hemodynamics for the Clinician*, ed. Stouffer GA, pp. 3–16. Blackwell

Futura, Malden, Mass.

- Faita F, Masi S, Loukogeorgakis S, Gemignani V, Okorie M, Bianchini E, Charakida M, Demi M, Ghiadoni L & Deanfield JE (2011*a*). Comparison of two automatic methods for the assessment of brachial artery flow-mediated dilation. *J Hypertens* **29**, 85–90.
- Faita F, Masi S, Loukogeorgakis S, Gemignani V, Okorie M, Bianchini E, Charakida M, Demi M, Ghiadoni L & Eric J (2011*b*). Comparison of two automatic methods for the assessment of brachial artery flow-mediated dilation. *J hy* **29**, 85–90.
- Falk E (2006). Pathogenesis of Atherosclerosis. *J Am Coll Cardiol* **47**, 0–5.
- Félétou M & Vanhoutte PM (2006). Endothelial dysfunction: a multifaceted disorder (The Wiggers Award Lecture). *Am J Physiol Heart Circ Physiol* **291**, H985–H1002.
- Fernandes I a., Sales ARK, Rocha NG, Silva BM, Vianna LC & Da Nóbrega ACL (2014). Preserved flow-mediated dilation but delayed time-to-peak diameter in individuals with metabolic syndrome. *Clin Physiol Funct Imaging* **34**, 270–276.
- Fernandez B, Oster J, Lohezic M, Mandry D, Pietquin O, Vuissoz P-A, Felblinger J & 1Global (2009). Adaptive Trigger Delay Using a Predictive Model Applied to Black Blood Fast Spin Echo Cardiac Imaging in Systole. 2–3.
- Ferrara KW (2000). Blood flow measurement using Ultrasound. In *The biomedical Engineering Handbook 1*, 2nd edn., ed. Bronzino JD, pp. 23–41. CRC Press LLC, Florida.
- Fierstra J, Sobczyk O, Mandell DM, Poublanc J & Crawley AP (2013). Measuring cerebrovascular reactivity : what stimulus to use ? **23**, 5809–5821.
- Findlay BB, Gupta P, Szigyarto IC & Pyke KE (2013). Impaired brachial artery flow-mediated vasodilation in response to handgrip exercise-induced increases in shear stress in young smokers. *Vasc Med* **18**, 63–71.
- Firbank MJ, Coulthard A, Harrison RM & Williams ED (1999). A comparison of two methods for measuring the signal to noise ratio on MR images. *Phys Med Biol* **44**, N261–N264.
- Fujii N, Reinke MC, Brunt VE & Minson CT (2013). Impaired acetylcholine-induced cutaneous vasodilation in young smokers: roles of nitric oxide and prostanoids. *Am J Physiol Heart Circ Physiol* **304**, H667–H673.
- Fung Y. (1997). *Biomechanics*. Springer New York, New York.

- Gao J & Liu H (2012). In flow effects on functional MRI. *Neuroimage* **62**, 1035–1039.
- Germain AM, Romanik MC, Guerra I, Solari S, Reyes MS, Johnson RJ, Price K, Karumanchi SA & Vald??s G (2007). Endothelial dysfunction: A link among preeclampsia, recurrent pregnancy loss, and future cardiovascular events? *Hypertension* **49**, 90–95.
- van Geuns RM, Wielopolski PA, Bruin HG De, Rensing BJ, Ooijen PMA Van, Hulshoff M, Oudkerk M & Feyter PJ De (1999). Basic principles of Magnetic Resonance Imaging. *Prog Cardiovasc Dis* **42**, 149–156.
- Ghiadoni L, Faita F, Salvetti M, Cordiano C, Biggi A, Puato M, Di Monaco A, De Siati L, Volpe M, Ambrosio G, Gemignani V, Muiesan ML, Taddei S, Lanza G a. & Cosentino F (2012). Assessment of flow-mediated dilation reproducibility. *J Hypertens* **30**, 1399–1405.
- Gibbs BB, Dobrosielski DA, Lima M, Bonekamp S, Stewart KJ & Clark JM (2011). The association of arterial shear and flow-mediated dilation in diabetes. *Vasc Med* **16**, 267–274.
- Gittleman JL (2016). Allometry. *Encyclopaedia Br*. Available at: <http://www.britannica.com/science/allometry> [Accessed February 14, 2016].
- Gkaliagkousi E & Douma S (2009). The pathogenesis of arterial stiffness and its prognostic value in essential hypertension and cardiovascular diseases. *Hippokratia* **13**, 70–75.
- Graham S & Henkelman R (1997). Understanding pulsed magnetization transfer. *J Magn Reson* ...903–912.
- Granger HJ, Borders JL, Meininger GA, Morff RJ & Goodman AH (1983). Microcirculatory control systems. In *Physiology and Pharmacology of the Microcirculation*, pp. 209–236. Academic Press, Bethesda MD.
- Griendling KK, Ushio-Fukai M, Lassegue B & Alexander RW (1997). Angiotensin II signaling in vascular smooth muscle. New concepts. *Hypertension* **29**, 366–373.
- Halcox JPJ, Donald AE, Ellins E, Witte DR, Shipley MJ, Brunner EJ, Marmot MG & Deanfield JE (2009). Endothelial function predicts progression of carotid intima-media thickness. *Circulation* **119**, 1005–1012.
- Halcox JPJ, Schenke WH, Zalos G, Mincemoyer R, Prasad A, Waclawiw MA, Nour KRA & Quyyumi AA (2002). Prognostic value of coronary vascular endothelial dysfunction. *Circulation* **106**, 653–658.
- Hamilton P, Lockhart CJ, McCann a J, Agnew CE, Harbinson MT, McClenaghan V, Bleakley

- C, McGivern RC & McVeigh G (2011). Flow-mediated dilatation of the brachial artery is a poorly reproducible indicator of microvascular function in Type I diabetes mellitus. *QJM* **104**, 589–597.
- Hansen KB & Shadden SC (2016). A reduced-dimensional model for near-wall transport in cardiovascular flows. *Biomech Model Mechanobiol* **15**, 713–722.
- Harris R a & Padilla J (2007). Proper “normalization” of flow-mediated dilation for shear. *J Appl Physiol* **103**, 1108; author reply 1109.
- Harris R a, Padilla J, Rink LD & Wallace JP (2006). Variability of flow-mediated dilation measurements with repetitive reactive hyperemia. *Vasc Med* **11**, 1–6.
- Harris RA, Nishiyama SK, Wray DW & Richardson RS (2010). Ultrasound Assessment of Flow-Mediated Dilation. *Hypertension* **55**, 1075–1085.
- Harrison M, Parkhurst K, Tarumi T, Lin HF & Tanaka H (2011). Low flow-mediated constriction: Prevalence, impact and physiological determinant. *Clin Physiol Funct Imaging* **31**, 394–398.
- Hartung MP, Grist TM & François CJ (2011). Magnetic resonance angiography : current status and future directions. *J Cardiovasc Magn Reson* **13**, 19–25.
- Hashemi R, Bradley WJ & Lisanti C (2010). *Flow Phenomena. In MRI: The Basics*, 3rd editio. Wolters Kluwer. Available at: <https://www.inkling.com/read/mri-the-basics-hashemi-bradley-lisanti-3rd/chapter-26/flow-phenomena>.
- Hashimoto M, Akishita M, Eto M, Ishikawa M, Kozaki K, Toba K, Sagara Y, Taketani Y, Orimo H & Ouchi Y (1995). Modulation of endothelium-dependent flow-mediated dilatation of the brachial artery by sex and menstrual cycle. *Circulation* **92**, 3431–3435.
- Hayes C & Axel L (1985). Noise performance of surface coils for magnetic resonance imaging at 1.5 T. 604–607.
- Hendrick RE (2008). Tissue Relaxation. In *Breast MRI: Fundamentals and Technical Aspects.*, 1st edn., ed. Hendrick RE, pp. 19–29. Springer-Verlag, New York.
- Herscovitch P & Raichle ME (1985). What is the correct value for the brain--blood partition coefficient for water? *J Cereb Blood Flow Metab* **5**, 65–69.
- Hinshaw WS, Bottomley PA & Holland GN (1977). Radiographic thin-section image of the human wrist by nuclear magnetic resonance. *Nature* **270**, 722–723.

- Hoeben A, Landuyt B, Highley MS, Wildiers H, Oosterom ATVAN & Bruijn EADE (2004). Vascular Endothelial Growth Factor and Angiogenesis. *Pharmacol Rev* **56**, 549–580.
- Hopkins WG (2000). Measures of reliability in sports medicine and science. *Sports Med* **30**, 1–15.
- Hornak JP (2006a). Spin physics. “*The Basics MRI*” *Electron version* Chapter 3. Available at: <http://www.cis.rit.edu/htbooks/mri/chap-3/chap-3.htm> [Accessed December 20, 2015].
- Hornak JP (2006b). Image presentation. “*The Basics MRI*” *Electron version*. Available at: <http://www.cis.rit.edu/htbooks/mri/chap-10/chap-10.htm> [Accessed February 15, 2016].
- Hoskins PR & Hose DR (2017). The Arterial System I. Pressure, Flow and Stiffness. In *Cardiovascular Biomechanics*, ed. Hoskins PR, Lawford P V & Doyle BJ, pp. 65–81. Springer International Publishing, Cham. Available at: [https://doi.org/10.1007/978-3-319-46407-7\\_4](https://doi.org/10.1007/978-3-319-46407-7_4).
- Hoult DI & Lauterbur PC (1979). The sensitivity of the zeugmatographic experiment involving human samples. *J Magn Reson* **34**, 425–433.
- Huang T, James CA, Tichnell C, Brittney M, Xue J, Calkins H & Tereshchenko LG (2015). Statistical evaluation of reproducibility of automated ECG measurements: an example from arrhythmogenic right ventricular dysplasia/cardiomyopathy clinic. *Biomed Signal Process Control* **1**, 23–30.
- Hussain ST, Smith RE, Medbak S, Wood RF & Whipp BJ (1996). Haemodynamic and metabolic responses of the lower limb after high intensity exercise in humans. *Exp Physiol* **81**, 173–187.
- Hwang I-C, Kim K-H, Choi W-S, Kim H-J, Im M-S, Kim Y-J, Kim S-H, Kim M-A, Sohn D-W & Zo J-H (2012). Impact of acute exercise on brachial artery flow-mediated dilatation in young healthy people. *Cardiovasc Ultrasound* **10**, 39.
- Iglarz M, Steiner P, Wanner D, Rey M, Hess P & Clozel M (2015). Vascular effects of endothelin receptor antagonists depends on their selectivity for ETA vs. ETB receptors and on the functionality of endothelial ETB receptors. *J Cardiovasc Pharmacol* **66**, 1.
- ImageJ (2003). ImageJ User Guide. *IJ* **146r**187.
- Irace C, Tschakovsky ME, Carallo C, Cortese C & Gnasso A (2008). Endothelial dysfunction or dysfunctions? Identification of three different FMD responses in males with type 2 diabetes. *Atherosclerosis* **200**, 439–445.



- Jackson CE, Shirodaria CC, Lee JM & Francis JM et al (2009). Reproducibility and accuracy of automated measurement for dynamic arterial lumen area by cardiovascular magnetic resonance. *Int J Cardiovasc Imaging* **797–808**.
- Järvisalo MJ, Jartti L, Marniemi J, Rönnemaa T, Viikari JS a, Lehtimäki T & Raitakari OT (2006). Determinants of short-term variation in arterial flow-mediated dilatation in healthy young men. *Clin Sci (Lond)* **110**, 475–482.
- Jeong E-K, Parker DL, Tsuruda JS & Won J-Y (2002). Reduction of flow-related signal loss in flow-compensated 3D TOF MR angiography, using variable echo time (3D TOF-VTE). *Magn Reson Med* **48**, 667–676.
- Jiang B, Seddon M, Fok H, Donald A & Chowienczyk P (2011). Flow-mediated dilation of the radial artery is offset by flow-induced reduction in transmural pressure. *Hypertension* **57**, 1145–1150.
- Joannides R, Haefeli WE, Linder L, Richard V & Bakkali EH (1995). Nitric Oxide Is Responsible for Flow-Dependent Dilatation of Human Peripheral Conduit Arteries In Vivo. *Circulation* **91**, 1314–1319.
- Jones H, Green DJ, George K & Atkinson G (2010). Intermittent exercise abolishes the diurnal variation in endothelial-dependent flow-mediated dilation in humans. *Am J Physiol Regul Integr Comp Physiol* **298**, R427–R432.
- Joyner MJ & Dietz NM (1997). Nitric oxide and vasodilation in human limbs. *J Appl Physiol* **83**, 1785–1796.
- Jun SS, Chen Z, Pace MC & Shaul PW (1998). Estrogen upregulates cyclooxygenase-1 gene expression in ovine fetal pulmonary artery endothelium. *J Clin Invest* **102**, 176–183.
- Kelm M (1998). Nitric Oxide Metabolism and Breakdown.pdf. *Biochim Biophys Acta* **1411**, 273–289.
- Kelm M (2002). Flow-mediated dilatation in human circulation: diagnostic and therapeutic aspects. *Am J Physiol Hear Circ Physiol* **2002**, H1–H5.
- Khademi A, Venetsanopoulos A & Moody AR (2014). Generalized method for partial volume estimation and tissue segmentation in cerebral magnetic resonance images. *J Med Imaging* **1**, 014002.
- Khademi AE (2012). Medical Image Processing Techniques for the Objective Quantification of Pathology in Magnetic Resonance Images of the Brain by.

- Khurana I (2007). Cardiovascular system. In *Textbook of human physiology for dental students*, pp. 161–270. Elsevier, New Delhi.
- Kim S & Parker DL (2012). Time of Flight Angiography. In *Magnetic Resonance Angiography: Principles and Applications*, ed. Carr JC & Carroll TJ, pp. 39–51. Springer New York, New York, NY. Available at: <http://link.springer.com/10.1007/978-1-4419-1686-0> [Accessed January 31, 2014].
- Kim YC, Yun KH, Woo SH, Jeong YH, Lim JH, Hwang KB, Jeong JW, Lee MR, Lee JM, Rhee SJ, Kim N-H, Oh SK & Jeong J-W (2015). Diurnal variation of flow-mediated dilatation in healthy humans. *Clin Hypertens* **21**, 6.
- Kimura T, Ikedo M & Takemoto S (2009). Hybrid of opposite-contrast MR angiography (HOP-MRA) combining time-of-flight and flow-sensitive black-blood contrasts. *Magn Reson Med* **62**, 450–458.
- Klabunde RE (2007). Hemodynamics (Pressure, Flow, and Resistance). *Cardiovasc Physiol Concepts*. Available at: <http://www.cvphysiology.com/Hemodynamics/H001.htm> [Accessed February 1, 2016].
- Kobayashi N, DeLano FA & Schmid-Schönbein GW (2005). Oxidative stress promotes endothelial cell apoptosis and loss of microvessels in the spontaneously hypertensive rats. *Arterioscler Thromb Vasc Biol* **25**, 2114–2121.
- Kohan DE, Rossi NF, Inscho EW & Pollock DM (2011). Regulation of Blood Pressure and Salt Homeostasis by Endothelin. *Physiol Rev* **91**, 1–77.
- Kooijman M, Thijssen DHJ, de Groot PCE, Bleeker MWP, van Kuppevelt HJM, Green DJ, Rongen G a, Smits P & Hopman MTE (2008). Flow-mediated dilatation in the superficial femoral artery is nitric oxide mediated in humans. *J Physiol* **586**, 1137–1145.
- Koulouris S, Marousis P, Anninos H, Melpidou A, Lekakis J, Pitsavos C, Zoulien Z & Manolis AS (2010). Postprandial Endothelial Function : The Effect of Various Types of Fat and of Red Wine Intake on Flow- Mediated Dilatation in Healthy Volunteers. **5**, 146–153.
- Kuhl CK, Traber F & Schild HH (2008). Whole-Body High-Field- Strength (3.0-T) MR Imaging in Clinical Practice Part I. Technical Considerations and Clinical Applications1. *Radiology* **246**, 675–696.
- Kylintireas I, Shirodaria C, Lee JMS, Cunningon C, Lindsay A, Francis J, Robson MD, Neubauer S, Channon KM & Choudhury RP (2011). Multimodal cardiovascular magnetic

- resonance quantifies regional variation in vascular structure and function in patients with coronary artery disease: relationships with coronary disease severity. *J Cardiovasc Magn Reson* **13**, 61.
- Labes D (2016). PowerTOST: Power and Sample Size Based on Two One-Sided t-Tests (TOST) for (Bio) Equivalence Studies. R package version 3.1.3.
- Lambiase MJ, Dornb J, Thurston RC & Roemmich JN (2014). Flow-mediated dilation and exercise blood pressure in healthy adolescents. *J Sci Med Sport* **17**, 425–429.
- Langham MC, Li C, Englund EK, Chirico EN, Mohler ER, Floyd TF & Wehrli FW (2013). Vessel-wall imaging and quantification of flow-mediated dilation using water-selective 3D SSFP-echo. *J Cardiovasc Magn Reson* **15**, 100.
- Laredo J & Lee B (2008). Upper extremity arterial diseases. In *Textbook of peripheral vascular interventions*.
- Laub G, Gaa J & Drobnitzky M (1998). Magnetic Resonance Angiography Techniques. *Electromedia* **66**, 68–75.
- Lauer T, Heiss C, Balzer J, Keymel S, Kelm M, Preik M & Rassaf T (2008). Resting microvascular resistance and conduit artery tone: relevance to endothelium-dependent flow-mediated dilation. *Eur J Cardiovasc Prev Rehabil* **15**, 677–682.
- Laurent S, Cockcroft J, Bortel L Van, Boutouyrie P, Giannattasio C, Hayoz D, Pannier B, Vlachopoulos C & Wilkinson I (2006). Expert consensus document on arterial stiffness : methodological issues and clinical applications. *Eur Heart J* **27**, 2588–2605.
- Lavoie JL (2003). Minireview: Overview of the Renin-Angiotensin System--An Endocrine and Paracrine System. *Endocrinology* **144**, 2179–2183.
- Lee JMS, Shirodaria C, Jackson CE, Robson MD, Antoniadis C, Francis JM, Wiesmann F, Channon KM, Neubauer S & Choudhury RP (2007). Multi-modal magnetic resonance imaging quantifies atherosclerosis and vascular dysfunction in patients with type 2 diabetes mellitus. *Diabetes Vasc Dis Res* **4**, 44–48.
- Lee JMS, Wiesmann F, Shirodaria C, Leeson P, Petersen SE, Francis JM, Jackson CE, Robson MD, Neubauer S, Channon KM & Choudhury RP (2008). Early changes in arterial structure and function following statin initiation : Quantification by magnetic resonance imaging. *Atherosclerosis* **197**, 951–958.
- Lee W (2014). General principles of carotid Doppler ultrasonography. *Ultrasonography* **33**, 11–

17.

Leeson (2006). Cardiovascular Magnetic Resonance Imaging for Non-Invasive Assessment of Vascular Function : 381–387.

Leeson, Leeson C, Robinson M, Francis J, Robson M, Channon K, Neubauer S & Wiesmann F (2006). Cardiovascular Magnetic Resonance Imaging for Non-Invasive Assessment of Vascular Function: Validation against Ultrasound. *J Cardiovasc Magn Reson* **8**, 381–387.

Leeson P, Thorne S, Donald a, Mullen M, Clarkson P & Deanfield J (1997). Non-invasive measurement of endothelial function: effect on brachial artery dilatation of graded endothelial dependent and independent stimuli. *Heart* **78**, 22–27.

Lefferts WK, Augustine JA, Heffernan KS & Phillips AA (2014). Effect of acute resistance exercise on carotid artery stiffness and cerebral blood flow pulsatility. **5**, 1–10.

Lekakis J et al. (2011). Methods for evaluating endothelial function: a position statement from the European Society of Cardiology Working Group on Peripheral Circulation. *Eur J Cardiovasc rehab*; DOI: 10.1177/1741826711398179.

Lenders J, Janssen GJ, Smits P & Thien T (1991). Role of the wrist cuff in forearm plethysmography. *Clin Sci (Lond)* **80**, 413–417.

Lesage D, Angelini ED, Bloch I & Funka-Lea G (2009). A review of 3D vessel lumen segmentation techniques: Models, features and extraction schemes. *Med Image Anal* **13**, 819–845.

Levy BI, Schiffrin EL, Mourad J-JJ, Agostini D, Vicaute E, Safar ME & Struijker-Boudier H a J (2008). Impaired tissue perfusion: a pathology common to hypertension, obesity, and diabetes mellitus. *Circulation* **118**, 968–976.

Lewis SJ (1999). Quantifying measurement error. In S. Anderson (Ed.), Current and recent research in osteoarchaeology. In *Proceedings of the 4th, 5th and 6th meetings of the Osteoarchaeological Research Group.*, pp. 54–55. Oxbow Books, Oxford.

Lipton ML (2008). Image Contrast: T1, T2, T2\*, and Proton Density. In *Totally accessible MRI: a user's guide to principles, technology, and applications*, pp. 38–46. Springer, New York, NY.

Liuni A, Luca MC, Lisi M, Dragoni S, di Stolfo G, Mariani JA, Uxa A, Gori T & Parker JD (2010). Observations of time-based measures of flow-mediated dilation of forearm conduit arteries: implications for the accurate assessment of endothelial function. *Am J Physiol*

*Heart Circ Physiol* **299**, H939–H945.

Lowry JL, Brovkovich V, Zhang Y & Skidgel R a (2013). Endothelial nitric-oxide synthase activation generates an inducible nitric-oxide synthase-like output of nitric oxide in inflamed endothelium. *J Biol Chem* **288**, 4174–4193.

Lu H, Clingman C, Golay X & Van Zijl PCM (2004). Determining the longitudinal relaxation time (T1) of blood at 3.0 tesla. *Magn Reson Med* **52**, 679–682.

Lu H & van Zijl PCM (2005). Experimental measurement of extravascular parenchymal BOLD effects and tissue oxygen extraction fractions using multi-echo VASO fMRI at 1.5 and 3.0 T. *Magn Reson Med* **53**, 808–816.

Luca MC, Liuni A, Mclaughlin K, Gori T & Parker JD (2013). Daily Ischemic Preconditioning Provides Sustained Protection From Ischemia–Reperfusion Induced Endothelial Dysfunction: A Human Study. *J Am Heart Assoc*; DOI: 10.1161/JAHA.112.000075.

Luke H (1999). The origins of the sampling theorem. *IEEE Commun Mag* **37**, 106–108.

Macovski A (1996). Noise in MRI. *Magn Reson Med* **36**, 494–497.

Maczewski M & Beresewicz A (1998). The role of adenosine and ATP-sensitive potassium channels in the protection afforded by ischemic preconditioning against the post-ischemic endothelial dysfunction in guinea-pig hearts. *J Mol Cell Cardiol* **30**, 1735–1747.

Magnotta V a. & Friedman L (2006). Measurement of signal-to-noise and contrast-to-noise in the fBIRN multicenter imaging study. *J Digit Imaging* **19**, 140–147.

Mannion TC, Vita J a, Keaney JF, Benjamin EJ, Hunter L & Polak JF (1998). Non-invasive assessment of brachial artery endothelial vasomotor function: the effect of cuff position on level of discomfort and vasomotor responses. *Vasc Med* **3**, 263–267.

Marinos A, Celedonio JE, Ramirez CE, Gottlieb J, Gamboa A, Hui N, Yu C, Michael Stein C, Biaggioni I & Shibao CA (2015). Time-Course Analysis of Flow Mediated Dilatation for the Evaluation of Endothelial Function After a High-Fat Meal in African Americans. *J Am Heart Assoc* **4**, e002388.

Martins WP, Natri CO, Ferriani R a & Filho FM (2008). Brachial artery pulsatility index change 1 minute after 5-minute forearm compression: comparison with flow-mediated dilatation. *J Ultrasound Med* **27**, 693–699.

Matsuzawa Y, Kwon T-G, Lennon RJ, Lerman LO & Lerman A (2015). Prognostic Value of

Flow-Mediated Vasodilation in Brachial Artery and Fingertip Artery for Cardiovascular Events: A Systematic Review and Meta-Analysis. *J Am Heart Assoc* **4**, e002270–e002270.

- McBride G (2005). A proposal for strength of agreement criteria for Lin's concordance correlation coefficient. *NIWA Client Rep HAM2005-0621–10*. Available at: <http://www.medcalc.org/download/pdf/McBride2005.pdf> [Accessed March 20, 2016].
- McLay K (2012). *Reliability of flow-mediated dilation measures in the popliteal artery and implications for use in clinical and research practices* (thesis). The University of Western Ontario. Available at: <http://ir.lib.uwo.ca/etd/831/>.
- McRobbie DW, Moore EA, Graves M & Prince MR (2006a). What you set is what you get: basic image optimization. In *In MRI from picture to proton*, Second., pp. 70–71. Cambridge University Press, New York.
- McRobbie DW, Moore EA, Graves M & Prince MR (2006b). The devil's in the detail: pixels, matrices and slices. In *In MRI from picture to proton*, Second., pp. 46–62. Cambridge University Press, New York.
- McRobbie DW, Moore EA, Graves M & Prince MR (2006c). Go with the flow: MR angiography. In *MRI from picture to proton*, Second., ed. McRobbie DW, pp. 271–281. Cambridge University Press, New York.
- McRobbie DW, Moore EA, Graves M & Prince MR (2006d). Improving your image: how to avoid artefacts. In *MRI from picture to proton*, Second., pp. 79–107.
- Mezrich R (1995). A perspective on k-space. *Radiology* **195**, 297–315.
- Al Mheid I & Quyyumi A a (2013). Allometric scaling of endothelium-dependent vasodilation: brachial artery flow-mediated dilation coming of age? *Vasc Med* **18**, 368–371.
- Mitchell J a, Ali F, Bailey L, Moreno L & Harrington LS (2008). Role of nitric oxide and prostacyclin as vasoactive hormones released by the endothelium. *Exp Physiol* **93**, 141–147.
- MMcRobbie DW, Moore EA, Graves M & Prince MR (2006). Spaced out: spatial encoding. In *In MRI from picture to proton*, Second., pp. 108–136. Cambridge University Press, New York.
- Moens AL, Goovaerts I, Claeys MJ & Vrints CJ (2005). Flow-mediated vasodilation: a diagnostic instrument, or an experimental tool? *Chest* **127**, 2254–2263.
- Mohandas N, Evans E, Kukan B & Leung A (1985). Sickle erythrocyte adherence to vascular

- endothelium. Morphology correlates and the requirement for divalent cations and collagen-binding plasma proteins. *J Clin Invest* **76**, 1605–1612.
- de Montalembert M, Aggoun Y, Niakate A, Szezepanski I & Bonnet D (2007). Endothelial-Dependent Vasodilation Is Impaired In Children With Sickle Cell Disease. *Hematologica* **92**, 1709–1710.
- Mortensen SP, Bune LT, Saltin B & Pilegaard H (2009). ATP-induced vasodilation and purinergic receptors in the human leg : roles of nitric oxide , prostaglandins , and adenosine. 1140–1148.
- Mott RL (2006). Reynolds number, Laminar flow, Turbulent flow and energy losses due to friction. In *Applied Fluid Mechanics*, Sixth Edit., pp. 226–254. Prentice Hall, Upper Saddle River NJ.
- Mullen MJ, Kharbanda RK, Cross J, Donald AE, Taylor M, Deanfield JE, Macallister RJ & Vallance P (2001). Heterogenous Nature of Flow-Mediated Dilatation in Human Relevance to Endothelial Dysfunction in Hypercholesterolemia. *Circ Res* 145–151.
- Mungrue IN & Husain M (2002). The Role of NOS in Heart Failure : Lessons from Murine. 407–422.
- Nacif SM, Zavodni A, Kawel N, Choi E-Y, Lima JAC & Bluemke DA (2012). Cardiac magnetic resonance imaging and its electrocardiographs (ECG): tips and tricks. *Int J Cardiovasc Imaging* **28**, 1465–1475.
- Nakayama T (2006). Prostacyclin analogues: prevention of cardiovascular diseases. *Cardiovasc Hematol AgentsMed Chem* **4**, 351–359.
- Newby DE, Boon NA & Webb DJ (1997). Comparison of Forearm Vasodilatation to Substance P and Acetylcholine: Contribution of Nitric Oxide. *Clin Sci* **92**, 133–138.
- Nishiyama SK, Walter Wray D, Berkstresser K, Ramaswamy M & Richardson RS (2007). Limb-specific differences in flow-mediated dilation: the role of shear rate. *J Appl Physiol* **103**, 843–851.
- Oelhafen M, Schwitter J, Kozerke S, Luechinger R & Boesiger P (2006). Assessing arterial blood flow and vessel area variations using real-time zonal phase-contrast MRI. *J Magn Reson Imaging* **23**, 422–429.
- Oliver J, Swoboda P, Plein S, English K, Ballard G & Greenwood JP (2012). Reproducibility of brachial artery flow-mediated and glyceryl trinitrate-mediated dilatation by 3Tesla CMR. *J*

*Cardiovasc Magn Reson* **14**, P292.

Ong PJJ, Webb CM, Sorensen MB, Hayward CS & Collins P (2002). A comparison of brachial artery reactivity measured by external and intravascular ultrasound. *Ultrasound Med Biol* **28**, 911–916.

Onkelinx S, Cornelissen V, Goetschalckx K, Thomaes T, Verhamme P & Vanhees L (2012). Reproducibility of different methods to measure the endothelial function. *Vasc Med* **17**, 79–84.

Osada T & Radegran G (2005). Alterations in the rheological flow profile in conduit femoral artery during rhythmic thigh muscle contractions in humans. *JpnJ Physiol* **55**, 19–28.

Oshinski JN, Delfino JG, Sharma P, Gharib AM & Pettigrew RI (2010). Cardiovascular magnetic resonance at 3.0 T: current state of the art. *J Cardiovasc magn Reson* **12**, 55.

Oshio K & Jolesz F (1993). Simultaneous acquisition of proton density, T1, and T2 images with triple contrast RARE sequence. *J Comput Assist Tomogr* **17**, 333–338.

Ostrem JD, Dengel DR, Marlatt KL & Steinberger J (2014). Comparison of baseline brachial artery measurements and effect on peak flow-mediated dilation. *Clin Physiol Funct Imaging* **34**–40.

Oswald S (2015). FlexParamCurve: Tools to Fit Flexible Parametric Curves. *Compr R Arch Netw*. Available at: [cran.r-project.org/web/packages/FlexParamCurve/FlexParamCurve.pdf](http://cran.r-project.org/web/packages/FlexParamCurve/FlexParamCurve.pdf).

Oswald SA, Nisbet ICT, Chiaradia A & Arnold JM (2012). FlexParamCurve: R package for flexible fitting of nonlinear parametric curves. *Methods Ecol Evol* **3**, 1073–1077.

Otto ME, Svatikova A, De Mattos Barretto RB, Santos S, Hoffmann M, Khandheria B & Somers V (2004). Early morning attenuation of endothelial function in healthy humans. *Circulation* **109**, 2507–2510.

Oyre S, Ringgaard S, Kozerke S, Paaske WP, Scheidegger MB, Boesiger P & Pedersen EM (1998). Quantitation of circumferential subpixel vessel wall position and wall shear stress by multiple sectored three-dimensional paraboloid modeling of velocity encoded cine MR. *Magn Reson Med* **40**, 645–655.

Ozgun Z, Ucerler H & Aktan Ikiz ZA (2009). Branching patterns of the popliteal artery and its clinical importance. *Surg Radiol Anat* **31**, 357–362.

Ozkor MA & Quyyumi AA (2011). Endothelium-derived hyperpolarizing factor and vascular



- function. *Cardiol Res Pr* **2011**, 156146.
- Padilla J, Harris R a, Fly AD, Rink LD & Wallace JP (2006). A comparison between active- and reactive-hyperaemia-induced brachial artery vasodilation. *Clin Sci (Lond)* **110**, 387–392.
- Padilla J, Johnson BD, Newcomer SC, Wilhite DP, Mickleborough TD, Fly AD, Mather KJ & Wallace JP (2008). Normalization of flow-mediated dilation to shear stress area under the curve eliminates the impact of variable hyperemic stimulus. *Cardiovasc Ultrasound* **6**, 44.
- Padilla J, Johnson BD, Newcomer SC, Wilhite DP, Mickleborough TD, Fly AD, Mather KJ & Wallace JP (2009). Adjusting flow-mediated dilation for shear stress stimulus allows demonstration of endothelial dysfunction in a population with moderate cardiovascular risk. *J Vasc Res* **46**, 592–600.
- Pai VM (2007). Phase contrast using multiecho steady-state free precession. *Magn Reson Med* **58**, 419–424.
- Pamboucas C & Nihoyannopoulos P (2006). Cardiovascular magnetic resonance at 3 Tesla: advantages, limitations and clinical potential. *Hell J Cardiol* **47**, 170–173.
- Papaioannou TG & Stefanadis C (2005). Vascular wall shear stress: basic principles and methods. *Hellenic J Cardiol* **46**, 9–15.
- Paradisi G, Biaggi A, Savone R, Ianniello F, Tomei C, Caforio L & Caruso A (2006). Cardiovascular risk factors in healthy women with previous gestational hypertension. *J Clin Endocrinol Metab* **91**, 1233–1238.
- Parker B a, Ridout SJ & Proctor DN (2006). Age and flow-mediated dilation: a comparison of dilatory responsiveness in the brachial and popliteal arteries. *Am J Physiol Heart Circ Physiol* **291**, H3043–H3049.
- Pasini FL, Capecchi P & Di Perri T (2000). Adenosine and chronic ischemia of the lower limbs. *Vasc Med* **5**, 243–250.
- Peretz A, Leotta DF, Sullivan JH, Trenga C a, Sands FN, Aulet MR, Paun M, Gill E a & Kaufman JD (2007). Flow mediated dilation of the brachial artery: an investigation of methods requiring further standardization. *BMC Cardiovasc Disord* **7**, 11.
- Perrin V (2013). *Flow. In MRI techniques*. John Wiley & Sons, Inc, Hoboken, NJ USA.
- Phillips SA, Das E, Wang J, Pritchard K & Gutterman DD (2011). Resistance and aerobic exercise protects against acute endothelial impairment induced by a single exposure to

- hypertension during exertion. *J Appl Physiol* **110**, 1013–1020.
- Pohl U, De Wit C & Gloe T (2000). Large arterioles in the control of blood flow: role of endothelium-dependent dilation. *Acta Physiol Scand* **168**, 505–510.
- Ponzini R, Vergara C, Rizzo G, Veneziani A, Roghi A, Vanzulli A, Parodi O & Redaelli A (2010). Womersley number-based estimates of blood flow rate in Doppler analysis : In vivo validation by means of phase-contrast MRI. *IEEE Trans Biomed Eng* **57**, 1807–1815.
- Pooley RA (2005). AAPM/RSNA Physics Tutorial for Residents: Fundamental Physics of MR Imaging. *Radiographics* **25**, 1087–1099.
- Pozniak M, Zagzebski J & Scanlan K (1992). Spectral and color Doppler artifacts. *Radiographics* **12**, 35–44.
- Pyke K, Green DJ, Weisbrod C, Best M, Dembo L, O’Driscoll G & Tschakovsky M (2010). Nitric oxide is not obligatory for radial artery flow-mediated dilation following release of 5 or 10 min distal occlusion. *Am J Physiol Hear Circ Physiol* **298**, H119–H126.
- Pyke KE, Dwyer EM & Tschakovsky ME (2004). Impact of controlling shear rate on flow-mediated dilation responses in the brachial artery of humans. *J Appl Physiol* **97**, 499–508.
- Pyke KE & Jazuli F (2011). Impact of repeated increases in shear stress via reactive hyperemia and handgrip exercise: no evidence of systematic changes in brachial artery FMD. *Am J Physiol Hear Circ Physiol* **300**, H1078–H1089.
- Pyke KE & Tschakovsky ME (2005). The relationship between shear stress and flow-mediated dilatation: implications for the assessment of endothelial function. *J Physiol* **568**, 357–369.
- Pyke KE & Tschakovsky ME (2007). Peak vs. total reactive hyperemia: which determines the magnitude of flow-mediated dilation? *J Appl Physiol* **102**, 1510–1519.
- Quyyumi A (1998). Endothelial function in health and disease: new insights into the genesis of cardiovascular disease. *Am J Med* **105**, 325–395.
- Raitakari OT & Celermajer DS (2000). Flow-mediated dilatation. 397–404.
- Rakobowchuk M, Tanguay S, Burgomaster KA, Howarth KR, Gibala MJ & MacDonald MJ (2008). Sprint interval and traditional endurance training induce similar improvements in peripheral arterial stiffness and flow-mediated dilation in healthy humans. *AJP Regul Integr Comp Physiol* **295**, R236–R242.

- Ramalho M, Heredia V, de Campos RO, Dale BM, Azevedo RM & Semelka RC (2012). In-phase and out-of-phase gradient-echo imaging in abdominal studies: intra-individual comparison of three different techniques. *Acta radiol* **53**, 441–449.
- Rasband W (2005). Export intensity value. *ImageJ Free forum by Nabble*. Available at: <http://imagej.1557.x6.nabble.com/export-intensity-value-tp3704494p3704495.html> [Accessed October 12, 2015].
- Rasband W, Dougherty B, Collins T, Karperian A & Stervbo U (2006). ImageJ: Multi-Measure plugin (version 4). Available at: <http://www.optinav.com/Multi-Measure.htm> [Accessed June 17, 2015].
- Rasband W & Landini G (2004). ImageJ: Calculator Plus plugin (version 4). Available at: <http://rsb.info.nih.gov/ij/plugins/calculator-plus.html> [Accessed June 20, 2015].
- Rassaf T, Preik M, Kleinbongard P, Lauer T, Heiß C, Strauer BE, Feelisch M & Kelm M (2002). Evidence for in vivo transport of bioactive nitric oxide in human plasma. *J Clin Invest* **109**, 1241–1248.
- Resnick L, Militianu D, Cunnings A, Pipe J, Evelhoch J & Soulen R (1997). Direct magnetic resonance determination of aortic distensibility in essential hypertension: relation to age, abdominal visceral fat, and in situ intracellular free magnesium. *Hypertension* **3**, 654–659.
- Richards JA, Wigmore SJ & Devey LR (2010). Heme oxygenase system in hepatic ischemia-reperfusion injury. *World J Gastroenterol*.
- Ridler T & Calvard S (1978). Picture thresholding using an iterative selection method. *IEEE Trans Sys, Man, Cyber* **SMC-8**, 630–632.
- Robinson A (2016). Equivalence: Provides Tests and Graphics for Assessing Tests of Equivalence. R package version 3.1.3.
- Rodbard D (1974). Statistical Quality Control and Routine Data Processing for Radioimmunoassays and Immunoradiometric Assays. **20**, 1255–1270.
- Roes SD, Korosoglou G, Schar M, Westenberg JJ, Osch MJP van, Roos A de & Stuber M (2008). Correction for Heart Rate Variability During 3D Whole Heart MR Coronary Angiography. **1053**, 1046–1053.
- Rudolph TK, Ruempler K, Schwedhelm E, Tan-Andresen J, Riederer U, Böger RH & Maas R (2007). Acute effects of various fast-food meals on vascular function and cardiovascular disease risk markers: the Hamburg Burger Trial. *Am J Clin Nutr* **86**, 334–340.

- Sanada H, Higashi Y, Goto C, Chayama K, Yoshizumi M & Sueda T (2005). Vascular function in patients with lower extremity peripheral arterial disease: a comparison of functions in upper and lower extremities. *Atherosclerosis* **178**, 179–185.
- Sandgren T, Sonesson B, Ahlgren A & Lanne T (1998). Factors predicting the diameter of the popliteal artery in healthy humans. *J Vasc Surg* **28**, 284–289.
- Sandoo A, Carroll D, Metsios GS, Kitas GD & Veldhuijzen van Zanten JJCS (2011). The association between microvascular and macrovascular endothelial function in patients with rheumatoid arthritis: a cross-sectional study. *Arthritis Res Ther* **13**, R99.
- Schächinger V & Zeiher AM (1995). Quantitative Assessment of Coronary Vasoreactivity in Humans In Vivo. *Circulation* **92**, 2087–2094.
- Schroeder S, Enderle MD, Ossen R, Meisner C, Baumbach A, Pfohl M, Herdeg C, Oberhoff M, Haering HU & Karsch KR (1999). Noninvasive determination of endothelium-mediated vasodilation as a screening test for coronary artery disease: Pilot study to assess the predictive value in comparison with angina pectoris, exercise electrocardiography, and myocardial perfusion imaging. *Am Heart J* **138**, 731–739.
- Scissons R (2008). Characterizing Triphasic, Biphasic, and Monophasic Doppler Waveforms. *J Diagnostic Med Sonogr* **24**, 269–276.
- Secomb TW & Pries AR (2007). Basic Principles of Hemodynamics. In *Handbook of Hemorheology and Hemodynamics*, ed. Baskurt OK, pp. 289–366. IOS Press, Amsterdam.
- Shan Y, Lin J, Xu P, Zeng M, Lin H & Yan H (2014). The combined effect of hypertension and type 2 diabetes mellitus on aortic stiffness and endothelial dysfunction: An integrated study with high-resolution MRI. *Magn Reson Imaging* **32**, 211–216.
- Shan Y, Lin J, Xu P, Zhou J & Zeng M (2012). Comprehensive Assessment of Aortic Compliance and Brachial Endothelial Function Using 3.0-T High-Resolution MRI: A feasibility study. *J Comput Assist Tomogr* **36**, 437–442.
- Silber HA, Bluemke DA, Ouyang P, Du YP, Post WS & Lima JAC (2001). The Relationship Between Vascular Wall Shear Stress and Flow-Mediated Dilatation: Endothelial Function Assessed by Phase-Contrast Magnetic Resonance Angiography. *J Am Col Cardiol* **38**, 1860–1865.
- Silber HA, Ouyang P, Bluemke DA, Gupta SN, Foo TK & Lima J a C (2005). Why is flow-mediated dilatation dependent on arterial size? Assessment of the shear stimulus using phase-

- contrast magnetic resonance imaging. *AJP Hear Circ Physiol* **288**, H822–H828.
- Singh RB, Mengi SA, Xu YJ, Arneja AS & Dhalla NS (2002). Pathogenesis of atherosclerosis: A multifactorial process. *Exp Clin Cardiol* **7**, 40–53.
- Sonka M, Liang W & Lauer RM (2002). Automated analysis of brachial ultrasound image sequences: Early detection of cardiovascular disease via surrogates of endothelial function. *IEEE Trans Med Imaging* **21**, 1271–1279.
- Sorensen KE, Celermajer DS, Spiegelhalter DJ, Georgakopoulos D, Robinson J, Thomas O & Deanfield JE (1995). Non-invasive measurement of human endothelium dependent arterial responses: accuracy and reproducibility. *Br Heart J* **74**, 247–253.
- Sorensen MB, Collins P, Ong PJJ & Al E (2002). Long-Term Use of Contraceptive Depot Medroxyprogesterone Acetate in Young Women Impairs Arterial Endothelial Function Assessed by Cardiovascular Magnetic Resonance. *Circulation* **106**, 1646–1651.
- Standring S (2009). *Gray's Anatomy, 40th Edition The Anatomical Basis of Clinical Practice*. Churchill Livingstone.
- Stoner L & McCully KK (2012). Peak and time-integrated shear rates independently predict flow-mediated dilation. *J Clin Ultrasound* **40**, 341–351.
- Stoner L & Sabatier MJ (2011). The use of shear rate-diameter dose-response curves to assess endothelial function. *Cardiovasc Med* **14**, 339–344.
- Stoner L, Sabatier MJ, Black CD & McCully KK (2008). Occasional Cigarette Smoking Chronically Affects Arterial Function. *Ultrasound Med Biol* **34**, 1885–1892.
- Stoner L, Sabatier MJ, Mahoney ET, Dudley GA & McCully KK (2007). Electrical stimulation-evoked resistance exercise therapy improves arterial health after chronic spinal cord injury. *Spinal Cord* **45**, 49–56.
- Stoner L, Tarrant M a, Fryer S & Faulkner J (2013). How should flow-mediated dilation be normalized to its stimulus? *Clin Physiol Funct Imaging* **33**, 75–78.
- Stout M (2009). Flow-mediated dilatation: a review of techniques and applications. *Echocardiography* **26**, 832–841.
- Strinden ST & Steliwagen RH (1984). Inhibition of guanylate cyclases by methylxanthines and papaverine. *Biochem Biophys Res Commun* **123**, 1194–1200.

- Stroz MJ & Fenster A (2010). Measuring flow-mediated dilation through transverse and longitudinal imaging: comparison and validation of methods. *Phys Med Biol* **55**, 6501–6514.
- Szabó C, Ischiropoulos H & Radi R (2007). Peroxynitrite: biochemistry, pathophysiology and development of therapeutics. *Nat Rev Drug Discov* **6**, 662–680.
- Szjgyarto IC (2013). The impact of acute mental stress on brachial artery flow-mediated dilation differs when shear stress is elevated by reactive hyperemia versus handgrip exercise. *Appl Physiol Nutr Metab* **38**, 498–506.
- Taddei S, Virdis a, Ghiadoni L, Magagna a & Salvetti a (1998). Vitamin C improves endothelium-dependent vasodilation by restoring nitric oxide activity in essential hypertension. *Circulation* **97**, 2222–2229.
- Tanaka H, Dinunno FA, Monahan KD, Clevenger CM, Desouza CA & Seals DR (2000). Aging, Habitual Exercise, and Dynamic Arterial Compliance. *Circulation* **102**, 1270–1275.
- Teragawa H, Kato M, Kurokawa J, Yamagata T, Matsuura H & Chayama K (2001). Usefulness of flow-mediated dilation of the brachial artery and/or the intima-media thickness of the carotid artery in predicting coronary narrowing in patients suspected of having coronary artery disease. *Am J Cardiol* **88**, 1147–1151.
- Thijssen DHJ, van Bommel MM, Bullens LM, Dawson E a, Hopkins ND, Tinken TM, Black M a, Hopman MTE, Cable NT & Green DJ (2008). The impact of baseline diameter on flow-mediated dilation differs in young and older humans. *Am J Physiol Heart Circ Physiol* **295**, H1594–H1598.
- Thijssen DHJ, Black MA, Pyke KE, Padilla J, Atkinson G, Harris R a, Parker B, Widlansky ME, Tschakovsky ME & Green DJ (2011a). Assessment of flow-mediated dilation in humans: a methodological and physiological guideline. *Am J Physiol Heart Circ Physiol* **300**, H2–H12.
- Thijssen DHJ, Bullens LM, van Bommel MM, Dawson E a, Hopkins N, Tinken TM, Black M a, Hopman MTE, Cable NT & Green DJ (2009). Does arterial shear explain the magnitude of flow-mediated dilation?: a comparison between young and older humans. *Am J Physiol Heart Circ Physiol* **296**, H57–H64.
- Thijssen DHJ, Rowley N, Padilla J, Simmons GH, Laughlin MH, Whyte G, Cable NT & Green DJ (2011b). Relationship between upper and lower limb conduit artery vasodilator function in humans. *J Appl Physiol* **111**, 244–250.

- Thuillez C & Richard V (2005). Targeting endothelial dysfunction in hypertensive subjects. *J Hum Hypertens* **19 Suppl 1**, S21–S25.
- Tindall AJ, Shetty AA, James KD, Middleton A & Fernando KW (2006). Prevalence and surgical significance of a high-origin anterior tibial artery. *Pain* **123**, 204–209. Epub 2006 Apr 4.
- Tinken TM, Thijssen DHJ, Black M a, Cable NT & Green DJ (2008). Time course of change in vasodilator function and capacity in response to exercise training in humans. *J Physiol* **586**, 5003–5012.
- Tongpun P, Bumrunghaichaichan E & Wattananusorn S (2014). Investigation of entrance length in circular and noncircular conduits by computational fluid dynamics simulation. *Songklanakarin J Sci Technol* **36**, 471–475.
- Tousoulis D, Antoniadis C & Stefanadis C (2005). Evaluating endothelial function in humans: a guide to invasive and non-invasive techniques. *Heart* **91**, 553–558.
- Toyota S & Amaki Y (1998). Hemodynamic Evaluation of the Prone Position by Transesophageal Echocardiography. *J Clin Anesth* **10**, 32–35.
- Triboulet J, Nasr E, Poignet P, Dombre E & Dautzat M (2006). Evaluation of the influence of probe pressure on the B-mode ultrasound measurement of arterial diameter. *Annu Int Conf IEEE Eng Med Biol - Proc* 3831–3835.
- Tschakovsky ME, Pyke KE & Fergus S (2007). Reply to Drs. Harris and Padilla. *J Appl Physiol* **103**, 1109–1109.
- Uehata A, Lieberman EH, Gerhard MD, Anderson TJ, Ganz P, Polak JF, Creager MA & Yeung AC (1997). Noninvasive assessment of endothelium-dependent flow-mediated dilation of the brachial artery. *Vasc Med* 87–92.
- Uppot RN, Sahani D V, Hahn PF, Gervais D & Mueller PR (2007). Impact of obesity on medical imaging and image-guided intervention. *AJR* **188**, 433–440.
- Uzwiak A (2014). Blood Vessels. In *Anatomy and Physiology online*. Available at: [http://www.rci.rutgers.edu/~uzwiak/AnatPhys/Blood\\_Vessels.html](http://www.rci.rutgers.edu/~uzwiak/AnatPhys/Blood_Vessels.html).
- Vanoni V (2006). *Density and Viscosity of Water 0 ° C – 40 ° C*. Available at: <http://ascelibrary.org/doi/pdf/10.1061/9780784408230.ap02>.
- Vaz S, Falkmer T, Passmore AE, Parsons R & Andreou P (2013). The case for using the

- repeatability coefficient when calculating test-retest reliability. *PLoS One* **8**, e73990.
- Verhaar MC (2004). Free radical production by dysfunctional eNOS. *Heart* **90**, 494–495.
- Vickers a J (2001). The use of percentage change from baseline as an outcome in a controlled trial is statistically inefficient: a simulation study. *BMC Med Res Methodol* **1**, 6.
- Voehringer M, Sechtem U & Friedrich MG (2008). Magnetic resonance imaging in vascular biology. *Artery Res* **2**, 9–20.
- Voets T & Nilius B (2009). TRPCs, GPCRs and the Bayliss effect. *Eur Mol Biol Organ J* **28**, 4–5.
- Vogel R a, Corretti MC & Plotnick GD (2000). A comparison of brachial artery flow-mediated vasodilation using upper and lower arm arterial occlusion in subjects with and without coronary risk factors. *Clin Cardiol* **23**, 571–575.
- van de Vosse F & van Dongen M (1998). Cardiovascular Fluid Mechanics, Lecture notes. *Eindhoven Univ Technol*.
- Wallis JW, Wu-conolly L, Rocchini AP & Juni JE (1986). Dynamic Arrhythmia Filtration for Gated Blood-Pool Imaging : Validation Against List Mode Technique. *J Nucl Med* **27**, 1347–1353.
- Walter SD, Eliasziw M & Donner A (1998). Sample size and optimal designs for reliability studies. *Stat Med* **17**, 101–110.
- Weishaupt D, Köchli VD & Marincek B (2006). *Factors Affecting the Signal-to-Noise Ratio. In How does MRI work?: an introduction to the physics and function of magnetic resonance imaging*, 2nd edn. Springer Berlin Heidelberg.
- Weiss EP, Arif H, Villareal DT, Marzetti E & Holloszy JO (2008). Endothelial function after high-sugar food ingestion is improved by endurance exercise performed on the previous day. *Am J Clin Nutr* **15**, 1203–1214.
- Welker KM, Tsuruda JS, Hadley JR & Hayes CE (2001). Radio-frequency coil selection for MR imaging of the brain and skull base. *Radiology* **221**, 11–25.
- West GB & Brown JH (2005). The origin of allometric scaling laws in biology from genomes to ecosystems: towards a quantitative unifying theory of biological structure and organization. *J Exp Biol* **208**, 1575–1592.



- Westerhof N, Stergiopoulos N & Noble MIM (2010). Law of Poiseuille. In *Snapshots of Hemodynamics: An Aid for Clinical Research and Graduate Education*, pp. 9–14. Springer.
- Westman J, Hällgren J, Wahlbeck K, Erlinge D, Alfredsson L & Osby U (2013). Cardiovascular mortality in bipolar disorder: a population-based cohort study in Sweden. *BMJ Open*; DOI: 10.1136/bmjopen-2012-002373.
- Wever RM, van Dam T, van Rijn HJ, de Groot F & Rabelink TJ (1997). Tetrahydrobiopterin regulates superoxide and nitric oxide generation by recombinant endothelial nitric oxide synthase. *Biochem Biophys Res Commun* **237**, 340–344.
- Wheeler EC & Brenner ZR (1995). Peripheral vascular anatomy, physiology, and pathophysiology. *AACN Clin Issues* **6**, 505–514.
- Whitney RJ (1953). The measurement of volume changes in human limbs. *J Physiol* **121**, 1–27.
- Widlansky M, Vita J, Keyes M, Larson M, Hamburg N, Levy D, Mitchell G, Osypiuk E, Vasani R & Benjamin E (2007). Relation of Season and Temperature to Endothelium-Dependent Flow-Mediated Vasodilation in Subjects Without Clinical Evidence of Cardiovascular Disease (From The Framingham Heart Study). *Am J Cardiol* **100**, 518–523.
- Wiesmann F, Petersen SE, Leeson PM, Francis JM, Robson MD, Wang Q, Choudhury R, Channon KM & Neubauer S (2004). Global impairment of brachial, carotid, and aortic vascular function in young smokers: direct quantification by high-resolution magnetic resonance imaging. *J Am Coll Cardiol* **44**, 2056–2064.
- Wilkinson IB & Webb DJ (2001). Venous occlusion plethysmography in cardiovascular research: methodology and clinical applications. *Br J Clin Pharmacol* **52**, 631–646.
- Wilson JMG & Jungner G (1968). *Principles and practice of screening for disease*. Geneva, Switzerland: World Health Organization.
- Womersley J. (1955). Method for the calculation of velocity, rate of flow and viscous drag in arteries when the pressure gradient is known. *J Physiol* **127**, 553–563.
- Wray DW et al. (2011). Progressive handgrip exercise : evidence of nitric oxide-dependent vasodilation and blood flow regulation in humans Progressive handgrip exercise : evidence of nitric oxide-dependent vasodilation and blood flow regulation in humans. *Am J Physiol Heart Circ Physiol* 3001101–1107.
- Wray WD, Witman MAH, Ives SJ, McDaniel J, Trinity JD, Conklin JD, Supiano MA & Richardson RS (2014). DOES BRACHIAL ARTERY FMD PROVIDE A BIOASSAY

- FOR. *Hypertension* **62**, 345–351.
- Wynne BM, Chiao C-W & Webb RC (2009). Vascular Smooth Muscle Cell Signaling Mechanisms for Contraction to Angiotensin II and Endothelin-1. *J Am Soc Hypertens* **3**, 84–95.
- Wythe S, Davies T, Martin D, Feelisch M & Gilbert-Kawai E (2015). Getting the most from venous occlusion plethysmography: proposed methods for the analysis of data with a rest/exercise protocol. *Extrem Physiol Med* **4**, 8.
- Xia C, Meng Q, Liu L-Z, Rojanasakul Y, Wang X-R & Jiang B-H (2007). Reactive oxygen species regulate angiogenesis and tumor growth through vascular endothelial growth factor. *Cancer Res* **67**, 10823–10830.
- Xu S & Touyz RM (2006). Reactive oxygen species and vascular remodelling in hypertension: Still alive. *Can J Cardiol* **22**, 947–951.
- Yamanaka G, Kikura H, Takeda Y & Aritomi M (1999). Flow measurement on Oscillating pipe flow near the Entry using UVP method. In *ISUD: International Symposium on Ultrasonic Doppler Methods for Fluid Mechanics and Fluid Engineering*, pp. 21–24.
- Yanagisawa M, Kurihara H, Kimura S, Tomobe Y, Kobayashi M, Mitsui Y, Yazaki Y, Goto K & Masaki T (1988). A novel potent vasoconstrictor peptide produced by vascular endothelial cells. *Nature* **332**, 411–415.
- Yeboah J, Folsom AR, Burke GL, Johnson C, Polak JF, Post W, Lima JA, Crouse JR & Herrington DM (2009). Predictive value of brachial flow-mediated dilation for incident cardiovascular events in a population-based study: The multi-ethnic study of atherosclerosis. *Circulation* **120**, 502–509.
- Yinon Y, Kingdom JCP, Odutayo A, Moineddin R, Drewlo S, Lai V, Cherney DZI & Hladunewich M a (2010). Vascular dysfunction in women with a history of preeclampsia and intrauterine growth restriction: insights into future vascular risk. *Circulation* **122**, 1846–1853.
- Young H (2011). *Velocity profile of arterial blood flow and severity of peripheral arterial disease (Maste's thesis)* (thesis). The University of Georgia, Athens, Georgia. Available at: [https://getd.libs.uga.edu/pdfs/young\\_hui-ju\\_201105\\_ms.pdf](https://getd.libs.uga.edu/pdfs/young_hui-ju_201105_ms.pdf).
- Zhuo J & Gullapalli RP (2006). MR Artifacts, Safety, and Quality Control. *RadioGraphics* **26**, 275–297.

Zierler ER & Sumner DS (2014). Arterial Physiology. In *Rutherford's Vascular Surgery*, 8th edn., ed. Cronenwett JL & Johnston KW, pp. 132–149. Elsevier Health Sciences, Philadelphia, PA.